Investigating the Electronic Properties of Next Generation Moiré Materials

Ellis Thompson

A dissertation
submitted in partial fulfillment of the
requirements for the degree of

Doctor of Philosophy

University of Washington

2025

Reading Committee:

Matthew Yankowitz, Chair

Xiaodong Xu

David Cobden

Program Authorized to Offer Degree:
Physics

University of Washington

Abstract

Investigating the Electronic Properties of Next Generation Moiré Materials

Ellis Thompson

Chair of the Supervisory Committee:
Matthew Yankowitz
Physics

Since the discovery of monolayer graphene in 2004, van der Waals (vdW) materials have become a mainstay in condensed matter physics. Their layered nature enables us to isolate atomically thin sheets and stack them together with virtually limitless possibility. These designer 2D heterostructures also introduce a new twisting degree of freedom, in which layers are stacked with a rotational offset. The beating pattern formed between their crystalline lattices is known as a moiré superlattice and often leads to new and unexpected properties absent in the parent materials. In this dissertation, I will push the boundaries of this ever-growing parameter space through electronic characterization of various novel moiré materials.

The prototypical example of a moiré heterostructure consists of two graphene layers stacked with a small interlayer twist and has been shown to exhibit a wide variety of novel electronic properties driven by strong electron-electron interactions. In the first part of this thesis, we show that adding more layers to this basic framework preserves much of the same physics and in some cases leads to entirely new electronic phenomena. Furthermore, we find that signatures of the moiré superlattice survive into bulk graphite structures, composed of up to 40 layers of graphene.

The second part of this thesis focuses on moiré systems composed of transition metal dichalcogenides, a class of vdW materials composed of alternating layers of transition metal and chalcogen atoms. In particular, twisted molybdenum ditelluride (tMoTe2) was recently found to exhibit the long-sought fractional quantum anomalous Hall (FQAH) effect, a consequence of strong electron interactions and robust band topology. We use scanning tunneling microscopy to image the energy-dependent nanoscale wave function of tMoTe2, illustrating a connection between its microscopic structural properties and band topology.

TABLE OF CONTENTS

LIST OF FIGURES

LIST OF ABBREVIATIONS

2DEG Two-dimensional electron gas.

AFM Atomic force microscopy.

AHE Anomalous Hall effect.

BI Band insulator.

BZ Brillouin zone.

CI Correlated insulator.

DFT Density functional theory.

DOS Density of states.

DW Domain wall.

FFT Fast Fourier transform.

FQAH Fractional quantum anomalous Hall.

hBN/BN Hexagonal Boron Nitride.

HM Half metal.

IQAH Integer quantum anomalous Hall.

IVC Inter-valley coherent state.

LDOS Local density of states.

MATBG Magic angle twisted bilayer graphene.

MBZ Moiré Brillouin zone.

NM Normal metal.

PFM Piezoresponse force microscopy.

QAHE Quantum anomalous Hall effect.

QHE Quantum Hall effect.

QM Quarter metal.

QOs Quantum oscillations.

STM Scanning tunneling microscopy.

SVP Spin-valley polarized.

TBG Twisted bilayer graphene.

TMD Transition metal dichalcogenide.

vHS Van-Hove singularity.

ACKNOWLEDGMENTS

First, I have to thank my advisor Prof. Matthew Yankowitz. I'm profoundly grateful for your endless supply of scientific and professional guidance. I appreciate all the opportunities you've given me especially in the midst of certain equipment disasters. Above all, I've appreciated your willingness to take on a student with minimal experience in this field and for believing in my ability to succeed. I can't think of a better introduction to the world of 2D materials than my experience in your group.

I also want to acknowledge the many other professors who've had an impact on my research career at UW. In particular, thank you to Prof. Dave Cobden for your insightful contributions towards solving various experimental mysteries and for your constant supply of helpful skepticism; to Prof. Di Xiao and Prof. Ting Cao for your invaluable theoretical contributions to our work and for enduring and answering all of my naive questions in research meetings; to Prof. Xiaodong Xu for lending your TMD wisdom to our STM team as well as your professional guidance; and to the other members of my doctoral committee, Prof. Mark Rudner, Prof. Masha Baryakhtar, and Prof. Alexandra Velian.

I've had the privilege of learning from two extremely capable postdoctoral researchers, and I am so grateful for the knowledge they shared. Thank you to Dr. Dacen Waters for being a true mentor during the first half of my PhD. You guided me through so many new experiences, from trouble-shooting my many failed devices to setting up a lab, and I learned so much from watching you work. Thank you as well to Dr. Florie Mesple for sharing your immense knowledge of STM and always advocating for me. I'll always strive to emulate your careful scientific thought and confident approach to building and fixing equipment.

The graduate student community at UW is truly unparalleled and I'd like to thank many of my peers for helping me both in research and in life during my PhD. I must extend a special thanks to my collaborator Toby Chu who contributed so much to the development of the STM sector of our group. I also want to thank my long-time office mate, Anna Okounkova, who's endless support and lively presence got me through so many hard days in lab. Thank you as well to other past and current students in the Yankowitz Lab, Dr. Chun-Chih Tseng, Dr. Xuetao Ma, Manish Kumar, Derek Waleffe, Abigail Sohm, and Jackson Chapman, for creating a truly wonderful research environment. In addition, I've had the pleasure of collaborating with and learning from many other people in our condensed matter community:

Dr. Paul Nguyen, Eric Lester, Dr. Elliott Runburg, Gianluca Delgado, Dr. Jordan Fonseca, Dr. Minhao He, Dr. Jiaqi Cai, Dr. Heonjoon Park, Dr. Eric Anderson, Jack Barlow, Dr. Chaowei Hu, Dr. Laurel Anderson, and Dr. Dmitry Ovchinnikov. What a privilege it's been to get to know all of you and work work with so many people I admire!

I'd also like to acknowledge the help of Pysics and UW staff members who've played a pivotal role in keeping our experiments running smoothly. In particular, thank you to the Physics machine shop staff, the physics IT team, the WNF Cleanroom staff scientists, and the MEMC shared equipment superusers and managers.

I entered my PhD program at the height of the COVID-19 pandemic and I truly don't think I could have succeeded without so many friendly faces in my graduate cohort and in the broader UW physics community. To name a few, thank you to Sam Borden, Gillian Shen, CJ Nave, Eli Lilleskov, Grace Song, Jimmy Sinnis, Harry Ni, Adina Ripin, Kent Wilson, Murali Saravanan, Zhiyao Li and Nikita Zemlevskiy.

Lastly I want to thank my family for their endless support throughout my PhD. Thank you to my partner, Sam, for helping me through every lab mishap and bad day with his kindness and positive spirit. Thank you to my sisters, June and Pearl, for making me laugh and reminding me that life is more than your PhD research. Finally, thank you to my mom and dad for a lifetime of encouragement and advice; you're the kindest and boldest people I've known and you inspire me every day.

DEDICATION

To my mom, inspired by her unrelenting sense of curiosity and wonder

Chapter 1
INTRODUCTION

1.1 Motivation

To many people, the term '2D material' sounds unphysical. The objects we interact with on a daily basis occupy a 3 dimensional volume of space. Even the thinnest sheet of paper has some small visible width. Is it even possible to realize a truly two dimensional object? And if so, how are these objects fundamentally different from three dimensional ones? These questions have motivated a large part of the condensed matter physics community since the mid-20th century. More rigorously, if we can confine an electronic system into a 2 dimensional space, what kind of collective behavior will emerge?

By now physicists have conducted an enormous amount of theoretical and experimental research showing how electrons can be effectively confined into two dimensions using a variety of material platforms and that this dimensional reduction leads to profound changes in collective electronic behavior. This was first realized experimentally in layered semiconducting heterostructures, such as silicon field effect transistors or gallium arsenide (GaAs)/aluminum gallium arsenide (AlGaAs) junctions. In these devices, charges are electrostatically confined to the interface between semiconducting and insulating layers so that their motion is strongly suppressed in the direction perpendicular to the interface, forming a two dimensional electron gas (2DEG).[1,2] Still, these 2DEG systems are based on confinement within 3D materials; the question of realizing a truly two-dimensional crystal remained. In 2004, Geim and Novoselov answered this call by isolating monolayer graphene, which consists of one layer of carbon atoms arranged in a hexagonal lattice.[3] A zoo of other layered van der Waals (vdW) materials were soon realized in their monolayer form, each with unique properties, from magnetism to superconductivity.[4,5] After 20 years of advancements in nanofabrication, we now have the ability to combine these materials into multi-layer vdW heterostructures, with an essentially unlimited number of combinations.[6–9]

Moiré materials are a class of heterostructures which exploit the unique degrees of freedom enabled by a vdW interace. Thin sheets of one vdW material can be stacked on top of any other arbitrary vdW material with arbitrary orientation between the two crystal lattices. Due to the absence of out-of-plane covalent bonds in the constituent materials, this procedure leads to a relatively stable composite structure with a pristine interface. Stacking two vdW layers with a slight lattice mismatch creates a long range beating pattern between their crystal lattices, known as a moiré superlattice. This new mesoscopic lengthscale

modifies the structural, electronic, and optical properties of the constituent materials, and often leads to intruiging collective behavior.[10] The formation of a moiré superlattice was first demonstrated in monolayer graphene aligned to insulating hexagonal boron nitride (hBN).[11–13] Soon after, it was discovered that stacking two vdW layers with a small interlayer twist also generates a moiré superlattice through the rotational misalignment of the two crystal lattices. Since it is often difficult to find pairs of vdW materials with close but slightly mismatched crystal structures, this twist degree of freedom provides a powerful tool to engineer the electronic properties of vdW heterostructures. A moiré superlattice created by twisting was first realized with twisted bilayer graphene (TBG), which exhibits electrically tunable symmetry-broken correlated insulating states and superconductivity.[14–16] Since this foundational discovery, the study of moiré materials has exploded in popularity with newer and more complex moiré systems realized every year.

The goal of this thesis is to extend the prototype of TBG into new moiré systems with different degrees of freedom. Specifically, we study the electronic properties of several 'next generation' moiré systems both macroscopically, with electronic transport measurements, and microscopically, with scanning tunneling microscopy (STM). Our results introduce and characterize a set of moiré building blocks for the development of designer 2D quantum systems with unprecedented tunability of electron-electron interactions.

1.1.1 Outline of Thesis

In the rest of this chapter, I will describe the theoretical framework necessary to understand the basic electronic behavior of moiré materials. This is not meant to serve as a review of all possible electronic properties; it will focus mainly on those relevant to the experimental work presented in later chapters.

In chapter 2, I will detail the experimental methods we use to create and study vdW heterostructures. It is organized into 3 broad sections. The first focuses on fabrication of different types of vdW devices used in the following chapters. The second details the utility of electronic transport measurements and provides a guide for interpreting transport data acquired from moiré materials. The third explains the theory and uses of STM, as well the experimental considerations necessary to perform STM on vdW devices.

In chapter 3, I will present our transport studies of a family of twisted multilayer graphene heterostructures which are distinct from TBG by their spatial symmetry. We demonstrate that these structures host similar topological flat bands, but exhibit slightly varied presentation of interaction-driven phases. In chapter 4, we generalize this construction to the limit of bulk graphite by studying the impact of a single twisted interface within a graphite thin film. We find that this embedded 2D moiré superlattice

unexpectedly modifies the transport properties of the entire graphite film, particularly at high magnetic fields.

In chapter 5, I will present our STM studies of twisted molybdenum ditelluride (tMoTe$_2$), which has been shown to exhibit the long-sought fractional quantum anomalous Hall effect in previous optical and transport studies. Our measurements reveal direct evidence of a real-space topological texture of electronic layer polarization on the scale of the moiré superlattice. Since this texture has been theoretically linked to the particular topological properties of tMoTe$_2$, our study provides unprecedented insight into the details of this complex relationship. In addition, I will present a brief summary of our efforts to study the microscopic properties of tMoTe$_2$ as a function of electrostatic gating.

Finally, in chapter 6, I will provide concluding remarks on the impact and open questions generated by our experimental work in chapters 3-5.

1.2 Electrons in 2 dimensions

Though the many experimentally available 2D systems discussed in the previous section exhibit varied electronic properties, they exhibit several ubiquitous phenomena which arise simply as a consequence of dimensional reduction. In this section, I will detail some general characteristics of two-dimensional electronic systems which are particularly relevant to this thesis.

1.2.1 Quantum Hall Effect

Applying a perpendicular magnetic field to a 2DEG leads to a transport phenomenon known as the Quantum Hall Effect (QHE).[1] The QHE is characterized by vanishing longitudinal resistivity, $\rho_{xx} = 0$, coincident with transverse resistivity quantized in units of h/e^2, $\rho_{xy} = \frac{h}{e^2}\frac{1}{\nu}$, $\nu \in \mathbb{Z}$. Figure 1.1a shows a representative example of the measured longitudinal and Hall resistance in a GaAs 2DEG as a function of perpendicular magnetic field strength. What makes the QHE truly remarkable is its insensitivity to sample details; since it's discovery dozens of individual samples made with different materials and fabrication procedures, featuring various amounts of disorder, all exhibiting the same values of quantized Hall resistivity, differing by only millionths of a percent.[17]

The robustness of this quantization can be understood from a semiclassical picture illustrated schematically in figure 1.1. Consider a free electron confined in rectangle of finite size in the xy plane subject to a perpendicular magnetic field, $\mathbf{B} = (0, 0, B)$. Due to the Lorentz force, the electron will move in a circular orbit at the cyclotron frequency, $\omega_C = \frac{eB}{m_e}$, where e and m_e are the charge and mass of the electron respectively. If the electron is close enough to the boundary of the rectangle, it cannot complete its orbit; instead, it will reflect off of the boundary and enter another orbit, enabling a skipping motion

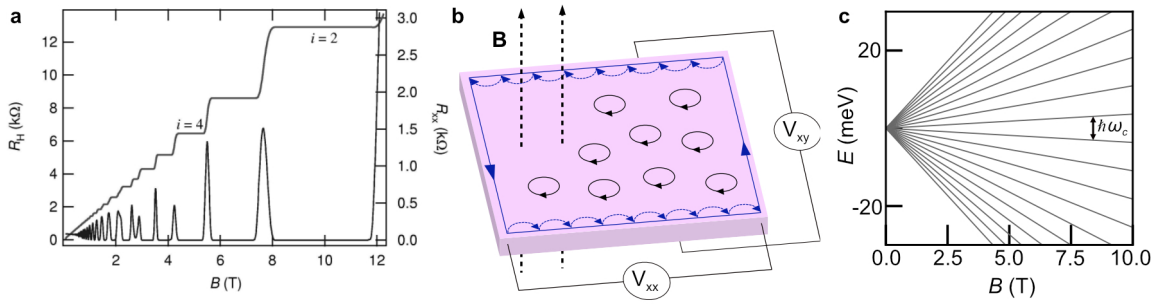

Figure 1.1: **Quantum Hall Effect in a 2DEG**, **a**, Londitudinal and Hall resistance, R_{xx} and R_H, of a 2DEG as a function of magnetic field. Plot is taken from Jeckelmann and Jeanneret. *Reports on Progress in Physics* **64** (2001).[17] **b**, Schematic illustration of semiclassical picture of Landau levels. Black circles represent bulk cyclotron orbits and blue semi-circles represent skipping orbits that form a chiral edge state. **c**, Spectrum of Landau levels in a 2DEG separated by $\hbar\omega_c$, where ω_c is the cyclotron frequency.

along the edge. The result is a chiral edge state: electrons move in one direction along the edge without back-scattering. This edge state is responsible for the peculiar transport signature of the QHE, and the absence of back-scattering is what makes this phenomenon so robust.

A fully quantum treatment of a 2DEG in a perpendicular magnetic field finds that spectrum of electron eigenstates develops into a set of discrete energy levels separated by gaps on the order of the cyclotron frequency, ω_C, plotted in figure 1.1c. By incorporating a confining potential that simulates the physical edge of a 2DEG system, the emergence of chiral edge states of the quantization of ρ_{xy} can be explicitly derived.[18]

The QHE is somewhat ubiquitous to 2D systems and underpins an abundance of complex electronic phenomena. Landau levels are perfectly flat in momentum space, which strongly enhances the role of Coulomb interactions (the importance of enhanced electron-electron interactions within flat bands will reoccur numerous times in this thesis). Landau levels thus host various interaction driven phases—most notably the fractional quantum Hall effect.[19] The spectrum of Landau levels that emerges in a given material also depends on its low energy dispersion, which has led to the observation of different variants of the QHE in different systems.[19–21]

1.2.2 Topology in two dimensions

Topology in general is concerned with classifying invariant properties of mathematical objects. In the context of quantum mechanics, this means studying the invariant properties of a given Hamiltonian and the implications of these properties in the corresponding physical system. A full explanation of this complex mathematical concept is beyond the scope of this thesis, but topological analyses of 2D

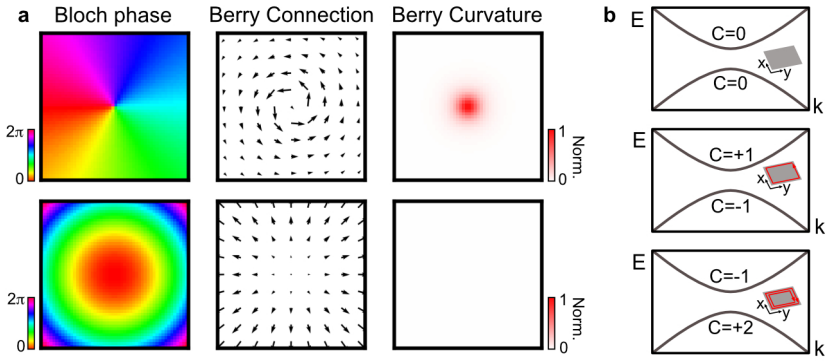

Figure 1.2: **Topology in 2D systems**, **a**, Schematic plots of the Bloch phase, Berry connection, and Berry curvature projected into a 2D $\mathbf{k}$-space for topologically nontrivial (top) and trivial (bottom) bands. **b**, Illustration of correspondence between Chern number of occupied bands and number of chiral edge states for several cases.

condensed matter systems often yield physically meaningful results.[22]

Within the electronic energy bands of a two dimensional crystal, one relevant topological invariant is the Chern number. It is defined for each electronic band as,

$$C = \frac{1}{2\pi}\int_{BZ} \mathbf{\Omega}\cdot d\mathbf{S} = n, \;\; n \in \mathbb{Z} \tag{1.1}$$

In this equation, $\mathbf{\Omega}$, is the berry curvature which is defined as,

$$\mathbf{\Omega}(\mathbf{k}) = \nabla_{\mathbf{k}} \times \mathbf{A}(\mathbf{k}) = \nabla_{\mathbf{k}} \times i\langle\psi(\mathbf{k})|\nabla_{\mathbf{k}}\psi(\mathbf{k})\rangle \tag{1.2}$$

where $\mathbf{A}(\mathbf{k}) = i\langle\psi(\mathbf{k})|\nabla_{\mathbf{k}}\psi(\mathbf{k})\rangle$ is known as the Berry connection. The Berry connection describes how the phase of the Bloch wavefunction evolves with crystal momentum, and the Berry curvature characterizes the winding of this phase. Figure 2a illustrates this concept schematically. If there is a nontrivial phase winding, the Chern number will be nonzero and we refer to the band as topologically nontrivial. Otherwise, it is topologically trivial. *

The value of the Chern number is directly connected the presence of edge states, like those discussed in Chapter 1.1.1. In general, the number of chiral edge states is equal to the sum of the Chern numbers of all filled bands, illustrated in figure 2a.† In fact, Landau Levels each have a Chern number of 1, faciliting

*It is worth noting that this mathematical formalism only works in two dimensions. The electronic bands in 2D live on a 2-dimensional manifold, over which the surface integral in 1.1 can be easily computed. In 3D, electronic bands live on a 3-dimensional manifold, and a similar integral of the Berry curvature will not converge to a single integer as in 2D. Three-dimensional crystals can still host topologically nontrivial bands, but understanding the physical consequences requires a more complicated analysis.

†This is a notable example of the concept of bulk-boundary correspondence: the topological properties of a system's bulk Hamiltonian directly determine what happens at the edge of the physical system.

a topological interpretation of the QHE.[23] This leads to an important point: a non-zero Chern number requires broken time-reversal symmetry. In the case of Landau levels, time-reversal symmetry is broken by an external magnetic field. In other cases, time reversal symmetry can be broken spontaneously by electron-electron interactions. These varying manifestations of topology in different 2D systems will be a central focus throughout this thesis.

1.3 Van der Waals materials

Van der Waals materials are composed of atomically thin crystalline layers held together by weak van der Waals forces. The relative strength of intralayer covalent bonds compared to interlayer vdW forces allows for isolation of independent atomically-thin sheets, which naturally host a wealth of 2-dimensional physics. Compared to more traditional 2D platforms, vdW materials possess several key advantages. For one thing, researchers have now realized an abundance of different vdW materials with widely different properties: metals, semi-metals, insulators, magnets, superconductors etc. This simply allows for more varied and nuanced channels to study the effects of reduced dimensionality. Additionally, vdW layers are often stacked on top of each other to realize vdW heterostructures, which often have interesting properties absent in the parent materials. Lastly, electrostatic gates can be easily incoporated into vdW heterostructures to modulate the carrier density and electric field within atomically thin layers. These advantages conspire to make vdW materials a highly tunable and versatile platform for studying many-body systems in two dimensions. In the following subsections, I will describe the vdW materials used in the experiments presented in this thesis.

1.3.1 Graphene and graphite

Though known by many as the inner component of a pencil, graphite is also one of the most elementary and fruitful vdW materials. It is composed of layers of carbon atoms arranged in a hexagonal 2D lattice, illustrated in figure 1.3a. The corresponding first Brillouin zone is illustrated in figure 1.3b. One sheet of carbon atoms with this crystal structure is known as graphene.[24] Isolated graphene was first realized using the now ubiquitous scotch tape exfoliation method, and its discovery received the Nobel prize in 2010.[3]

On its own, graphene has many remarkable electronic properties, owing to its linear dispersion at low energies. This can be derived with a tight binding approach considering two triangular sublattices and nearest neighbor hopping between them.[24,25] This model leads to the following Bloch Hamiltonian,

$$H = \begin{pmatrix} 0 & t\sum e^{i\mathbf{k}\cdot v_n} \\ t\sum e^{-i\mathbf{k}\cdot v_n} & 0 \end{pmatrix} \tag{1.3}$$

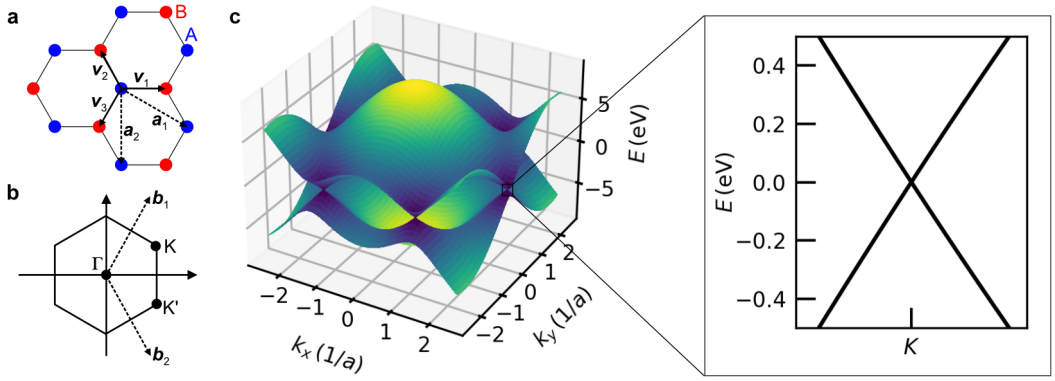

Figure 1.3: **Monolayer graphene bandstructure**, **a**, Crystal structure of graphene. $\mathbf{a}_i$ are real space lattice vectors and $\mathbf{v}_i$ are the nearest neighbor hopping paths used in the two band tight binding model. **b**, Brilloin zone of graphene, with high symmetry points marked by black dots. $\mathbf{b}_i$ are the reciprocal lattice vectors. **c** (Left) Dispersion of the graphene valence and conduction bands calculated from equation 1.4. (Right) Zoom in of the Dirac dispersion near the K point plotted against the the k_y direction.

where **t** is the strength of nearest neighbor hopping and v_1,v_2, and v_3 are the positions of the three nearest neighbors, defined in 1.3a. The resulting energy eigenvalues are

$$E = \pm t\sqrt{f(\mathbf{k})} = \pm t\sqrt{1 + 4\cos(\frac{\sqrt{3}}{2}ak_x)\cos(\frac{1}{2}ak_y) + 4\cos^2(\frac{\sqrt{3}}{2}ak_x)} \tag{1.4}$$

where a is the lattice constant of graphene. This energy spectrum is plotted in figure 1.3c. At zero energy, there are Dirac crossings at the six corners of the Brillouin Zone known as the K/K' points. The inset in figure 1.3c shows a zoom in to the K/K' point that reveals a linear dispersion around the Dirac point at low energies. The model presented does not take into account the electron spin degree of freedom, but the net effect is a two-fold spin degeneracy of the conduction and valence bands.

An important aspect of the graphene energy bands is the subtle relationship between the K and K' points, often referred to as the K and K' valleys. To demonstrate this explicitly, we can expand the Bloch Hamiltonian in equation 1.3 around the K point, where $\mathbf{k} = \mathrm{K} + \mathbf{q}$, and $|\mathbf{q}| \ll |\mathrm{K}|$. To first order in $\mathbf{q}$, this procedure yields,

$$H_{\mathrm{K}} = \frac{\sqrt{3}}{2}ta\begin{pmatrix} 0 & q_x - iq_y \\ q_x + iq_y & 0 \end{pmatrix}$$

If we do the same procedure, but expand around the K' point, we get,

$$H_{\mathrm{K}'} = \frac{\sqrt{3}}{2}ta\begin{pmatrix} 0 & -q_x - iq_y \\ -q_x + iq_y & 0 \end{pmatrix}$$

These expressions can be combined to yield,

$$H = \frac{\sqrt{3}}{2} ta \begin{pmatrix} 0 & \tau q_x - i q_y \\ \tau q_x + i q_y & 0 \end{pmatrix} \tag{1.5}$$

where τ is a valley index that is 1 for the K valley and -1 for the K' valley. Regardless of the value of τ, this Hamiltonian leads to the well-known Dirac dispersion of graphene,

$$E = \pm \hbar v_F |\mathbf{q}| \tag{1.6}$$

where $v_F = \frac{\sqrt{3}}{2} \frac{ta}{\hbar}$ is the Fermi velocity. However, it is clear that the low energy Hamiltonian is not equivalent at K and K'; more explicitly, they are related by time reversal symmetry.

Adding more layers of carbon atoms strongly modifies this dispersion. The lowest energy stacking configuration of graphene layers within a graphite crystal is known as Bernal stacking. Bernal stacked layers are arranged such that the atoms in the A sublattice of a given layer are aligned to the atoms in the B sublattice of the adjacent layers, illustrated schematically in figure 1.4a. The Brillouin zone of graphite is essentially the same as in graphene, pictured in figure 1.3b. It is simplest to examine the Bernal bilayer graphene Hamiltonian and then generalize these characteristics to a larger number of layers. The dispersion of Bernal bilayer graphene can be captured by a tight binding model involving 2 sublattices on each layer, leading to the following 4 by 4 Bloch Hamiltonian near the K point,

$$H = \hbar v_F \begin{pmatrix} -V & q_x - i q_y & 0 & 0 \\ q_x + i q_y & -V & \gamma_1 & 0 \\ 0 & \gamma_1 & V & q_x - i q_y \\ 0 & 0 & q_x + i q_y & V \end{pmatrix} \tag{1.7}$$

where γ_1 is the nearest-neighbor interlayer hopping strength, and V is the potential difference between the layers.[26] The eigenvalues of the matrix in equation 1.7 do not have as simple a form as those in equation 1.4, but they yield a roughly parabolic dispersion at low energies when $V = 0$. When $V \neq 0$, a gap opens at zero energy, distorting the bottom (top) of the conduction (valence) band. Figure 1.4b shows a calculation of the bilayer graphene dispersion at $V = 0$ and $V \neq 0$. One key difference between this Hamiltonian and that of monolayer graphene is that inversion symmetry can be broken by a nonzero potential difference between the layers. The Dirac point in monolayer graphene is protected by C_2T symmetry (the combination of inversion and time-reversal symmetry); broken inversion symmetry in bilayer graphene thus opens a gap at the Dirac point. ‡

‡The theoretical treatment of graphene and bilayer graphene presented from this chapter are largely adapted from review paper by Castro Neto et al.,[24] which is an excellent source for further reading on this subject.

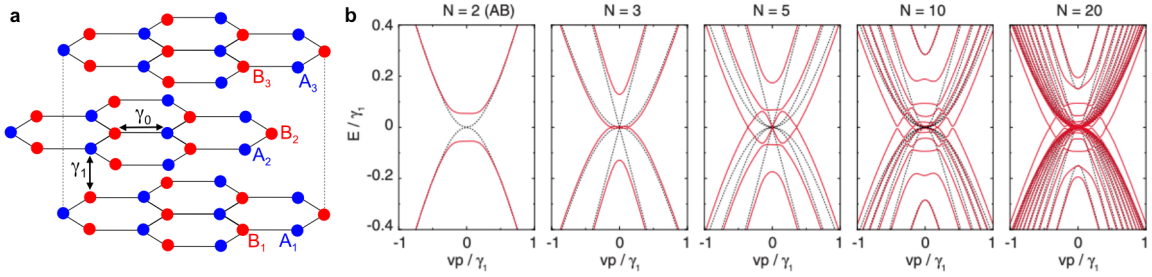

Figure 1.4: **Bernal stacked graphite bandstructure**, **a**, Crystal structure of Bernal stacked trilayer graphite. γ_0 and γ_1 denote nearest-neighbor intra- and inter-layer hopping, respectively. **b** Band structure of N-layer thick graphite with varying N for zero potential difference across the layers (black curves), and nonzero (red curves). The potential drop across the N layers is incorporated using a self-consistent model of screening. Plots are taken from Koshino. *PRB* **81** (2010).[27]

To generalize this Hamiltonian to N-layers of Bernal stacked graphite, one can construct an N by N matrix with the same general form as equation 1.7,

$$H = \begin{pmatrix} H_1 & U & & & & \\ U^\dagger & H_2 & U & & & \\ & U^\dagger & H_3 & U & & \\ & & \ddots & \ddots & \ddots & \\ & & & U^\dagger & H_N & U \end{pmatrix} \tag{1.8}$$

and

$$H_j = \begin{pmatrix} V_j & q_x - iq_y \\ q_x + iq_y & Vj \end{pmatrix}, \quad U = \begin{pmatrix} 0 & 0 \\ \gamma_1 & 0 \end{pmatrix} \tag{1.9}$$

where V_j is the potential at the jth layer.[27] This is relatively simple when $V = 0$, but it is not so straightforward to incorporate a potential difference between layers as you generalize to a large N. This is because the potential difference at each layer depends sensitively on the screening properties of graphite. Figure 1.4b shows calculations of the 3-, 5-, 10-, and 20-layer graphite dispersion with and without finite V using a self-consistent treatment of screening to approximate the potential at each layer.[27] For the case of $V = 0$ in N-layer graphite, each pair of Bernal stacked layers contributes a parabolic band, and the unpaired layer in the case of odd N contributes a Dirac crossing. Applying a nonzero potential difference across the layers distorts the parabolic/Dirac crossings and pushes some parabolic bands to higher energies. Though not as simple as bilayer graphene, the bandstrucure of Bernal stacked graphite posseses the same basic symmetries and evolves similarly with added potential difference.

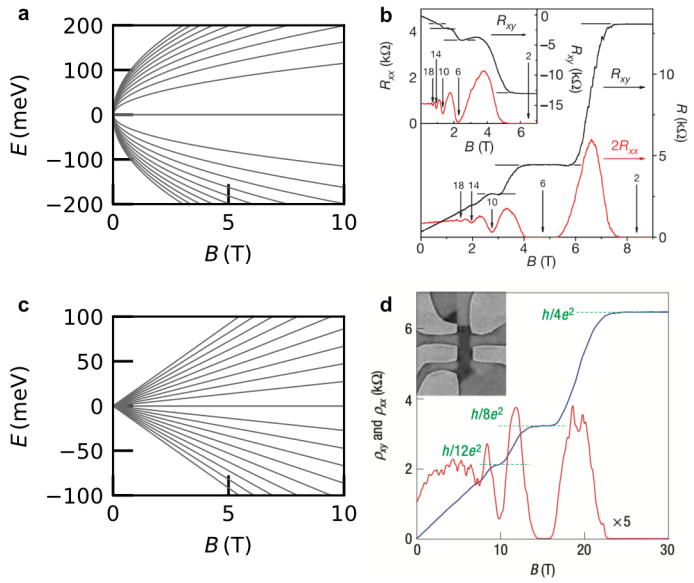

Figure 1.5: **Quantum hall effect in monolayer and bilayer graphene**, **a** Spectrum of Landau levels in monolayer graphene. **b**, Longitudinal and Hall resistance, R_{xx} and R_{xy}, in monolayer graphene as a function of magnetic field. Inset shows a similar measurement where the chemical potential is set below the Fermi energy instead of above. Plot taken from Zhang at al. *Nature* **438** (2005).[28] **c**, Spectrum of Landau levels in bilayer graphene. **d** Longitudinal and Hall resistivity, ρ_{xx} and ρ_{xy}, in bilayer graphene as a function of magnetic field. Inset shows an image of the device used for the measurements. Plot taken from Novoselov at al. *Nature Physics* **2** (2006).[29]

QHE and topology in graphene

Shortly after its discovery, graphene was shown to host the QHE with a slightly different flavor than in conventional 2DEG devices. Its linear dispersion modifies the spectrum of resulting Landau levels such that they follow a square root dependence on magnetic field strength,

$$E_{\pm\nu} = \pm v_F \sqrt{2e\hbar B\nu} \tag{1.10}$$

for $\nu \geq 1$. In addition there is one Landau Level at zero energy arising from the symmetry-protected Dirac point.[28,30] Figure 1.5a plots this dispersion up to $\nu = 10$. All the Landau Levels are four-fold degenerate, two for electron spin, and two for valley K/K'. This leads to quantized Hall resistance of $\frac{1}{2+\nu}\frac{h}{e^2}$ where ν starts from 0. This is shown in transport measurements in figure 1.5b.

Bilayer graphene also hosts the QHE, but with a linear dependence on magnetic field strength,

$$E_\nu = \hbar\omega_C\sqrt{\nu(\nu-1)} = \frac{2\hbar e v_F^2}{\gamma_1} B\sqrt{\nu(\nu-1)} \tag{1.11}$$

where ν is an integer. All the Landau levels are four-fold degenerate, except for the zero energy Landau level which is eight-fold degenerate. This extra factor can be thought of as an orbital degeneracy, since the $\nu = 0$ and $\nu = 1$ quantized orbit conditions both lead to $E_\nu = 0$. As a result, Hall resistance is quantized to $\frac{1}{4\nu}\frac{h}{e^2}$, where ν starts from ± 1, shown in figure 1.5d.[29]

The particular nature of the QHE in graphene and bilayer graphene can be linked to topological considerations. This is slightly simpler for monolayer graphene, given the Dirac hamiltonian near the K/K' points given in equation 1.5. The eigenstates of this Hamiltonian are analogous to those of a relativistic spin-1/2 fermion, where the spin is replaced by a sublattice pseudospin. The wavefunctions are represented by spinors,

$$|\psi_{\mathrm{K}\pm}\rangle = \frac{1}{\sqrt{2}}\begin{pmatrix} 1 \\ \pm e^{i\phi} \end{pmatrix}, \quad |\psi_{\mathrm{K}'\pm}\rangle = \frac{1}{\sqrt{2}}\begin{pmatrix} 1 \\ \pm e^{-i\phi} \end{pmatrix} \tag{1.12}$$

where $\phi = \arctan(\frac{q_y}{q_x})$. $\psi_{\mathrm{K/K'}+}$ ($\psi_{\mathrm{K/K'}-}$) represents an eigenstate with crystal momentum $\mathbf{q}$ near the K/K' point and in the conduction (valence) band.[24] The pseudospin can then be defined as,

$$\mathbf{S}_{\mathrm{K}\pm} = \langle\psi_{\mathrm{K}\pm}|\boldsymbol{\sigma}|\psi_{\mathrm{K}\pm}\rangle, \quad \mathbf{S}_{\mathrm{K}'\pm} = \langle\psi_{\mathrm{K}'\pm}|\boldsymbol{\sigma}|\psi_{\mathrm{K}'\pm}\rangle \tag{1.13}$$

where $\boldsymbol{\sigma} = \sigma_x\hat{k_x} + \sigma_y\hat{k_y} + \sigma_z\hat{k_z}$. Given equation 1.12, the pseudospin reduces to,

$$\mathbf{S}_{\mathrm{K}\pm} = \pm\cos\phi\hat{k_x} \pm \sin\phi\hat{k_y}, \quad \mathbf{S}_{\mathrm{K}'\mp} = \mp\cos\phi\hat{k_x} \pm \sin\phi\hat{k_y} \tag{1.14}$$

This tell us that the pseudospin points in the k_x-k_y plane and winds through one full rotation as you encircle the Dirac point. The direction of the winding depends on whether $\mathbf{S}$ is defined for the conduction

or valence bands and/or the K or K' point. Figure 1.6a illustrates this pseudospin winding. When an s=1/2 spin moves along some closed loop, its wavefunction acquires a geometric phase factor determined by the solid angle, Ω, traced by the spin, $e^{i\Omega/2}$. This is called a Berry phase and is equivalent to the integral of the Berry connection over the same closed loop. The 2π pseudospin winding around K/K' in momentum space is analogous to this situation, and results in a $\pm\pi$ Berry phase associated with the graphene Dirac points. This implies some divergence of the Berry curvature at the Dirac points. However, since the Dirac point is shared in a sense between the conduction and valence band and these have opposite phase winding, the Berry curvature cannot be well defined at the Dirac points of graphene. Nevertheless, this $\pm\pi$ Berry phase has physical consequences, namely it leads to an offset in the Chern number of the resulting Landau Levels.

The situation in bilayer graphene is very similar. The four by four Hamiltonian in equation 1.7 can be reduced to a two by two Hamiltonian with a similar Dirac form. This is because the carbon atoms in the A sublattice of the top layer sit directly above those in the B sublattice of the bottom layer. These pairs of carbon atoms essentially dimerize and create energy eigenstates at large energies. Thus, the low energy Hamiltonian is mostly governed by the B sublattice of the top layer and the A sublattice of the bottom layer, and the Hamiltonian is reduced to,

$$H_K = \frac{\hbar^2 v_F^2}{\gamma_1}\begin{pmatrix} 0 & (q_x - iq_y)^2 \\ (q_x + iq_y)^2 & 0 \end{pmatrix} \tag{1.15}$$

setting the potential difference across the two layers to zero. The spinor eigenstates in this case are instead given by[24]

$$|\psi_{\mathrm{K}\pm}\rangle = \frac{1}{\sqrt{2}}\begin{pmatrix} 1 \\ \pm e^{i2\phi} \end{pmatrix}, \quad |\psi_{\mathrm{K}'\pm}\rangle = \frac{1}{\sqrt{2}}\begin{pmatrix} 1 \\ \pm e^{-i2\phi} \end{pmatrix} \tag{1.16}$$

which produces a peudospin,

$$\mathbf{S}_{\mathrm{K}\pm} = \pm\cos 2\phi\hat{k_x} \pm \sin 2\phi\hat{k_y}, \quad \mathbf{S}_{\mathrm{K}'\pm} = \mp\cos 2\phi\hat{k_x} \pm \sin 2\phi\hat{k_y} \tag{1.17}$$

This tells us that the pseudospin in bilayer graphene winds in the same direction as in monolayer graphene but winds twice as fast, (figure 1.6b). The parabolic band touchings at K and K' thus contribute a 2π Berry phase and a corresponding offset in the Chern numbers of the Landau level spectrum (figure 1.5c-d).

1.3.2 Transition metal dichalcogenides

Transition metal dichalcogenides (TMDs) are a class of vdW materials with the general chemical formula MX_2, where M represents a transition metal and X represents a chalcogen (S, Se, Te). Like graphite, these materials have existed for many years, mainly for industrial purposes, but were not studied in their

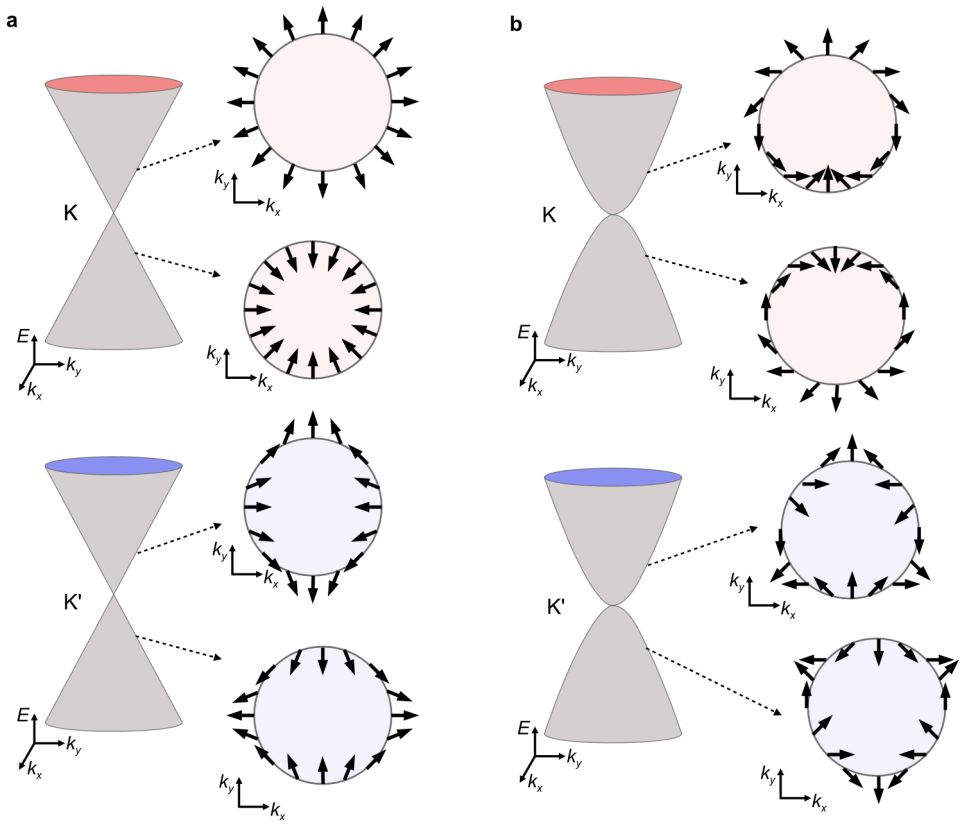

Figure 1.6: **Pseudospin in monolayer and bilayer graphene**, **a** Pseudospin in monolayer graphene in the valence and conduction bands near the K (top) and K' (bottom) valleys. **b** Same as (**a**) for bilayer graphene.

monolayer form until recently.[30] They occur in a variety of different 2D crystal structures and in general exhibit a variety of different electronic properties.[31] One notable category are the group VI transition metal (W,Mo) TMDs in the 2H crystal phase which act as 2D semiconductors and have been studied extensively for their wide applicability to electronic and optical devices.[32–34]

The 2H crystal phase, shown schematically in figure 1.7a, consists of monolayer crystalline sheets that are 3 atoms thick: one layer of transition metal atoms sandwiched between two layers of chalcogen atoms. Within each sheet, atoms are arranged in a hexagonal crystal structure analogous to that of graphene. This makes the Brillouin zone essentially equivalent to that in graphene, but normalized by a different lattice constant, a'. Unlike in graphene, the two triangular sublattices are energetically inequivalent: one contains transition metal atoms and the other contains chalcogen atoms. This breaks inversion symmetry, even at nonzero displacement field, resulting in a band gap at the Fermi energy.[32,33]

The minimal tight binding model for group VI 2H TMDs is not written in a sublattice basis since the orbital composition of the transition metal and chalcogen valence electrons are quite different. The chalcogen atoms contribute mainly p-orbitals while transition metal atoms contribute mainly d orbitals (illustrated in figure 1.7a). When subject to the crystal field that results from the 2H structure, the energies of these orbital are renormalized such that the highest energy occupied states are d_{xy} and $\mathrm{d}_{x^2-y^2}$ orbitals and the lowest energy unoccupied states are d_{z^2} orbitals. Thus to effectively model the conduction and valence band edges, we can contruct a Hamiltonian in the basis of

$$|\phi_c\rangle = |d_{z^2}\rangle\,, \;\; |\phi_v^\tau\rangle = \frac{1}{\sqrt{2}}(|d_{x^2-y^2}\rangle + i\tau|d_{xy}\rangle) \tag{1.18}$$

where $\tau = \pm 1$ corresponds to the Hamiltonian around the K/K' valley. This produces the following 2 by 2 Bloch Hamiltonian,

$$H_0 = \begin{pmatrix} \frac{\Delta}{2} & at(\tau k_x - ik_y) \\ at(\tau k_x + ik_y) & -\frac{\Delta}{2} \end{pmatrix} \tag{1.19}$$

where t is the effective hopping between d_{z^2} orbitals and $d_{xy}/d_{x^2+y^2}$ orbitals on neighboring sites, and Δ is the difference in energy between $|\phi_c\rangle$ and $|\phi_v^\tau\rangle$.[33,35]

The final step in describing the low energy eigenstates in this system is to include the effects of spin-orbit coupling. Spin-orbit coupling is essentially negligible in graphene, at least for the purposes of this thesis, but is quite large in TMDs due to the inclusion of d orbital electrons which have larger angular momentum. The spin orbit-induced band splitting is much stronger in the valence band since it is composed of d_{xy} and $d_{x^2-y^2}$ orbitals which have a large component of angular momentum in the z direction which is the natural quantization axis in 2D. For our minimal model we can neglect spin-orbit interactions in the conduction band and approximate spin-orbit interactions in the valence band by adding

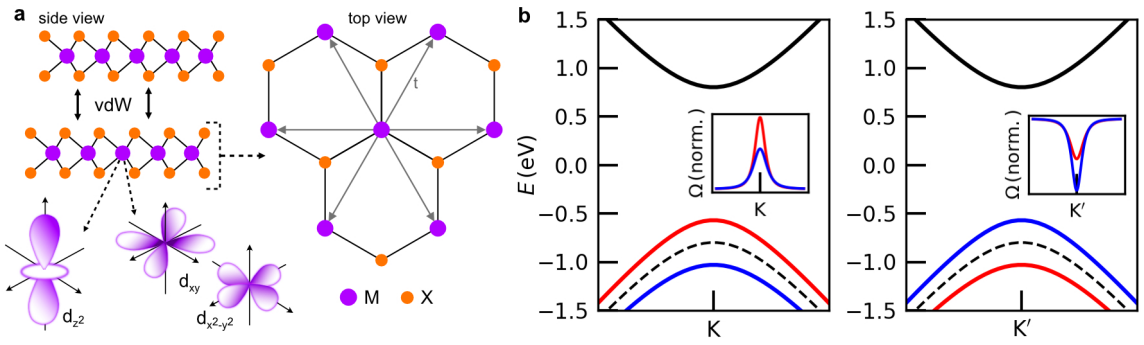

Figure 1.7: **Properties of monolayer 2H TMDs**, **a** Schematic illustration of lattice structure in 2H-TMDs. Orbital diagrams represent the two basis vectors for the 2 band tight binding model bands at the K/K' point. Grey arrows represent the relevant hopping paths between the M lattice sites. **b** Eigenvalues of two-band tight model including spin orbit coupling in the valence band (red corresponds to spin up and blue corresponds to spin down) at the K/K' points. Insets plot the Berry curvature of the spin-split valence band.

the following to H_0,

$$H_{\mathrm{SOC}} = -\lambda\tau\frac{\hat{\sigma_z}-1}{2}\hat{s_z} \tag{1.20}$$

where $\hat{\sigma_z}$ acts on the subspace of $|\phi_c\rangle$ and $|\phi_v^\tau\rangle$, $\hat{s_z}$ acts on the subspace of electron spin, and λ is a constant that describes the strength of spin orbit coupling. This makes the total Hamiltonian for the valence band edge,

$$H_s = H_0 + H_{\mathrm{SOC}} = \begin{pmatrix} \frac{\Delta}{2} & at(\tau k_x - ik_y) \\ at(\tau k_x + ik_y) & -\frac{\Delta}{2} + \lambda\tau s \end{pmatrix} \tag{1.21}$$

where $s = \pm\frac{1}{2}$ is the quantum number associated with $\hat{s_z}$. Figure 1.7b plots the energy bands that result from this model, which are parabolic with $\mathbf{k}$. The conduction band edge is given by the positive eigenvalues of H_0 and the valence band edge is given by the negative eigenvalues of H_s. An important feature of the valence band edge is that the spin up states are at higher energy than the spin down states at the K valley, while the reverse is true at the K' valley. This is often referred to as 'spin-valley locking' because at a given energy, the value of τ determines the values of s and vise versa.[32,33,35]

One can also examine the topological properties of this minimal model by using the corresponding Bloch wavefunctions to calculate the Berry curvature. For the valence band, the Berry curvature is given by the following expression,

$$\Omega_v(\mathbf{k}) = \tau\frac{2a^2t^2\Delta'}{[\Delta'^2 + 4a^2t^2k^2]^{3/2}} \tag{1.22}$$

where $\Delta' \equiv \Delta - \tau s\lambda$. The insets in figure 1.7 show Ω_v as a function of $\mathbf{k}$ for the spin up and spin down valence bands at the K/K' points. The berry curvature of the conduction band, Ω_c, is given by $\Omega_c = -\Omega_v$, where $\Delta' = \Delta$.[32,33] Similarly to graphene and bilayer graphene, the direction of phase

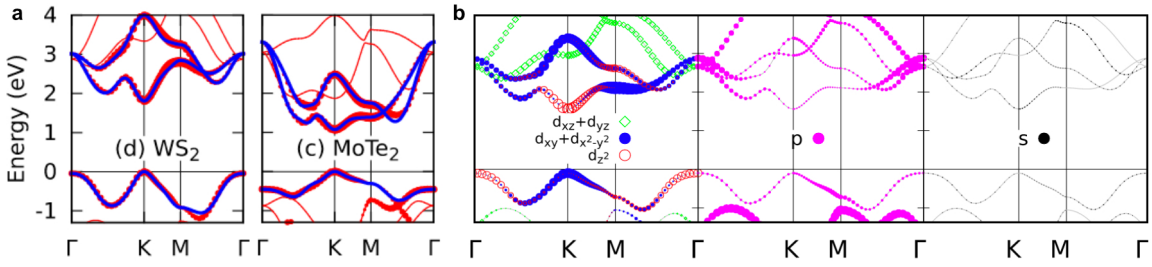

Figure 1.8: **Bandstructure of monolayer 2H TMDs**, **a** Calculated bandstructure of 2H WS_2 and $MoTe_2$ across different high symmetry points in the monolayer Brillouin zone. Red bands are derived from first principles, while blue bands are calculated using a 3 band tight binding model with basis vectors, $|d_{z^2}\rangle$,$|d_{xy}\rangle$, $|d_{x^2-y^2}\rangle$, including up to third nearest neighbor hopping. **b**, Energy dependent orbital composition of 2H-TMD bands at different high symmetry points. The data presented is calculated for MoS_2 but all the group VI 2H TMDs exhibit the same overall orbital structure. Plots in $(\mathbf{a})$ and $(\mathbf{b})$ are taken directly from Liu et al. *PRB* **88** (2013).[36]

winding is opposite at the K and K' valleys, so the valence and conduction bands have a net Chern number of $C = 0$. Unlike in graphene, the local Berry curvature does not have a singularity at the K/K' point, instead it is smoothly distributed at the band edge and largest at the K/K' point. To understand this difference further, we can look at the structure of the Bloch wavefunctions which have a similar spinor form to those in graphene,

$$|\psi_{\mathrm{K}+}\rangle = \frac{1}{\sqrt{2}}\begin{pmatrix}\cos\frac{\theta}{2}e^{i\phi}\\ \sin\frac{\theta}{2}\end{pmatrix}, \quad |\psi_{\mathrm{K}-}\rangle = \frac{1}{\sqrt{2}}\begin{pmatrix}\sin\frac{\theta}{2}e^{i\phi}\\ \cos\frac{\theta}{2}\end{pmatrix} \tag{1.23}$$

Here, $\theta = \arccos\left(\frac{\frac{\Delta}{2}}{\sqrt{a^2t^2k^2+(\frac{\Delta}{2})^2}}\right)$ and $\phi = \arctan(\frac{k_y}{k_x})$.[22] Due to the band gap Δ, these states are parametrized by two angles, θ and ϕ, instead of just one like in the case of graphene; in fact, if you set $\Delta = 0$, the Hamiltonian reduces to that of graphene. We can then define a pseudospin vector,

$$S_{K\pm} = \pm 2\cos\frac{\theta}{2}\sin\frac{\theta}{2}\cos\phi\hat{\mathbf{k}_\mathbf{x}} \pm 2\cos\frac{\theta}{2}\sin\frac{\theta}{2}\sin\phi\hat{\mathbf{k}_\mathbf{y}} + \cos\theta\hat{\mathbf{k}_\mathbf{z}} \tag{1.24}$$

According to this expression, the pseudospin winds around the K/K' point once as it does in graphene. However, it is not strictly pointing in the $k_x - k_y$ plane; instead it is canted slightly in the k_z direction. This modification leads to the more diffuse distribution of Berry curvature in the TMD bands when compared to the topological structure of graphene.

The bandstructure in the full Brillouin zone can be calculated from a more complex tight binding model that includes higher order hopping strengths and contributions from other metal d orbitals as well as s and p orbitals from metal and chalcogen atoms.[36] Figure 1.8a shows the bands that result from such a calculation for WS_2 and $MoTe_2$, plotted along a cut in the Brillouin zone which includes Γ, K, and M.

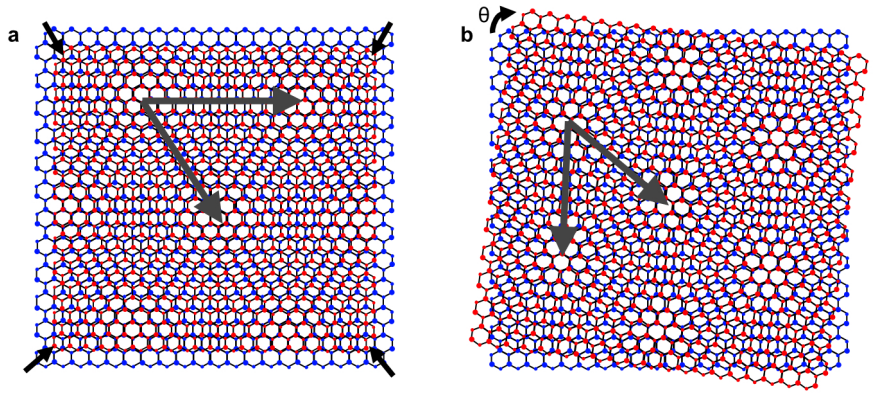

Figure 1.9: **Formation of a moiré superlattice.a** Schematic representation of a moiré superlattice formed between two hexagonal lattices with different lattice constant. Arrows indicate relative scaling between the lattice constant of blue and red layers. **b** Schematic representation of a moiré superlattice formed between two identical hexagonal lattices with an interlayer twist, given by the angle θ. Grey arrows in **a** and **b** indicate the lattice vectors of each moiré superlattice.

These plots show that while the lowest/highest energy states in the conduction/valence band live at the K/K' points, there exist other critical points in the dispersion located at the M and Γ point. For example, the valence band has a local maximum at the Γ point below the valence band edge, whose exact energy varies between different TMDs. The difference between the WS_2 and $MoTe_2$ bands demonstrates the complex interplay between different intralayer hopping paths and their sensitivty to atomic composition. Figure 1.8b illustrates the general orbital composition of group IV 2H TMD bands at different high symmetry points. As stated previously, the low energy bands are mostly composed of metal d orbitals, while s and p orbital contribute to higher energy states. The conduction and valence band also have mixed orbital composition, e.g. the portion of the valence band located at the K point is composed of d_{xy} and $d_{x^2-y^2}$ orbitals while the portion located at the Γ point is composed of d_{z^2} orbitals.[36]

1.4 Moiré materials

A moiré superlattice is a long-range beating pattern that results from a mismatch between two crystalline structures. This can come from a difference in lattice constant or symmetry, as illustrated in figure 1.9a, or a rotational offset between the two crystals, illustrated in figure 1.9b. The interference patterns seen in figure 1.9 reflect a periodic modulation of atomic density. A moiré superlattice will form at the inferface of any two 'mismatched' crystals, but it is particularly relevant in 2D systems due to spatial confinement around the moiré interface. Moiré patterns formed in layered vdW heterostructures often strongly modify the properties of the individual vdW materials and often lead to novel electronic behavior that is absent in

the parent vdW materials. The ability to engineer 2D systems with tailored moiré patterns, often referred to as twistronics, is a major advantage of vdW materials and has grown into a field of its own.[37,38]

The role of a moiré superlattice in determining the electronic properties of hybrid 2D system is two-fold. The first is that it mediates the strength of interlayer tunneling between the constituent crystals. If the spatial mismatch between the two crystal structures is small enough, their energy spectra will hybridize together due to interlayer-hopping between atomic orbitals. The moiré superlattice can be thought of as a periodic modulation of the interlayer hopping strength, mediating the hybridization of constituent bands. The second is similar to the role of an atomic crystal in modifying the properties of a free electron. An electron confined to a crystal lattice can be modeled as a nearly free electron subject to a periodic potential which results from the periodic arrangements of positively charged atomic nuclei. Since the wavefunctions of a quantum system must respect the symmetry of its Hamiltonian, an electron subject to a periodic potential must have a wavefunction that respects this periodicity; Bloch's theorem states that if $V(\mathbf{r}) = V(\mathbf{r} + \mathbf{R})$, then $|\psi(\mathbf{r})\rangle = |\psi(\mathbf{r} + \mathbf{R})\rangle$. The periodic modulation of the density of atomic nuclei in a moiré superlattice creates a roughly periodic moiré potential. Invoking Bloch's theorem, this moiré potential creates an analogous condition for the electronic wavefunctions: if $V(\mathbf{r}) = V(\mathbf{r} + \mathbf{R}_M)$, then $|\psi(\mathbf{r})\rangle = |\psi(\mathbf{r} + \mathbf{R}_M)\rangle$, where $\mathbf{R}_M$ is the lengthscale of the moiré superlattice.[§] It follows that the energy spectrum of electrons in a moiré superlattice can be thought of as energy bands in a moiré Brillouin zone (also referred to as the mini Brillouin zone) whose dimensions are given by the inverse of the moiré lengthscale. In other words, the hybridized bands from the two constituent crystals are folded into a smaller Brillouin zone and modified further by interactions with the moiré potential.[37–40]

1.4.1 Modeling moiré bands

Developing model Hamiltonians for these so-called moiré materials initially required some theoretical advances. A traditional tight binding approach would involve specifying the positions of all the atomic orbitals within one moiré unit cell. In real systems, the typical moiré length scale is around 5-15 nm; this means diagonalizing a matrix with a dimension on the order of 10^3-10^4. In addition, moiré superlattices are not exactly crystalline on an atomic scale, so a traditional tight binding method can only evaluate the spectrum of systems in which the moiré pattern is commensurate with the underlying atomic lattices.[40] In 2011, Bistrizter and MacDonald developed a new method to model moiré bands which involves a more compact Hamiltonian and can be applied to systems with arbitrary moiré length scales, regardless of commensuration with the atomic lattice.[39] In the rest of this section, I will describe this Bistrizter-

[§]It is important to note that in general, a moiré superlattice is not exactly crystalline unless its lengthscale is commensurate with the atomic lattices of the constituent materials, but in many cases it can be effectively approximated as periodic, at least in order to capture the relevant physical changes to the electronic structure of some material.

Macdonald model, which was originally used to calculate the bandstructure in twisted bilayer graphene (TBG)—two graphene layers stacked with a small interlayer twist.

The model is built by considering interlayer tunneling between Fermi pockets in k-space. Figure 1.10a shows the Brillouin zones of two graphene layers, represented by blue and red, with some interlayer twist between them, θ. Since the low energy Fermi surface in graphene is located at the K/K' points, the tunneling processes relevant to the low energy properties of TBG are those between the respective K/K' points of the blue and red layers. Considering the three K points in the first Brillouin zone, there are three basic interlayer scattering vectors, $\mathbf{q}_1$, $\mathbf{q}_2$, and $\mathbf{q}_3$, shown in figure 1.10a. If we also consider scattering processes in an extended Brillouin zone, the interlayer scattering processes that are permitted by conservation of crystal momentum are,

$$\mathbf{k}_{f,r} + n\mathbf{G}_{i,r} = \mathbf{k}_{0,b} + m\mathbf{G}_{i,b} \tag{1.25}$$

where $\mathbf{k}_{0,b}$ is the initial crystal momentum in the blue layer, $\mathbf{k}_{f,r}$ is the final crystal momentum in the red layer, $\mathbf{G}_{i,b}(\mathbf{G}_{i,r})$ are reciprocal lattice vectors in the blue(red) layer, and n, m are integers. This is analogous to Umklapp scattering between electrons and a crystal lattice. Since the reciprocal lattice vectors of the two layers are related by the basic interlayer scattering vectors, $\mathbf{q}_i$, equation (1.25) can be rewritten as,

$$\mathbf{k}_{f,r} = \mathbf{k}_{0,b} + p\mathbf{q}_i \tag{1.26}$$

where p is an integer. The vectors given by $p\mathbf{q}_i$ form a hexagonal lattice, pictured in figure 1.10b. The unit cell of this lattice is the moiré Brillouin zone.

The innovation of the Bistritzer-Macdonald model is to use this k space lattice as the basis for a tight binding model. We consider each scattering vector as a lattice site which holds a Dirac Hamiltonian and then allow some tunneling between the sites. In matrix form, the full Bistritzer-Macdonald Hamiltonian has dimension equal to the number of k-space lattice sites. In principle this would be an infinite dimensional matrix, but in practice the matrix can be truncated to some finite dimension and effectively capture the properties of the TBG bands. The diagonal elements are given by a rotated Dirac Hamiltonian,

$$h_{\mathbf{k}}(\theta) = -\hbar v_F |\mathbf{k}| \begin{pmatrix} 0 & e^{i(\theta_{\mathbf{k}}-\theta)} \\ e^{-i(\theta_{\mathbf{k}}-\theta)} & 0 \end{pmatrix} \tag{1.27}$$

where $\theta_{\mathbf{k}} = \arctan(\frac{k_y}{k_x})$ is the polar angle of $\mathbf{k}$. The off-diagonal elements describe the tunneling processes between each point in the k space lattice. Determining the form of these elements is more involved, so I will simply sketch out the general process and then state the results. The process starts from an assumption that interlayer tunneling strength as a function of real space will be periodic with the moire

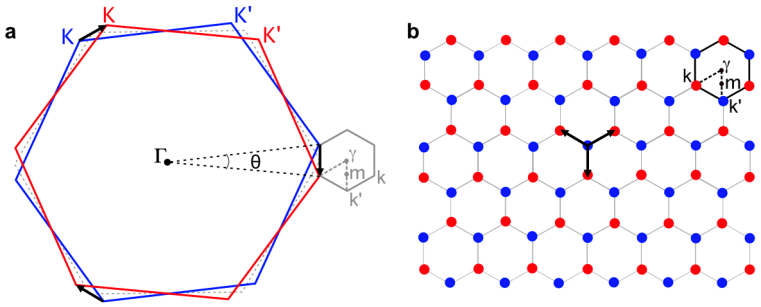

Figure 1.10: **Creation of a moiré Brillouin zone**, **a**, Schematic illustration of the formation of a moiré Brillouin zone in TBG. Red and blue hexagons represent the rotated Brillouin zones of each graphene layer. Dashed grey hexagon represents the Brillouin zone of an unrotated graphene layer. Smaller solid grey hexagon represents the moiré Brillouin zone formed from K point of the graphene layers. High symmetry points in the monolayer Brillouin zones are labeled by capital letters, while those in the moiré Brillouin zone are labeled by lower case letters. Black arrows show interlayer scattering paths, $\mathbf{q}_i$ between the two layers at the three K points. **b**, Momentum space lattice formed by scattering processes described by equations 1.25 and 1.26. Red and blue dots represent 'lattice sights' from the red and blue graphene layers respectively, which hold a copy of the single layer Dirac Hamiltonian, $h_{\mathbf{k}}(\theta)$. These are coupled together by the scattering vectors, $\mathbf{q}_i$ denoted by black arrows. Small black hexagon denotes the moiré Brillouin zone.

unit cell vectors $\mathbf{a}_M$:

$$T^{\alpha\beta}(\mathbf{r}) = T^{\alpha\beta}(\mathbf{r} + \mathbf{a}_M) \tag{1.28}$$

where α and β correspond to either the A and B sublattice in graphene layers. For example, T^{AA} describes the moiré periodic hopping between the A sublattice of the blue layer and the A sublattice of the red layer. If this is true, then the function $T(\mathbf{r})$, can be written in terms of Fourier components,

$$T^{\alpha\beta}(r) = \sum_{\mathbf{G_M}} c_{\mathbf{G_M}} e^{i\mathbf{G_M}\cdot\mathbf{r}} \tag{1.29}$$

where $\mathbf{G_M}$ are integer linear combinations of the moiré reciprocal lattice vectors, $\mathbf{q}_1$, $\mathbf{q}_2$, and $\mathbf{q}_3$. We have already established that the dominant tunneling processes will be the nearest neighbor processes in the k-space lattice shown in figure 1.10. Assuming that all other tunneling processes have negligible effects, we can rewrite equation 1.29 as,

$$T^{\alpha\beta}(r) = \sum_{\mathbf{q}_i} T_i^{\alpha\beta} e^{i\mathbf{q}_i\cdot\mathbf{r}} \tag{1.30}$$

By symmetry analysis of the moiré lattice, the values of $T_i^{\alpha\beta}$ can be specified as,

$$T_1 = w\begin{pmatrix} 1 & 1 \\ 1 & 1 \end{pmatrix},\ T_2 = w\begin{pmatrix} e^{-i\phi} & 1 \\ e^{i\phi} & e^{-i\phi} \end{pmatrix},\ T_3 = w\begin{pmatrix} e^{i\phi} & 1 \\ e^{-i\phi} & e^{i\phi} \end{pmatrix} \tag{1.31}$$

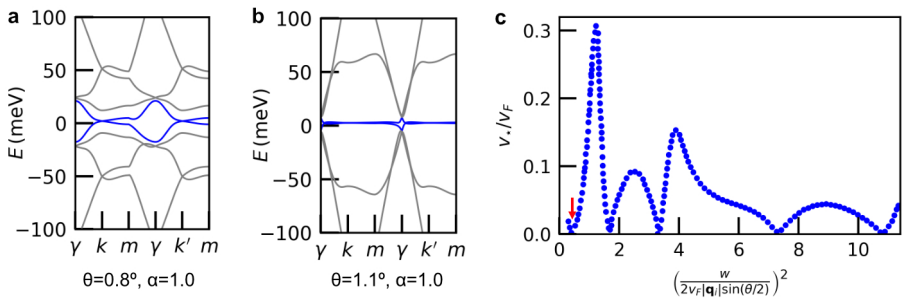

Figure 1.11: **Twisted bilayer graphene band structure**, **a**-**b**, Band structure of TBG calculated using the Bistritzer Macdonald model at twist angles of (**a**) 0.8° and (**b**) 1.1°. Both are calculated with $\alpha = 1$, signifying that they assume a rigid moiré superlattice with no lattice relaxations. Lowest energy conduction and valence bands are highlighted in blue. **c**, Numerical calculation of the Fermi velocity of the TBG bands at the Fermi energy, $v_\star$, normalized by the Fermi velocity of monolayer graphene, v_F, plotted as a function of dimensionless parameter, $(\frac{w}{2v_F|\mathbf{q}_i|\sin(\theta/2)})^2$. This calculation shows that at specific combinations of model parameters, including the twist angle, θ, the Fermi velocity goes to zero. The red arrow corresponds to the conditions shown in (**b**) where $\theta = 1.1°$. Data plotted in (**c**) was extracted from figure 4 in Bistritzer and Macdonald, *PNAS* **108** (2011).[39]

Here, w is an energetic hopping strength generally set at 110 meV, and $\phi = \frac{2\pi}{3}$. These matrices are written in the same basis as $h_{\mathbf{k}}(\theta)$, i.e. T_1^{11} couples the A sublattice of the blue layer to the A sublattice of the red layer through a momentum scattering process described by $\mathbf{q}_i$. To help the reader visualize the structure of Hamiltonian, the following equation shows the explicit form of the Bistritzer MacDonald Hamiltonian, truncated after the first 3 tunneling processes:

$$H^0_{\mathrm{BM}} = \begin{pmatrix} h_{\mathbf{k}}(\theta/2) & T_1 & T_2 & T_3 \\ T_1^\dagger & h_{\mathbf{k}+\mathbf{q}_1}(-\theta/2) & 0 & 0 \\ T_2^\dagger & 0 & h_{\mathbf{k}+\mathbf{q}_2}(-\theta/2) & 0 \\ T_3\dagger & 0 & 0 & h_{\mathbf{k}+\mathbf{q}_3}(-\theta/2) \end{pmatrix} \tag{1.32}$$

The full Bistritzer Macdonald Hamiltonian is often notated as,

$$H_{BM} = \begin{pmatrix} H_1(\mathbf{k}) & T(\mathbf{r}) \\ T(\mathbf{r}) & H_2(\mathbf{k}) \end{pmatrix} \tag{1.33}$$

$H_i(\mathbf{k})$ denote that the on diagonal terms are dictated by the momenum-space Hamiltonian of the two layers ($i = 1\,2$), and $T(\mathbf{r})$ signifies that the the layers are coupled together by a moiré-periodic tunneling amplitude which enters the momentum space Hamiltonian through it's Fourier components.

Figure 1.11a and b show examples of the moiré bands calculated using the Bistritzer Macdonald Hamiltonian for $\theta = 0.8°$ and $\theta = 1.1°$ respectively. The bands are plotted along a cut in the moiré Brillouin zone, pictured in figure 1.10. The bands highlited in blue represent those which are generally

experimentally accessible. It it clear from these examples that the moiré band dispersions depend sensitively on the exact twist angle of the structure. At $\theta = 1.1°$, the first two valence and conduction bands become almost perfectly flat. Figure 1.11c illustrates this further as it plots the fermi velocity of the moiré bands at zero energy for different model parameters. At various values of θ, the fermi velocity goes to zero, indicating a vanishingly small bandwidth; these are known as 'magic angles'.

Since the first conduction and valence band originate from Dirac points of the two graphene layers, they are imbued with nontrivial topology. As discussed previously, the conduction (valence) band of monolayer graphene has a π ($-\pi$) Berry phase concentrated at the K Dirac point. The sign of this Berry phase is opposite at the K' Dirac point. When considering the entire graphene conduction (valence) band, the total Berry phase is zero, leading to a trivial chern number, $C = 0$. In TBG, there are two copies of the monolayer graphene conduction (valence) band that contribute to the moiré band structure each contributing a π or $-\pi$ Berry phase. When discrete moiré bands are formed, the total Berry phase of each must be an integer multiple of 2π. Each band also inherits an additional 'valley' degeneracy in addition to spin since the Bistritzer Macdonald model can be applied near either the K or K' points of the two graphene layers. The first moiré conduction (valence) band thus inherits the Berry phase from the Dirac points and has a total phase winding of 2π (-2π) for the K copy of the band and -2π (2π) for the K' copy of the band. Although this structure still yields bands with zero total Chern number, we can say that that the moiré bands have a nonzero valley Chern number, C_v: $C_K = 1$ and $C_{K'} = -1$ for the conduction band, $C_K = -1$ and $C_K = 1$ for the valence band.[41]

The Bistritzer Macdonald method of modeling moiré bandstructures has been applied to many moiré materials, and it will serve as a starting point for understanding the electronic structure of the moiré systems investigated in future chapters.

1.4.2 Lattice relaxations in moiré materials

At one to several atoms thick, vdW materials are extremely flexible; they have a strong tendency to bend, wrinkle, and deform according to their environment. This can happen on a macroscopic lengthscales. For example, a graphene monolayer will form a bubble over a tall piece of residue on a substrate. It can also happen on a microscopic scale where individual atoms undergo nanoscale displacements to lower the overall energy of the system. This is particularly relevant in moiré systems since a moiré superlattice creates a continuous modulation of the interlayer stacking order. Regions with energetically favorable stacking order tend to expand, while those with unstable stacking order tend to shrink and deform out of plane.[42–44]

Figure 1.12a shows the interlayer binding energy for TBG without considering any lattice relaxations.

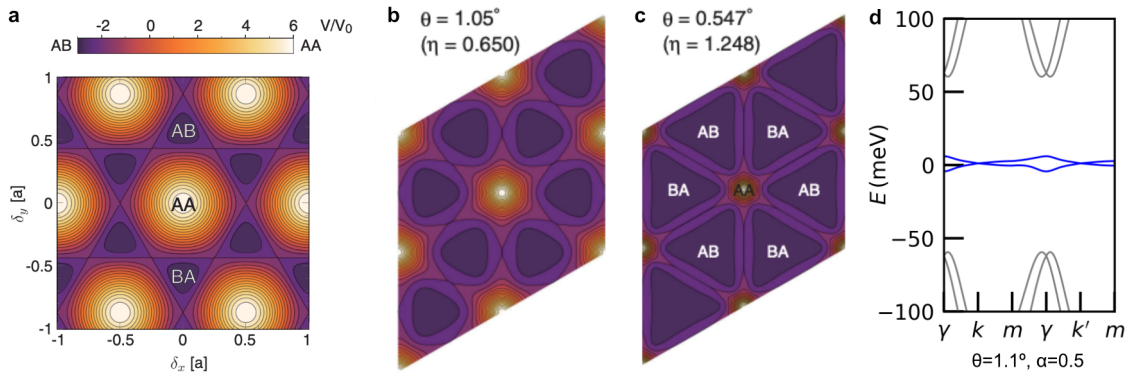

Figure 1.12: **Atomic relaxations in a moiré superlattice**, **a**, Interlayer binding energy, V/V_0 calculated for a rigid TBG moiré superlattice. Lines on color plot are constant energy contours. δ_x and δ_y are the displacement of the two sheets of graphene in the x and y directions. **b**-**c**, Similar plots of V/V_0 for a relaxed moiré superlattice at (**b**) 1.05° and (**c**) 0.547°. Color scales in (**b**-**c**) are the same as the color scale defined in (**a**). **d** Banstructure of TBG at 1.1° calculated using the Bistritzer Macdonald model incorporated lattice relaxations ($\alpha = 0.5$). Panels **a**-**c** are taken from Koshino and Nam. *PRB* **101** (2020).[45]

It is smallest at AB/BA sites, which correspond to natural Bernal stacking, and largest at the AA sites, which refers to stacking the carbon atoms of the top layer directly atop those in the bottom layer. This geometry holds true for a rigid moiré pattern at any twist angle. In real moiré superlattices, atoms will move towards a global energy minimum which is a balance between two factors: (1) decreasing the overall interlayer binding energy and (2) the energy cost of creating local strain. Panels a and b in figure 1.12 show calculations of the interlayer binding energy after incorporating the effects of in-plane atomic relaxations, for a twist angle of $1.05°$ and $0.547°$ respectively. When compared to the rigid case, both twist angles show larger areas of AB/BA regions and smaller AA regions. This effect generally becomes more drastic with decreasing twist angle because the AB/BA regions in the rigid case are larger and thus contain more atoms. This means that individual atoms can move smaller distances to collectively enlarge the AB/BA regions, lowering the energy of the system without creating as much strain. These effects are generally accompanied by out of plane deformation which increases the local interlayer separation at the AA regions.[42]

These types of lattice relaxations occur to varying degrees in all moiré materials and generally modify their electronic properties.[44] The effects of lattice relaxations can be incorporated into the Bistritzer Macdonald with the following modifications to the matrices T_i,

$$T_1 = w\begin{pmatrix}\alpha & 1\\ 1 & \alpha\end{pmatrix},\ T_2 = w\begin{pmatrix}\alpha e^{-i\phi} & 1\\ e^{i\phi} & \alpha e^{-i\phi}\end{pmatrix},\ T_3 = w\begin{pmatrix}\alpha e^{i\phi} & 1\\ e^{-i\phi} & \alpha e^{i\phi}\end{pmatrix} \tag{1.34}$$

Recall that these are written in the sublattice basis, so the diagonal elements, T_i^{AA} and T_i^{BB}, couple the A/B sublattice in the top layer to the same sublattice in the bottom layer. The parameter α thus primarily influences the AA regions as these are the regions where the sublattice sites in the two layers overlap directly. α is generally set at about 0.5, lowering the tunneling strength in the AA regions where there is a larger interlayer separation.[42] Figure 1.12d shows a calculation of the TBG band structure at the magic angle with $\alpha = 0.5$. In this case, lattice relaxations essentially induce gaps between the flat bands at zero energy and the higher energy conduction and valence bands.

1.4.3 QHE in moiré materials

We have already established that in the presence of an external magnetic field, the energy spectrum of a 2D material will evolve into a sequence of discrete highly degenerate Landau levels. This can be understood as a consequence of confining electron motion to a two dimensional plane, and in principle does not require a crystal lattice. An important extension is what happens to the Landau levels when electrons also interact with a spatially periodic potential, i.e. a crystal lattice. The solution, proposed by Hofstatder in 1976, is that a single energy band evolves into a fractal set of energy levels governed by the amount of magnetic flux, Φ, that threads each crystal unit cell. This is called the Hofstadter spectrum and is shown in figure 1.13. ¶ The fractal structure is based on special values of B, given by,

$$\frac{\Phi}{\Phi_0} = \frac{p}{q} \tag{1.35}$$

where $\Phi = BA$, with A the area of the unit cell, and Φ_0 is the fundamental quanta of magnetic flux, $\Phi_0 = h/e$. At these values, the energy spectrum splits into q sub-bands, as indicated for several values of $\frac{p}{q}$ in figure 1.13.

One way to understand this structure is to consider the symmetries of the Hamiltonian for an electron in a crystal lattice under the influence of a magnetic field,

$$H = \frac{1}{2m_e}(\hbar\mathbf{k} + e\mathbf{A})^2 + V(\mathbf{r}) \tag{1.36}$$

$\mathbf{A}$ is the magnetic vector potential, and $V(\mathbf{r})$ is the periodic crystal potential which is invariant under translations by unit vectors, $\mathbf{a}_i$, $V(\mathbf{r}+\mathbf{a}_i) = V(\mathbf{r})$. When $\mathbf{A} = 0$, H is invariant under this discrete translational symmetry, but when $\mathbf{A} \neq 0$, this symmetry is not necessarily preserved. When the rational flux condition in equation 1.35 is satisfied, H regains discrete translational symmetry, but under a translation of $q\mathbf{a}_i$ instead of $\mathbf{a}_i$. The unit cell is effectively enlarged by a factor of q which restructures the single zero field band into q sub-bands.[46] At low magnetic fields, the Hofstadter spectrum essentially reduces back

¶The original Hofstadter spectrum was calculated from a single band model on a square lattice, but the aspects of the Hofstatder spectrum discussed in this thesis are generalizable to other lattice symmetries.

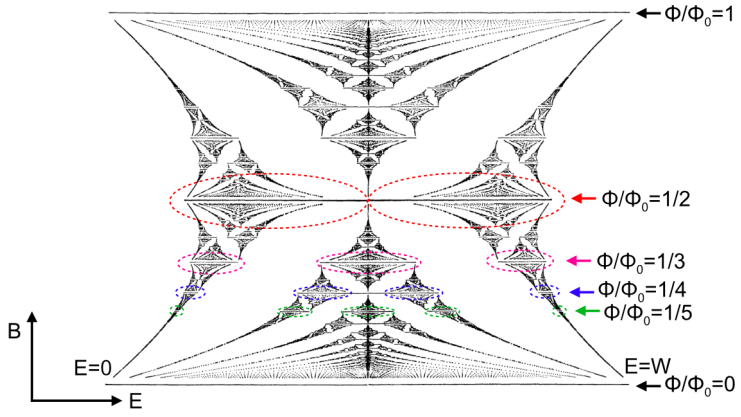

Figure 1.13: **Hofstadter spectrum** Energy spectrum for electrons on a square lattice in a magnetic field, B. Arrows denote selected values of B which meet the commensuration condition $\frac{\Phi}{\Phi_0} = \frac{p}{q}$. Dashed circles highlight the q subbands at each selected value of B. The x axis spans from $E = 0$ to $E = W$, where W is the width in energy of zero field band. Calculated spectrum is from Hofstadter, *PRB* **14** (1976).[47]

to the original Landau level; at small rational fractions of Φ, the spectrum consists of q equally spaced sub-bands which grow further apart in energy when q, and hence B, is increased. More intuitively, the size of cyclotron orbits is much larger than the size of the crystal lattice, leading to a very large effective magnetic unit cell and thus a large number of sub-bands.

The Hoftsadter spectrum is essentially inaccessible to experimental studies of monolayer 2D materials like graphene because of the large magnetic fields needed to observe signatures of its fractal structure. The area of the graphene unit cell is about 0.05 nm, so you would need a magnetic field of over 2000 T to reach $\frac{\Phi}{\Phi_0} = \frac{1}{4}$. However, a moiré superlattice introduces a much larger periodic lengthscale, typically around 5-20 nm. For TBG at the magic angle, $\frac{\Phi}{\Phi_0} = \frac{1}{4}$ corresponds to about 6.5 T, which is easily accessible in experiments. Another difficulty in observing the Hofstadter spectrum in traditional 2D crystals is the relatively small energy range accessible to experiments. One standard method to tune through the energy spectrum of a vdW material is to use gates to induce electrostatic doping and thus move the chemical potential of the material. Moving the chemical potential through one energy band requires you to add one electron (or hole) per unit cell, times the degeneracy of the band. For the conduction band of monolayer graphene, this corresponds to a carrier density of $n = 3.4 \times 10^{15}\mathrm{cm}^{-2}$, which is orders of magnitude beyond the usual range of doping induced by electrostatic gates. To fill the first four-fold degenrate moiré band in TBG, you need to induce four electrons per moiré unit cell, which corresponds to an experimentally reasonable carrier density of around $n = 2.4 \times 10^{12}\mathrm{cm}^{-2}$. Hence, it is also possible to probe the entire energy range of the spectrum presented in figure 1.13 in certain moiré

materials.[12, 13, 48]‖

1.4.4 Flat bands in moiré materials

TBG is not the only moiré system that hosts flat electronic bands at certain twist angles; in fact, this is a somewhat general feature of moiré materials. The bandstructures presented so far in this thesis are all calculated with a single particle assumption. In other words, they model how individual electrons interact with the potential imposed by a crystal lattice, but they neglect any interactions between electrons. If the bandwidth becomes comparable to the strength of electron-electron, $U/W \geq 1$, kinetic energy is quenched and electron-electron interactions (Coulomb repulsion, Pauli exclusion, etc.) start to modify the single-particle electronic structure. This can often lead to various complex interaction-driven phases such as superconductivity and spontaneous symmetry breaking, as in the case in TBG.

There are a variety of theoretical frameworks to interpret interaction-driven phenomena observed in electronic measurements, but one simple model that is relevant to all the systems explored in this thesis is Stoner ferromagnetism.[49] Consider a band with some degeneracy, such that there are two identical copies of the dispersion. This degeneracy can be labeled by some isospin— one band corresponds to isospin up and the other isospin down. Consider next a situation where this band in half filled while maintaining isospin degeneracy. If the total number of occupied states is given by $2n$, the number of occupied states with isospin up is $n_\uparrow = n$ and the number of occupied states with isospin down is $n_\downarrow = n$. Suppose there is some small fluctuation in the number of isospin up states near the fermi energy, E_F, such that $n_\uparrow = n + \delta n$ and $n_\downarrow = n - \delta n$. This requires isospin down states at energies slightly below the fermi energy, $E_F - dE$ to be converted to isospin up states slightly above the fermi energy, $E_F + dE$ The imbalance, δn, will thus modify the total energy of the system. The change in kinetic energy will be,

$$\mathrm{d}KE = \delta n \times \mathrm{dE} = \frac{\delta n^2}{g[E_F]} \tag{1.37}$$

using the fact that $\delta n = g[E_F]\mathrm{d}E$, where $g[E_F]$ is the density of states near the fermi energy. The potential energy of the system can be model as $PE = Un_\uparrow n_\downarrow$, where U describes the effective exchange interactions between isospin up and down electrons.

$$\mathrm{d}PE = U(n+\delta n)(n-\delta n) - U(n)(n) = -U\delta n^2 \tag{1.38}$$

The change in total energy is then,

$$\mathrm{d}TE = \frac{\delta n^2}{g[E_F]} - U\delta n^2 \tag{1.39}$$

‖To understand how the Hofstadter spectrum translates to $n - B$ phase, see section 2.2.3.

Thus a fluctuation in isospin occupation, δn, will lower the total energy of the system if,

$$Ug[E_F] > 1 \tag{1.40}$$

This is known as the Stoner criterion and it implies that degenerate partially filled bands can become spontaneously isospin polarized under certain conditions. The flat bands in TBG manifestly have a large density of states, which increases the likelihood of isospin polarization. They are also 4 fold degenerate, 2 for electron and 2 for valley K/K', which facilitates spontaneous isospin symmetry breaking near quarter filling, half filling, and three quarter filling of the flat bands. At half filling, it is favorable to break one degeneracy, either spin or valley.** At quarter or three quarter filling, it is favorable to break both isospin degeneracies.[14,16,50]

The Stoner model derives a condition for isospin ferromagnetism, that is the upper energy band is entirely composed of isospin up states and the lower energy band is composed entirely of isospin down states. In reality, there are other isospin configurations for the upper and lower symmetry broken bands which still lower the energy of the system. This is particularly relevant to the valley degeneracy, since moiré bands can a have nonzero valley Chern number, C_v (see section 1.4.1). In other words, a band fully polarized into the K or K' valley band will have Chern number, $C = C_v$, leading to a topological gap between the valley polarized bands.[51,52] However, this is not the only allowed scenario. Another common mechanism for valley symmetry breaking is the formation of an inter-valley coherent (IVC) state.[53] This is where the upper and lower energy bands are composed of states in either a symmetric or antisymmetric quantum superposition of K' and K. This still breaks valley degeneracy, but the inherent balance between K and K' leads to topologically trivial symmetry broken bands.

**Empirically this genereally turns out to be spin in TBG and related graphitic moiré materials. This will de discussed more in chapter 3.

Chapter 2

EXPERIMENTAL METHODS

2.1 Device fabrication

The first step in studying the electronic properties of moiré materials is of course fabricating high quality electronic devices containing said materials. Fortunately, the past two decades of vdW materials research has built us an arsenal of foolproof techniques to do so. In this section, I will describe the subset of techniques used in this thesis.

2.1.1 Assembly of vdW heterostructures

A vdW device starts with isolated 2D sheets of different vdW materials. These are derived from millimeter-scale single crystals through a process called exfoliation.[3,30] This surprisingly simple process involves cleaving a bulk crystal with scotch tape repeatedly, pictured in figure 2.1a, and pressing this tape onto a flat substrate, typically 90-300 nm of silicon dioxide (SiO_2) on doped silicon (Si). The result is a collection of vdW "flakes" with randomly distributed thickness and lateral size. We estimate the thickness of each flake by measuring its optical contrast relative to the substrate. For example, figure 2.1b shows an optical image of a graphite flake containing a monolayer and bilayer region. The inset shows that the bilayer region has roughly double the optical contrast of the monolayer region. In this thesis, we use scotch tape exfoliation to obtain a variety of differently shaped flakes composed of different vdW materials, shown in figure 2.1c-e.

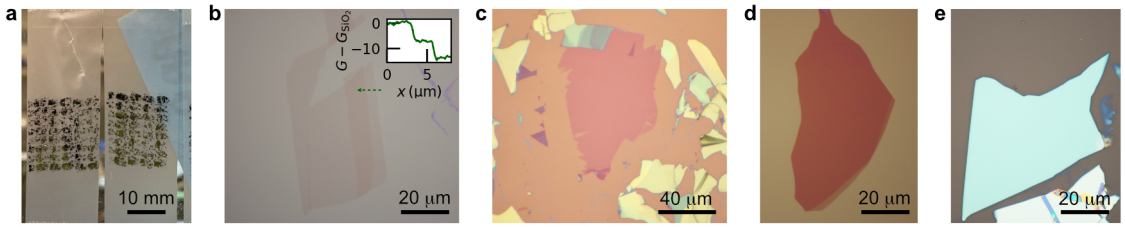

Figure 2.1: **Exfoliated vdW crystals**, **a**, Image of exfoliated graphite on scotch tape. **b**, Optical micrograph of flake with regions of graphene and bilayer graphene. Inset shows a line cut of the green contrast along the arrow indicated on the image, showing two equal height steps. **c**, Optical micrograph of a monolayer $MoTe_2$ flake. **d**, Optical micrograph of a multilayer graphite flake. **e**, Optical micrograph of a roughly 35 nm thick hBN flake. Flakes from **b**-**d** are resting on 285 nm SiO_2/Si substrates and flakes in **e** is resting on a 90 nm SiO_2/Si substrate.

The next step is to create a stack of vdW layers, where each layer serves a unique purpose. In a process referred to as a dry-transfer, we use a sticky polymer to peel each layer off of its substrate.[7] For the devices in this thesis, we use a polycarbonate (PC) film draped onto a polydimethylsiloxane (PDMS) puck, often called a stamp. We bring the stamp into contact with a vdW flake while applying heat to increase adhesion between the PC film and/or the other flakes on the stamp. Through precise control of temperature and stamp position, we can assemble an arbitrary number of vdW layers into a desired stack on the stamp. This process is detailed schematically in figure 2.2a. We deposit each stack onto a clean SiO_2/Si substrate by melting the PC film. We can then use various nanofabrication techniques to turn the stack into an electronic device.[7]

Figures 2.2b-c show a schematic illustration and optical image of a vdW stack, respectively. Stacks are built around some 2D system of interest, which in this thesis will always be some type of moiré system, consisting of two or more vdW layers stacked with some interlayer twist. To ensure a specific target twist angle between two layers, they need to come from the same exfoliated flake. This can be achieved using a "tear-and-stack" method where part of the flake is torn away from the rest in one pickup and the rest of the flake is picked up next, after introducing the desired twist.[8] However, this is relatively turbulent, so it often leads to partial rotation or relaxation of the twisted layers. Some parts of this thesis employ a more reliable method where anodic etching with an atomic force microscopy (AFM) tip is used to create two isolated pieces of one flake,[54] which can be picked up sequentially in a more controlled manner. The moiré system of interest is stacked on top of 10-50 nm thick hexagonal boron nitride (hBN) layers. hBN is an insulating analog of graphene with a hexagonal lattice composed of boron and nitrogen atoms. It's atomic flatness and relative charge homogeneity make it an excellent substrate for metallic and semiconducting vdW materials. In fact, it has been shown that kBN encapsulation increases the mobility of graphene by orders of magnitude.[55] The hBN layers also function as dielectric spacers between the moiré system of interest and few-layer graphite flakes which serve as electrostatic gates. Applying a voltage to a graphite gate creates an electric field through the hBN dielectric which induces a corresponding change in carrier density in the moiré system. Completed stacks require careful geometric consideration depending on the intended purpose of the eventual vdW device. We employ two styles of vdW devices in this thesis described in the following subsections: (1) dual-gated devices for electronic transport measurements, and (2) surface-exposed devices for STM measurements.

2.1.2 Dual gated devices

Dual gated devices consist of a vdW system of interest dual encapsulated with hBN dielectrics, with graphite gates on both the top and bottom of the stack. This is the structure illustrated in figure 2.2b.

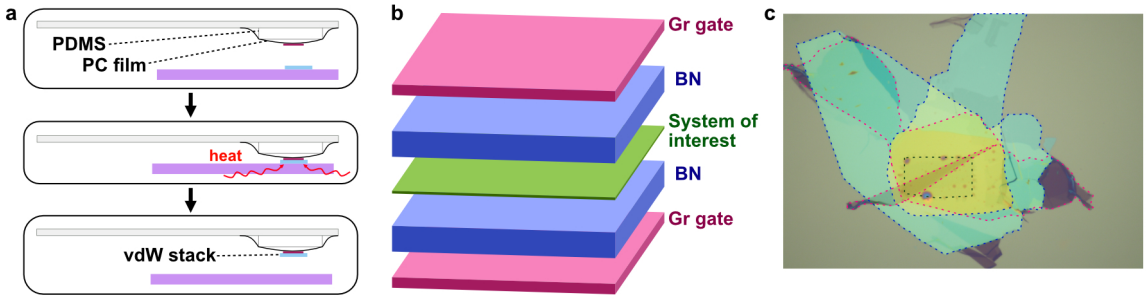

Figure 2.2: **Assembly of vdW stacks with a dry transfer process**, **a**, Schematic illustration of the dry-transfer process using a PC/PDMS stamp. Purple rectangle represents SiO_2/Si substrate, light gray rectangle represents a glass slide, and small multicolored rectangles represent vdW flakes. **b**, Schematic showing a typical vdW heterostructure. **c**, Optical micrograph of a vdW stack with the structure in **b**. Dashed lines outline individual vdW flakes that make up the stack, with their color corresponding to the colors in **b**.

We choose a top gate flake that is larger laterally than the system of interest and a bottom gate flake that is longer than system of interest in one dimension but much thinner in the other. This difference in shape between the top and bottom gate flakes can be seen in the top-down optical image of an example stack in figure 2.2c. The stacks made for transport devices presented in these thesis were assembled in entirety on a PC/PDMS stamp and then deposited onto a clean SiO_2/Si substrate by heating above the melting point of PC.*

To convert a stack of flakes into a functioning electronic device, we must establish independent electrical contact to the system of interest and both graphite gates. We use several rounds of nanofabrication,[7] laid out in figure 2.3. First, we etch the large top gate flake into a relatively small region that is mostly contained within the area of the system of interest. We leave some some small part of the top gate that extends past the system of interest in order to contact the top gate independently. Whenever possible, we define a top gate area that slightly overhangs the area of the back gate flake; this decreases the effects of p-n junctions formed in the contacts by creating an area of the contacts that is independently tuned by the top gate and additional voltage applied to Si substrate. To create an etch mask, shown in figure 2.3b, we spin a thick layer of polymethyl methacrylate (PMMA) resist over the stack, and then use electron beam lithography (EBL) to expose the area we want to etch away. We then perform the etch with O_2 plasma, which etches graphite effectively but has minimal effect on hBN. We use a second etch step to define the device geometry and expose contacts to the dual encapsulated system of interest. The transport devices in this thesis employ a Hall bar geometry that consists of a small narrow channel,

*It is also common practice to assemble the stack in two halfs: (1) bottom BN and back gate, (2) top gate, top BN, system of interest. Half 1 is made and deposited onto a substrate; then, half 2 is made and deposited on top of half 1.

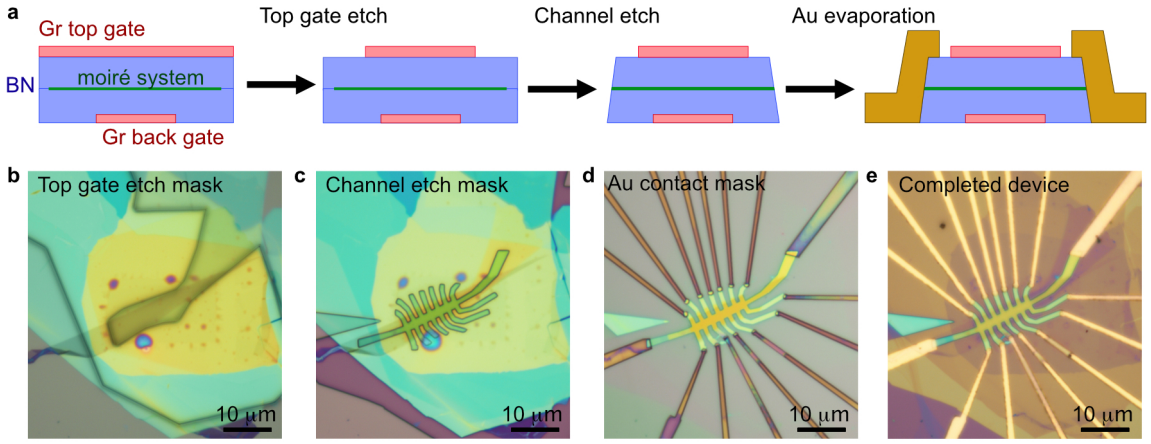

Figure 2.3: **Nanofabrication of a dual-gated vdW device**, **a**, Schematic diagram of the fabrication processes needed to turn a vdW stack into a functioning dual gated electronic device. **b-e** Optical micrographs of vdW device at various points in the fabrication process.

ideally contained within the area of the back gate, and a number of contacts that extend past the area of both gates, meeting the channel at a roughly perpendicular angle.[7] The images in figure 2.3c-e feature a Hall bar shape. We again use EBL to create an etch mask that defines the channel as well as contact regions for the top and back gates. We then perform the etch using CHF_3 plasma which etches both graphite and hBN. Finally, we establish electrical contact to the gates and the arms of the Hall bar. We use EBL to define a contact mask and then use electron beam evaporation to deposit a sticking layer of Cr (7 nm) and a thin Au film (70 nm).[7] After evaporation, we remove the PMMA resist revealing a completed electronic device, pictured in figure 2.3e.

2.1.3 Surface-exposed devices

The methods described in the previous section have been meticulously honed over the past decade to yield exceptionally functioning electronic devices with very low disorder. However, they do not suffice for scanning tunneling microscopy (STM) studies because they fully encapsulate the system of interest. In an STM measurement, the scanning tip must be brought within nanometers of the system of interest which essentially requires it to be exposed on one end. Furthermore, the nano-fabrication process used to create dual gated devices would induce polymer residues on the exposed system which could collect on the scanning tip during measurement. This can introduce spurious artifacts to scanning probe data and, in some cases, render the scanning tip essentially useless. To perform accurate STM measurements, we much fabricate vdW devices with a pristine exposed surface.

This is still an active area of research, but we follow a procedure first used to study twisted bilayer

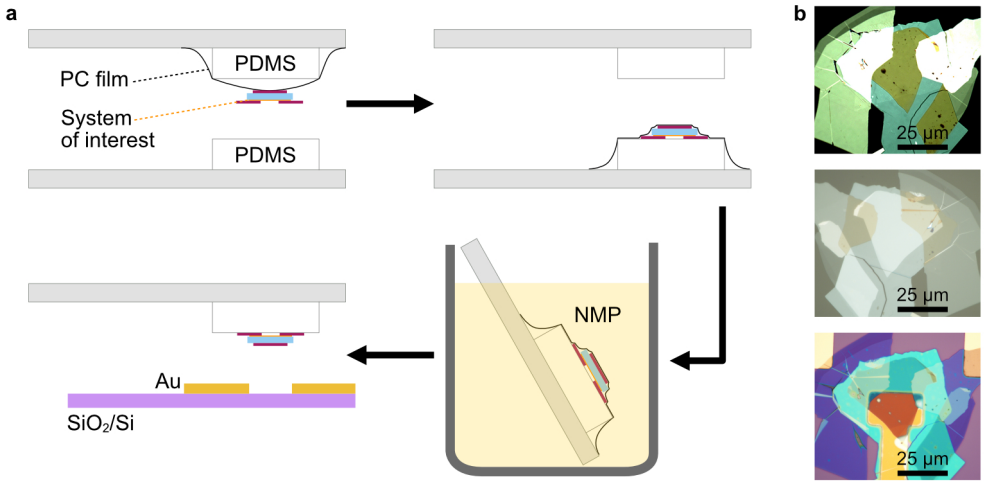

Figure 2.4: **Fabrication of a surface exposed vdW device**, **a**, Schematic diagram of post-stacking flipping and solvent process used to make surface exposed vdW devices. **b**, Optical micrographs a surface exposed device directly after stacking (top), after flipping and solvent step (middle), and after it was deposited onto Au contacts (bottom).

and trilayer graphene with STM.[56] First, we assemble a vdW stack on a PC/PDMS stamp. We assemble the stack in a "bottom-up" fashion so that the system-of-interest does not touch the PC film directly. For a single-gated device, we pick up the following flakes in the specified order, (1) a few-layer graphite gate, (2) a BN dielectric, (3) the system of interest (4) graphite contacts to the system of interest.[†] We then peel the PC film off of the stamp, invert it, and place it atop a fresh piece of PDMS. At this point, the system of interest is in direct contact with the new PDMS and and the entire vdW stack is covered by the PC film. We dissolve the PC film with N-Methyl-2-pyrrolidone (NMP). Finally, we transfer the stack onto a a set of pre-patterned Au contacts on a SiO_2/Si substrate. The crux of this method is that the system of interest is only ever in direct contact with PDMS, which leaves far less residue than PC or PMMA. We can also mitigate the small amounts of residue left by PDMS to some extent using rigorous AFM cleaning performed on the completed devices.

In chapter 5 of this thesis, I will present STM measurements of vdW devices composed of molybdenum ditelluride ($MoTe_2$). This material is highly air sensitive: it will oxidize quickly if exposed to ambient conditions. To avoid degradation of the exposed surface, we perform the process described in the previous paragraph in an inert argon environment ($<$0.1 ppm O_2 and H_2O). For the solvent step, we use annhydrous NMP ($<$0.05% H_2O) which is dried with molecular sieves for several weeks prior to use. After AFM cleaning, we transfer the devices to an ultra-high vacuum (UHV) environment with a vacuum transfer

[†]Note that in some cases, layers (3) and (4) are inverted and this does not change the function of the device or the details of the fabrication.

suitcase.

2.2 Electronic transport measurements

2.2.1 Basics of electron transport

Though relatively simple to measure, the resistance (or conductance) of a material serves as a surprisingly powerful experimental probe. In general, resistance is a complicated function of the intrinsic electronic properties of a material as well as device-specific properties such as disorder and geometry. However, to understand most of the experimental results in this thesis, it will suffice to understand the role of two contributing factors, (1) the effective mass of current carriers, and (2) their mean free path.[‡]

Within a semiclassical description of electrons in crystals, current is carried by electronic quasiparticles modeled by wavepackets built out of the Bloch states for some energy band which are centered at some defined position and crystal momentum. In the simplest conditions (e.g. a parabolic band which is mostly empty or filled), these Bloch quasiparticles behave as electrons with some effective mass renormalized by the periodic potential of the crystal lattice. The effective mass is proportional to the curvature of the electronic bands. In cases where the curvature, and hence the effective mass, is negative, quasiparticles are described more naturally as holes which have positive effective mass and positive charge, $+e$. Just like free charged particles, quasiparticles with smaller effective mass will accelerate faster in an electric field. Thus, the resistance of a material is proportional to the effective mass of current carrying quasiparticles.

On the other hand, resistance is inversely proportional to mean free path of carriers, which is the distance an electron (or hole) travels before undergoing some scattering process that kicks it into a different quantum state. There are three main types of scattering processes with contribute to the mean free path of quasiparticles, (1) inter-particle scattering, (2) scattering of quasiparticles with the crystal lattice, i.e. electron-phonon scattering, and (3) scattering off of disorder, such as crystalline defects of long range potential variations. The rate of scattering processes in categories (1) and (2) depends mostly on the intrinsic electronic properties of the material, including details of the bandstrucure and mechanical properties of the lattice. Scattering processes in category (3) are device dependent. Some examples of contributing disorder sources in vdW devices are crystalline defects in the system of interest, potential disorder from the BN substrate, and physical inhomogeneities like wrinkles, bubbles, and edges. [§]

Electronic transport studies are systematic measurements of resistance as a function of various tuning

---

[‡]Section 2.2.1 is based on material from chapter 8 of 'Modern Condensed Matter Physics" by Steven Girvin and Kun Yang.[57]

[§]It is worth noting that graphite crystals grown with state-of-the-art methods are virtually defect free on the scale of hundreds of nm to several microns. The same is true for BN single crystals, which impart minimal spatially dependent potential disorder.

knobs including temperature, magnetic field, and carrier density. Since the resistance of a material depends on so many inter-connected factors, it is often most useful to study its dependence on other experimental parameters. A simple example of this concept is how metals and insulators can be distinguished by the dependence of their resistance on temperature. At a given temperature, the Bloch states that contribute to current-carrying quasiparticles are determined by the Fermi-Dirac distribution centered at the Fermi energy, E_F.[¶] In an insulator, E_F lies within a band gap. Any current that flows through an insulator relies on the broadening of the Fermi-Dirac distribution at finite temperature which permits a small number of accessible Bloch states. At higher temperatures there are more accessible Bloch states which allows for more current carrying quasiparticles. Thus, the resistance of an insulator decreases with increasing temperature. In a metal, E_F lies within an energy band, which leads to lower resistance compared to an insulator, as there are many Bloch states available. In this case, a broadened Fermi-Dirac distribution allows for Bloch states with a larger range of energy and crystal momentum. This effectively leads to more quasiparticle scattering processes because it provides a broader array of initial and final momentum-energy states. Thus, increasing temperature causes increased resistance in a metal. This is just one illustrative example; the evolution of resistance under different conditions often serve as evidence for specific electronic phases. For example, the quantized resistance plateaus characteristic of the QHE are a signature of Landau Level formation at finite magnetic field. As an attempt to guide the reader through the daunting array of possible transport behaviors, the following sections detail a typical transport measurement of a vdW device and the resistance signatures that relate to its unique properties.

2.2.2 Details of transport measurements

Chapters 3 and 4 present transport studies of dual-gated vdW devices, introduced in figures 2.2 and 2.3. Our devices employ a Hall bar geometry, pictured in figure 2.3c-e, which facilitates simultaneous four probe measurements of the longitudinal and Hall resistances, R_{xx} and R_{xy} respectively. Recall that R_{xx} is the resistance in the direction parallel to the flow of current and R_{xy} is the resistance in the perpendicular direction. In the Hall bar geometry, the longitudinal resistivity, ρ_{xx} is related to the R_{xx} as $\rho_{xx} = \frac{L}{W} R_{xx}$, where W is the width of the Hall bar channel, and L is the distance between contacts, while the Hall resistivity, ρ_{xy}, is equal to R_{xy}.[‖] Figure 2.5a illustrates the setup for four-probe

---

[¶] This is of course dependent on the current carrying quasiparticles obeying fermionic statistics, which is not strictly true especially considering the effects of electron-electron interactions. But in this thesis, we assume that the dominant quasiparticles will be electrons or holes.

[‖] Resitivity in this case is actually a bit of a misnomer. In the strictest definition, resistivity is defined by Ohm's law, $\mathbf{E} = \rho \mathbf{J}$ where $\mathbf{J}$ is the current density per unit volume. The quantities, ρ_{xx} and ρ_{xy} defined here are actually the sheet resistance, which for a thin sheet, is the three dimensional resistivity divided by the thickness of sheet. It is common practice to use the terms resistivity and sheet resistance interchangeably.

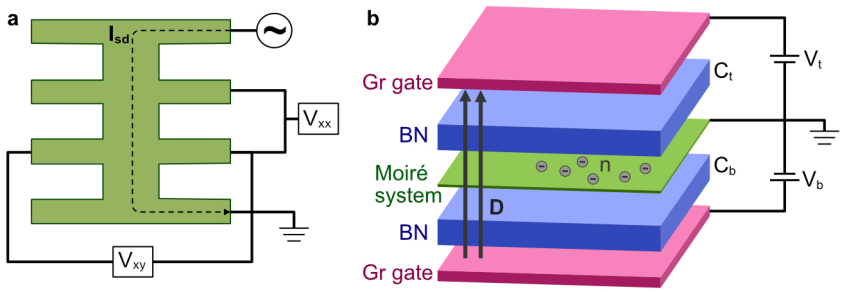

Figure 2.5: **Transport measurements of a dual gated device**, **a**, Diagram of the Hall bar geometry and set-up for a four-probe AC measurement. **b**, Schematic illustration of operating electrostatic gates in a vdW device. Applying top and bottom gate voltages, V_t and V_b, tunes the charge density, n, and the perpendicular displacement field, D, in the system of interest, depending on the capacitances of the top and bottom hBN dielectrics, C_t and C_b.

measurements of R_{xx} and R_{xy}. The basic idea is that a current is sent through the central channel of the Hall bar via a source and drain electrode, and the voltage difference between adjacent arms in the Hall bar (or those accross from each other in the case of V_{xy}) are measured. R_{xx} and R_{xy} are then calculated by dividing V_{xx} and V_{xy} by the current, I_{sd}, that flows through the Hall bar channel.

We use top and bottom graphite gates to modulate the carrier density per unit area, n, in the system of interest and to create a tunable perpendicular displacement field, D, through the channel (see schematic in figure 2.5b). With two gates, we can tune n and D independently so that we measure the resistance of the device within a two dimensional $n - D$ phase space. Using a parallel plate capacitor model, n and D can be calculated using the following expressions,

$$\begin{aligned} n &= \frac{1}{e}(C_t V_t + C_b V_b) + n_0 \\ D &= \frac{1}{2\epsilon_0}(C_t V_t - C_b V_b) \end{aligned} \tag{2.1}$$

where C_t (C_b) is the capacitance per unit area of the top (bottom) BN dielectric and V_t (V_b) is the voltage applied to the top (bottom) gate. The capacitance of a BN layer with some thickness, d, can be roughly estimated using an assumed dielectric constant of $\kappa = 3 - 4$ by the expression $C = \frac{k\epsilon_0}{d}$. The actual capacitances of each device often vary significantly from this estimate, so it is usually necessary to calculate them directly from features of the transport data, discussed in the following section. In addition to n and D, we also vary the temperature and apply a perpendicular/parallel magnetic field.

We measure R_{xx} and R_{xy} using a lock-in amplifier to reduce the effects of high frequency electrical noise. We first generate an AC source current with amplitude, I_{sd}, typically between 10 and 200 nA and frequency, ω, which we apply between source and drain contacts on either end of the Hall bar channel. We use a frequency of $\omega = 17.777$ Hz which is low enough to keep the measurement in the DC limit and

is unlikely to correspond to some harmonic of a higher frequency noise signal. We then use the lock-in amplifier to measure the AC voltage response between pairs of contacts at frequency ω. The in-phase amplitude of this signal is equal to the longitudinal or Hall voltage, V_{xx} or V_{xy}. This method allows us to detect of very small changes in the device resistivity.

We obtained most of the data presented in chapters 3 and 4 with a Cryomagnetics variable temperature insert at a base temperature of 1.5 K. We obtained a small subset of the data with a Bluefors dilution refrigerator at base temperature of 10 mK or 30 mK.

2.2.3 Interpretation of transport data

The transport studies presented in chapters 3 and 4 are performed on graphitic moiré systems: multilayer graphite heterostructures with one or more moiré interfaces between crystalline layers. The following decriptions detail common measurements performed on these systems and how to relate these data-sets to specific electronic properties. This is not an exhaustive list of all measurements presented in chapters 3 and 4, but is intended to give the reader a general understanding of how to interpret resistance data from this type of sample.**

Dual-gate maps

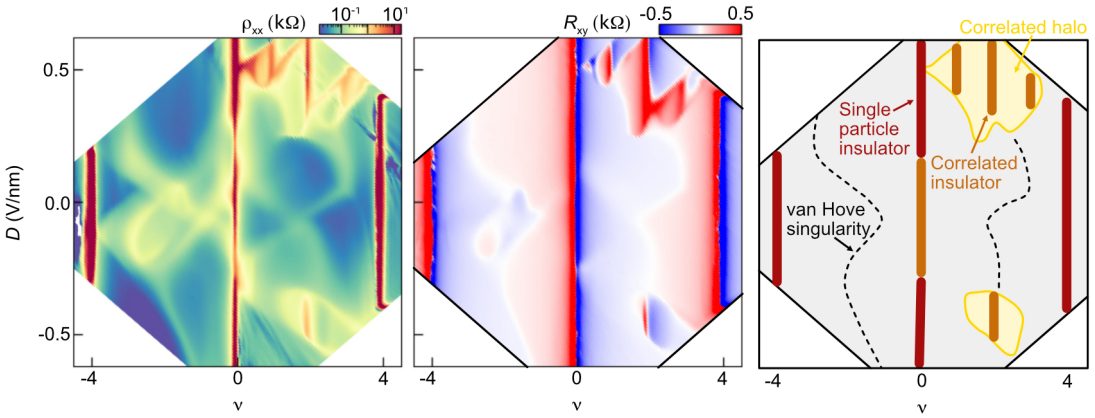

Figure 2.6: **Interpreting a dual gate map**, Example dual-gate map measurement acquired with a twisted bilayer-trilayer graphene device with twist angle, $\theta = 1.45°$. Left panel shows the longitudinal resistivity, ρ_{xx}, and middle panel shows the Hall resistance, R_{xy}. Right panel is a schematic diagram of key transport features associated with data in left/middle panel.

A dual-gate map is a two dimensional data set that records resistance as a function of top and back gate voltages, V_t and V_b. A square array of resistance point in V_t-V_b space is often sheared into n-D space

**The analysis in this section is based on previous studies of twisted monolayer-bilayer and bilayer-bilayer graphene.[58–69] The data presented in this section was acquired from a twisted bilayer-trilayer graphene device with a twist angle of $\theta = 1.45°$, which is revisited in much more detail in chapter 3.

using equation 2.1, as shown in figure 2.6. Tuning carrier density, n, is essentially equivalent to tuning the chemical potential in the sample, while tuning the displacement field, D, deforms the electronic bands. Band deformation can be understood from the competition between diagonal interlayer potential terms and off diagonal hopping terms in the graphite Hamiltonian as well as changes to the moiré interlayer coupling. Plotting the resistance data in n-D space thus provides a more natural link between transport features and features of the system's electronic bands. In chapter 4, we will detail the transport behavior of moiré systems composed of many graphene layers (≥ 6), in which screening prevents electric fields from penetrating through the full graphite film. In this case, the conversion of V_t and V_b to n and D used for thinner structures breaks down, and it makes more sense to think about the data in terms of V_t and V_b. This will be explained in much more detail in chapter 4.

Figure 2.6 shows an example dual-gate map of the longitudinal resistivity, ρ_{xx}, and Hall resistance, R_{xy}, for a moiré multilayer graphene system in the thin limit. We usually observe some amount of mixing between ρ_{xx} and R_{xy} signals due to slight deviations from an ideal Hall Bar geometry present in our devices. To minimize mixing, we symmetrize/antisymmetrize ρ_{xx}/R_{xy} with respect to a small perpendicular magnetic field. We take dual gate maps at some small positive field B and then repeat the measurement $-B$; then the symmetrized/antisymmetrized longitudinal and Hall resistivities are,

$$\begin{aligned} \rho_{xx} &= \frac{1}{2}[\rho_{xx}(B) + \rho_{xx}(-B)] \\ R_{xy} &= \frac{1}{2}[R_{xy}(B) - R_{xy}(-B)] \end{aligned} \tag{2.2}$$

The third panel shows a schematic map of the identifiable transport features in the dataset. As explained in section 1.4.1, moiré graphite systems feature many moiré bands which may be gapped or overlapping. The number of states in each moiré band is equal the number of moiré unit cells in the sample times the degeneracy of the band. In order to move the chemical potential such that the first moiré conduction band is completely full, the carrier density needs to reach $n = n_s$, where n_s is the carrier density which corresponds to four electrons per moiré unit cell. n_s can be calculated geometrically as $4/A_M \approx \frac{8\theta^2}{\sqrt{3}a}$. Since θ varies between moiré samples, it is useful to convert n to filling factor, $\nu = 4\frac{n}{n_s}$. With this construction, $\nu = 4$ ($\nu = -4$) corresponds to full filling of the first 4 fold degenerate moiré conduction (valence) band. Given typical twist angles between 1-1.5° and the dielectric constant of BN, experimentally accessible values of filling factor span around $|\nu| = 4 - 6$.

Most of the $n - D$ phase space in figure 2.6 shows fairly low ρ_{xx} around 0.1-1 kΩ (blue-yellow in the selected color scale). In these regions the chemical potential intersects one or more moiré bands and the system behaves as a metal. The gate map also features vertical stripes of large ρ_{xx} that exceeds 10-20 kΩ (orange and red in the selected color scale), indicating insulating behavior. These are accompanied by a diverging R_{xy} signal with a sign reversal near the middle of the resistive strip, suggesting that

dominant carrier type switches from electrons to holes or vise-versa. These signatures show that the chemical potential lies in a gap between two moiré bands. Apparent gaps that appear at n-D values that align with a single particle picture of electrons in the system are referred to as 'single particle insulators.' Gaps that appear at n-D values which contradict a single particle picture are referred to as 'correlated insulators,' since they result from enhanced electron interactions. Correlated insulators that appear at $\nu = 1, 2, 3$ for certain values of D arise from spontaneous symmetry breaking of the spin and valley degeneracies through a Stoner mechanism (see section 1.4.4)††. These symmetry-broken insulators are surrounded by an amorphous region of slightly elevated resistance, which is referred to as a correlated halo. The metallic regions also feature small bumps in ρ_{xx} which drift in a complicated fashion through n-D space, concomitant with sign changes in R_{xy}. This behavior is consistent with a van Hove singularity, a saddle point in the moiré bands where the mass of quasiparticles changes sign, i.e. the dominant carrier type switches between electrons and holes. Other small peaks and dips in resistance may reflect changes in electron/hole mobility as a consequence of band deformation or interaction effects.

Signatures of nontrivial topology

Since the low energy moiré bands of graphite heterostructures often have a nonzero valley Chern number, C_v, spontaneous valley polarization leads to nontrivial topology at zero magnetic field, B (See section 1.4.4). This leads to a large R_{xy} signal due to the presence of circulating edge currents. In an ideal system, the signature of a topological gap is quantized $R_{xy} = \frac{1}{C}\frac{h}{e^2}$, but graphitic moiré systems often exhibit R_{xy} signals that are not fully quantized due to twist angle disorder. This complicates the identification of nontrivial band topology, especially when R_{xy} can be enlarged by unwanted mixing between R_{xx} and R_{xy} signals or by a small magnetic field. Fortunately, nonzero Berry curvature also leads to a nonzero orbital magnetic moment of Bloch quasiparticles.[22] This orbital magnetic moment points up (down) for positive (negative) Berry curvature, so it sums to zero unless there is some valley polarization. Chiral edge states formed in the gap between topological bands also contribute to this emergent orbital magnetism. Unlike the electron spin, the orbital magnetic moment cannot rotate; it is fixed to point up or down, aligned with the overall angular momentum of electrons in the sample. It thus leads to a characteristic magnetic hysteresis signature which is used to identify topological phases in transport measurements.

Magnetic hysteresis curves are obtained by sweeping the magnetic field forward and backward through $B = 0$ while recording the resistance. In the absence of a magnetic field, there may be two possible orbital magnetic states, corresponding to polarization in either the K or K' valley. Applying an out

††The insulating state at $\nu \approx 0$ is specific to this moiré heterostructure and is not a general feature of graphitic moiré systems. This is explained in detail in chapter 3.

of plane magnetic field energetically favors the valley whose orbital magnetic moment points in the same direction as B. If the direction of B is anti-aligned with the orbital magnetic moment, the system may recondense into the other valley to lower its total energy. Suppose the starting value of B is negative. Then, the orbital magnetization would point down and the system would be polarized into the corresponding valley for this state. As B is swept through zero, the field becomes anti-aligned with the orbital magnetic moment. For some range of B larger than zero, the energy gain available by flipping to other valley is not larger than the cost. At a critical B value, known as the coercive field, the gain in energy exceeds the cost, and the system abruptly flips its orbital magnetization, leading to an abrupt change in resistance. The process repeats as you sweep B backwards through zero. This forms a hysteresis loop, illustrated schematically by figure 2.7.

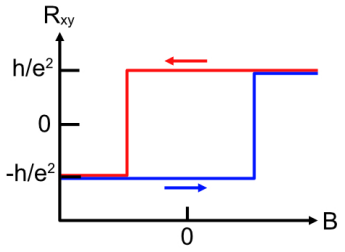

Figure 2.7: **Schematic of magnetic hysteresis**

Landau fan measurements

Landau fan measurements, which record resistance as a function of B and n, probe the Hofstadter spectrum of the sample. In order to interpret this data, it is necessary to understand how the Hofstader spectrum translates from E-B space to n-B space.

Recall that at rational fractions of magnetic flux, $\Phi = \frac{p}{q}\Phi_0$, the Hosftadter spectrum contains q sub-bands. For a given rational flux value, the number of filled sub-bands, r, can be related to p and q by the Diophantine equation,

$$r = sq + tp \tag{2.3}$$

where s is and integer related to the filling of the zero field Bloch bands and t is the sum of the Chern numbers of the filled sub-bands. At a given value of $\frac{p}{q}$, the Chern numbers of all sub-bands must sum to zero. This condition, along with the condition that s and t must be integers, specifies a unique value of s and t for each sub-band.[23,70] From this relation, one can derive the locations of gaps between sub-bands in terms of n and B. Filling one of the q sub-bands corresponds to a carrier density of $\frac{1}{q}n_0$, where n_0 corresponds to one electron per unit cell (moiré unit cell in this case). Thus the carrier density needed to fill r of the q sub-bands is $n = \frac{r}{q}n_0$. Using this expression as well as the definition of magnetic flux per unit cell, $\Phi = BA_{uc} = \frac{B}{n_0}$, the Diophantine equation can be rewritten as,

$$n = sn_0 + \frac{t}{\Phi_0}B \tag{2.4}$$

This final expression can be generalized to all values of B by taking s and t to be any integer. This

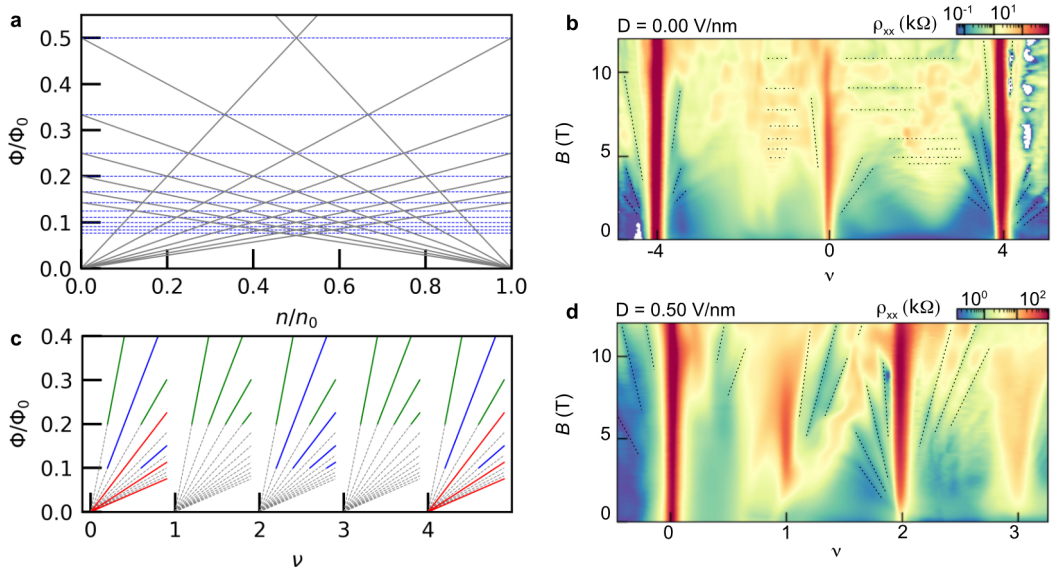

Figure 2.8: **Interpreting a Landau fan**, **a**, Schematic diagram of trajectories of topological gaps in the Hofstadter spectrum in n-B phase space, assuming one zero field band. Grey lines represent locations of gaps, using $t = 1 - 7$, while dashed blue lines represent rational values of magnetic flux, $\frac{\Phi}{\Phi_0} = \frac{p}{q}$, where unit cell is effectively enlarged by the magnetic field and the electrons experience an effective magnetic field of zero. **b**, Example of a Landau fan measurement showing dips in ρ_{xx} that move linearly with B and project to $\nu = -4, 0, 4$. The data also exhibits Brown-Zak oscillations, denoted by horizontal dashed lines, which occur at rational flux conditions and manifest as dips in $\rho_x x$. **c**, Schematic diagram of symmetry breaking in the Hofstadter spectrum with increasing magnetic flux. Red trajectories correspond to four fold-degeneracy. Blue and green trajectories occur when the Zeeman splitting between isospin flavors exceeds the characteristic energy spread due to finite temperature and potential disorder. The green and blue features appear at different magnetic fields due to the difference in effective g-factor between different isospins. **d**, Example of a Landau fan measurements which shows symmetry broken Hofstadter features. In this example, these features occur at fairly low values of B, which indicates that enhanced electron-electron interactions making isospin symmetry breaking favorable at lower fields compared to a non-interacting picture with only Zeeman splitting.

form of the Diophantine equation is a powerful tool because it tracks the positions of gaps within the Hofstadter spectrum as a function of n and B.[70]

Figure 2.8a plots the linear trajectories of gaps in the Hofstadter spectrum of a single band for $t = 1 - 7$, for $s = 0$ and $s = 1$. The resulting trajectories form two 'fans' of straight lines with slope t that project to either 0 or n_0 at $B = 0$; this is where the term 'Landau fan' comes from. For a system with multiple moiré bands, 'fans' will project to the carrier densities that correspond to full filling of each band as well as the charge neutrality point. Figure 2.8b shows an example of a Landau fan measurement taken on twisted bilayer-trilayer graphene. Linearly dispersing topological gaps manifest as quantum Hall gaps with dips in ρ_{xx} and steps in R_{xy}. Due to twist angle disorder in moiré graphitic heterostructures,

the quantum Hall effect is often not completely developed; that is, ρ_{xx} does not dip all the way to zero and R_{xy} is not quantized at the correct value of $\frac{1}{t}\frac{h}{e^2}$. Linear features project to $\nu = -4, 0, 4$, since the moiré bands have a four-fold degeneracy. This data-set also features horizontal dips in the resistance at certain rational fractions of Φ/Φ_0. Recall that the Hofstadter butterfly's fractal structure is built on the fact that at $\frac{\Phi}{\Phi_0} = \frac{p}{q}$, the discrete time reversal symmetry of the zero B Hamiltonian is temporarily restored with a translation vector of $q\mathbf{a}_i$, where $\mathbf{a}_i$ is the crystalline unit vector. The Bloch electrons (holes) which live in this enlarged magnetic unit cell, known as Brown-Zak fermions, feel an effective magnetic field of $B = 0$. This leads to a disruption of the linear trajectories in the Landau fan and a minimum in resistance. These horizontal stripes are known as Brown-Zak oscillations.[48]

Another relevant question in interpreting a Landau fan is how its structure changes when the spin and/or valley degeneracy of the moiré bands in lifted. As explained previously, strong electronic correlations in flat moiré bands can lead to spontaneous symmetry breaking near integer values of ν. In addition a large enough magnetic field may break the spin and valley degeneracy degeneracy through a Zeeman interaction,

$$H_Z = g_s \mu_B \mathbf{S} \cdot \mathbf{B} \tag{2.5}$$

where g is the effective isospin g-factor, μ_B is the Bohr-magneton, and $\mathbf{S}$ is the isospin operator. There are two main impacts of spin and valley symmetry breaking on the Hofstadter spectrum. (1) Additional fan features may develop which project to $\nu = 1, 2, 3$ corresponding to new gaps that would form in the zero field band structure. (2) The number of linear gapped trajectories projecting to zero field in each fan will double for a single broken degeneracy and quadruple for fully broken degeneracy. Figure 2.8c summarizes these effects considering only the effects of Zeeman splitting. At low B, fan features project to $\nu = 0, 4$ and are four fold degenerate, i.e. t values are multiples of 4. At a large enough B, the Zeeman term induces a sizable splitting between between the flavors of one isospin (e.g. spin up vs. spin down), which leads to additional fan features projecting to $\nu = 2$ and additional trajectories where t are multiples of 2. When both isospin symmetries are broken, fan features also project to $\nu = 1, 3$ and the trajectories take integer values of t.[71] The Landau fan data presented in figure 2.8d features gap trajectories that project to all integer fillings. In this case the isospin symmetry-broken features appear at fairly low magnetic fields compared to the Zeeman splitting expected for spin and valley degrees of freedom, indicating spontaneous symmetry breaking due to electron-electron interactions.[72,73]

Twist angle determination

Since the trajectories of gaps in a Landau fan diagram are linearly related to the filling factor of moiré bands, these measurements are also used to extract the exact twist angle, θ, of the corresponding moiré

heterostructure. This is generally easiest for a Landau fan where D is held approximately constant; changing D deforms the moiré bands and can thus introduce artifacts into the observed spectrum of quantum Hall states. Typically we choose $D = 0$, since this is an unlikely part of the n-D phase diagram for spontaneous symmetry breaking to occur for the structures studied in this thesis. From resistance data as a function of gate voltage and magnetic field, we use the following procedure to extract θ (1) Fit groups of linear features that project to what is presumed to be $\nu = 0$ and $\nu = \pm 4$. (2) Using equations (2.3) and (2.1), determine the exact capacitance of the top and bottom BN, C_t and C_b. (3) Use the experimentally determined values of C_t and C_b to convert voltage to n. (4) The value of n at which $\nu = 4$ is related to θ by $n_s = \frac{8\theta^2}{\sqrt{3}a^2}$.

2.3 Scanning tunneling microscopy

2.3.1 Theory of STM

Section 2.2 explains how resistance serves as a powerful probe of electronic structure, particularly when identifying certain many-body phases like the quantum Hall effect. However, transport measurements reflect a macroscopically averaged signal over a micron-scale device. The microscopic properties of moiré materials are often just as important in understanding their electronic behavior. Local scanning probe techniques like STM can thus provide a necessary complement to transport measurements by visualizing the electronic structure of these systems on the atomic scale.

STM operates by measuring the tunneling current, I, between a sharp metal tip and a conductive sample under an applied bias voltage, V_b. Figure 2.9a shows a schematic of this set-up. For a measureable tunneling signal, the distance between the tip apex and sample surface, z, must be on the order of one nm or less. An ideal STM tip is atomically sharp, such that the tunneling primarily occurs between one metal atom and the electronic states that reside near the sample surface. The tip is attached to a sensitive piezo-scanner which rasters the tip back and forth to obtain angstrom-scale spatial resolution of the tunneling current. Since I depends on z, STM can visualize the crystal structure of the sample along with structural defects and boundaries. I also depends on the electronic properties of the tip and sample, so STM provides additional nanoscale information about the sample's electronic structure.[74]

To understand the relative dependence of I on structural and electronic factors, it is helpful to model the tunneling current more rigorously. We will follow the formalism of Tersoff and Hamann.[74]Suppose that there is a positive voltage applied to the tip, V_b, and that the sample is held at ground. Figure 2.9b shows a schematic of the electronic spectra of the tip and sample and their alignment. This picture illustrates that the dominant contribution to the tunneling current will be electrons tunneling from sample to tip, $I_{t\to s}$. The rate of elastic electron tunneling from tip to sample at an energy, E, depends on several

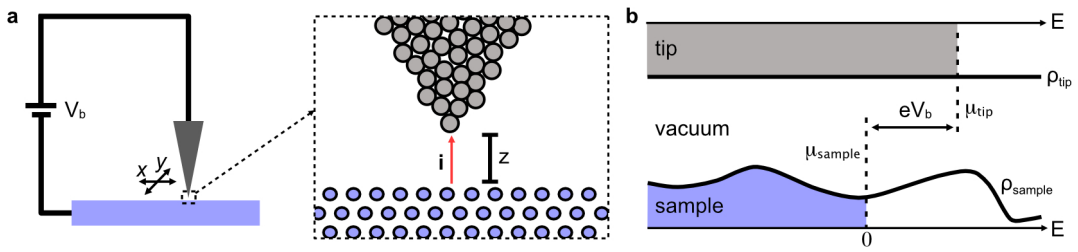

Figure 2.9: **Working principles of STM**, **a**, Diagram of STM experimental setup, blue represents the conducting sample while gray represents the metal scanning tip. Inset shows that the tip is made to be atomically sharp and positioned a short distance from the sample. **b** Energy alignment between tip and sample. Blue/gray color represents filled states in the sample/tip.

factors: (1) the number of accessible electron states in the sample, determined by the density of states, $\rho_s(E)$, and the occupation of those states given by the Fermi-Dirac distribution, $f(E)$, (2) the number of accessible electron states in the tip, determined similarly by $\rho_t(E)$ and $f(E+eV)$, (3) the quantum probability of a transition from state, ψ_t, to state ψ_s, given by the matrix element, $|M_{ts}|^2$. Borrowing from time-dependent perturbation theory, the tunneling current can be approximated as,

$$I_{t\to s} = -2e \cdot \frac{2\pi}{\hbar} \int_0^{eV_b} |M_{ts}|^2 \cdot \rho_s(E)(1-f(E)) \cdot \rho_t(E+eV_b) f(E+eV_b) dE \tag{2.6}$$

Note that the limits of the integral are restricted to the interval $[0, eV_b]$, since there are a negligible number of empty states in the sample when $E < 0$ and a negligible number of filled states in the tip when $E > eV_b$. This expression can be simplified with a few further approximations. First, a tip material is chosen such that ρ_t is roughly constant. Second, at low enough temperatures, $f(E) \approx 1$ and $1 - f(E+V_b) \approx 1$. Third, using the WKB approximation, the matrix element can be approximated as $|M_{ts}|^2 = e^{-\kappa z}$, where $\kappa = \frac{\sqrt{2m(E-\phi)}}{\hbar}$, and ϕ is height of the tunneling barrier which is a convolution of the work functions of the tip and the sample. Under these assumptions, the tunneling current obeys the following form,

$$I \propto e^{-\kappa z} \int_0^{eV_b} \rho_s(E) dE \tag{2.7}$$

The tunneling current is linearly proportional to integrated density of states in the sample and exponentially proportional to the tip-sample distance, z.

2.3.2 Types of STM measurements

Since the tunneling current depends on both the tip-sample distance and the sample density of states, STM usually operates in one of several modalities that probe different sample properties.

Topography

In a topography measurement, the height of the tip is controlled by a feedback loop which maintains a specified constant current at a constant bias. The tip is scanned in x and y with the feedback loop on to produce a plot of z as a function of space. Equation 2.6 shows that topography signal is a convolution of the actual height of sample and the density of states up to eV_b, as illustrated in figure 2.10. Since the spatially resolved density of states often obeys the same symmetries as the crystal lattice, topography is generally sufficient to characterize the crystal structure of the sample. It is also helpful in discerning strain in the crystal structure or large structural defects which yield a very strong change in sample height. Spatial modulations of ρ_s of course show up in the signal, but it is difficult to make conclusions about the exact form of ρ_s due to contributions from different energies. At large values of V_b, the density of states contribution is integrated over a large energy range, so spatial fluctuations in the density of states that change with energy often appear washed out and faint. Thus, the topography signal at high V_b can sometimes function as a proxy for sample height.

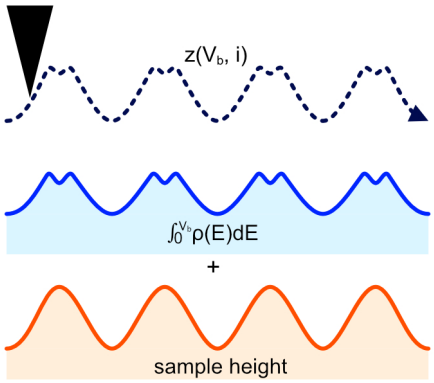

Figure 2.10: **Schematic of topography measurements**

Spectroscopy

Since $I \propto \int_0^{eV_b} \rho_s(E)dE$, the derivative of I with respect to V_b, $\mathrm{d}I/\mathrm{d}V$, is proportional to $\rho_s(E = eV_b)$. In a spectroscopy measurement, the tunneling current is measured at one location in space as a function of V_b. The resulting $\mathrm{d}I/\mathrm{d}V$ signal as a function of V_b directly probes $\rho_s(E)$, up to some multiplicative factor depending on the tip-sample separation, material-dependent decay constant κ, and density of states of the tip. This makes tunneling spectroscopy an extremely powerful probe of the sample's many-body electronic structure at and away from the sample's Fermi energy. Since the tip can be positioned in space with sub-nm resolution, spectra can be obtained at arbitrary locations within the crystal lattice, giving information about the Bloch wavefunctions, atomic defect states, and the electronic imprints of disorder.

$\mathrm{d}I/\mathrm{d}V$ can be obtained by taking the derivative of an $I(V)$ curve, but this leads to poor resolution and low signal. An alternative, and more common, method of obtaining $\mathrm{d}I/\mathrm{d}V$ involves applying a small AC modulation to V_b and using a lock-in amplifier to measure $\mathrm{d}I/\mathrm{d}V$. With this setup, the voltage applied to the tip then has the form, $V = V_b + V_m \sin(\omega t)$, where $V_m \ll V_b$ and ω is typically chosen to lie between 500 and 1000 Hz to bypass low frequency noise and avoid generating capacitive signals

comparable to or larger than the tunneling signal. Under these assumptions, the time dependent current, $I(t)$ can be expressed in terms of harmonics of ω,

$$I(V_b + V_m \sin(\omega t)) = I(V_b) + V_m \frac{\partial I}{\partial V} \sin(\omega t) + \frac{V_m^2}{2} \frac{\partial^2 I}{\partial V^2} \sin^2(\omega t) + \frac{V_m^3}{6} \frac{\partial^3 I}{\partial V^3} \sin^3(\omega t) + \dots \quad (2.8)$$

By rewriting $\sin^k(\omega t)$ in terms of $\sin(k\omega t)$, where $k \in \mathbb{N}$, equation 2.7 can be approximated as,

$$I = I_0 + \sum_{i=1}^{\infty} \frac{\mathrm{d}^i I}{\mathrm{d}V^i} \sin(n\omega t) \quad (2.9)$$

Thus, $\mathrm{d}I/\mathrm{d}V$ can be obtained with a lock-in amplifier by measuring the magnitude of AC current at the first harmonic of the reference frequency, ω, in-phase with the reference signal.

It is worth noting that the AC modulation applied to the tip also drives a capacitive coupling between the tip and sample which adds an additional term to the tunneling current, $I_{\mathrm{total}} = I_{\mathrm{tunnel}} + I_{\mathrm{capacitive}}$. For an ideal tunneling junction and circuit, the capacitive current induced is roughly,

$$I_{\mathrm{capacitive}} = i\omega C V_m \cos(\omega t) \quad (2.10)$$

provided that the applied AC modulation is $V_m \sin(\omega t)$. Note that a signal of this form is out of phase with Fourier components expressed in equation 2.8, so it does not affect the in-phase signal measured by the lockin.

Spectra are typically acquired with the feedback loop off so that z stays constant during the measurement. In most cases, this yields the most accurate measurement of relative changes in ρ_s, since changes in z can also induce changes in I. An exception arises when the tunneling decay constant, κ, varies significantly as a function of V_b. This can occur due to changes in the sample's electronic wavefunction as a function of energy. It can be helpful in this case to acquire spectra with the feedback loop on, so that the tip can move closer or further from the sample depending on the energy-dependent decay constant. This situation will be discussed in much more detail in chapter 5.

Local density of states maps

Measuring $\mathrm{d}/\mathrm{d}V$ as a function of tip position yields a spatial map of the local density of states (LDOS) at a given energy, $E = eV_b$. The measured LDOS is a proxy for the electronic wavefunction averaged over all crystal momenta. It can also reveal electrostatic potential disorder that does not show up in topography as well as interference patterns formed by Bloch quasiparticles reflecting off of structural defects.

LDOS maps can be acquired in tandem with topography by recording $\mathrm{d}I/\mathrm{d}V$ during the topography scan. In this scheme, it is necessary to set the scan speed such that the amount of time spent at each

point in the scan is greater than or equal to the lock-in time constant used to measure $\mathrm{d}I/\mathrm{d}V$. The drawback of this method is that obtaining a large enough $\mathrm{d}I/\mathrm{d}V$ signal often requires a large current setpoint, which sets the tip closer to the sample. This can cause unwanted interaction with the surface or unstable tip movement during scanning. Grid spectroscopy is an alternative way to collect LDOS maps that circumvents this issue. In this method, energy-dependent $\mathrm{d}I/\mathrm{d}V$ spectra are obtained in a grid of points in space. This gives a three dimensional data set which contains the spectrum at different points on the sample surface as well as maps of the LDOS at different energies, illustrated by figure 2.11.

2.3.3 Details of STM measurements

We used a Scienta-Omicron Polar UHV-STM system with a liquid Helium cryostat to obtain the STM data presented in chapter 5. The STM apparatus is contained in a UHV chamber with pressure $< 1 \times 10^{-9}$ mbar and held at a base temperature of 5 K. STM tips are inserted into a tip-holder attached to piezo tube which enables fine scanning in the x and y directions with sub-nanometer precision as well a coarse piezo motor which moves the tip in the z direction in micron-scale steps. Surface-exposed vdW devices are mounted on sample plates with ten isolated electrical contacts with feed-through outside the UHV chamber. Sample plates are inserted into a sample holder which is attached to coarse piezo motors to move in the x and y directions in micron-scale steps. To minimize vibrational noise, the STM tip and sample are suspended on springs within the vacuum chamber and the entire chamber is lifted by floating air legs. Nevertheless, small relative vibrations between the tip and sample are present in some data sets. Since these do not reflect physical properties of the samples measured, they have been filtered out and notated as such.

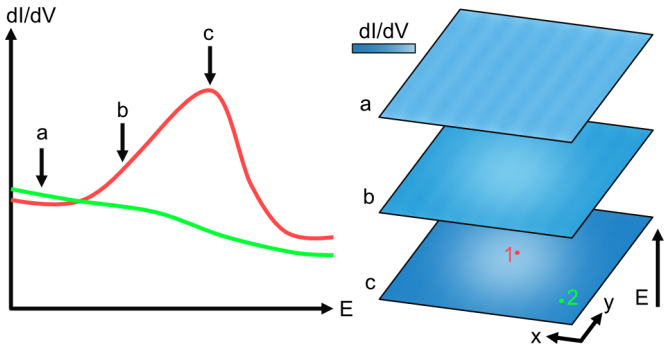

Figure 2.11: **Schematic representation of grid spectroscopy** Synthetic grid-spectroscopy dataset displayed in two ways: individual spectra corresponding to two spatial points (left) and spatial maps of the $\mathrm{d}I/\mathrm{d}V$ signal at different energies (right).

We make each scanning tip by electrochemically etching a tungsten wire (0.375 mm diameter) into a sharp point using a solution of $1:5$ NaOH and H_2O by weight. To make the apex atomically sharp with an ideal s-wave termination, we condition tips on either amorphous evaporated Au, cleaved Au(111) grown on mica, or single crystal Cu(111). To change the tip apex, we apply large voltage pulses between

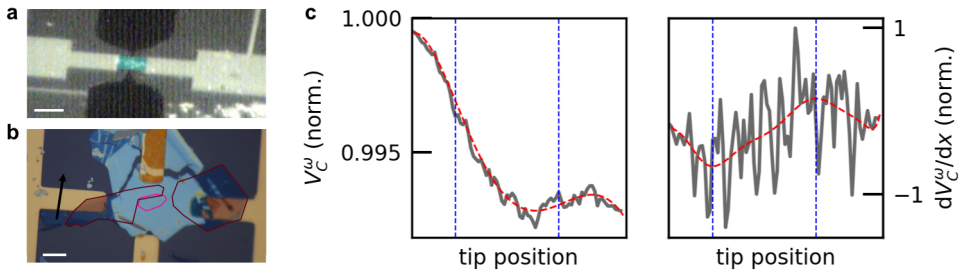

Figure 2.12: **Capacitive navigation to STM samples**, **a**, Image of STM tip and tip reflection when brought close to a surface-exposed vdW device with stepped arrow Au contacts taken with high resolution camera mounted outside the UHV chamber. **b**, Optical micrograph of device, whose size and position are coincident with blue box in **a**. The target region for measurement is outlined in pink, while graphite contacts to this region are outlined in red. All other areas of the sample besides the evaporated contacts are insulating. **c** Capacitive signal (right) and its spatial derivative (right) as the tip is moved acrross the path denoted by a black arrow in **b**. Dashed blue lines denote locations of the edges of the Au contact step. Scale bars correspond to **a** 400 μm and **b** 10 μm.

the tip and the metal surface and/or poke the tip apex directly into the metal surface. We prepared the Cu(111) surface using argon ion bombardment and subsequent thermal annealing in the UHV chamber. We consider the tip ideal when it meets the following standards: (1) forward and backward topography images appear identical and reproducible at all possible scan angles, (2) the spectrum is consistent with the prep material, completely linear for amorphous Au or shows a Shockley surface state for Au(111)/Cu(111), (3) when we dip the tip into the metal surface and slowly bring it out of resistive contact, the measured current between the tip and the sample rapidly decays to zero in a step-like fashion. These standards indicate a tip terminated by a single s-wave atom. On Au(111)/Cu(111), we can directly confirm that the tip apex is sharp and spherical by measuring the protrusion created by the process in (3).

We obtain spectra with lock-in $\mathrm{d}I/\mathrm{d}V$ measurements using an AC excitation with a peak-to-peak amplitude of 5 mV and a frequency at either 317 or 419 Hz. In our STM system, the capacitive current that results from this excitation often acquires an extra phase, $I_C = \omega C V_m \cos(\omega t + \delta)$, due to parasitic capacitance and inductive components within the full tunneling circuit. This adds an unwanted offset to the measured $\mathrm{d}I/\mathrm{d}V$ signal which is particularly problematic when deciphering the difference between dips and hard gaps in the tunneling spectrum. To offset this phase shift in the capacitive current, we introduce a relative phase, α, between the excitation and lock-in reference. We determine the optimal α by bringing the tip out of tunneling contact with the sample but still close enough to pick up a large capacitive signal. In this geometry, the value of α which minimizes the in-phase channel of the lock-in corresponds to the minimum possible in-phase capacitive coupling.

We use a high resolution camera mounted outside the UHV chamber to visualize the tip position

relative to the sample. However, surface-exposed vdW devices fabricated using the methods described by section 2.2.3 have an effective sample area of around 20-200 $\mu\mathrm{m}^2$, illustrated by the annotated optical micrograph in figure 2.12b. Since this is much smaller than the scale of discernible features in the camera image, we use capacitive sensing techniques to reliably land on vdW devices.[75] To aid this procedure, we fabricate contacts which are large relative to the camera resolution and are shaped into a stepped arrow structure, shown in figure 2.12a. We apply an AC modulation of the form $V_m \sin(\omega t)$ to the contacts, where $V_m \approx 1$ V and $\omega \approx 500$ Hz. We apply a second modulation with the form, $V_m \cos(\omega t + \pi)$, to the base of the Si/SiO_2 substrate. The combination of these two signals creates an electric potential profile which changes sharply near the edges of the contacts. We then bring the tip close enough to the contacts to pick up a measurable capacitive current. Due to the particular electric field profile around the contacts, the capacitive current will reach a minimum when the tip is positioned near the middle of the contact steps and will exhibit a turning point when we move the tip over the edge of the contact. We see this more clearly by taking a numerical derivative of the capacitive current signal, exhibited in figure 2.12c. We use these signatures to map out the location of the contacts so that we can navigate to the exposed vdW material without crashing into insulating or contaminated areas of the sample.

2.3.4 Interpreting STM data from vdW devices

Interpreting STM data from vdW devices is often more straightforward than interpreting transport data, since the tunneling current is a direct measure of the height and DOS of the sample. Nevertheless, it sometimes requires a trained eye. The following explains two aspects of STM data from moiré materials which are particularly relevant to the data presented in chapter 5.

Analysis of twist angle and strain

Determining the twist angle of a moiré sample using using STM is straightforward since topography/LDOS maps give you a real space image of the moiré superlattice. In a symmetric moiré pattern formed between two rotated hexagonal lattices with periodicity a, the periodicity of the moiré pattern, or the moiré wavelength can be calculated as,

$$a_M = \frac{a}{\sqrt{2(1-\cos\theta)}} \tag{2.11}$$

In principle, we can just measure a_M directly from the STM image and use it to calculate θ. The problem with this is that moiré heterostructures almost always have some spatially varying interlayer heterostrain introduced by the fabrication procedure, which makes the moiré superlattice nonisotropic. However, its shape is extremely sensitive to small changes in the amount of heterostrain, acting almost as a strain-magnifying glass. By analyzing the shape and size of the moiré, we can determine the unique local twist

angle and heterostrain for the region pictured in an STM image.

An example topography scan of a moiré superlattice in twisted molybdenum ditelluride along with the corresponding fast fourier transform (FFT) is shown in figure 2.13. Arrows on the image denote the three moiré lattice vectors, $\mathbf{a}_{M,i}$, that define the hexagonal moiré superlattice. The small periodicity in the image corresponds to the $MoTe_2$ atomic lattice, with lattice vectors $\mathbf{a}_i$. The FFT shows both the fourier lattice vectors, $\mathbf{b}_i = 1/\mathbf{a}_i$ and fourier moiré lattice vectors, $\mathbf{b}_{M,i} = 1/\mathbf{a}_{M,i}$.

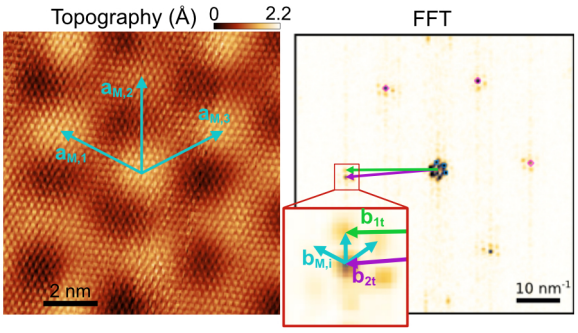

Figure 2.13: **Structural characterization of a moiré superlattice**, Topography map and corresponding fast fourier transform (FFT) obtained on a region of $tMoTe_2$ with a twist angle of $\theta = 4.45°$. Based on the locations of Fourier space lattice vectors from the top and bottom $MoTe_2$ layers, $\mathbf{b}_{i,t}$ and $\mathbf{b}_{i,b}$, we calculate that there is $\varepsilon_{bi} = 0.56\%$ biaxial strain and $\varepsilon_{uni} = 0.71\%$ oriented at $17°$ with respect to the real space moiré lattice, defined by vectors $\mathbf{a}_{M,i}$ $\mathbf{a}$ indicated on the topography image.

Since this topography image has atomic resolution, we can calculate the twist angle and strain profile exactly by following the procedure described in Refs.[76,77] All we need is the positions of two atomic lattice peaks from the top layer and two from the bottom layer, which we can decipher by zooming in around the atomic lattice peaks in the FFT, illustrated in figure 2.13. The relative strain between the $MoTe_2$ layers is determined in the most general case by solving the following equation relating the top layer atomic lattice, $\mathbf{a}_{t_i}, i = 1, 2$, and the bottom layer atomic lattice, $\mathbf{a}_{b_i}, i = 1, 2$, as determined from atomically resolved images:

$$\begin{pmatrix} \mathbf{a}_{t_1} \\ \mathbf{a}_{t_2} \end{pmatrix} = \begin{pmatrix} \cos\theta_2 & \sin\theta_2 \\ -\sin\theta_2 & \cos\theta_2 \end{pmatrix} \begin{pmatrix} 1+\varepsilon_{uni} & 0 \\ 0 & 1 \end{pmatrix} \begin{pmatrix} \cos\theta_1 & \sin\theta_1 \\ -\sin\theta_1 & \cos\theta_1 \end{pmatrix} \begin{pmatrix} 1+\varepsilon_{bi} & 0 \\ 0 & 1+\varepsilon_{bi} \end{pmatrix} \begin{pmatrix} \mathbf{a}_{b_1} \\ \mathbf{a}_{b_2} \end{pmatrix}.$$

In this scheme, starting with the bottom lattice which is assumed to be undeformed, a biaxial deformation quantified by ε_{bi} is first applied, then the lattice is rotated by θ_1, after which a uniaxial deformation quantified by ε_{uni} is applied in the original $\mathbf{a}_{b_1}$ direction, and finally the lattice is further rotated by θ_2, yielding the top lattice. The twist angle is thus $\theta = \theta_1 + \theta_2$, and the uniaxial strain is applied in the direction θ_1 with respect to the moiré wavevector.

For STM images without atomic resolution, we can use the $\mathbf{b}_{M,i}$ vectors to estimate the strain and twist angle up to some uncertainty. We follow reference[78] and neglect biaxial strain. In this model, an applied uniaxial heterostrain, ε, oriented in the direction θ_s with respect to the moiré lattice vectors can be related to the atomic lattice vectors by the Poisson ratio, δ. The Poisson ratio in an intrinsic elastic

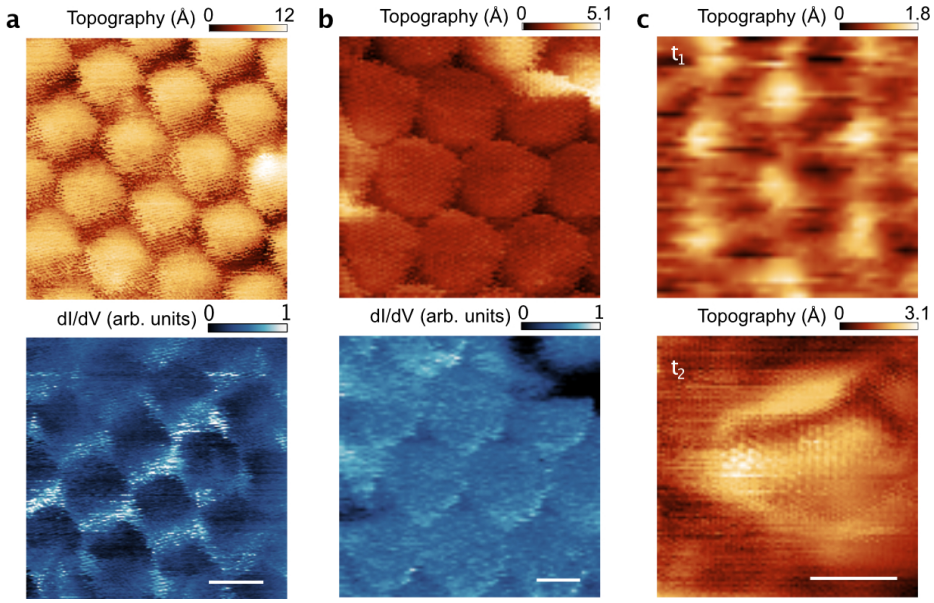

Figure 2.14: **Signatures of tip-sample interaction effects.** **a**-**b**, Low-bias imaging of $tMoTe_2$ with $\theta = 3.68°$ and setpoints (I_t,V_b) of **a**, $(10$ pA,-0.9 V$)$ and **b**, $(10$ pA,-0.915 V$)$. These tunneling parameters correspond to small tip-sample separations. **c**, Topography maps of the same region both before (t_1, top row) and after (t_2, bottom row) performing a series of low-bias LDOS maps. Scale bars are 5 nm.

property of a material which characterizes its movement in response to strain. For $MoTe_2$, we use a Poisson ratio of $\delta = 0.37$[79] for our calculations. We minimize the following equation using $\mathbf{a}_{M,i}$ as input parameters:

$$\begin{pmatrix} \mathbf{a}_{t_1} \\ \mathbf{a}_{t_2} \end{pmatrix} = \begin{pmatrix} \cos\theta_s & -\sin\theta_s \\ \sin\theta_s & \cos\theta_s \end{pmatrix} \begin{pmatrix} 1+\varepsilon & 0 \\ 0 & 1-\delta\varepsilon \end{pmatrix} \begin{pmatrix} \cos\theta_s & \sin\theta_s \\ -\sin\theta_s & \cos\theta_s \end{pmatrix} \begin{pmatrix} \cos\theta & \sin\theta \\ -\sin\theta & \cos\theta \end{pmatrix} \begin{pmatrix} \mathbf{a}_{b_1} \\ \mathbf{a}_{b_2} \end{pmatrix},$$

Since this method neglects biaxial strain, which the previous calculation method has found to be non-negligible in $tMoTe_2$ samples, the values of the twist angle determined with this method are likely overestimated by a fraction of a degree.

Tip-sample interactions

Section 1.4.2 explains how the reduced dimensionality of vdW materials makes them more susceptible to deformation and strain. An STM tip brought close to the surface of an exposed vdW surface can thus interact strongly with the surface and introduce transient mechanical deformations.

A well known effect is pressure-induced lattice commensuration that occurs when an STM tip is

brought close enough to the surface of a moiré material. The pressure exerted by the tip on the vdW layers promotes expansion of energetically favorable stacking configurations and shrinking of disfavored ones. In the case of a TBG moiré, the most energetically favorable stacking configuration is AB stacking, while AA stacking is extremely energetically costly. Pressure induced commensuration in this case will expand the AB regions and shrink the AA regions[56,80] This phenomena was first observed in graphene/hBN moiré lattices.[43] The excess strain created by expansions of the AB region leads to tall domain walls that show up as sharp edges on the hexagonal moiré pattern in STM topography. Through a similar mechanism, the tip may also drag the position of domain walls as it scans accross the surface, leading to sharp jumps in the topography signal. This effect should generalize to non-graphene based moiré systems; in fact, we commonly observe signatures of this effect in our STM measurements of $tMoTe_2$, shown in figure 2.14a-b. This phenomenon obscures the natural shape of the moiré superlattice and may introduct artifacts in the $\mathrm{d}I/\mathrm{d}V$ spectra.

In the case of $tMoTe_2$, tip-sample interactions can also lead to permanent local degradation of the sample after many repeated scans at small tip-sample distances. Figure 2.14c shows the condition of a small region of $tMoTe_2$ before (top) and after (bottom) performing a set of $\mathrm{d}I/\mathrm{d}V$ maps with a small tip-sample-distance, which show a clear degradation of the surface. We often notice either a similar degradation, or a local doping of the imaged $tMoTe_2$ region. We thus try to minimize tip-interaction whenever possible when measuring this material.

Chapter 3

TOPOLOGICAL FLAT BANDS IN A FAMILY OF MULITLAYER GRAPHENE MOIRÉ LATTICES

This chapter is adapted from previously published work: Dacen Waters*, Ruiheng Su*, Ellis Thompson*, Anna Okounkova, Esmeralda Arreguin-Martinez, Minhao He, Katherine Hinds, Kenji Watanabe, Takashi Taniguchi, Xiaodong Xu, Ya-Hui Zhang, Joshua Folk†, Matthew Yankowitz†. Topological flat bands in a family of mulitlayer graphene moiré lattices. *Nature Communications* **15** 10552 (2024). * denotes equal contribution and † denotes corresponding author.

3.1 Introduction

As discussed in chapter 1, twisting two monolayer graphene sheets by an angle of $\theta \approx 1.1^\circ$ creates magic-angle twisted bilayer graphene (MATBG), in which several new phases of matter have been realized.[14–16, 37–40, 50] A much broader range of novel physics can be unveiled in closely related structures having three or more sheets of graphene. Early experiments investigated the strongly correlated and topological physics arising in twisted monolayer-bilayer and double-bilayer graphene, noting intriguing similarities between the two systems that were, nevertheless, qualitatively distinct from MATBG.[58–69] Whereas the investigation of MATBG has expanded to alternating-twist structures up to five layers,[81–85] the study of structures that include Bernal–stacked components has until now been limited to just those two, despite many others in the twisted $M + N$ family carrying predictions of closely related flat bands (t$M + N$, where M and N are positive integers representing the number of Bernal–stacked graphene layers twisted atop one another).[86]

From a symmetry perspective, t$M + N$ structures differ fundamentally from the family of alternating–twist magic–angle graphene stacks by the breaking of C_{2z} symmetry (in–plane rotation by 180°). Unlike in TBG, this allows a gap to be opened between the lowest valence and conduction bands at charge neutrality by an electric displacement field, D. The collective Berry curvature of many graphene layers contributes to a non-zero valley Chern number of the moiré bands, yielding topological electronic states when interactions generate a spontaneous valley polarization. Experimentally, an intriguing result is that the correlated electronic states appearing in t$1 + 2$ are rich with emergent topology,[?, 58, 59, 61] and are furthermore remarkably similar to many of the states seen in t$2 + 2$.[63–69] The intertwined correlated and topological states are most similar when the direction of D is oriented from the monolayer to the bilayer

of t$1+2$, which localizes the conduction band mostly to the bilayer side.

In this work, we extend the study of t$M+N$ graphene structures to include configurations as thick as six total layers, focusing on t$1+3$, t$2+3$, t$1+4$, and t$2+4$. Despite the inclusion of these additional layers of graphene in the moiré structure, we find striking commonalities in both the non–interacting and correlated physics across this entire family. Continuum model calculations indicate that these unexpected similarities likely arise because low–energy states in the conduction band are localized to just three graphene sheets, irrespective of the total number of layers in the structure: the two layers at the twisted interface and one more immediately adjacent. Ultimately, the result is that adding graphene sheets above and below does not significantly affect the band structure, it simply protects the trio of active layers and strengthens the roles of topology and correlations in shaping the electronic system.

3.2 Theoretical predictions for tM+N graphene

3.2.1 Band structure calculations.

We utilize a generalized Bistritzer–MacDonald Hamiltonian for the single particle band structure calculations. This follows the same ansatz as the Bistritzer-MacDonald model for TBG including the effects of lattice relaxations presented in sections 1.4.1 and 1.4.2 The effective Hamiltonian can be written as

$$H = \begin{pmatrix} H_M & H_{\text{int}}^\dagger \\ H_{\text{int}} & H_N \end{pmatrix}, \tag{3.1}$$

where H_M and H_N are Hamiltonians for the M– and N–layer graphene, respectively, and H_{int} captures the interlayer coupling of the twisted moiré interface. The multilayer graphene Hamiltonians are given by

$$H_M = \begin{pmatrix} H_1 - \Delta_1 & \Gamma & \tilde{\Gamma} & 0 & \\ \Gamma^\dagger & H_1 - \Delta_2 & \Gamma^\dagger & \tilde{\Gamma}' & \\ \tilde{\Gamma} & \Gamma & H_1 - \Delta_3 & \Gamma & \\ 0 & \tilde{\Gamma}' & \Gamma^\dagger & H_1 - \Delta_4 & \\ & & & & \ddots \end{pmatrix},$$

with

$$H_1 = \begin{pmatrix} 0 & \frac{\sqrt{3}}{2}\gamma_0(k_x - ik_y) \\ \frac{\sqrt{3}}{2}\gamma_0(k_x + ik_y) & 0 \end{pmatrix},$$

$$\Gamma = \begin{pmatrix} -\frac{\sqrt{3}}{2}\gamma_4(k_x - ik_y) & -\frac{\sqrt{3}}{2}\gamma_3(k_x + ik_y) \\ \gamma_1 & -\frac{\sqrt{3}}{2}\gamma_4(k_x - ik_y) \end{pmatrix},$$

$$\tilde{\Gamma} = \begin{pmatrix} \frac{1}{2}\gamma_2 & 0 \\ 0 & \frac{1}{2}\gamma_5 \end{pmatrix}, \ \tilde{\Gamma}' = \begin{pmatrix} \frac{1}{2}\gamma_5 & 0 \\ 0 & \frac{1}{2}\gamma_2 \end{pmatrix},$$

$$\text{and } \Delta_{\text{i}} = \begin{pmatrix} \delta_i & 0 \\ 0 & \delta_i \end{pmatrix} \tag{3.2}$$

The Hamiltonian is appropriately truncated according to how many layers there are. We use hopping parameters $(\gamma_0, \gamma_1, \gamma_2, \gamma_3, \gamma_4, \gamma_5) = (2610, 361, -20, -283, -140, 20)$ meV. The parameter δ_i captures the effect of a potential difference across the layers. For simplicity, we assume that the potential drops uniformly across the structure with a total magnitude given by $\delta = \sum_{i=1}^{M+N} |\delta_i|$. For example, the potentials for the t$1+2$ system would be $\delta_1 = \delta/2, \delta_2 = 0, \text{ and } \delta_3 = -\delta/2$. By this definition, $\delta > 0$ corresponds to an experimentally applied $D > 0$ that points from the thinner layer to the thicker layer. In the continuum approximation, the M– and N–layer systems are coupled when the Bloch wave vectors differ by $\vec{q}_j$, where $\vec{q}_0 = (0,0),\ \vec{q}_1 = 1/L_M \left(-\frac{2\pi}{\sqrt{3}}, -2\pi\right)$, $\vec{q}_2 = 1/L_M \left(\frac{2\pi}{\sqrt{3}}, -2\pi\right)$, and $L_M = a/\theta$ is the moiré wavelength. The interlayer Hamiltonian is then given by

$$H_{\text{int}} = \sum_{j=0}^{2} t_M \begin{pmatrix} \alpha & \exp\left(-i\frac{2\pi j}{3}\right) \\ \exp\left(i\frac{2\pi j}{3}\right) & \alpha \end{pmatrix}, \tag{3.3}$$

where $t_M = 110$ meV and $\alpha = 0.5$.

Example band structures calculated for the t$1+3$ system are shown in figure 3.1a–c. Across many t$M+N$ constructions, we generally find overlap between the moiré conduction and valence bands with $\delta = 0$. Further, the moiré valence band tends to be more dispersive than the moiré conduction band, consistent with our experimental observations that correlated states primarily occur on the electron–doped side. We performed a series of calculations for a range of θ and Δ for all t$M+N$ layer combinations up to t$3+6$, resulting in over 5000 individual band structures.

We use the method from Ref.[87] to calculate Berry curvature. The moiré Brillouin zone (MBZ) is discretized into a 50×50 grid. For each $\mathbf{k}$ in the MBZ, we calculate the $U(1)$ link:

$$U_\mu(\mathbf{k}) = \frac{\langle u(\mathbf{k} + \delta k_\mu \hat{k}_\mu) | u(\mathbf{k}) \rangle}{N_\mu(\mathbf{k})}, \tag{3.4}$$

where $N_\mu(\mathbf{k}) = |\langle u(\mathbf{k} + \delta k_\mu \hat{k}_\mu) | u(\mathbf{k}) \rangle|$ and $\mu = 1, 2$. The Berry curvature is then given by:

$$\Omega(\mathbf{k}) = -\frac{\text{i} \ln W(\mathbf{k})}{\delta k_1 \delta k_2}, \tag{3.5}$$

where $W(\mathbf{k})$ is $U_1(\mathbf{k}) U_2(\mathbf{k} + \delta k_1 \hat{k}_1) U_1^{-1}(\mathbf{k} + \delta k_2 \hat{k}_2) U_2^{-1}(\mathbf{k})$. We ensure that $-\pi < -\text{i} \ln W(\mathbf{k}) \leq \pi$. The valley Chern number is then calculated as usual by integrated the Berry curvature over the moiré Brillouin zone (see section 1.2.2).

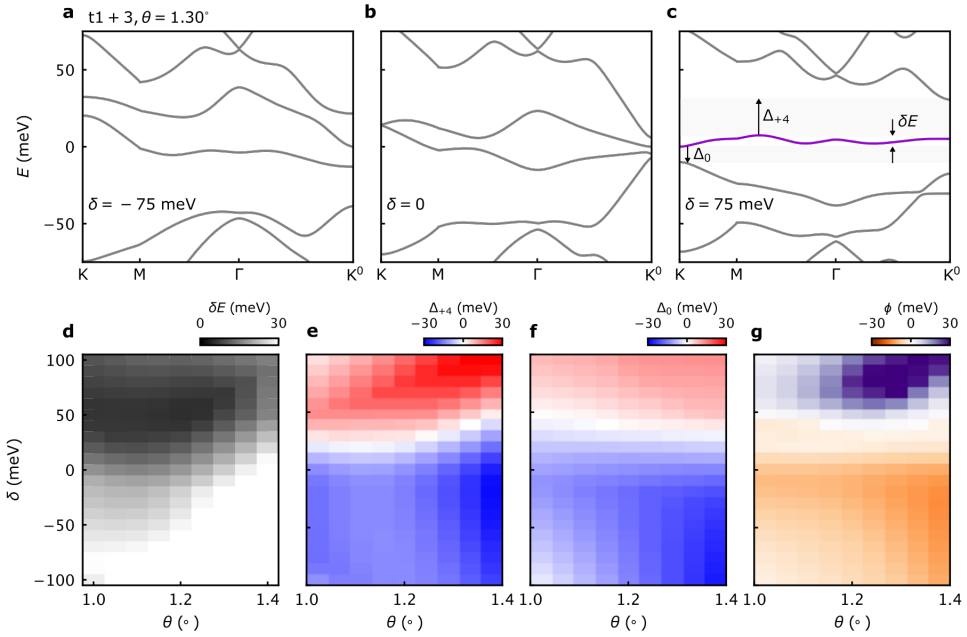

Figure 3.1: **Band structure calculations for t1 + 3**, **a-c**, Band structures for the t1+3 system at $1.30°$, with interlayer potentials $\delta = -75, 0,$ and 75 meV, respectively. Panel **c** shows the definitions of Δ_0, Δ_{+4}, and δE. **d**, Bandwidth, δE, of the moiré conduction band calculated as a function of θ and δ. **e**, Energy separation between the top of the moiré conduction band and the top of the remote conduction band, Δ_{+4}. Positive (negative) values of Δ_{+4} indicate a band gap (band overlap). **f**, Similar plot, but for the energy separation between the moiré conduction and valence band, Δ_0 (i.e., the gap at the charge neutrality point). **g**, The isolated flat band parameter, ϕ , as a function of twist angle and interlayer potential. Large positive values of ϕ (purple), corresponds to a flat and isolated moiré conduction band. Negative values of ϕ (orange) correspond to the moiré conduction band overlapping with other bands. The optimal twist angle is around $1.30°$, corresponding to the band structures shown in panels **a-c**.

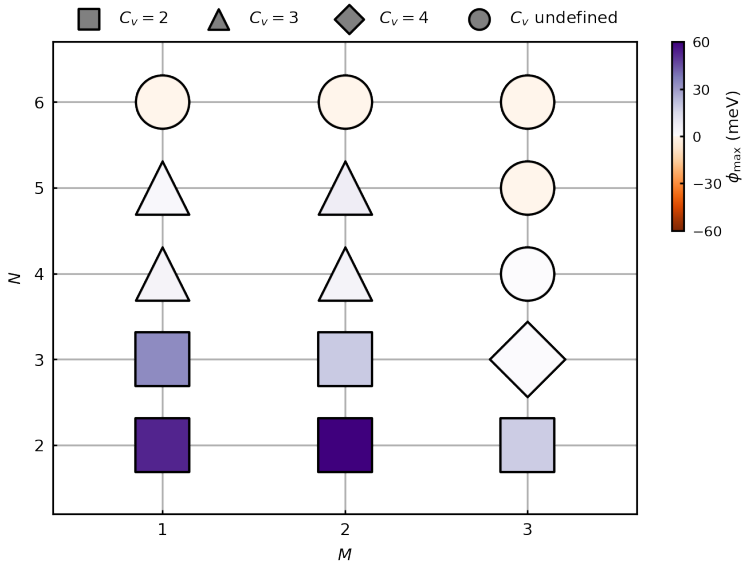

Figure 3.2: **Calculated band isolation, flatness, and topology of various t$\mathbf{M+N}$ structures**, Summary of the band structure calculations for all t$M+N$ combinations up to t$3+6$. The color of each marker indicates the maximum value of ϕ obtained after searching over all combinations of θ and δ. The valley Chern number of the moiré conduction band for each layer combination is also calculated for the optimal parameters of θ and δ, i.e., where $\phi = \phi_{max}$. The shape of the markers indicates the valley Chern number. We do not calculate the valley Chern number for systems where the moiré conduction band cannot be isolated ($\phi_{max} \leq 0$), indicated by the circle markers.

3.2.2 Quantifying the optimal twist angle for each M,N

To inform our experimental search, we quantify how isolated and flat the moiré conduction band is for each set of parameters by defining

$$\phi = \xi \frac{|\Delta_{+4}||\Delta_0|}{\delta E}, \tag{3.6}$$

where Δ_{+4} (Δ_0) is the energy difference between the top (bottom) of the moiré conduction band and the remote conduction band (moiré valence band), and δE is the bandwidth of the moiré conduction band (figure 3.1c). We define $\xi = +1$ when Δ_{+4} and Δ_0 are both positive, and $\xi = -1$ otherwise.

With this definition, ϕ becomes more positive as the moiré conduction band becomes more flat and isolated. When ϕ is negative, the moiré conduction band overlaps with the moiré valence band and/or the remote conduction band. Figure 3.1d–g shows δE, Δ_{+4}, Δ_0, and ϕ as function of θ and δ for the t$1+3$ system, in which we find the optimal angle condition (defined as when ϕ achieves its largest positive value, shown in purple) to be at $\theta \approx 1.30°$ and $\delta \approx +75$ meV. We summarize the results for all layer combinations in figure 3.2, where each data point is color–coded according to the maximum value of ϕ that is obtained for each system. Systems up to t$2+3$ have appreciably flat and isolated moiré conduction

bands, but for t$1+4$, t$2+4$, and thicker, ϕ is very small or negative. For each layer combination in which we find that a flat and isolated moiré conduction band is predicted (i.e., $\phi_{max} > 0$), we further calculate the valley Chern number of the moiré conduction band at the optimal parameter condition (i.e., for the values of θ and δ where $\phi = \phi_{\max}$). We find that all systems have non–zero C_v, reaching as large as $C_v = 3$ for thicker layer combinations.

We note that we use the continuum model predictions of the nominally optimal twist angle only as a rough guide for our experiments. Theoretically, it is not clear whether band flatness, band isolation, or some specific combination of the two is the most important parameter to optimize for achieving strongly correlated states. Even upon choosing a metric for the nominally optimal twist angle in theory, the particular value differs for each t$M+N$ construction and depends on detailed parameters in the continuum model which are not necessarily well known. Experimentally, determining the optimal twist angle for even a single t$M+N$ construction requires studying dozens of devices, which is also beyond the scope of this work. We thus leave a careful determination of the evolution of the optimal twist angle on the layer number construction to future efforts.

3.3 Summary of devices

For this study, we probe the transport behavior of a number of t$M+N$ devices, fabricated using the methods described in sections 2.1.1 and 2.1.2. We assemble the twisted M and N layer structure from multilayer Bernal stacked graphite flakes containing connected regions of M and N layer graphene. We note that, in principle, there could be regions of the exfoliated graphite flakes with metastable stacking orders other than Bernal. However, these non–Bernal domains are known to relax to the ground–state Bernal stacking configuration during stacking unless great care is taken to isolate only non–Bernal domains and minimize strains during transfer.[88] Since we do not take any such precautions, it is overwhelmingly likely that all non–Bernal domains relax to the Bernal configuration in our final samples. Another possible ambiguity in our sample construction is AB vs. BA stacking configurations between the twisted components. For example, t2+2 can host symmetry–broken states when twisted slightly away from 0° (tAB+AB) or away from 60° (tAB+BA).[89] While we fabricated all of our devices by twisting slightly away from 0°, it is known that AB–BA stacking faults naturally exist in bilayer graphene flakes,[90] and these cannot be observed optically. It is therefore possible that t$M+N$ devices with $M \geq 2$ and $N \geq 2$ have unintentional domains of AB–BA at the twisted interface. These could, in principle, have different band structures and valley Chern numbers. Further work is needed to carefully distinguish these potential scenarios. Optical micrographs of all devices measured in this work are shown in figure 3.3 and a summary of our observations across all devices is provided in the following table.

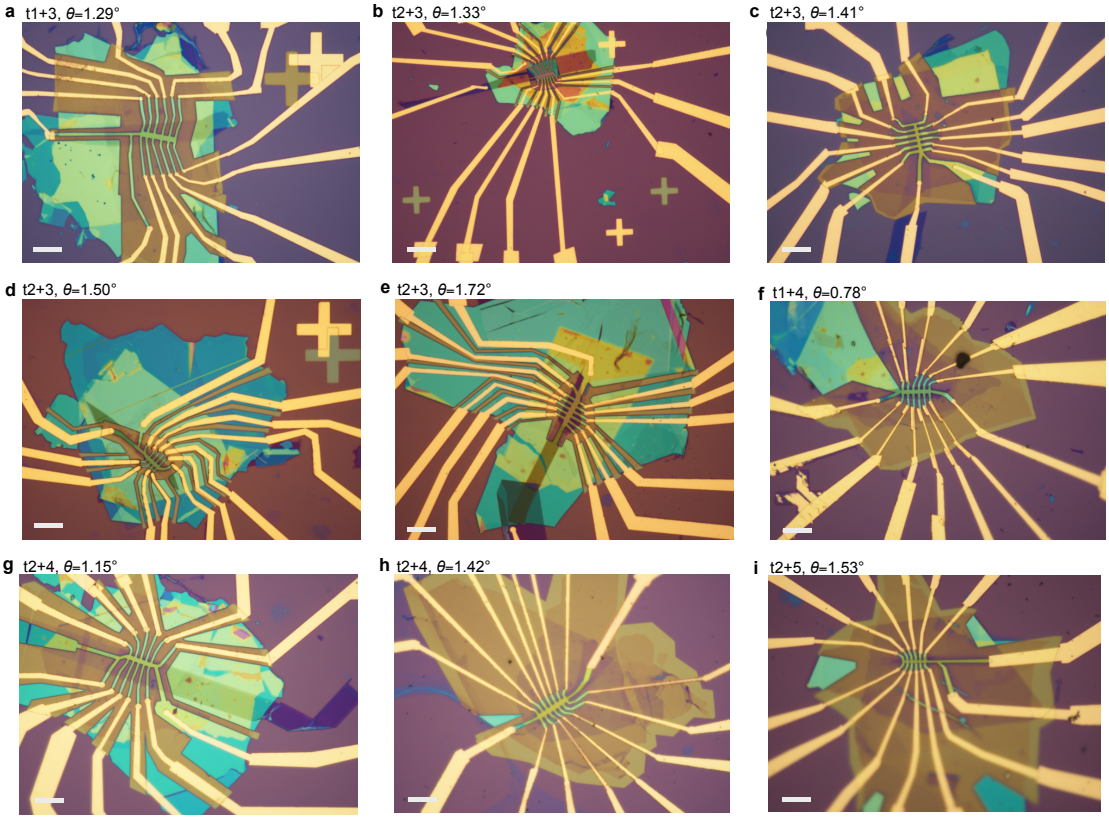

Figure 3.3: **Optical micrographs of the t$\mathbf{M}+\mathbf{N}$ devices a-i,** All scale bars are 10 μm.

Summary of transport properties for all tM+N devices

tM+N	θ	D										
		$D \approx 0$	$D < 0$				$D > 0$					
		$\nu = 0$	$\nu = -4$	$\nu = 0$	$\nu = 2$	$\nu = 4$	$\nu = -4$	$\nu = 0$	$\nu = 1$	$\nu = 2$	$\nu = 3$	$\nu = 4$
t1+2	1.13°	-	BI	BI	CI†	BI	BI	BI	CI, AHE	CI	CI†	BI
t2+2	1.30°	-	BI	BI	CI	BI	BI	BI	CI†	CI	CI†	BI
t1+3	1.29°	-	BI	-	-	-	-	BI	CI†	CI	CI†, AHE	BI
t2+3	1.33°	I†	-	-	-	BI	BI	BI	-	-	-	BI
t2+3	1.41°	I	BI	BI	CI, $B > 0$	BI	BI	BI	CI, AHE	CI†	CI†	BI
t2+3	1.50°	I	BI	BI	CI†	BI	BI	BI	CI†, AHE	CI	CI†	BI
t2+3	1.72°	I		BI				BI				
t1+4	0.78°	-	BI	-	-	-	-	BI	-	-	-	BI
t2+4	1.15°	-	BI	-	-	-	-	BI	-	CI, $B > 0$	-	BI

t2+4	1.42°	I†	BI	-	-	-	-	BI	-	-	-	BI
t2+5	1.53°	I†	BI	-	-	-	-	BI	-	-	-	

- BI denotes a band insulator
- CI denotes a correlated insulator
- I denotes an insulator of unknown origin (i.e., cannot unambiguously distinguish between BI and CI)
- $B > 0$ indicates that the state is only observed in a magnetic field
- † indicates that transport features are suggestive of an incipient insulator, but not well developed at $B = 0$
- AHE denotes the presence of the anomalous Hall effect
- - indicates a metallic state
- Empty cell indicates that our gate range does not include the specific state

3.4 Isolated moiré-localized flat bands

We first compare the band structures of various representative t$M + N$ structures (t$1 + 2$, t$1 + 3$, t$2 + 3$, t$2 + 4$, figures 3.4a–d) as predicted by the Bistritzer–MacDonald continuum model[39] (see Methods). Upon incorporating an interlayer potential arising from an external D pointing from the thinner to the thicker graphene constituent, the moiré conduction band in each of these structures (purple in figures 3.4a–d) becomes relatively flat and isolated by gaps to both the moiré valence band and higher moiré conduction band. Other gaps between neighboring bands can also open for each particular t$M + N$ construction, with the details depending sensitively on θ and both the magnitude and sign of D owing to broken mirror symmetry (see Methods).

Band structure predictions for each of these structures are corroborated by maps of the longitudinal resistivity, ρ_{xx}. The data are collected as a function of top– and back–gate voltages, shown in figures 3.4e–h after converting the gate voltages to moiré band filling, ν, and displacement field, D (see Methods). In qualitative agreement with the band structure calculations, all exhibit insulating states at the charge neutrality point ($\nu = 0$) and at full–filling of the lowest moiré valence and conduction bands ($\nu = \pm 4$) over certain ranges of D, marked by large values of ρ_{xx} that exceed h/e^2 and diverge as the temperature is lowered (h is Planck's constant and e is the charge of the electron).

It is not immediately obvious that isolated flat bands would form in many of these t$M + N$ structures. Bernal graphene films with three or more layers feature multiple low–energy bands,[91,92] all of which must

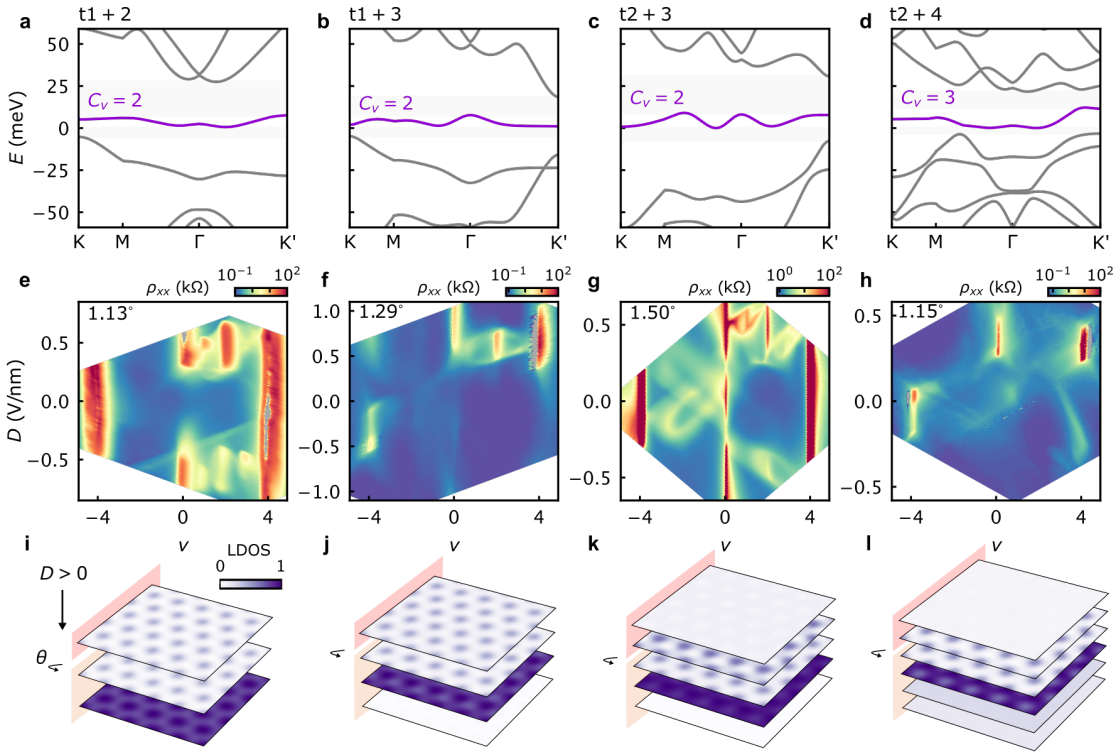

Figure 3.4: **Non-interacting features of t$M + N$ graphene. a**, Band structure calculations for t$1 + 2$ at its nominally optimal twist angle ($\theta = 1.13°$) and interlayer potential ($\delta = 50\text{meV}$); defined as when the moiré conduction band (purple curve) has the narrowest dispersion while being simultaneously gapped (grey shaded regions) from both neighboring bands. Energy is measured with respect to the bottom of the moiré conduction band. The calculated valley Chern number, C_v, is shown for the moiré conduction band (see Methods for details). **b-d**, Similar calculations for (**b**) t$1 + 3$ ($\theta = 1.3°, \delta = 50\text{meV}$); (**c**) t$2 + 3$ ($\theta = 1.45°, \delta = 90\text{meV}$); and (**d**) t$2 + 4$ ($\theta = 1.15°, \delta = 50\text{meV}$). **e**, Resistivity at zero magnetic field as a function of ν and D in a t$1 + 2$ device at $\theta = 1.13°$. Gray color denotes experimental artifacts where negative resistance is observed, attributed to the effects of highly resistive states. **f-h**, Similar measurements for (**f**) t$1 + 3$ with $\theta = 1.29°$; (**g**) t$2 + 3$ with $\theta = 1.50°$; and (**h**) t$2 + 4$ with $\theta = 1.15°$. Positive D is defined as pointing from the thin component to the thick component for all systems. Measurements taken at $T = 1.7$ K, except for **e**, where $T = 0.3$ K. **i-l**, Layer-resolved LDOS calculated for the moiré conduction band, corresponding to the layer combinations and parameters in panels **(a-d)**. Red and orange shadings delineate the M and N layers above and below the twisted interface. The interlayer potential used in the calculations corresponds to positive D in the experiment.

hybridize with the bands from the other twisted constituent to yield an isolated moiré band. To help explain how different t$M+N$ constructions form similar moiré flat bands, figures 3.4i–l show calculations of the layer–resolved local density of states (LDOS) at full–filling of the lowest moiré conduction band (i.e., integrated over the purple bands in figures 3.4a–d).

Considering first the t$1+2$ structure (figure 3.4i), the moiré potential localizes the LDOS on a triangular lattice of ABB–stacked sites, with most weight appearing on the graphene sheet one below the moiré interface. The layer–resolved LDOS configuration of t$1+2$ recurs in the thicker t$M+N$ structures, with the additional layers of graphene away from the twisted interface carrying a comparatively small density of states. In this sense, the t$1+2$ structure can be considered as the basic building block of all of the thicker t$M+N$ constructions. Given that their low–energy bands are all similarly localized nearby the moiré interface, it is natural to expect that the physics of all of these t$M+N$ structures may exhibit common features.

3.5 Common features of the correlated phases

The transport measurements in figures 3.4e–h exhibit insulating states at certain integer values of ν beyond those predicted by the single–particle band structure. As previously observed in a variety of other moiré systems, these correlated insulators arise as a consequence of spontaneous symmetry breaking within the moiré flat bands due to Coulomb interactions.[?,?,15,16,37–40,50,58,59,61–69,81–85] The most prominent correlated insulators for the devices in figure 3.4 appear for $D>0$, where the asymmetry with D is due to the lack of mirror–symmetry (see Methods). The differences between the $D>0$ and $D<0$ correlated insulators has been explored in detail for the case of t$1+2$.[58,61] Here, we turn our attention to analyzing the properties of the correlated phases common across the family of t$M+N$ structures, i.e. for $D>0$, comparing to what is known about the symmetry–broken states in t$1+2$ and t$2+2$.

Figure 3.5 shows high–resolution zoom–ins of both longitudinal and Hall resistances, ρ_{xx} and R_{xy}, for t$1+2$, t$2+2$, t$1+3$, and t$2+3$, along with simple schematics of the material structure. As was seen for the non-interacting features in figures 3.4e–h, the qualitative arrangement of correlated states are similar across all of these t$M+N$ constructions. The most robust insulating state arises at $\nu=2$ in all, spanning the largest range of D and exhibiting the largest value of ρ_{xx} at low temperature. R_{xy} reverses sign across the $\nu=2$ state, consistent with an interaction–induced band gap with hole–like carriers at $\nu\lesssim 2$ and electron–like carriers at $\nu\gtrsim 2$. All samples exhibited a region of ν and D surrounding the insulator at $\nu=2$ characterized by a slight increase in ρ_{xx} and an abrupt sign reversal in R_{xy}. These features have previously been explained for t$1+2$ and t$2+2$ as arising due to the formation of a spin–polarized half–metal state with a reduced isospin degeneracy of two. Resistive states additionally appear

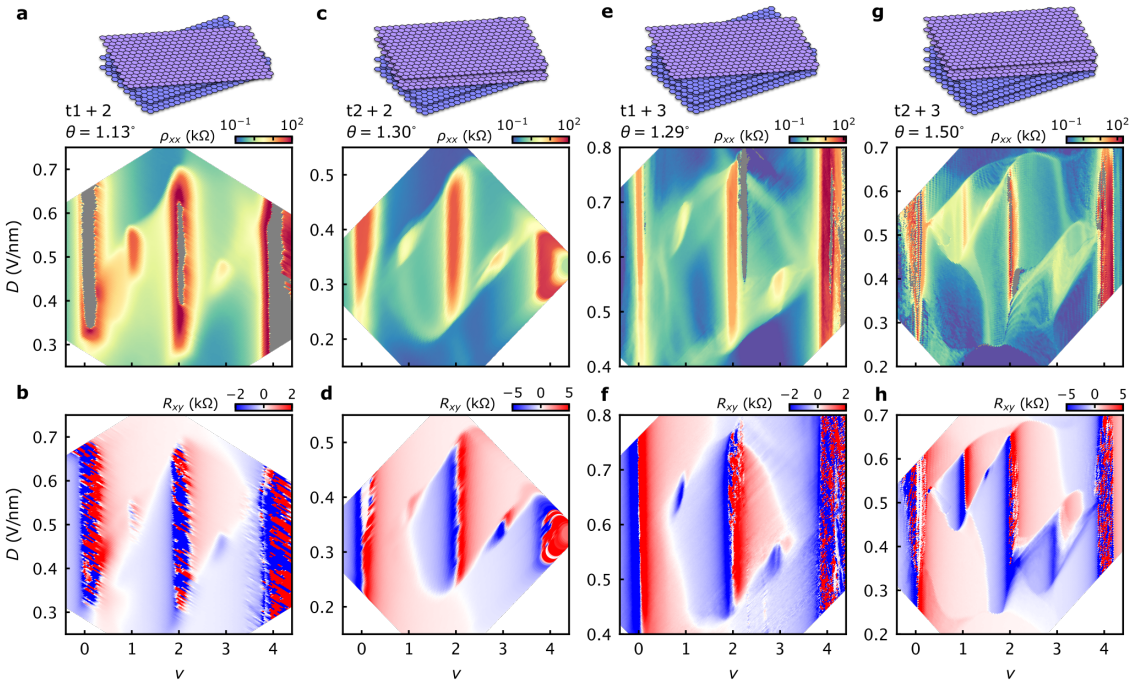

Figure 3.5: **Symmetry-broken states in various t$M+N$ systems. a**, Map of the longitudinal resistivity around the correlated states in the t$1+2$ device at $\theta = 1.13°$. The map is symmetrized at $B = \pm 0.5$ T. **b**, Similar map of the Hall resistance, anti-symmetrized at $B = \pm 0.5$ T. **c,e,g**, Analogous ρ_{xx} maps for the **(c)** t$2+2$ device with $\theta = 1.30°$; **(e)** t$1+3$ device with $\theta = 1.29°$; and t$2+3$ device with $\theta = 1.50°$. **d**,**f**,**h**, Analogous R_{xy} maps for the same set of devices. Schematics in the top panels indicate the layer combination for each measurement. The measurements are performed at nominal sample temperatures of **(a-b)** $T = 300$ mK, **(c-f)** $T = 20$ mK, **(g-h)** $T = 100$ mK.

at $\nu = 1$ and 3 in each of the ρ_{xx} maps in figure 3.5. These feature additional sign reversals (or large enhancements) in R_{xy}, indicating the formation of additional symmetry–broken states with no remaining isospin degeneracies.

3.5.1 Determination of isospin polarization at integer filling

Previous measurements of the evolution of the $\nu = 2$ states in $\mathrm{t}1 + 2$ and $\mathrm{t}2 + 2$ with in–plane magnetic field indicate that they are likely spin polarized;[58,63–65] analogous measurements in our $\mathrm{t}1 + 3$ and $\mathrm{t}2 + 3$ samples are also consistent with spin–polarized insulators). We employ a combination of out–of–plane and in–plane magnetic field measurements of ρ_{xx} and R_{xy} in order to infer the isospin polarization of the correlated states seen at $\nu = 1$, 2, and 3. In–plane magnetic field couples primarily to the spin degree of freedom in graphene owing to its very weak spin–orbit coupling strength (although there can be orbital contributions in multilayer graphene samples[93]). Previous measurements of the correlated insulator at $\nu = 2$ in $\mathrm{t}1{+}2$ and $\mathrm{t}2{+}2$ showed that the energy gap, as extracted from thermal activation measurements, grows with in–plane field .[58,63–65]This behavior is consistent with spin–polarization, as the in–plane field adds a Zeeman contribution to the energy gap. We have performed similar measurements in our $\mathrm{t}1 + 3$ ($\theta = 1.29°$) and $\mathrm{t}2 + 3$ ($\theta = 1.50°$) devices. Figures 3.6a–b show measurements of ρ_{xx} as a function of ν in the moiré conduction band at various values of the in–plane magnetic field, $B_{||}$. In both devices, ρ_{xx} is highly sensitive to $B_{||}$ very near $\nu = 2$, exhibiting enhanced resistance for larger in–plane fields. These observations are consistent with spin–polarized correlated insulators at $\nu = 2$ in $\mathrm{t}1 + 3$ and $\mathrm{t}2 + 3$. For the $\mathrm{t}1 + 3$ device, we further performed temperature–dependent measurements at several values of $B_{||}$. In the Arrhenius plot shown in figure 3.6c, we can extract the gap size of the $\nu = 2$ insulator in the thermally activated regime following $\rho_{xx}^{\nu=2} \propto e^{\Delta^{\nu=2}/2k_BT}$, where $\Delta^{\nu=2}$ is the gap size and k_B is the Boltzmann constant. The results are shown in figure 3.6d. The measured gap size grows monotonically as a function of $B_{||}$. By fitting with a line, assuming $\Delta^{\nu=2}(B) = g\mu_B B + \Delta^{\nu=2}(0)$, we find $g \approx 2$, consistent with a spin–polarized insulating state.

Previous studies of $\mathrm{t}1 + 2$ and $\mathrm{t}2 + 2$ suggest that the ground–state ordering of odd ν phases is less consistent, as spin–valley polarized (SVP) states compete closely with intervalley coherent (IVC) states.[?,58,59,61,63–67] At $\nu = 1$ and 3, calculations typically find the most competitive ground states to be either IVC states or SVP states.[93] When C_v is non–zero, these states are distinguished by the Chern number of the symmetry–broken state, which is 0 for the IVC and non-zero for the SVP. A well–developed IVC state with non–zero C_v would be a trivial insulator at integer band filling, whereas an SVP would exhibit the QAHE. Although these are in principle straightforward to distinguish, there can be various complicating factors in experiments. One example is twist–angle inhomogeneity in the sample, which can

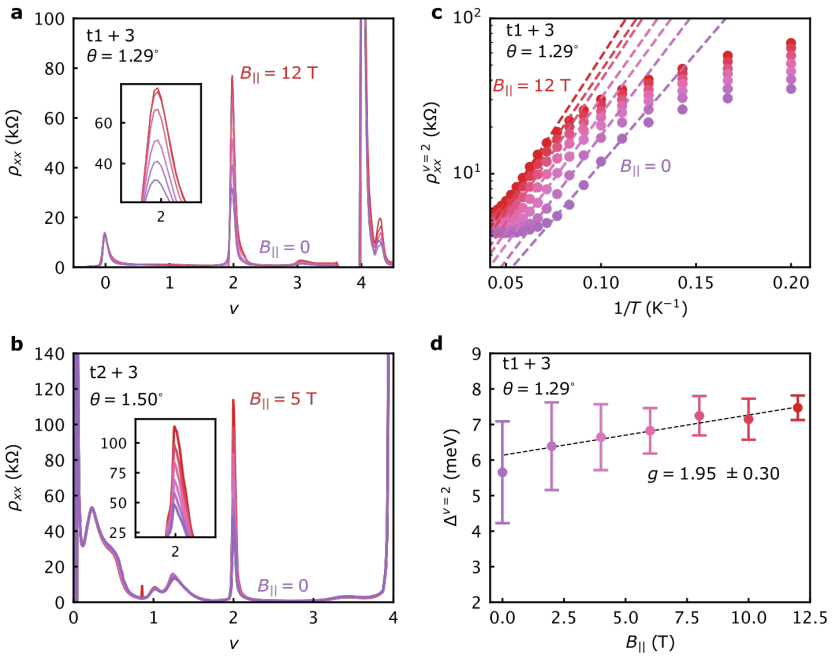

Figure 3.6: **Evidence for spin-polarization at $\nu = 2$, a**, Measurement of ρ_{xx} versus ν for the t1 + 3 sample with $\theta = 1.29°$ acquired at different values of $B_{||}$. The measurement is acquired at variable D in order to cut through the correlated states at each integer ν. The inset shows a zoom-in around $\nu = 2$, showing an increase in the resistance of the correlated insulator with $B_{||}$. The measurement was performed at $T = 1.7$ K. **b**, Similar measurement for the t2 + 3 device with $\theta = 1.50°$, acquired at $D = 0.531$ V/nm and $T = 4$ K. **c**, ρ_{xx} acquired at $\nu = 2$ in the t1 + 3 device as a function of temperature, shown at different values of $B_{||}$ in increments of 2 T. The dashed lines show the linear fits in the thermally activated regime used to extract the gap size of the correlated insulator (see Methods). **d**, Extracted gap sizes determined by the fits shown in **c**. Error bars are standard deviations from the fits. The dashed black line shows the best linear fit to the experimentally determined gap sizes. The slope yields a g-factor consistent with $g = 2$, consistent with a spin-polarized insulator.

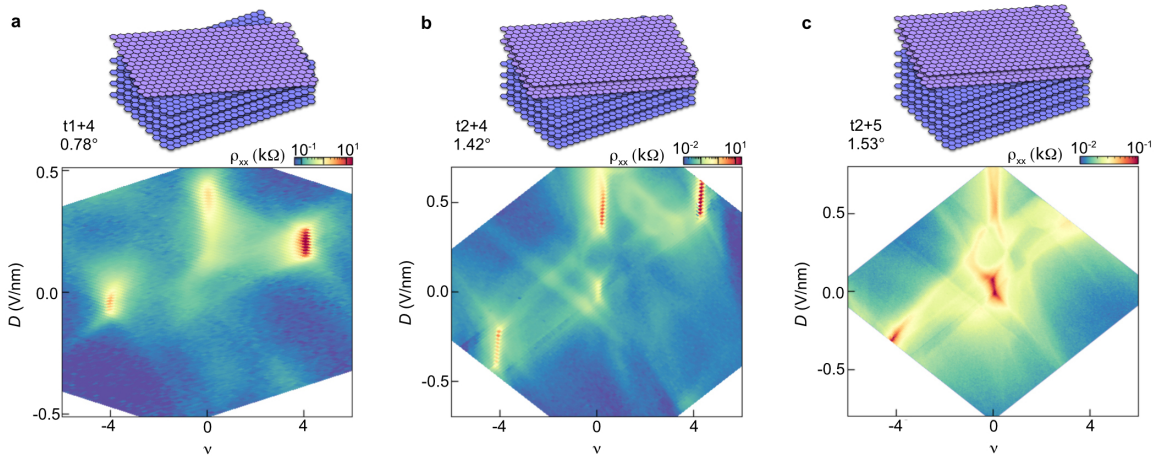

Figure 3.7: **Additional tM + N devices**, **a**, ρ_{xx} map of a t$1+4$ device with $\theta = 0.78°$ acquired at $B = 0$ T. High-resistance states emerge over a small range of D at $\nu = 0$ and $\nu = \pm 4$, indicating the emergence of isolated moiré bands. **b**, Similar measurement for a t$2+4$ device with $\theta = 1.42°$. **c**, Similar measurement for a t$2+5$ device with $\theta = 1.53°$. Schematic above each map shows cartoon representations of the given twisted M- and N-layer combination. Measurements for **a**-**b** were acquired at $T = 1.5$ K. Measurements for **c** were acquired at $T = 100$ mK.

greatly obscure the QAHE. Another is that the correlated state may not be fully gapped at zero magnetic field, preventing a straightforward determination of the topology of the state. There are also exotic forms of IVC ordering that break time–reversal symmetry, leading to a metallic AHE.[61] Although band structure calculation of C_v can provide guidance, the complexity of the calculation for thick t$M+N$ structures may result in incorrect predictions. Furthermore, interactions can potentially renormalize the Chern number of the symmetry–broken states at partial band filling. In general, we are not able to unambiguously determine the ground state ordering at $\nu = 1$ and 3 in our devices, except for the select cases shown in Fig. 3.13.

3.5.2 Signatures of symmetry breaking in thicker structures

It is interesting to note that the t$2+4$ device from figures 3.4d,h,l, as well as the additional t$1+4$, t$2+4$ and t$2+5$ devices we have studied, did not show correlated insulating states or pronounced regions of enhanced resistivity with an R_{xy} sign reversal at a small magnetic field (figure 3.7 and figure A1) This may be due to: (i) the smaller band gaps to higher moiré bands in these thicker structures, (ii) bands that are more dispersive in reality than those predicted by calculations, (iii) devices made away from the optimal flat–band twist angle for each layer number construction, or some combination of all of these. Indications of a symmetry–broken Fermi surface at $\nu = 2$ in t$2+4$ did appear over a small range of

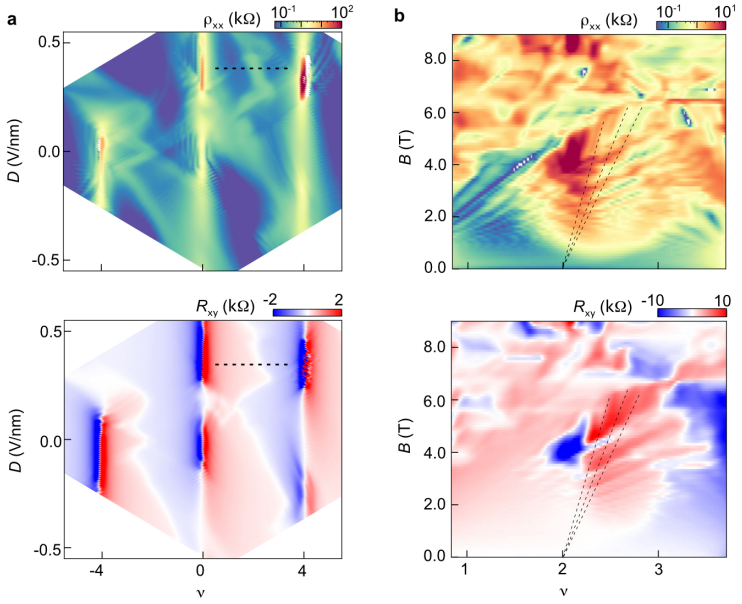

Figure 3.8: **High-field correlated state in a t2 + 4 device**, **a**, ρ_{xx} (top) and R_{xy} (bottom) maps for the t$2+4$ device with $\theta = 1.15°$ (the same as shown in figure 3.4h). The longitudinal (Hall) maps are symmetrized (anti-symmetrized) at $B = 0.5$ T. **b**, Landau fan diagrams acquired at $D = 0.35$ V/nm over the range of doping range indicated by dashed line in **a**. A high-resistance state accompanied by an abrupt sign reversal in R_{xy} emerges at $\nu = 2$ for $B \approx 4$ T. There are additionally quantum oscillations associated with this state that project to $\nu = 2$ at $B = 0$. Together, these observations indicate the emergence of a symmetry-broken state at $\nu = 2$ in a magnetic field. This state is destroyed at higher field by competition with other quantum Hall states. All measurements were acquired at $T = 100$ mK.

magnetic field around $B \approx 4$ T (see figure 3.8). However, this correlated phase is quickly suppressed by competing quantum Hall states originating from $\nu = 0$. Nevertheless, the new Fermi surface formed at $\nu = 2$ in a modest magnetic field indicates that this sample is also close to a strongly correlated regime.

3.6 Abundance of correlated states in twisted bilayer-trilayer graphite

Among all the t$M+N$ samples we have studied, t$2+3$ devices had the largest extent of symmetry–broken phases as a function of ν and D (figure 3.9, see also figure 3.10). In addition to exhibiting symmetry–broken correlated insulators for both signs of D in the lowest moiré conduction band, the samples showed evidence for symmetry broken phases distinct from the usual states seen in the other t$M + N$ systems (see figure 3.4g, figure A2).

Figure 3.9a summarizes our experimental observations for a t$2 + 3$ device with a 1.50° twist angle, incorporating observations from figures 3.5g,h, 3.9b,c, and figure A2. States labeled in black or dark gray are insulating or highly resistive (the unexpected gapped state at $\nu = 0.25$ will be discussed in future

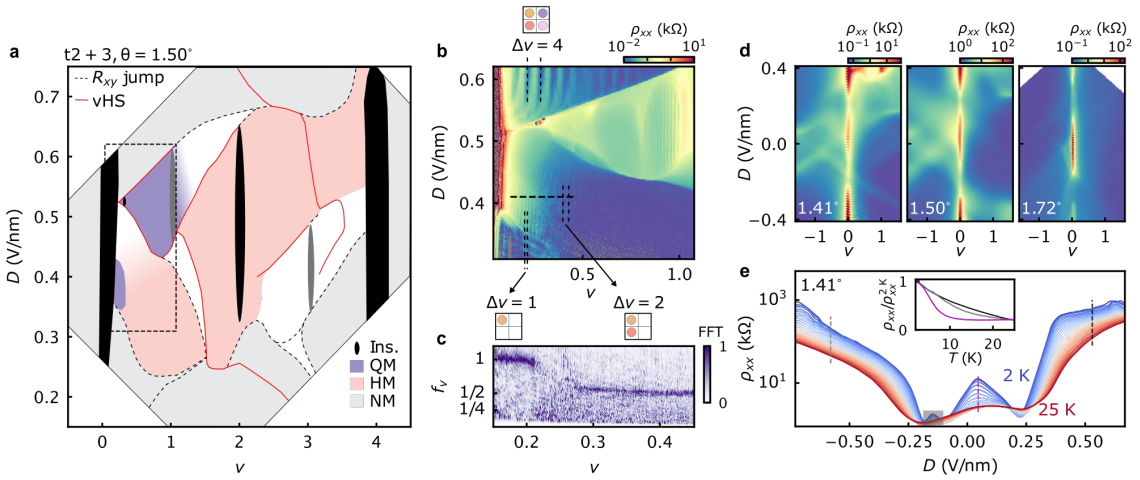

Figure 3.9: **Correlated states in t2 + 3 graphene.** **a**, Summary phase diagram determined from magnetotransport measurements in the $\theta = 1.45°$ device. Black vertical features indicate insulating states (Ins). The $\nu = 1$ and 3 states are in shaded dark grey to indicate that it is a weakly-developed resistive state corresponding to an incipient insulator. Shaded regions indicate where the metallic states are either normal-metals (NM), half-metals (HM), or quarter-metals (QM). White regions within the bounding box indicate situations in which the degeneracy cannot be uniquely determined. Solid red lines denote likely van Hove singularities (vHS) with R_{xy}=0. Dashed black lines denote abrupt jumps in R_{xy}. **b**, Map of ρ_{xx} acquired at $T = 20$ mK and symmetrized at $B \pm 0.9$ T, corresponding to the black dashed box in **(a)**. Spacing of the quantum oscillations ($\Delta\nu$) indicates the degeneracy of the metallic phases. Corresponding schematics indicate the degeneracy for representative regions of normal-metal ($\Delta\nu = 4$, top), half-metal ($\Delta\nu = 2$, bottom right), and quarter-metal ($\Delta\nu = 1$, bottom left) phases. **c**, Fourier transform analysis (FFT) of the SdH measurements taken along the dashed black line at $D = 0.41$ V/nm in **(b)**. The FFT amplitude is normalized to the maximum value of the measurement, and the frequency of oscillations is normalized to the density. **d**, Measurements of ρ_{xx} for three t2+3 devices with different θ acquired around $\nu = 0$. All measurements are performed at $T = 2$ K. **e**, Temperature dependence of ρ_{xx} as a function of D, acquired in the $\theta = 1.41°$ device at $\nu = 0$. Line cuts at select values of D are shown for each state in the inset, normalized by their respective values at $T = 2$ K. The gray shaded region indicates a region of the data influenced by artifacts from the electrical contacts.

work). Solid red curves denote sign changes in R_{xy} that likely correspond to van Hove singularities, whereas dashed black curves denote abrupt jumps in R_{xy} without a sign change, possibly indicating the formation of a new interaction–induced Fermi surface. Shaded regions in figure 3.9a correspond to metallic states with different isospin degeneracies.

Experimentally, the degeneracy can be identified either from the spacing, $\Delta\nu$, between Shubnikov de Haas (SdH) oscillations in $\nu - D$ maps taken at finite magnetic field (figures 3.5g and 3.9b) or from the Fourier transform of SdH oscillations collected by sweeping the magnetic field at fixed gate voltage. For the t2+3 device with $\theta = 1.45°$, we extract the degeneracy from the frequency of quantum oscillations, f_ν, in low–field Landau fan measurements taken at constant D. We first extract the frequency of oscillations with field, f_B, from the Fourier transform (FFT) of each field sweep with respect to $1/B$. The frequency is then normalized by the total carrier density, $f_\nu = f_B/(\Phi_0 n)$. For the case of a singly connected Fermi surface at the Fermi level, the inverse quantity f_ν^{-1} represents the degeneracy of charge carriers.[88]

The degeneracy extracted is four outside the correlated region (e.g., $\Delta\nu = 4$ in the top of the map shown figure 3.9b), consistent with the four–fold spin and valley degeneracy of graphene. The degeneracy is reduced to two inside the region surrounding the correlated insulator at $\nu = 2$ (light red in figure 3.9a), consistent with our inference of a spin–polarized ground state. The degeneracy is harder to discern in the regions surrounding $\nu = 1$ and 3, although there is a region of ν closely surrounding $\nu = 1$, colored in purple, where $\Delta\nu$ is unambiguously one. There is also a small pocket of a symmetry–broken phase over a narrow range of $D \approx 0.4$ V/nm between $\nu = 0$ and $\nu \approx 0.21$. Figure 3.9c shows the normalized Fourier transform of the SdH oscillations measured at a fixed D cutting through this small pocket, as denoted by the horizontal black dashed line in figure 3.9b. We see that all isospin degeneracies are lifted in this pocket, corresponding to a quarter–metal phase for $\nu < 0.21$. This is, to our knowledge, the first observation of a quarter–metal state in the t$M + N$ family that is not directly associated with the $\nu = 1$ insulator, pointing to the unusually strong interactions in this system. Interestingly, it does not exhibit the anomalous Hall effect (AHE), suggesting that it may either carry a very small Berry curvature or instead be in an IVC ordered state.

Regions of parameter space in the t$2 + 3$ device shown in figure 3.9a colored in white correspond to situations in which we are unable to unambiguously determine the degeneracy of the Fermi surface. Especially around $\nu = 3$, this ambiguity likely arises due to multiple Fermi surface pockets coexisting within the moiré Brillouin zone. Figure A5 shows evidence for this in the form of curved trajectories of quantum Hall states seen in Landau fan diagrams. Such curved trajectories violate the Středa formula, which always predicts linear trajectories of topological gapped states, and generally arise due to the need to fill charge carriers simultaneously into two separate bands that each have their own sequence of Landau

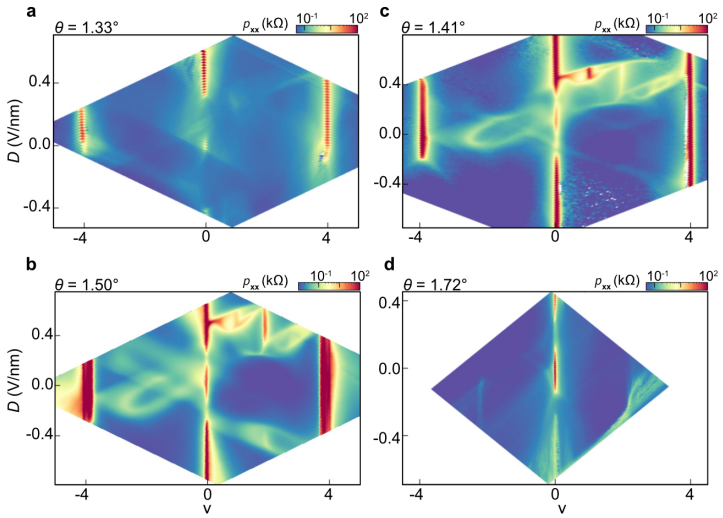

Figure 3.10: **Twist angle dependence of t2+3**, ρ_{xx} map as a function of ν and D for four 2+3 devices with different twist angles: **a**, $\theta = 1.33°$ **b**, $1.41°$ **c**, $1.56°$, and **d** $1.72°$. Data shown in **a**, **b** and **c** feature insulating states at $\nu = 0$ and $\nu = \pm 4$. Only devices shown in **b** and **c** exhibit correlated insulating states at positive D for partial filling of the moiré conduction band. In addition, **c** further shows a correlated insulating state at negative D. All data taken at $T = 1.5$ K.

levels.[94]

3.6.1 Correlated Insulating state at $D = 0$

We further see an unexpected insulating state at $\nu = 0$ near $D = 0$ across several t2 + 3 devices with different twist angles (figure 3.9d and figure 3.10). Our single–particle band structure calculations do not predict such a gap for any reasonable model parameters (see Methods), suggesting that it may arise spontaneously. This hypothesis is supported by measurements of the temperature dependence at $\nu = 0$ for the device with $\theta = 1.41°$ (figure 3.9e). The sample resistance at $|D| > 0.3$ steadily increases as the temperature is lowered (grey and black curves in the inset), consistent with a band insulator. Near $D = 0$, on the other hand, insulating behavior abruptly onsets below $T \leq 10$ K (purple curve in the inset). Thermal activation measurements of this state yield a maximum gap size of $\Delta_{\max}^{\nu=0} = 1.54 \pm 0.05$ meV (see figure 3.11). Although not definitive, the abrupt emergence of the gapped state with temperature at $D \approx 0$ and its relatively small size suggests that it may arise owing to interactions, similarly to the correlated insulators at charge neutrality in bilayer graphene[95–98] and rhombohedral few–layer graphene.[99–102]

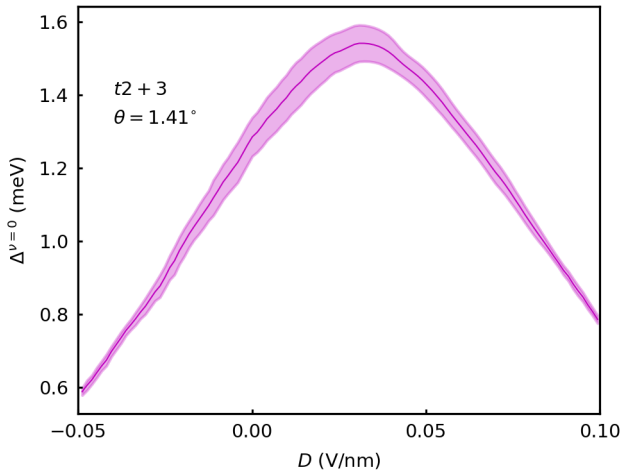

Figure 3.11: **Measured gap size of the $\nu = 0$ insulating state in the t2 + 3 device with $\theta = 1.41°$,** Gap size as a function of D at $\nu = 0$ (extracted from the data shown in figure 3.9e). The solid purple line denotes the best fit value from fitting Arrhenius plots, assuming $\rho_{xx} \propto \exp\left(\Delta^{\nu=0}/2k_BT\right)$. The shaded region denotes the standard deviation of the best fit value. The maximum value is found to be $\Delta^{\nu=0} = 1.54 \pm 0.05$ meV.

3.6.2 Comparison to theoretical description of t2+3

It remains an open question as to why t$2 + 3$ exhibits the most robust and prevalent symmetry–broken phases over a wide range of ν and D, as our band structure modeling does not predict that the bandwidth should be small compared to other t$M + N$ structures.

Specifically, we consider the effect of changing the Hamiltonian parameters to potentially explain the unexpected insulating state at $\nu = 0$ and $D \approx 0$ in t$2 + 3$ system. Within reasonable values of the tight binding parameters (γ_i), we find that there is always band overlap for twist angles between $1.33°$ and $\theta = 1.72°$. The only parameter that has a significant effect at $\nu = 0$ and $D = 0$ is the strength of the moiré coupling, t_M. In figure 3.12, we show band structure calculations varying t_M around the nominal value of 110 meV. Increasing t_M has the effect of flattening the bands further, but does not create a gap at charge neutrality. Reducing t_M can create a small gap at charge neutrality, but in this case the moiré bands are much more dispersive and overlap with the remote bands. Both scenarios are inconsistent with the observations in our experiment. Taken together with the temperature dependence measurements shown in figure 3.9e, we conclude that the insulating state at $\nu = 0$ and $D \approx 0$ is most likely to be a correlated state.

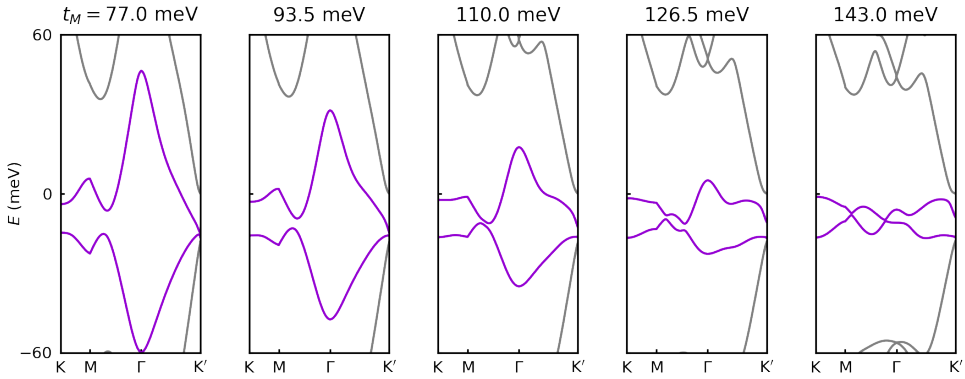

Figure 3.12: **Band structure calculations for the $\theta = 1.50^\circ$ t2 + 3 at $\delta = 0$.** Calculation results shown for varying values of the moiré coupling parameter t_M. The nominal value we used for all other calculations is $t_M = 110$ meV (center panel). Here both the moiré conduction and moiré valence band are shown in purple, to emphasize that the bands always overlap, inconsistent with our observation of an insulating state in figure 3.9d-e of the main text.

3.7 Topological states in tM+N graphene

Finally, we turn our attention to the topological properties of the t$M + N$ moiré bands. The AHE has been seen previously in both t$1 + 2$ and t$2 + 2$.[58,59,61,67] In the former, anomalous Hall resistances close to the quantized values $h/2e^2$ and h/e^2 have been observed, consistent with a SVP state formed from bands with a θ–dependent valley Chern number of either $C_v = 1$ or 2.[58,59] The AHE is typically not observed in t$2 + 2$ at $\nu = 1$ and 3, despite strong indications of a valley Chern number of 2, potentially indicating IVC order.[63–66] Nevertheless, in select cases it has been observed for $\nu > 3$, pointing to the emergence of a SVP state.[67]

In our t$1 + 3$ sample, the correlated state at $\nu = 1$ is too weakly developed to determine its isospin ordering (even with an applied magnetic field, as shown in figure A4). However, the state at $\nu = 3$ exhibits a clear AHE characterized by hysteresis in R_{xy} upon sweeping B back and forth, as shown in figure 3.13a at optimal doping and displacement field. Figure 3.13b shows the doping dependence of the AHE, characterized by the difference between forward and backward sweeps in a magnetic field, $\Delta R_{xy} = (R_{xy}^{\uparrow} - R_{xy}^{\downarrow})/2$. The AHE state is most pronounced close to $\nu = 3$ and is quickly suppressed upon doping. The corresponding Landau fan diagram shows that the gapped state drifts to smaller ν upon applying B (figure 3.13c), with a slope indicating a Chern number of $C = -2$ as determined by the Středa formula ($\frac{dn}{dB} = C\frac{e}{h}$). These observations are all consistent with an incipient quantum anomalous Hall effect (QAHE) owing to a SVP state at $\nu = 3$. Band structure modeling predicts a valley Chern number of $C_v = 2$, consistent with our observation. The QAHE is not well developed, likely due to a

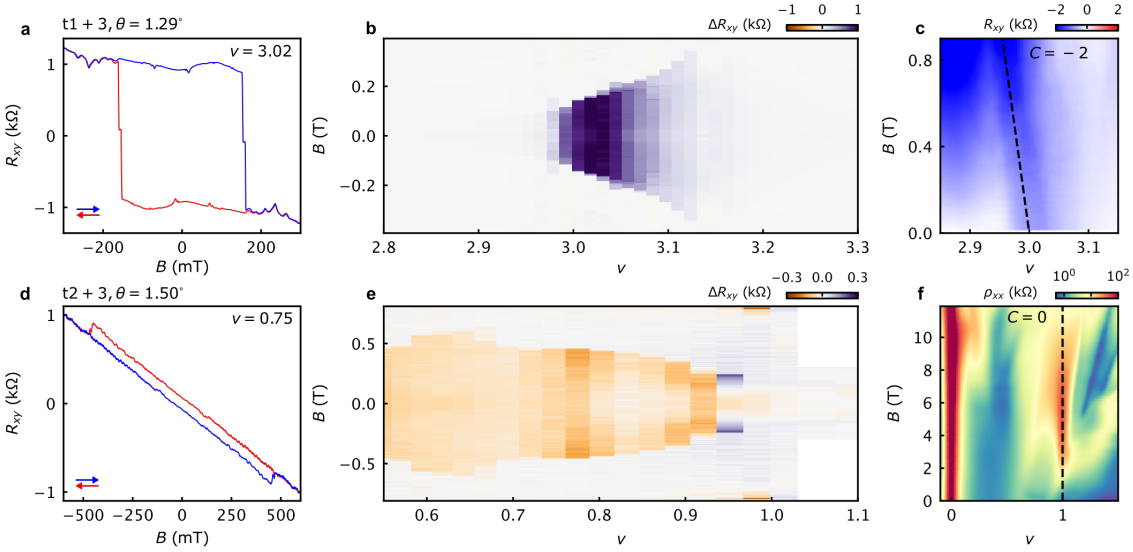

Figure 3.13: **Anomalous Hall effects in t1 + 3 and t2 + 3 devices. a**, R_{xy} measurement in the t1 + 3 device ($\theta = 1.29°$) acquired as B is swept back and forth at $\nu = 3.02$ and $D = 0.523$ V/nm. **b**, Doping dependence of the AHE effect at the same displacement field characterized by the difference in the forward and backward sweeps, $\Delta R_{xy} = (R_{xy}^{\uparrow} - R_{xy}^{\downarrow})/2$. **c**, Landau fan diagram of R_{xy} versus B around $\nu \approx 3$. The correlated Chern insulator emerging from $\nu = 3$ exhibits a slope consistent with $C = -2$. **d**, R_{xy} measurement in the t2 + 3 device ($\theta = 1.50°$) acquired at $\nu = 0.75$ and $D = 0.532$ V/nm. **e**, Doping dependence of the AHE in the same device. **f**, Landau fan diagram of ρ_{xx} versus B around $\nu \approx 1$. The correlated state at $\nu = 1$ projects vertically, consistent with $C = 0$. All data acquired at $T = 20$ mK.

combination of a small energy gap and substantial magnetic disorder in the sample.[103] These topological properties are reminiscent of those seen in t$1+2$ devices with similar twist angles.[59]

The topological properties of t$2+3$ are more unusual. We again find a valley Chern number of $C_v = 2$ in our band structure calculations and see clear signatures of an AHE, in this case below $\nu = 1$ (shown in figure 3.13d for $\nu = 0.75$). The magnitude of the AHE is small, but persists over a wide range of doping and vanishes very near $\nu = 1$ (figure 3.13e). However, the corresponding Landau fan diagram exhibits an insulating state emerging from $\nu = 1$ with zero slope up to high magnetic field (figure 3.13f), indicating that the $\nu = 1$ symmetry–broken state is topologically trivial. Although the $C = 0$ state may arise due to IVC ordering, the application of a modest B should favor a first–order phase transition to a SVP state. Notably, however, the absence of such a transition to a $C = 2$ Chern insulator state is inconsistent with this scenario. An alternative possibility is that, upon opening a gap at $\nu = 1$, interactions renormalize the Chern number of the filled band to $C = 0$. In this scenario, the AHE can arise due to Berry curvature hot spots in the reconstructed bands formed by spontaneous symmetry breaking, while the total Berry curvature of the symmetry–broken band integrates to zero. Further theoretical and experimental work is needed to better resolve the nature of this state.

3.8 Discussion and outlook

Taken collectively, our measurements establish a family of moiré graphene structures composed of Bernal–stacked graphene thin–film constituents with a small interfacial twist. By extending prior studies of twisted monolayer–bilayer and twisted double–bilayer graphene to thicker t$M+N$ variants, we discover a number of striking commonalities in both the single–particle and correlated states across this entire family.

The localization of low–energy states to the layers at and just below the moiré interface, which underlies this phenomenon, may also generalize to moiré systems built from other vdW materials. For instance, a promising future direction would be to extend studies of twisted homobilayer transition metal dichalcogenides to similar multilayer constructions. This could, for example, help to establish new control knobs over the recently discovered fractional quantum anomalous Hall states in twisted bilayer $MoTe_2$.[104–107] Accurately modeling these structures will require the development of new theoretical analyses beyond those considered here, including the effects of electrostatic screening of D and crystal fields at the twisted interface.[108] In parallel, further experimental studies into the largely unexplored physics of twisted monolayer–trilayer and bilayer–trilayer graphenes are very likely to reveal exciting new topological states. Our results thus establish a way to greatly expand the palette of topological flat bands available for study.

Chapter 4

MIXED-DIMENSIONAL MOIRÉ SYSTEMS OF TWISTED GRAPHITIC THIN FILMS

This chapter is adapted from previously published work: Dacen Waters*, Ellis Thompson*, Esmeralda Arreguin-Martinez, Manato Fujimoto, Yafei Ren, Kenji Watanabe, Takashi, Taniguchi, Ting Cao, Di Xiao, Matthew Yankowitz. Mixed-dimensional moiré systems of twisted graphitic thin films. *Nature* **620** 750-755 (2023). * denotes equal contribution and † denotes corresponding author

4.1 Introduction

So far, our study of twisted graphene structures has been limited to those assembled from thin multilayer building blocks (< 5 layers thick), so that the heterostructure can be modelled effectively as a 2D system. Thicker Bernal-stacked constituents contribute additional bands at low energy that complicate this approximation. Band structure modeling[109] and scanning tunneling microscopy studies of rotationally-faulted graphite[110] indicate that moiré bands are likely to persist to arbitrarily thick Bernal graphite structures, but remain localized at the twisted interface and coexist with conventional bulk graphite bands. However, it is currently not known whether and how these moiré surface states impact the electronic properties of the entire bulk graphitic thin film.

Here, we investigate the transport properties of graphitic structures with a moiré interface created by a single rotational fault within the crystal. We primarily focus on the case where the moiré potential is localized to one surface of the structure, achieved by rotating a flake of monolayer graphene by a small twist angle atop a Bernal graphite thin film. We also compare to the case where the moiré interface is buried at the center of the graphitic structure. We show that a single two-dimensional moiré interface can strongly modify the properties of the entire graphitic thin film, owing to a number of unique properties arising from its semimetallic nature.

4.2 Summary of devices

In this study, we focus primarily on twisted graphene-graphite (i.e., t1+Z, where 1 indicates monolayer graphene and Z corresponds to the number of graphene sheets in the bulk thin film). We measure devices with graphite thickness varying from $Z = 6$ to 40 layers, and with twist angles between $\theta = 0.84°$ and $1.31°$.

We fabricate t1+Z structures by finding an exfoliated bulk graphite thin film with a connected monolayer graphene region, isolating the two using an atomic force microscope tip, and then stacking one atop the other at the desired twist angle. We also fabricate one t7+7 sample by isolating two regions from a single 7-layer graphite sheet and stacking them atop each other. Our post-stack fabrication procedure is as described in chapter 2, with the exception of the t1+6 device, which has a an evaporated Cr/Au top gate instead of a graphite top gate. We determined the number of graphite layers in each device, Z, by atomic force microscopy measurements after encapsulation. Optical micrographs of all devices are shown in figure 4.1.

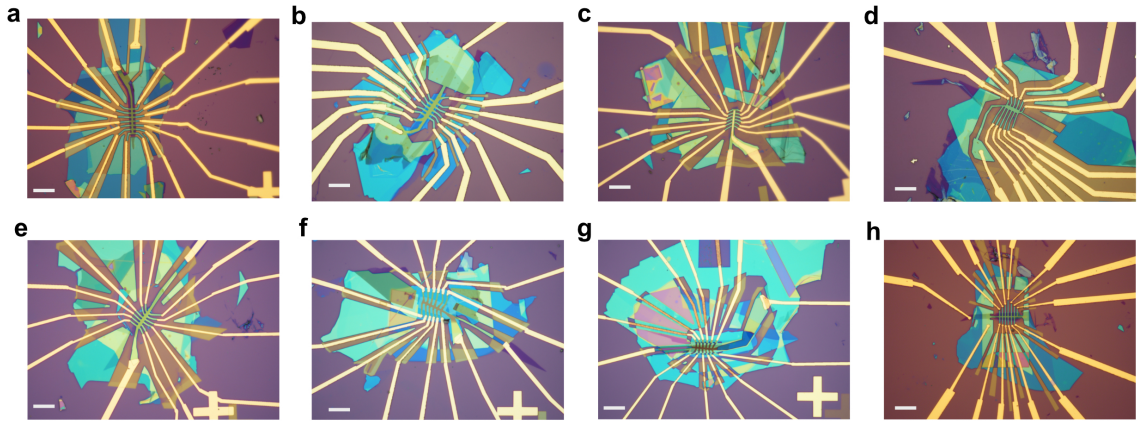

Figure 4.1: **Optical micrographs of the devices measured in this study. a**, 24-layer Bernal graphite device, **b**, 23 -layer Bernal graphite device, **c**, t1+6 device, **d**, t1+10 device, **e**, t1+17 device, **f**, t1+24 device, **g**, t1+40 device, **h**, t7+7 device. All scale bars are $10\ \mu\mathrm{m}$.

For most of the devices in this chapter, we determine the twist angle by analyzing their quantum Hall spectrum, as described in section 2.2.3. QOs projecting to full filling ($\nu = \pm 4$) are evident in all devices shown in Fig. 5.9 except for the t1+40 device. The twist angle for the t1+40 device was instead estimated through piezoelectric force microscopy (PFM) imaging of the moiré pattern (figure 4.2). We perform this imaging on the transfer slide during the sample fabrication directly after picking up the 40-layer graphite and the monolayer graphene.[111] We

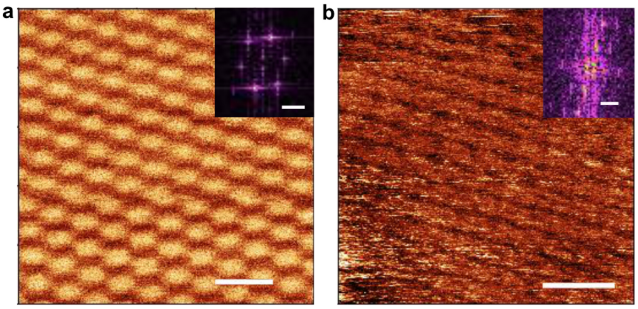

Figure 4.2: **Twist angle determination by PFM. a-b** Piezoelectric force microscopy (PFM) imaging of (a) t1+6 and (b) t1+40 structure. The t1+40 device appears to have a large amount of heterostrain, causing a distortion of the usual hexagonal shape of the moiré lattice points. Scale bars correspond to: (**a**) 20 nm (inset, 0.1 nm^{-1}), (**b**) 50 nm (inset, 0.1 nm^{-1}).

extract the twist angle by calculating the average of the three moiré lattice points in the Fourier transform of the PFM image. We also independently confimed the twist angle of the t1+6 device in this manner.

4.3 Transport in Bernal versus moiré graphite

We first compare the transport properties of Bernal graphite with a representative twisted graphene-graphite device. Figure 4.3 shows this for the case of a 23-layer Bernal graphite device and a t1+10 device with $\theta = 0.84°$.

A schematic of the Bernal graphite device is shown in figure 4.3a, with top and bottom gate voltages denoted as V_t and V_b, respectively. The color map in figure 4.3b shows the longitudinal resistance, R_{xx}, of the device at zero magnetic field as a function of the voltage on both gates (each gate voltage is normalized by the corresponding BN dielectric thickness). The resistance changes by only a few ohms with gating, consistent with the expectation that the gates are only able to dope the outer few layers of the nearest graphite surface due to screening in the bulk. Consequentially, the primary resistance features we observe evolve either vertically or horizontally in the map. This can also be seen by comparing the black traces in the panels above and to the right of the resistance map, which show R_{xx} as each gate is swept with the other held at ground. We further see corroborating behavior in the Hall resistance, R_{xy}, measured in a small magnetic field of $B = 0.2$ T. In particular, R_{xy} exhibits a sign change around zero bias in each gate sweep, signifying a corresponding sign change in the charge of the free carriers residing in the surface accumulation layer.

In contrast to our observations in Bernal graphite, transport in our t1+10 sample differs considerably depending on which gate is swept, as the mirror symmetry of the structure is broken by the rotated graphene sheet at the surface. Here, we denote the voltage on the gate facing the moiré (Bernal graphite) surface as V_m (V_{gr}) (see figure 4.3c). We see a much larger change in the resistance with gating in this device (figure 5.3d), with the highest resistance confined to a small region around $V_{gr} \approx 0$. Transport is reminiscent of Bernal graphite when sweeping V_{gr} (see R_{xx} and R_{xy} traces in the top panel), but exhibits fundamentally new behavior when sweeping V_m (right panel). In particular, repeated R_{xy} sign changes indicate multiple instances in which the free carriers on the twisted surface switch between electron- and hole-like. This behavior arises from the moiré reconstruction of the graphite band structure, marking the formation of a series of surface-localized moiré bands. These can be seen in calculations of the band structure of this material (figure 4.3e, see section 4.3.1 for calculation details). The bands are color-coded based upon their expectation value along the graphite c-axis, denoted as $\langle \mathrm{z} \rangle$, where a value of 1 (-1) corresponds to the moiré (Bernal graphite) surface. We find moiré bands localized on the outer graphene layers at the rotated interface (red colored bands), consistent with previous calculations

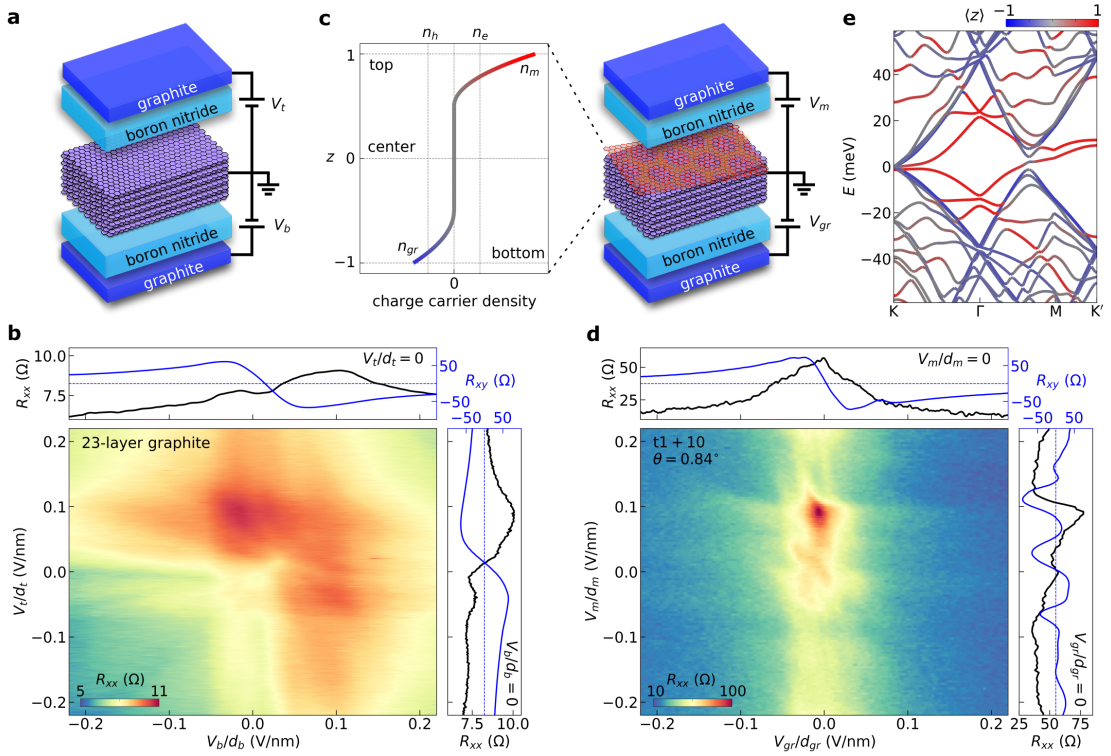

Figure 4.3: **Comparison of Bernal and moiré graphite at zero field**, **a**, Cartoon schematic of a Bernal graphite thin film device with top (V_t) and bottom (V_b) gates. **b**, Resistance of a 23-layer Bernal graphite thin film as a function of the top and bottom gate voltages. The top (bottom) gate voltage is normalized by the top (bottom) BN thickness, d_t (d_b). The panel above (to the right) of the color map shows cuts of R_{xx} and R_{xy} as V_b (V_t) is swept with $V_t = 0$ ($V_b = 0$). R_{xy} is acquired with $B = 0.2$ T. **c**, (Right) Cartoon schematic of a moiré graphite thin film device. The gate facing the moiré (Bernal graphite) surface is denoted V_m (V_{gr}). (Left) Schematic illustration of the free charge distribution in a dual-gated graphitic thin film as a function of the position along the c-axis of graphite (denoted as z). n_m and n_{gr} are the charge carrier densities on the moiré and Bernal graphite surfaces, respectively. These can be modified by tuning V_m and V_{gr}, shown here with arbitrarily chosen magnitudes and signs. n_e and n_h denote the density of electron and hole carriers in graphite, which are approximately equal such that the total doping is zero in the bulk. The doping in the bulk does not depend on gating. **d**, Resistance of a t1+10 graphite sample with $\theta = 0.84°$ as a function of V_m and V_{gr}, normalized by the appropriate BN thicknesses. The panels above and to the right of the color map show cuts of R_{xx} and R_{xy}, analogous to those in **b**. **e**, Calculation of the band structure of a t1+10 graphite sample with $\theta = 0.84°$. The cut is taken along a contour within the moiré Brillouin zone. The color of bands corresponds to their expectation value along the graphite c-axis, denoted as $\langle z \rangle$, where a value of 1 (-1) corresponds to the moiré (Bernal graphite) surface as shown in **c**.

performed for infinitely thick graphite slabs.[109]

The contrast between Bernal and moiré graphite becomes more obvious upon applying a small magnetic field oriented along the c-axis. Figure 4.4a shows a dual-gate resistance map for the 23-layer Bernal graphite sample acquired at a magnetic field of $B = 0.5$ T. The resistance is largest when the voltage on both gates is approximately zero, consistent with prior reports of a large magnetoresistance (MR) in bulk graphite crystals.[112] Upon gating, we additionally find a large MR everywhere along the condition of overall charge neutrality, $V_t/d_t + V_b/d_b = 0$, as evidenced by the diagonal resistance stripe in figure 4.4a. Measurements of the Hall resistance show a corresponding sign change across the line of overall neutrality. Our observations can be captured by a simple Drude transport model (see section 4.3.2 for details), indicating that transport is primarily determined by the total free charge density in the material, even when the gate-induced charge is mostly localized at the outer surfaces (see figure 4.3c).

Corresponding measurements of the moiré sample reveal a more complex dependence of transport on gating (figures 4.4b and 4.5). Rather than a single resistance stripe, R_{xx} exhibits a maximum that evolves with a peculiar zig-zag trajectory upon gating. The contour of $R_{xy} = 0$ tracks closely with the R_{xx} maximum. Notably, the periodic resets we observe upon biasing V_m correspond closely with integer multiples of the gate voltage required to completely fill the four-fold degenerate surface moiré minibands, denoted by the band filling factor, ν, on the right-hand axis (see Methods for definition of ν).

To understand this behavior, we compare to band structure calculations of twisted graphene-graphite with tunable gate-induced surface potentials (see section 4.3.1). Figures 4.4c-d show the evolution of the band structure for various values of the potential at the moiré surface, U_m. We find that gating primarily changes the energy of the moiré-like surface states, whereas the graphite-like states in the bulk remain at fixed energy. In contrast, the energy of the moiré-like bands remains fixed upon changing the potential at the Bernal graphite surface, U_{gr}, as shown in figure 4.4e. From this picture, we can generalize the transport properties of Bernal graphite to understand those of the moiré sample. The local behavior surrounding $V_{gr} \approx V_m \approx 0$ is similar for the two structures. However, whereas both surfaces of Bernal graphite can be doped with arbitrarily large densities of either electrons or holes, the twisted surface of the moiré sample hosts a series of narrow flat bands in which the free charge switches repeatedly between electron- and hole-like (figures 4.4c). When V_m corresponds to full filling of the moiré band ($\nu = \pm 4$), the surface free charge density returns to approximately zero, and the transport once again mimics the case of undoped Bernal graphite.

The zig-zag feature in the Hall resistance can be understood from the same picture. As seen in figure 4.4b, for fixed $V_{gr} \approx 0$, the sign of the Hall effect flips as V_m is tuned. This occurs as the doping at the moiré surface switches between electron- and hole-like, corresponding to instances in which

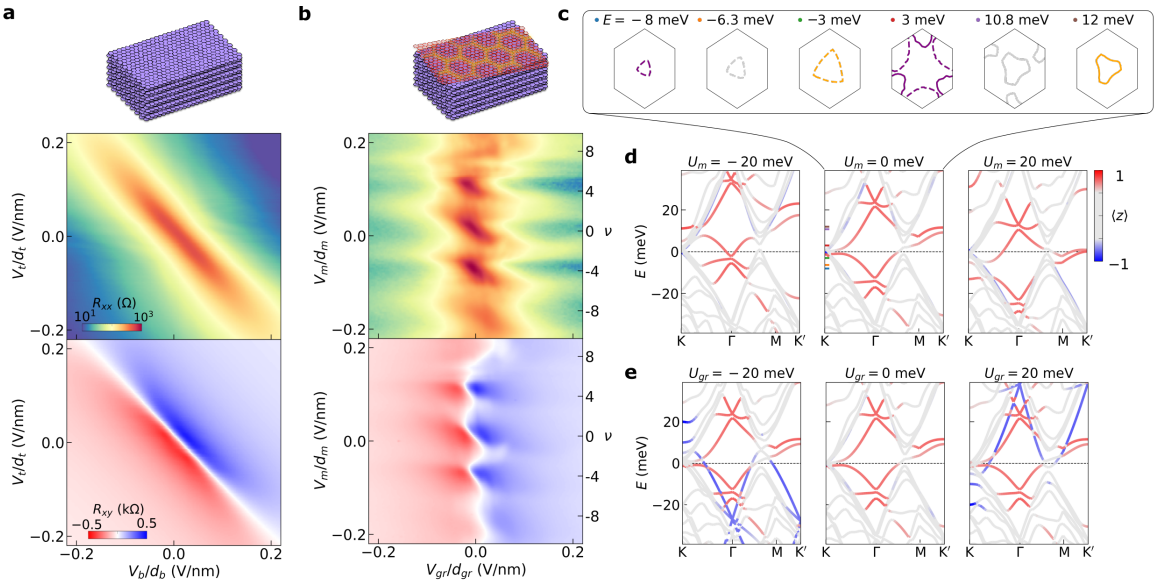

Figure 4.4: **Low-field magnetotransport and independent gating of surface-localized states**, **a**, Longitudinal (top) and Hall (bottom) resistance maps of the 23-layer Bernal graphite device acquired at $B = 0.5$ T. **b**, The same maps acquired in the t1+10 moiré graphite device. The vertical axis on the right indicates the filling factor, ν, of the moiré surface bands. The Hall resistance maps in **a**-**b** are antisymmetrized. Schematics of the Bernal graphite and t1+10 graphite are shown above each of the corresponding R_{xx} maps. **c**, Constant-energy contours of the surface-localized moiré bands at the denoted energies, calculated without any applied gate voltage (i.e., $U_m = U_{gr} = 0$). Dashed (solid) lines denote contours from the moiré valence (conduction) band. Energy labels for each panel have color-coded dots corresponding to the tick marks in **d**. Contours are color-coded by the sign of the local moiré band curvature, with orange denoting a hole-like Fermi surface, purple denoting an electron-like Fermi surface, and gray denoting a saddle point. The solid hexagon denotes the moiré Brillouin zone. **d**, Calculation of the band structure of a t1+10 graphite sample with $\theta = 0.84°$ as the surface potential at the moiré interface is changed from $U_m = -20$ meV (left) to 0 (center) to $+20$ meV (right). The potential at the Bernal graphite surface is $U_{gr} = 0$. The Fermi energy is held fixed at zero energy (black dashed line). The potential drop across graphite layers is modeled using a Thomas-Fermi screening approximation (see Methods).**e**, The same calculation but with $U_m = 0$ and a varying U_{gr}. In **d**-**e**, the bands are color-coded according to the expectation value of their z coordinate along the c-axis of the graphitic structure.

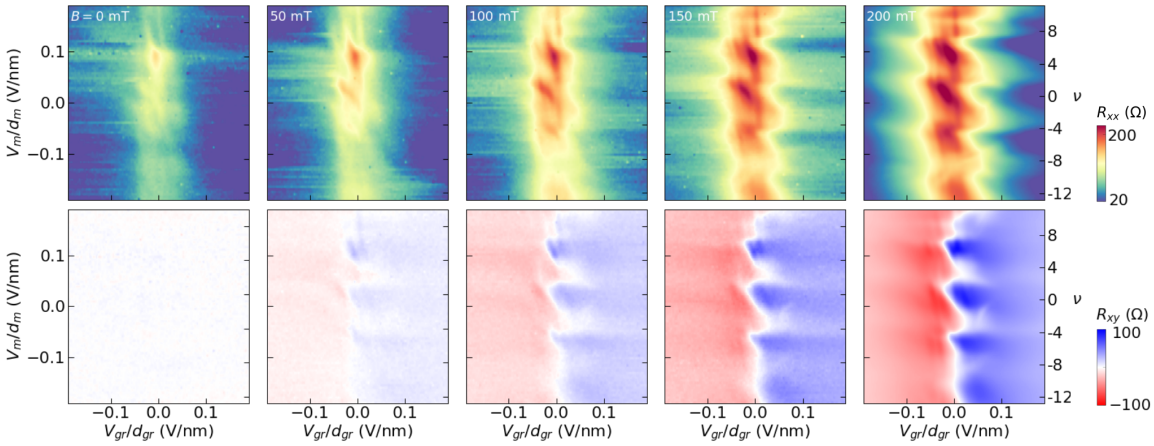

Figure 4.5: **Low-field evolution of transport in the t1+10 device.** Longitudinal (top) and Hall (bottom) resistance measurements acquired in steps of $B = 50$ mT, as indicated in the top left of each column. The zig-zag transport behavior first becomes evident at fields as low as 50 mT, and becomes more obvious as the field is raised.

Fermi energy crosses a moiré band extrema or a Lifshitz transition. The origin of these sign changes can be understood in more detail by examining calculations of the constant-energy contours of the surface-localized moiré bands (figure 4.4c). We color-code these contours according to the sign of the local band curvature, and see a repeated switching of the free carrier type between hole-like, neutral, and electron-like as the energy of the bands is varied. For sufficiently large values of V_{gr}, the doping of the Bernal graphite surface exceeds the maximum doping possible in the narrow moiré bands, and the sign of the Hall effect can no longer flip upon changing V_m. We can capture the salient features of this zig-zag effect following very simple assumptions about the amount of doping in each surface-localized band and applying these to a simple Drude transport model (demonstrated in section 4.3.2).

4.3.1 Band structure calculations

Our calculation is a generalization of the formalism for Bernal stacked graphite and twisted multilayer graphene explained in chapters 1 and 3. We first calculate the Hamiltonian for Z-layer Bernal graphite. We define $|k, A_l\rangle$ and $|k, B_l\rangle$ as the Bloch states at the K point of layer l. By arranging the basis as $|k, A_1\rangle, |k, B_1\rangle; |k, A_2\rangle, |k, B_2\rangle; ...; |k, A_Z\rangle, |k, B_Z\rangle;$, the Hamiltonian around the K point is given by

$$H_{\mathrm{ZG}}(k) = \begin{pmatrix} H_{\mathrm{D}}(k) - U_1 & \Gamma(k) & 0 & \\ \Gamma^{\dagger}(k) & H_{\mathrm{D}}(k) - U_2 & \Gamma^{\dagger}(k) & \\ 0 & \Gamma(k) & H_{\mathrm{D}}(k) - U_3 & \\ & & & \ddots \end{pmatrix},$$

with

$$H_{\mathrm{D}}(k) = \begin{pmatrix} 0 & \frac{\sqrt{3}}{2}\gamma_0(k_x - ik_y) \\ \frac{\sqrt{3}}{2}\gamma_0(k_x + ik_y) & 0 \end{pmatrix},$$

and

$$\Gamma(k) = \begin{pmatrix} -\frac{\sqrt{3}}{2}\gamma_4(k_x - ik_y) & -\frac{\sqrt{3}}{2}\gamma_3(k_x + ik_y) \\ \gamma_1 & -\frac{\sqrt{3}}{2}\gamma_4(k_x - ik_y) \end{pmatrix},$$

where U_j is the electronic potential at jth layer. We set the parameters $(\gamma_0, \gamma_1, \gamma_3, \gamma_4) = (2.6, 0.36, 0.28, 0.14)$ eV.[113]

To calculate the band structure of twisted graphene-graphite, we further place a single graphene layer on the Z-layer graphite and twist it by θ. The effective Hamiltonian can be written as

$$H = \begin{pmatrix} H_{\mathrm{MG}} & H_{\mathrm{int}}^{\dagger} \\ H_{\mathrm{int}} & H_{\mathrm{ZG}} \end{pmatrix},$$

where H_{MG} is the Hamiltonian for the twisted monolayer graphene. H_{int} is the interlayer coupling term between the monolayer and the topmost layer of the graphite. We define $|k', A_0\rangle$ and $|k', B_0\rangle$ as the Bloch states of the twisted graphene at $R(\theta)K$, where $R(\theta)$ is the rotation matrix in the xy-plane at an angle θ. By using this basis, the Hamiltonian for the graphene can be represented as

$$H_{\mathrm{MG}} = \begin{pmatrix} U_0 & \frac{\sqrt{3}}{2}\gamma_0(k'_x - ik'_y) \\ \frac{\sqrt{3}}{2}\gamma_0(k'_x + ik'_y) & U_0 \end{pmatrix}.$$

The Bloch wavevector of the twisted graphene and the Z-layer graphite are coupled when $k = k' + q_j$ $(j = 0, 1, 2)$, where $q_0 = (0, 0)$, $q_1 = \frac{1}{L_M}(-\frac{2\pi}{\sqrt{3}}, -2\pi)$ and $q_2 = \frac{1}{L_M}(\frac{2\pi}{\sqrt{3}}, -2\pi)$, where L_M is the moiré lattice constant. Under these constraints, the interlayer coupling is given by

$$H_{int} = \sum_{j=0}^{2} t_{int} \begin{pmatrix} \alpha & e^{-i\frac{2\pi j}{3}} \\ e^{i\frac{2\pi j}{3}} & \alpha \end{pmatrix},$$

and is otherwise zero. We take the parameters $t_{int} = 0.11$ eV and $\alpha = 0.5$,[45] the latter of which captures the effects of lattice relaxations.

We additionally consider the effective model for Z-layer graphite twisted atop Z-layer graphite, such that the moiré interface is buried at the center of the material. We will come back to this construction at a later point in this chapter. The Hamiltonian is constructed following same analysis as above, but replacing H_{MG} with $H_{\mathrm{ZG}}(k')$. The two rotated graphite constituents are coupled by H_{int} at their rotated interface.

We capture the effects of gating by adopting the Thomas-Fermi approximation to account for the screening of external electric fields by the graphite bulk.[27,114] For small gate voltages, the electric field is given by

$$U_j = U_m e^{-jd/\lambda_s} + U_{gr} e^{-(Z-j)d/\lambda_s} \quad (j = 0, ..., Z)$$

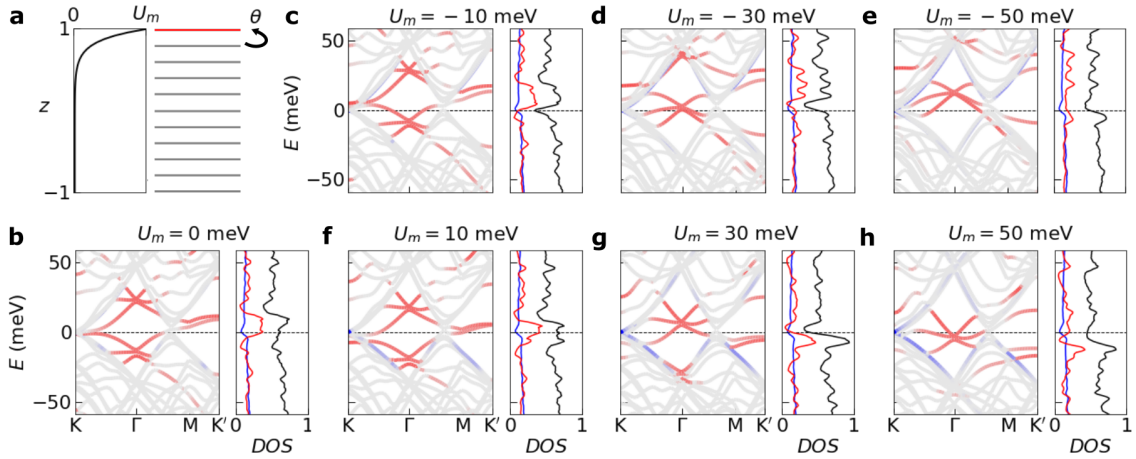

Figure 4.6: **Band structure calculations with varying U_m for the t1+10 device.** **a**, The assumed potential, U_m, as a function of z, given by a Thomas-Fermi screening approximation. The constituent graphene layers are indicated schematically to the right of the plot. The red layer denotes the monolayer graphene sheet twisted to $\theta = 0.84°$ with respect to the Bernal graphite layers beneath (grey lines). **b**-**h**, Calculated band structure (left) and density of states integrated over the moiré Brillouin zone (right) for selected values of U_m, as denoted above each panel. $U_{gr} = 0$ for all panels. The bands are color-coded following the same scheme as in figure 4.4d of the main text. The black curve shows the total density of states. The blue shows the density of states filtered by $\langle z \rangle < -0.6$, corresponding to the Bernal graphite surface states. The red line shows the same but for $\langle z \rangle > 0.6$, corresponding to moiré surface states. The normalization of the density of states is the same in all panels.

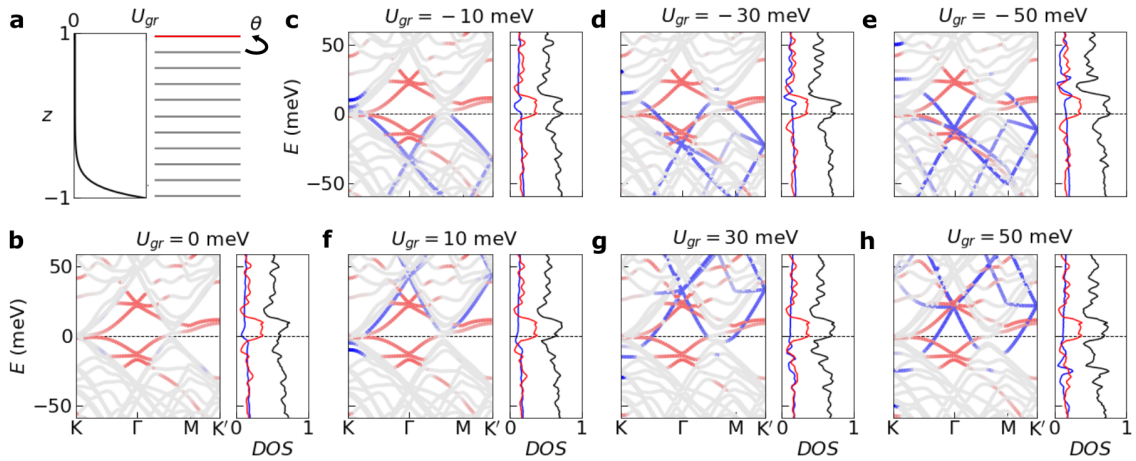

Figure 4.7: **Band structure calculations with varying U_{gr} for the t1+10 device.** Same as figure 4.6, but instead varying the potential on the graphite surface, U_{gr}, with $U_m = 0$.

where $\lambda_s \approx 1.3d$, and d is the interlayer distance. $U_{m/gr}$ is the potential for the moiré/graphite surface.

Finally, we numerically calculate the eigenvalues and eigenstates by truncating at a sufficiently large momentum and diagonalizing the Hamiltonian. The electron of the n-th eigenvalue is distributed along the graphite c-axis as follows:

$$\langle z_{nk} \rangle = \sum_l \sum_{\sigma=A,B} z_l |\phi_{nk,\sigma_l}|^2$$

where the eigenstate is written as $|\psi_{nk}\rangle = \sum_{\sigma,l} \phi_{nk,\sigma_l} |k, \sigma_l\rangle$ and $z_l = 2(z_0 - ld)/L_z$. L_z and z_0 denote the width and the center of the system, respectively. In figures 4.6 and 4.6, we show additional band structure calculations of t1+10 graphene with $\theta = 0.84^\circ$ for various values of U_m and U_{gr}, along with the associated density of states.

4.3.2 Drude transport model of Bernal graphite at low field

We capture the low-field transport behavior of Bernal graphite with a four-component Drude model. Magnetotransport is characterized by the conductivity tensor σ, with a corresponding current density $j = \sigma E$ under an electric field E. Each of the four carrier species are independent, and have a two-dimensional carrier density denoted as n_i, where i is t, b, e, or h. In order, these correspond to the charges on the top and bottom graphite surfaces, and the intrinsic electron and hole free carriers in the graphite bulk. Each carrier species has an associated mobility, μ_i. In the absence of a magnetic field, the conductivity is a scalar and the contribution from the i-th carrier is $\sigma_i = e n_i \mu_i$. In the presence of a magnetic field, the conductivity tensor is $\sigma = \sum_i \sigma_i$ where the contribution from the i-th carrier is

$$\sigma_i = \frac{\sigma_i}{1 + (\mu_i B)^2} \begin{pmatrix} 1 & \eta_i \mu_i B \\ -\eta_i \mu_i B & 1 \end{pmatrix},$$

with $\eta_i = \mp 1$ for electrons and holes, respectively. The resistivity tensor is $\rho = \sigma^{-1}$, where the diagonal and off-diagonal elements separately represent the longitudinal (ρ_{xx}) and transverse (ρ_{xy}) resistivities.

Graphite is a nearly compensated semimetal, and for simplicity we assume $n_e = n_h$. We take previously measured parameters of bulk graphite,[112,115] in which the three-dimensional bulk carrier density is $n_{3\mathrm{D}} = 3 \times 10^{18}\ \mathrm{cm}^{-3}$ and the mobility is $\mu_e = \mu_h = 1 \times 10^6\ \mathrm{cm}^2/\mathrm{Vs}$. We assume the same value for the surface mobilities, μ_t and μ_b. The bulk electron and hole carrier densities correspond to a two-dimensional density of $n_{2\mathrm{D}} = 2 \times 10^{12}\ \mathrm{cm}^{-2}$ per graphene sheet. To model our 23-layer Bernal graphite sample, we assign 21 layers of $n_{2\mathrm{D}}$ as the fixed bulk density, $n_e = n_h = 21 \times n_{2\mathrm{D}} = 4 \times 10^{13}\ \mathrm{cm}^{-2}$. We then vary the surface density of the two remaining layers, corresponding to changing the top and bottom gate voltages over typical experimentally accessible values.

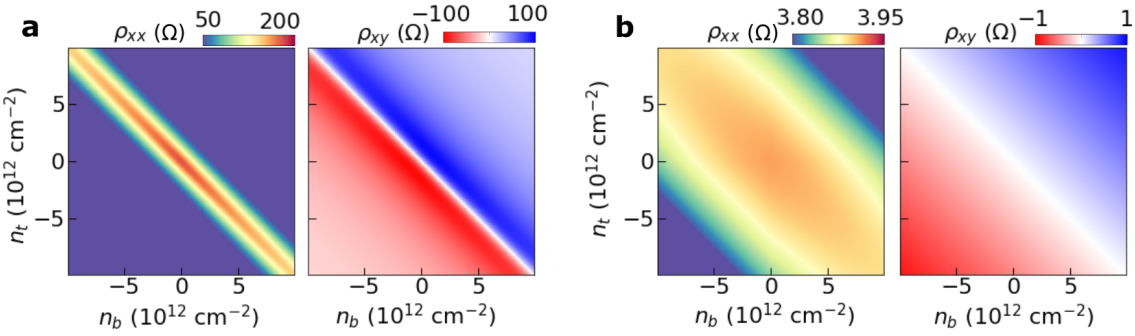

Figure 4.8: **Four-component Drude transport model of Bernal graphite at $B = 0.5$ T. a** Calculation of ρ_{xx} (left) and ρ_{xy} (right) for 23-layer graphite with $n_e = n_h = 21 \times n_{2\mathrm{D}} = 4 \times 10^{13}$ cm^{-2} and $\mu = 1 \times 10^6$ cm^2/Vs. Full details of the calculation are described in the Methods section. **b**, The same calculation with unrealistically large values of the intrinsic graphite doping, $n_e = n_h = 2 \times 10^{15}$ cm^{-2}. The change in resistivity with gating is orders of magnitude smaller than in **a**, indicating that the gate-tunability arises owing to the semimetallic nature of graphite.

Figure 4.8 shows the results of the calculation, which qualitatively match the experimental observations in figure 4.4a. In particular, we see the largest resistivity along the line of overall charge neutrality, with a corresponding change in the sign of the Hall effect. We also see that the resistivity is largest when both of the surfaces are undoped, also consistent with our experimental results. The qualitative agreement between experiment and theory does not depend strongly on the precise values of the graphite parameters we assume. However, as an additional check, we repeat the calculation with unrealistically large bulk density, $n_e = n_h = 2 \times 10^{15}$ cm^{-12} (figure 4.8b). In this case, we find that virtually no gate dependence can be observed in the longitudinal resistivity, which changes by only tenths of an ohm, compared to over a hundred ohms in the calculation performed with realistic graphite parameters. These calculations therefore establish that the gate-tunable transport we observe in graphite arises as a consequence of its modest intrinsic bulk doping.

We can modify this model to understand the origin of the zig-zag feature in the low field gate maps (in particular the $R_{xy} = 0$ contour of figure 4.4b). Our bandstructure calculations show that a potential applied to the moiré interface, U_m, primarily tunes moiré-like bands localized at the twisted interface (see figure 4.6) while a potential applied to the outer graphite surface, U_{gr}, primarily tunes the dispersive graphite-like bands (see figure 4.7). The graphite-like bands exhibit a single change between hole-like states and electron-like states when tuning U_{gr} through charge neutrality. In contrast, the moiré-like bands exhibit multiple changes in the carrier sign as the chemical potential is tuned, as illustrated by the constant energy contours shown in figure 4.4c of the main text. In principle, the net charge carrier density as a function of U_m and U_{gr} can be calculated from the relative sizes of moiré-like and graphite-like Fermi surfaces. However, such a calculation is technically challenging owing to mixing of the surface moiré bands with bulk graphite bands. Instead, we consider a simplified model in which we assume that the charge density of the graphite surface is a linear function of the graphite surface potential, $n_{gr} \propto U_{gr}$, whereas the charge density of the moiré surface is a sinusoid, $n_m \propto sin(U_m)$. The latter is an approximation to account for the repeated changes in the sign of the curvature of the moiré surface band. Figure 4.9 shows a plot of the sum of these two charge densities, $n_m + n_{gr}$, as each surface is tuned individually by changing U_m and U_{gr}. Without considering differences in surface mobilities, this quantity should be proportional to R_{xy}. We see that the charge neutrality feature ($n_m + n_{gr} = 0$) zig-zags back and forth upon changing U_m, qualitatively capturing the behavior observed in our Hall resistance measurements.

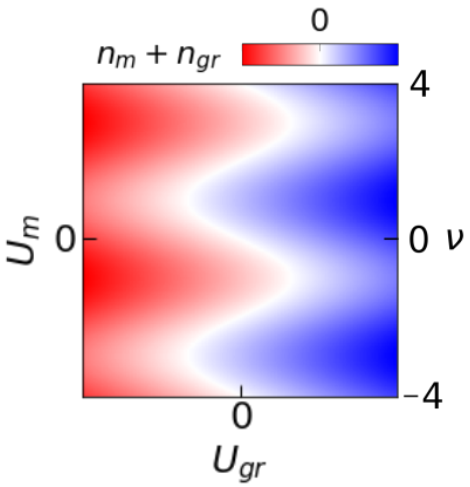

Figure 4.9: **Simple model capturing the $R_{xy} = 0$ zig-zag behavior.** Net charge density calculated in a simplified model where $n_{gr} \propto U_{gr}$ and $n_m \propto sin(U_m)$. Filling factor is denoted on the axis on the right, representing tuning U_m from negative full-filling to charge neutrality (on the moiré surface) to full-filling. This quantity should be approximately proportional to R_{xy}.

4.3.3 Temperature dependence of low field magnetotransport

We track the evolution of the low-field magnetotransport in the t1+17 device in figure 4.10. We see signatures of the zig-zag feature persisting up to at least 50 K. As the temperature is raised further, the structure in the R_{xx} map becomes washed out. R_{xy} continues to exhibit a sign change, but along a straight line with a slope that becomes more vertical in the map with higher temperature. At room

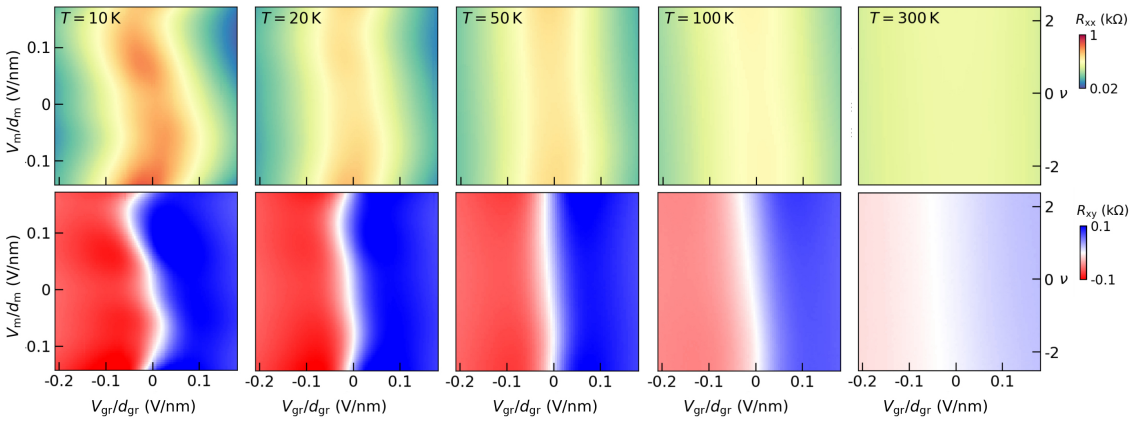

Figure 4.10: **Temperature dependence of the transport in the t1+17 device.** Maps of the longitudinal (top) and Hall (bottom) resistance at $B = 0.5$ T, acquired at various temperatures as indicated at the top left of each panel. The zig-zag behavior persists weakly up to approximately 50 K, above which R_{xx} becomes nearly featureless and R_{xy} becomes nearly independent of V_m.

temperature, transport is nearly unaffected by changing V_m, potentially due to lower mobility on the moiré surface compared to the Bernal graphite surface.

4.4 Hybridization of moiré and bulk states

So far, we have found that the charge accumulation layers on the two surfaces do not directly hybridize with each other, and are thus controlled independently by the nearest gate. However, this behavior is known to break down in Bernal graphite at higher magnetic fields.[116] In the ultra-quantum limit, only the two lowest (nearly-degenerate) Landau bands cross the Fermi energy, and the electron motion is primarily limited to the c-axis.[116,117] Electrons form a set of standing waves that penetrate across the entire bulk owing to the quasi-1D nature of these Landau bands. These states are thus controlled equally by the top and bottom gates. All other Landau bands are gapped within the bulk, and although they can be populated at the surfaces by gating, they form a screening layer and can only be controlled by the nearest gate. As a consequence, we find that Landau fans acquired by sweeping a single gate exhibit two distinct sets of quantum oscillations (QOs). One sequence projects to approximately zero gate voltage at $B = 0$, irrespective of the bias applied to the other gate. These QOs correspond to surface-localized states. The second sequence projects to a non-zero gate voltage determined by the bias applied to the opposite gate, in particular following a line of constant overall doping. These QOs correspond to states that are extended across the entire bulk (figure C.1).

The moiré surface states in t1+Z graphite form Hofstadter bands at high field,[47] which must smoothly

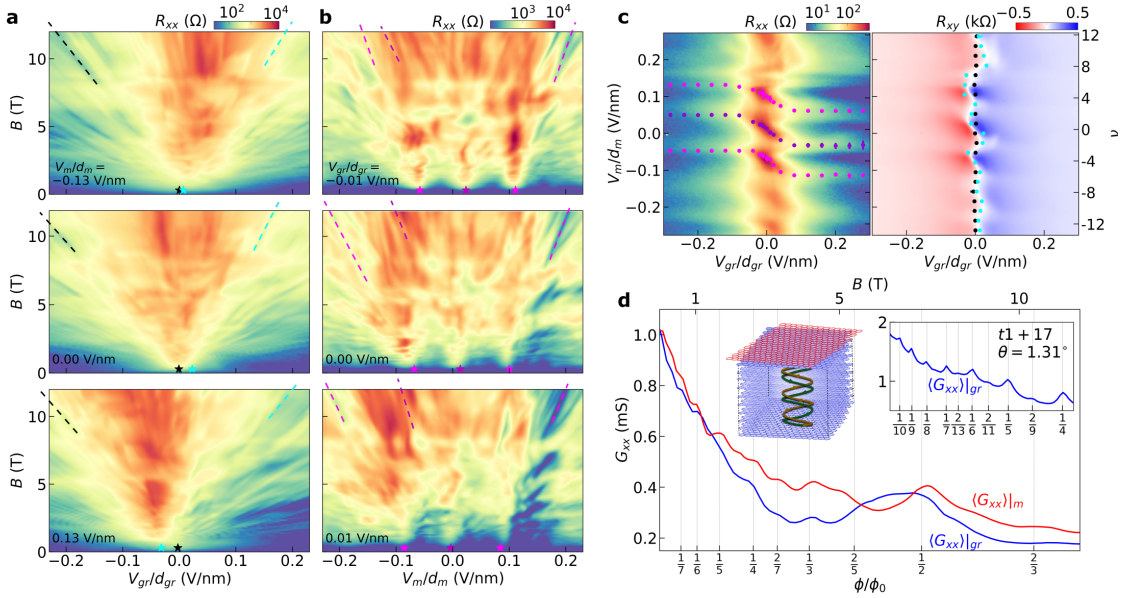

Figure 4.11: **Hybridization of moiré and bulk graphite states at high field**, **a**, Landau fan diagrams from the t1+10 device acquired by sweeping V_{gr} at the denoted values of V_m. The black dashed lines indicate selected QOs that project to $V_{gr} \approx 0$ at $B = 0$, whereas the blue dashed lines denote QOs that project to a value of V_{gr} that changes with V_m. **b**, Landau fan diagrams acquired by sweeping V_m at the denoted values of V_{gr}. The purple dashed lines indicate selected QOs that project to $\nu = 0$, whereas the pink dashed lines indicate QOs that project to $\nu = \pm 4$. **c**, Longitudinal (left) and Hall (right) resistance maps acquired at $B = 0.5$ T. Zero-field projections of the $\nu = 0$ and ± 4 states from the moiré gate Landau fans are overlaid on the longitudinal resistance map. Zero-field projections of QOs from the graphite gate Landau fans are overlaid on the Hall resistance map. Supplementary Videos 1-2 show the Landau fan diagrams used to extract all of the data points. **d**, Conductance, G_{xx}, as a function of magnetic field. The blue (red) line is averaged over all values of V_{gr} (V_m) for the Landau fan corresponding to the top panel in **a** (**b**), thereby eliminating contributions from individual QOs at a given field. Selected rational values of the magnetic flux filling of the moiré unit cell, ϕ/ϕ_0 are denoted by vertical gray lines. The top right inset shows G_{xx} averaged over all values of V_{gr} for a t1+17 device with $\theta = 1.31°$ (see figure 4.12 for the complete data set from this device). The top left inset shows a cartoon schematic illustrating the formation of a standing wave in the lowest Landau bands of graphite (formed by the stacked blue graphene sheets) at high field. The standing wave hybridizes the Bernal graphite bulk states with the moiré surface states. The moiré interface is indicated by the rotated graphene sheet colored in red.

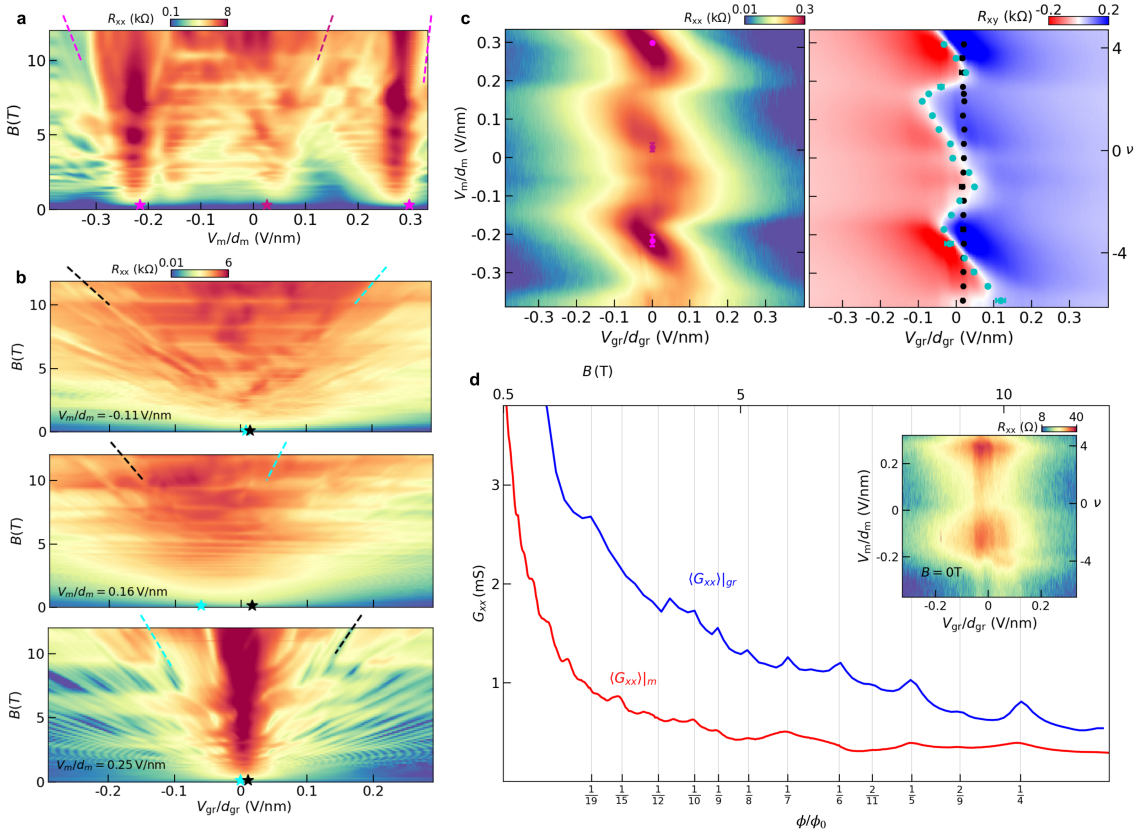

Figure 4.12: **High-field transport behavior in a t1+17 device with $\theta = 1.31°$. a**, Landau fan diagram acquired by sweeping V_m at $V_{gr} = 0$. The purple (pink) dashed lines denote selected QOs that project to $\nu = 0$ ($\nu = \pm 4$). **b**, Landau fan diagrams acquired by sweeping V_{gr} at various fixed values of V_m. The black dashed lines denote selected QOs that project to $V_{gr} \approx 0$ at $B = 0$. The blue lines denote selected QOs that project to a $V_{gr} \neq 0$ that depends on V_m. **c**, Longitudinal (left) and Hall (right) resistance maps acquired at $B = 0.5$ T. Zero-field projections of the $\nu = 0$ and ± 4 states from the V_m Landau fans are overlaid on the R_{xx} map. Zero-field projections of QOs from the V_{gr} Landau fans are overlaid on the R_{xy} map. **d**, Conductance, G_{xx}, as a function of magnetic field. The blue curve is averaged over all values of V_{gr} for the Landau fan in (**a**) acquired at $V_m/d_m = -0.11\,\mathrm{V/nm}$. The red curve is averaged over a range of V_m values corresponding to $|\nu| < 4$ for the Landau fan in (**b**) acquired at $V_{gr} = 0$. Brown-Zak oscillations case be seen upon sweeping either gate. (Inset) Longitudinal resistance map acquired at $B = 0$ T.

evolve into the Bernal graphite Landau bands in the bulk. Despite this additional complexity, our magnetotransport measurements reveal that ungapped bulk states remain extended across the entire sample. These extended states appear as diagonal features in dual-gate maps taken at fixed magnetic field, confirming their dependence on both gate voltages (figure C.2). We further probe these extended states by acquiring Landau fan diagrams while sweeping V_{gr} at various fixed values of V_m (figure 5.8a). Similar to our observations in Bernal graphite, we see two distinct sequences of QOs that project to different values of V_{gr} at $B = 0$. Selected QOs from the sequence corresponding to states localized at the Bernal graphite surface are denoted by black dashed lines, and project to $V_{gr} \approx 0$ irrespective of V_m. In contrast, the QOs corresponding to the bulk extended states (denoted by blue dashed lines) project to different values of V_{gr} depending sensitively on V_m.

Figure 5.8c shows the color-coded projections from many Landau fan diagrams overlaid atop the R_{xy} map acquired at $B = 0.5$ T (see figure 4.14 for details of the fitting procedure used to extract the projection points). The projection point of the extended states (blue dots) oscillates with V_m, tracking closely with the $R_{xy} = 0$ contour measured at low field. This behavior is enabled by the unique nature of the extended standing wave states in Bernal graphite. As illustrated schematically in the top left inset of figure 4.11d, the standing wave hybridizes the moiré surface states with the graphite bulk states, inextricably mixing them together. The low- and high-field zig-zag features we see in figure 4.11c arise from distinct physical mechanisms, yet exhibit remarkably consistent behavior that is primarily determined by the total gate-induced free charge in the sample.

Unlike in Bernal graphite, the Landau fan diagrams in twisted grahene-graphite differ substantially depending on which gate is swept. In particular, we see QOs corresponding to the moiré bands only upon sweeping V_m (figure 4.11b). We denote selected QOs projecting to full-filling of the moiré surface bands ($\nu = \pm 4$) with pink dashed lines, whereas QOs projecting to the charge neutrality point ($\nu = 0$) are denoted in purple. Figure 4.11c shows the $B = 0$ projection points of these states overlaid atop the R_{xx} map acquired at $B = 0.5$ T. The low-field transport around $V_{gr} \approx 0$ exhibits diagonal resistance features closely matching the evolution of the projection points of the high-field QOs at $\nu = 0$ and ± 4. We also find that both the resistance and the QO projections depend only weakly on V_{gr} as the bias is raised further. These observations suggest that the moiré bands can be doped by changing V_{gr} when the bias is small, but that surface states on the Bernal face screen the effect of changing V_{gr} when the bias is large.

Despite the obvious differences in the Landau fan diagrams acquired by sweeping each gate, Brown-Zak (BZ) oscillations[12, 47, 118–121] appear in both. The BZ oscillations correspond to conditions in which charge carriers experience zero effective magnetic field, and thus exhibit straight trajectories in real space.[121]

These oscillations occur as maxima in the magnetoconductance, $G_{xx} = R_{xx}/(R_{xx}^2 + R_{xy}^2)$, and arise at rational values of the magnetic flux filling of the moiré unit cell. BZ oscillations are anticipated when sweeping V_m (red curve in figure 4.11d), since charge carriers are directly populating the moiré bands. In contrast, the BZ oscillations seen upon sweeping V_{gr} (blue line in figure 4.11d) are more surprising, since this gate does not directly fill the moiré bands. This effect is more clearly visible in a t1+17 device with $\theta = 1.31°$, which exhibits very sharp magnetoconductance peaks averaged over V_{gr} (top right inset of figure 4.11d).

Although it is possible for the moiré to propagate through bulk graphite due to structural relaxations, this effect has been found to arise only at ultra-small twist angles,[122] and is therefore unlikely to be relevant in our samples. Instead, the observation of BZ oscillations upon sweeping V_{gr} indicates that carriers doped into the Bernal graphite surface obey transport properties dictated in part by the moiré potential on the opposite surface, providing further evidence of the hybridization of moiré and bulk states at high field. We additionally find that this effect persists in devices where the moiré interface is buried at the center of the sample (figure 4.13). In this case, the moiré bands lie deep in the bulk and cannot be filled by either gate, but nevertheless generate strong BZ oscillations by hybridizing with the bulk states of each rotated Bernal graphite constituent.

4.4.1 Fitting the quantum oscillation sequences

To determine the zero-field projection points of the QOs, we first take the second derivative of the R_{xx} signal numerically. QOs manifest as resistance dips in the R_{xx} measurements, and are therefore peaks in the second derivative. The raw data and second derivative for a representative Landau fan from the t1+10 device is shown in figure 4.14a-b. For clarity, we saturate the color scale to only show positive values of d^2R_{xx}/dV^2. We then identify QOs that persist over a magnetic field range of at least a tesla by determining linear trajectories in which d^2R_{xx}/dV^2 is a local maximum. We additionally cross check that the identified maxima in d^2R_{xx}/dV^2 correspond to obvious QO features in R_{xx}, since maxima in the second derivative can occasionally have other origins, such as two intersecting QOs or a QO crossing a BZ oscillation.

We then perform two different fitting procedures, which we refer to as "unconstrained" and "constrained" fits. For the unconstrained fit, we first perform a linear regression for each QO to extract its projection point at zero field, V_i^{u}. We can then group the QOs based on their projection points, forming groups that have projection points within a sufficiently small range of gate voltage. Figures 4.14c and e show an example of this analysis for the t1+10 device, in which V_{gr} was swept while fixing $V_m = 0$. We find two distinct sets of QOs, one that projects to approximately $V_{gr} = 0$ (associated with graphite

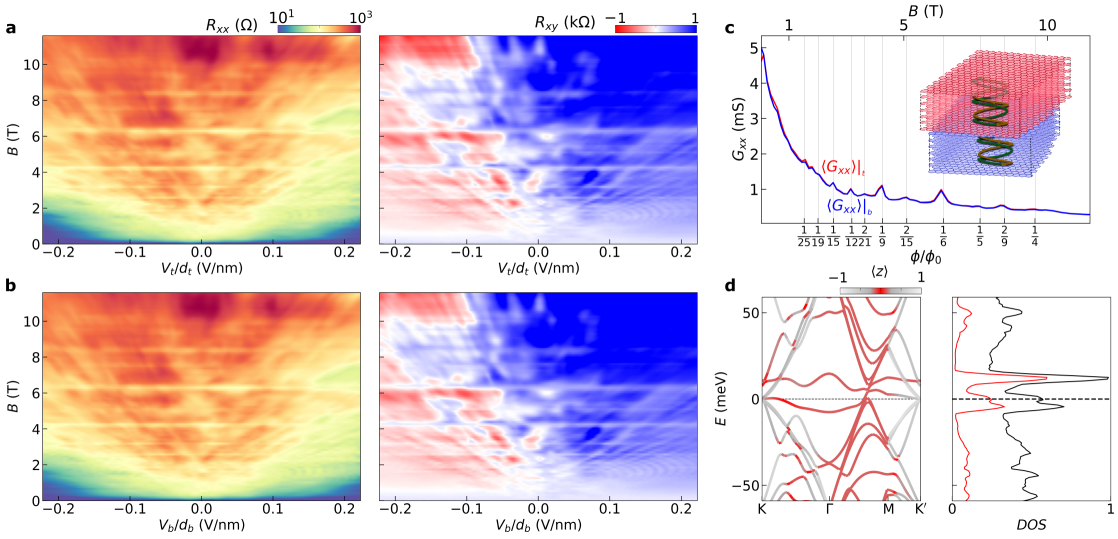

Figure 4.13: **High-field transport in a device with a buried moiré interface.** **a**, R_{xx} (left) and R_{xy} (right) Landau fans acquired as V_t is swept with $V_b = 0$ in a device consisting of 7 layers of Bernal graphite stacked and rotated atop another 7 graphite layers with $\theta = 1.26°$. **b**, Same as (**a**), but sweeping V_b with $V_t = 0$. The fans acquired by sweeping each gate are nearly identical to one another owing to the symmetry of the structure. Since the moiré is buried, we do not observe signatures of moiré band filling in either Landau fan. However, both fans show clear horizontal features corresponding to Brown-Zak oscillations arising from the buried moiré. **c**, Magnetoconductance averaged across all gate voltages for the top (red curve) and bottom (blue curve) gates. These are nearly identical, and both display a clear sequence of Brown-Zak oscillations. The inset shows a cartoon schematic in which separate standing waves couple the top and bottom bulk graphite states to the buried moiré interface. The hybridization of the buried moiré with the bulk states is required to generate the BZ oscillations seen in transport. **d**, (Left) Band structure calculation of this structure showing a moiré band localized at the center of the twisted graphitic thin film. The color scale is defined as in figure 4.4d of the main text. In this case, the moiré bands are found at $\langle z \rangle \approx 0$, since the moiré is located at the center of the structure. (Right) The density of states integrated over the moiré Brillouin zone. The red filtered curve corresponds to the four central graphene sheets, whereas the black corresponds to the total density of states.

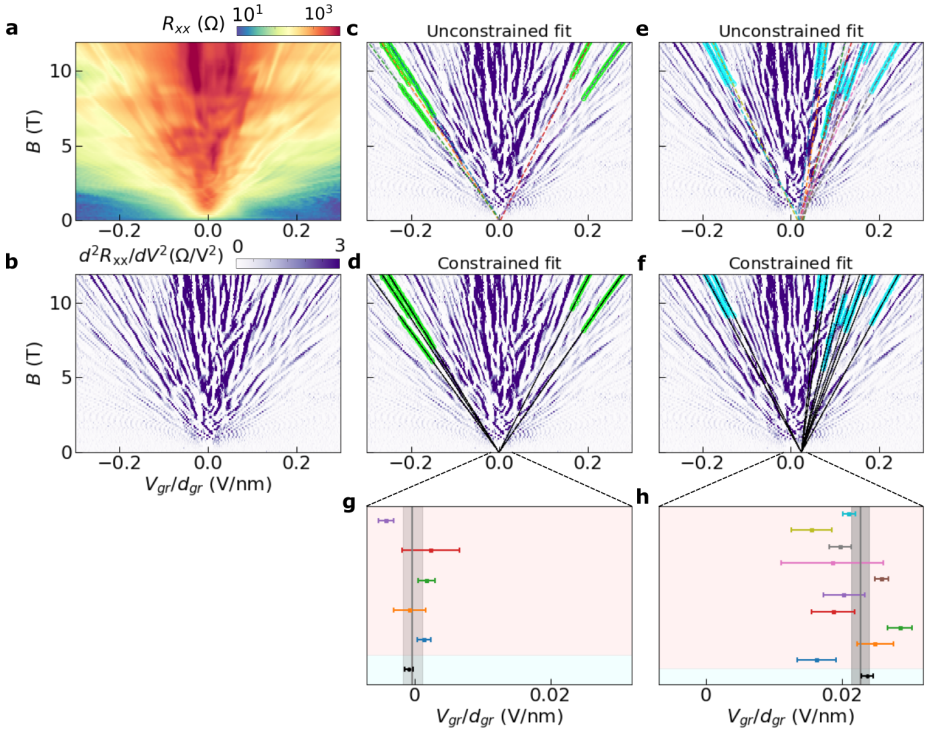

Figure 4.14: **Extracting the zero-field projection points of the QOs. a**, Landau fan diagram of R_{xx} in the t1+10 device, acquired by sweeping V_{gr} with $V_m = 0$. **b**, The numerical second derivative of the data in **a**. The color scale is saturated to only show positive values of d^2R_{xx}/dV^2, since peaks in d^2R_{xx}/dV^2 correspond to minima in R_{xx} (i.e., QOs). **c**, Fit results using the unconstrained fitting procedure for QOs that project to $V_{gr} \approx 0$. The green circles are extracted peaks in d^2R_{xx}/dV^2 that were used for each fit, and the dashed lines show the result of the fit for each individual QO. **d** Analogous results using the constrained fitting procedure for the QOs that project to $V_{gr} \approx 0$. The green data points are the same as in **c**, but now all the states are fit simultaneously and forced to share the same projection point at $B = 0$ with a defined relationship between their slopes (see Methods for full description). **e-f**, Similar fitting using the unconstrained and constrained fitting procedures, respectively, but for the sequence of QOs that project to $V_{gr} \neq 0$. **g**, Projection points determined from the fits shown in **c** and **d**. The shaded pink region contains data points and associated error bars from the unconstrained fit, $V_i^u \pm \sigma_i$, corresponding to the dashed lines in **c** of the same color. The vertical black line and surrounding shaded grey bar denote the weighted average and associated error of the unconstrained fit, $\overline{V_0^u} \pm \overline{\sigma^u}$. The shaded blue region contains the result of the constrained fit from **d**. The single black data point with error bars is the projection point determined by the constrained fit $V_0^c \pm \sigma^c$. Note that $\overline{V_0^u} \pm \overline{\sigma^u}$ and $V_0^c \pm \sigma^c$ are consistent with one another. **h**, Similar plot as **g**, but for the fits shown in **e** and **f**. Note that the extracted QO projection points in **g** and **h** differ significantly from one another, allowing us to unambiguously identify two distinct sets of QOs corresponding to the surface states and bulk states, respectively.

surface states) and another to $V_{gr} \neq 0$ (associated with the extended bulk states). The linear regression fit to each QO has an associated error on its projection point, σ_i. These are shown as the colored data points with error bars in figures 4.14g-h (collectively shown in the pink shaded region of the plot). After forming two groups of QOs based on their distinct projection points of $V_{gr} \approx 0$ and $V_{gr} \approx 0.02$ V/nm, we take a weighted average of all the QO projection points in each group in order to determine a single value for the projection point along with an associated error. The weights are $w_i = 1/\sigma_i^2$, such that the final projection point determined by the unconstrained fit is

$$\overline{V_0^u} = \frac{\sum_i w_i V_i^u}{\sum_i w_i}.$$

We assign the error to the unconstrained fit result as a weighted standard deviation:

$$\overline{\sigma^u} = \frac{1}{\sum_i w_i} \sqrt{\sum_i w_i^2 \left(V_i - \overline{V_0^u}\right)^2}.$$

The extracted $\overline{V_0^u}$ are denoted as vertical lines in figure 4.14g-h, with the surrounding shaded gray region indicating the fitting error. The unconstrained fits reveal two distinct sets of QOs with clearly distinguishable V_{gr} projection points. We stress that this fitting procedure is completely unbiased, as it simply picks out extended linear maxima in d^2R_{xx}/dV^2 and tracks their zero-field projection without making any underlying physical assumptions regarding the origin of those features.

We can strengthen this analysis by assuming that each distinct set of QOs must have the same projection point, as is conventional for quantum Hall states forming a Landau fan diagram. We thus proceed with a constrained fit, in which we additionally enforce a single projection point for each set of QOs, V_0^c. We further enforce that the QOs are related to one another through a Diophantine equation,

$$B = \frac{m}{t}\left(V - V_0^c\right),$$

where t is an integer (i.e. the Chern number) and $m = C\Phi_0/e$, with C the capacitance per unit area of the BN dielectric, e the charge of the electron, and $\Phi_0 = h/e$ the magnetic flux quantum. We use the results of the unconstrained fit to inform our assignment of the value of t for each fitted QO. We then perform a least squares regression to determined V_0^c and find the associated error, σ^c. In the Landau fans acquired by sweeping V_m, the difference between the fitted projection points associated with charge neutrality, $V^c_{0,\nu=0}$, and full-filling, $V^c_{0,\nu=\pm4}$, can be related to the moiré superlattice density, n_s, following $V^c_{0,\nu=\pm4} - V^c_{0,\nu=0} = \pm\frac{en_s}{C_m}$. Representative constrained fits are shown in figures. 4.14d and f.

The results of the constrained fit, V_0^c, are plotted as the black dots in figures 4.14g-h (shown within the blue shaded region of the plot). These black dots and associated error correspond very closely to the black lines and associated error from the unconstrained fits, indicating that the two procedures yield

highly consistent results. Given the physically realistic assumptions in the constrained fit, we adopt this procedure and further fit the projection points of the QO sequences from the remainder of the Landau fans acquired in this work. All data points shown in figure 4.11 report fits of V_0^c along with associated error bars, although the latter are typically smaller than the size of the corresponding data point marker. Figures B.1, B.2, and B.3 further show further results from the constrained fitting procedure for representative Landau fans acquired in the t1+10, t1+17, and t1+6 devices, respectively.

Finally, we note that in some cases we are able to identify additional sequences of QOs beyond those discussed in the main text (detailed in Appendix D). In particular, we find these in Landau fans acquired by sweeping V_{gr} in the t1+10 and t1+17 devices. We do not know the origin of these additional states, although we find that they are extremely sparse compared with those comprising the two primary sequences of QOs that we fit. These additional QO sequences could be related to Hofstadter states that penetrate deep into the bulk, or could arise from another unknown origin.

4.5 Thickness dependence of results

Our observations appear to be generic for t1+Z graphite, as we see qualitative similarities across different graphite thicknesses and twist angles. Figure 4.15 shows R_{xx} and R_{xy} maps acquired at $B = 0.5$ T for five samples with Bernal graphite components ranging from $Z = 6$ to 40 layers. The zig-zag resistance feature becomes increasingly obscured for thicker graphite, but we nevertheless see oscillations in R_{xy} that appear to correspond closely with four-fold multiples of ν. In the high-field regime, we see a similar evolution of the Landau fan diagram projections for both the t1+6 and t1+17 samples. The projection points from the Landau fans acquired by sweeping V_{gr} are plotted on the corresponding R_{xy} maps shown in figure 4.15a and c, and exhibit a familiar zig-zag progression. The full set of QO projections are shown in figures 4.12 and C.3.

4.5.1 Transition from 2D to bulk transport behavior

In presented in chapters 2 and 3, it is common to assume a parallel plate capacitor geometry in order to convert the combination of top and bottom gate voltages to doping and displacement field. This procedure assumes that the electric field drops uniformly across the 2D sheet. However, our devices are primarily constructed using bulk graphite, such that the conversion to the $n - D$ plane is not generally applicable. Here, we present additional data to document the transition from 2D-like transport behavior, where the $n - D$ conversion is justified, to our bulk 3D-like samples where the conversion is not justified.

Figure 4.16 shows longitudinal and transverse resistance maps of three different devices, with an increasing total number of graphene layers from 6 to 11. We apply the $n - D$ conversion to all data

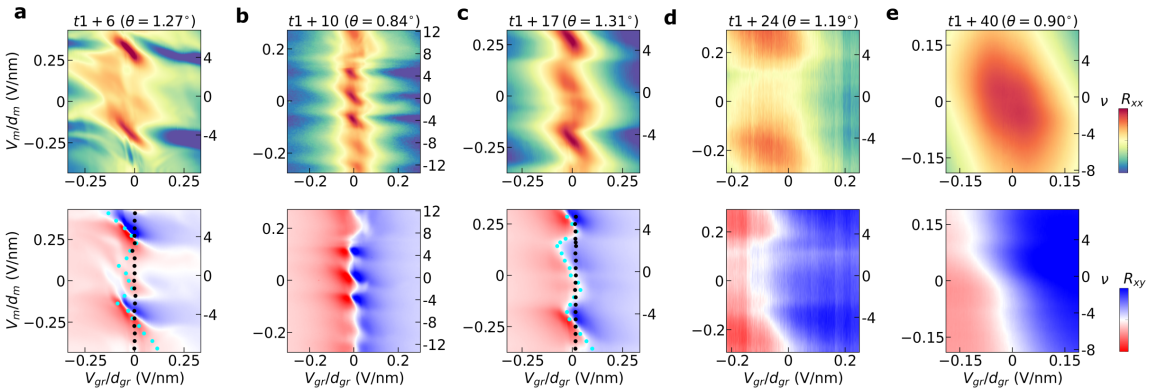

Figure 4.15: **Moiré modification of graphitic films with varying thickness and twist angle. a-e**, Maps of the longitudinal (top row) and Hall (bottom row) resistance for different moiré graphite devices, acquired at $B = 0.5$ T. All R_{xy} maps are antisymmetrized, except for that of the t1+40 device. The graphite thickness and twist angle is indicated above each plot. Zero-field projections of QOs from the Landau fans acquired by sweeping V_{gr} are overlaid on the Hall resistance map in **a** and **c**. The extrema of the color scales for each device vary due to the differing graphite thicknesses. The R_{xx} maps are plotted on logarithmic color scales, with extrema of: (**a**) $50\ \Omega$ to $1\ \mathrm{k}\Omega$, (**b**) $5\ \Omega$ to $500\ \Omega$ (**c**) $10\ \Omega$ to $500\ \Omega$, (**d**) $100\ \Omega$ to $175\ \Omega$, (**e**) $50\ \Omega$ to $150\ \Omega$. The R_{xy} maps are plotted on linear color scales, with extrema of: (**a**) $-0.5\ \mathrm{k}\Omega$ to $0.5\ \mathrm{k}\Omega$, (**b-c**) $-0.3\ \mathrm{k}\Omega$ to $0.3\ \mathrm{k}\Omega$, (**d-e**) $-50\ \Omega$ to $50\ \Omega$.

sets and plot R_{xx} and R_{xy} as a function of the filling factor $\nu = 4n/n_s$ and D. Figures 4.16a-b show measurements from a t2+4 device with $\theta = 1.17°$. We see resistive features associated with $\nu = 0$ and ± 4, consistent with previously studied moiré systems of twisted monolayer-bilayer (t1+2)[58–60] and twisted double bilayer (t2+2)[62–66] graphene. Notably, transport over the entire dual-gate map depends on the voltage of both gates. For example, insulating states in the device track vertically in the $\nu - D$ map, annotated with blue dashed ellipses as a guide to the eye. There are additional features that are not vertical in the $\nu - D$ map, but that also do not track a single gate alone. These features very likely arise from van Hove singularities that depend on D, as have also been seen previously in t1+2 and t2+2. Thus, we see that in t2+4 graphene, transport can be well understood by approximating the entire 6-layer graphene structure as a 2D film that only weakly screens an external electric field.

Figures 4.16c-d show similar maps for the t1+6 device. Applying the conversion to $\nu - D$ results in a somewhat complicated outcome. Some of the features track nearly vertically in the $\nu - D$ plane, including the resistive features associated with $\nu = \pm 4$ (annotated with the blue dashed ellipses). However, other features instead evolve with just a single gate voltage. These features are parallel to one of the diagonal boundaries of the map, and are annotated with the black dashed ellipses. The dependence of these features on a single gate implies that the other gate is being screened. We conclude that the t1+6 device lies at a crossover point between 2D-like and bulk-like behavior, where the $\nu - D$ conversion is only

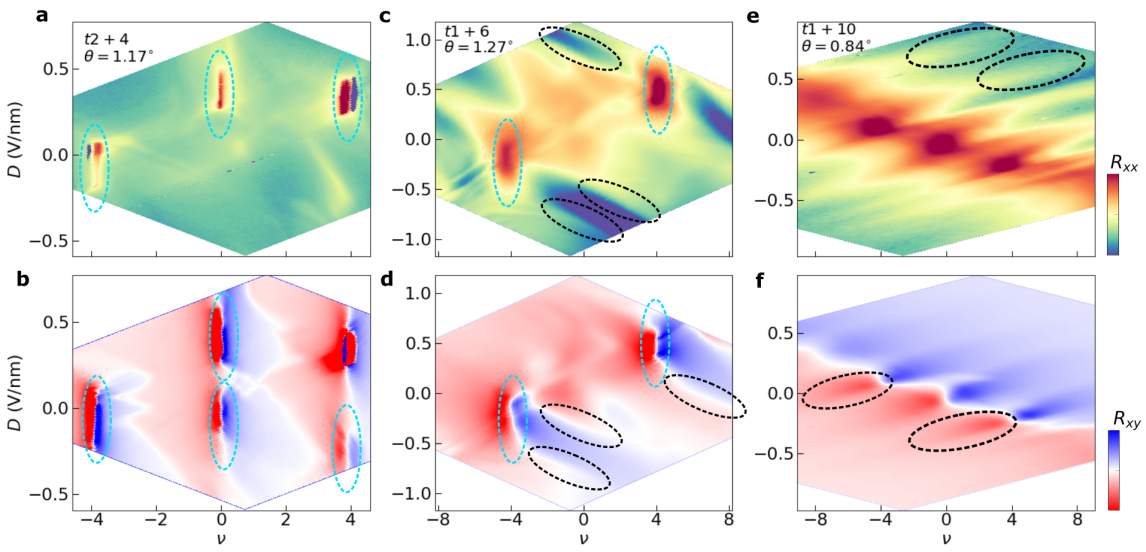

Figure 4.16: $\nu - D$ **maps as a function of number of graphene layers.** **a**, Longitudinal and **b**, Hall resistance measurements for a t2+4 device with $\theta = 1.17°$. Dashed blue ellipses are guides to the eye, showing features that track vertically in the $\nu - D$ plane. **c-d**, Similar maps for the t1+6 device. **e-f**, Similar maps for the t1+10 device. Black ellipses are guides to the eye, showing features that depend on only one gate voltage (i.e., parallel to a diagonal boundary of the map). The R_{xx} maps are plotted on logarithmic color scales, with extrema of: (**a**) $10\ \Omega$ to $50\ \mathrm{k}\Omega$, (**b**) $50\ \Omega$ to $1\ \mathrm{k}\Omega$ (**c**) $5\ \Omega$ to $500\ \Omega$, The R_{xy} maps are plotted on linear color scales, with extrema of: (**b**) $-2\ \mathrm{k}\Omega$ to $2\ \mathrm{k}\Omega$, (**d**) $-0.5\ \mathrm{k}\Omega$ to $0.5\ \mathrm{k}\Omega$, (**f**) $-0.5\ \mathrm{k}\Omega$ to $0.5\ \mathrm{k}\Omega$. .

appropriate within certain regions of the dual-gate map. This may explain why the QO projections we extract in the t1+6 device are much more complex than in thicker t1+Z samples.

Finally, we show the resistance maps of the t1+10 device converted to $\nu - D$ in figures 4.16e-f. In this case, we do not see any features that are vertical over an extended region of D (except for a very small region of $R_{xy} = 0$ around charge neutrality, although this is likely to be coincidental). Instead, all of the main features we see evolve with a single gate (a few selected examples are annotated by the black ellipses). The t1+10 is thus squarely in the bulk-like limit, where the low magnetic field gate response is dominated by changes in the surface states, as explained in the main text. Since the electric field cannot penetrate across the entire 11-layer sample, the conventional $n - D$ conversion is no longer appropriate.

4.6 Discussion

Overall, our results establish a new class of 'mixed-dimensional moiré materials,' in which a moiré potential localized to a single 2D interface fundamentally transforms the properties of an entire bulk crystal. This behavior may generalize to other layered semimetals with low intrinsic bulk doping, such as WTe_2 or $ZrTe_5$. Our work additionally motivates experiments with more complex graphitic structures, in which bulk standing waves couple moiré patterns at both the top and bottom surfaces or distributed throughout the bulk of the material. The standing-wave coupling may also be exploited to enable other means of interfacial engineering; for instance, by extending proximity-induced superconductivity, magnetism, or spin-orbit coupling into the graphite bulk. Finally, new complex moiré geometries in bulk graphitic thin films may help to unravel the origin of the superconductivity found both in natural few-layer graphene allotropes[88,123] and in a growing family of magic-angle twisted graphene structures.

Chapter 5

MICROSCOPIC SIGNATURES OF TOPOLOGY OF TWISTED MOLYBDENUM DITELLURIDE

This chapter is adapted from previously published work: Ellis Thompson*, Keng Tou Chu*, Florie Mesple*, Xiao-Wei Zhang*, Chaowei Hu, Yuzhou Zhao, Heonjoon Park, Jiaqi Cai, Eric Anderson, Kenji Watanabe, Takashi Taniguchi, Jihui Yang, Jiun-Haw Chu, Xiaodong Xu, Ting Cao†, Di Xiao†, Matthew Yankowitz†. Microscopic signatures of topology of twisted $MoTe_2$. *Nature Physics* **21** 1224-1230 (2025). * denotes equal contribution and † denotes corresponding author.

5.1 Introduction

Moiré bilayers of semiconducting transition metal dichalcogenides (TMDs) have rapidly emerged as rich platforms for studying novel strongly correlated phases of matter.[104–107,124–139] Strikingly, the topological properties of these correlated states are remarkably sensitive to the precise atomic structure and materials composition of the moiré lattice. At a doping of one hole per moiré unit cell, correlated insulators can have associated Chern numbers of either 0 or ± 1 depending on the specific TMDs (e.g., WSe_2 vs. $MoTe_2$) and the precise twist angle, θ, used to construct the moiré lattice.[104–107,124,132–135] Furthermore, the long-sought FQAH states have so far only been seen in t$MoTe_2$ over a relatively narrow range of twist angles between $2.6^\circ - 3.8^\circ$,[104–107,133,134] and have not been observed in analogous twisted WSe_2 structures. It is therefore critical to develop a more comprehensive understanding of the nature of the nontrivial topology in these materials.

The variability of these topological properties can be traced down to microscopic origins,[140] particularly the textures of electric polarization arising within the TMD homobilayer moiré unit cell. These generate a spatially-varying layer polarization of the flat-band wavefunction described by a layer-pseudospin skyrmion lattice. Charges hopping in this pseudospin skyrmion lattice acquire a geometric phase equivalent to the effect of a real-space magnetic field, giving rise to nontrivial band topology.[141,142] The locations of the north and south poles of the skyrmion lattice, where the flat-band wavefunctions become fully layer polarized, are determined by two competing mechanisms: out-of-plane ferroelectric dipole moments resulting from the broken inversion symmetry of the local stacking,[143–145] and strain-induced in-plane piezoelectric charges resulting from atomic relaxations in the moiré lattice.[44,79,111,146] Although these effects can be captured by calculations, their sensitivity to the precise modeling parameters has so far

precluded a complete understanding of the system, including fundamental properties such as the locations of the north and south poles of the skyrmion lattice. Notably, flipping the pole locations between different atomic stacking sites within the moiré unit cell results in a change in sign of the Chern number in cases where it is nonzero.[140] Atomic-scale imaging of the electronic structure of $tMoTe_2$ as a function of twist angle is therefore critical, as it can provide important experimental insights into microscopic fingerprints of band topology in the material and potentially lead to a more complete understanding of the array of correlation-driven topological states seen in transport experiments.[104–107, 133, 134]

Here, we map the spatial localization of valence band wavefunctions as a function of energy using scanning tunneling microscopy and spectroscopy. We fabricate high-quality van der Waals (vdW) devices consisting of $tMoTe_2$ atop monolayer graphene and hexagonal boron nitride (hBN), in which the graphene acts only as a local drain electrode for tunneling electrons.[127, 144, 147–149] We use several spectroscopy methods to distinguish valence band states originating from the K and Γ points of the monolayer $MoTe_2$ Brillouin zone. By studying the local density of states (LDOS) within the moiré unit cell as a function of energy, we find that the topological bands from the K points localize around only certain high-symmetry atomic stacking sites, whereas the trivial states from the Γ point localize at all positions within the moiré unit cell. Our observations of sub-moiré localization of the LDOS in the flat bands are generally consistent with the layer-pseudospin skyrmion textures predicted by our density functional theory (DFT) calculations, though the properties at very twist angles ($\theta \lesssim 2^\circ$) still require further understanding.

Additionally in section 3.7, we describe our progress towards measuring doped $tMoTe_2$ with STM. This task is severely complicated by fabrication difficulties stemming from the geometric restrictions require for an STM device. One strategy is to use a graphene sensor geometry, which would allow us effectively tune the charge density and displacement field in a $tMoTe_2$ layer, while monitoring nanoscale changes in a graphene sensor layer which is coupled via Coulomb interactions to the $tMoTe_2$. We construct these devices and demonstrate their functionality, but so far have not observed signatures doping-induced correlated and topological states in $tMoTe_2$ using this method.

5.1.1 Theoretical modeling of the layer-pseudospin texture

The layer-pseudospin texture in $tMoTe_2$ was first predicted using a continuum model of twisted group VI 2H TMDs (see section 1.3.2) based on the Bistritzer-Macdonald formalism described in section 1.4.1.[141, 142] The model employs the following Hamiltonian,

$$H_{\uparrow K}(\mathbf{k}) = \begin{pmatrix} -\frac{\hbar^2(\mathbf{k}-\boldsymbol{\kappa}_+)^2}{2m^\star} + \Delta_b(\mathbf{r}) & \Delta_T(\mathbf{r}) \\ \Delta_T^\dagger(\mathbf{r}) & -\frac{\hbar^2(\mathbf{k}-\boldsymbol{\kappa}_-)^2}{2m^\star} + \Delta_t(\mathbf{r}) \end{pmatrix} \tag{5.1}$$

which describes the spin up Hamiltonian, which, due to spin orbit-coupling, is locked to valley K. The Hamiltonian describing spin down locked to valley K' is related to this by time reversal symmetry. Similarly to the continuum Hamiltonian for TBG, the diagonal elements describe the spectrum at the K point of the top and bottom TMD monolayers and the off-diagonal elements describe the spatially varying interlayer tunneling strength modulated by the moiré superlattice. Here, $\boldsymbol{\kappa}_+$ ($\boldsymbol{\kappa}_-$) is the position in momentum space of the K point in the top (bottom) layer and $m^\star$ is the effective mass of carriers obtained from a parabolic approximation of the monolayer TMD bands at low energy. Δ_b (Δ_t) accounts for a spatially varying interlayer potential created by the intrinsic inversion symmetry breaking in the TMD moiré superlattice, which stems from the energy difference between chalcogen and metal atoms that sit on different atomic sublattices in each TMD monolayer. It can be parametrized in terms of Fourier components,

$$\Delta_l = 2V \sum_{j=1,3,5} \cos(\mathbf{G_j} \cdot \mathbf{d_0} + l\psi) \tag{5.2}$$

where $\mathbf{G}_j$ are obtained by rotating a monolayer reciprocal lattice vector by an angle $(j-1)\phi/3$, $\mathbf{d}_0 = \theta\hat{k} \times \mathbf{r}$, and V,ψ are set to $V = 8$meV and $\psi = -89.6°$ for tMoTe$_2$. This term is not present in the continuum model of twisted multilayer graphene since inversion symmetry is only broken by an applied displacement field. Δ_T is the spatially varying interlayer tunneling, which can be expressed in terms of Fourier components,

$$\Delta_T = w \sum_j e^{-i\mathbf{G}_j \cdot \mathbf{d}_0} \tag{5.3}$$

where w is the interlayer tunneling strength usually set at around -8.5 meV for tMoTe$_2$, and $\mathbf{G}_j$ are the reciprocal lattice vectors of the TMD monolayer. Any two dimensional hermitian Hamiltonian can be converted to the form $H = \boldsymbol{\Delta}(\mathbf{r}) \cdot \boldsymbol{\sigma}$ which describes some pseudospin interaction with an effective pseudospin magnetic field. Applying this to the Hamiltonian described above yields a spatially dependent pseudospin magnetic field of the form,

$$\boldsymbol{\Delta}(\mathbf{r}) = (\mathrm{Re}\Delta_T^\dagger, \mathrm{Im}\Delta_T^\dagger, \frac{\Delta_b - \Delta_t}{2}) \tag{5.4}$$

Since the continuum Hamiltonian is written the layer basis, this magnetic field acts on a layer pseudospin, which is essentially a mapping of the layer polarization of the wavefunction to the Bloch sphere.

Figure 5.1a plots the layer pseudospin magnetic field that arises from this continuum model. The black, green, and purple dots correspond to the three high symmetry stacking points of the TMD moiré superlattice which will be explained shortly in this chapter. It is clear from this plot that the layer pseudospin magnetic field winds around the MX and XM regions which have poles in south and north directions respectively. This is characteristic of a skyrmion texture in which a spin wraps the entirety of the Bloch sphere at least once. This can be parametrized more carefully by calculating the skyrmion winding

number of this pseudo magnetic field texture within one moiré unit cell, $N = \frac{1}{4\pi}\int \mathrm{d}\mathbf{r}\frac{\mathbf{\Delta}\cdot(\partial_x\mathbf{\Delta}\times\partial_y\mathbf{\Delta})}{|\mathbf{\Delta}|^3}$, which in this case is -1. The skyrmion winding number is considered a topological invariant, because it is robust to small changes in $\mathbf{\Delta}$ and can only be changed by rearranging the poles of the texture. This topologically nontrivial texture in the layer-pseudospin magnetic field provides an alternate way to understand the emergence of band topology in TMDs, analogous to the so-called topological Hall effect, in which skyrmion spin excitations in certain magnetic materials lead to an anomalous Hall current.

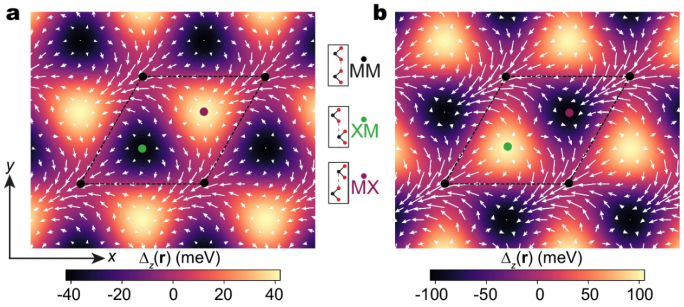

Figure 5.1: **Simulated layer pseudospin textures** Layer pseudospin textures produced by **a** the continuum model and **b** DFT calculations including lattice relaxations. Arrows represent the component of the layer pseusospin magnetic field in the x-y plane. Figure extracted directly from ref. by Zhang *et al.*[140]

Recently it was found that calculating the electronic structure of TMDs with a machine-learning-assisted density functional theory (DFT) approach yields a different layer pseudospin texture.[140] This method first calculates the most energetically stable relaxed atomic positions of all the atoms within one moiré unit cell and then calculates the electronic bandstructure and wavefunctions based on these positions. The result is shown figure 5.1b for the same value of θ used for the continuum calculation in a. Notably, the positions of the north and south poles of the skyrmion texture are flipped with respect to the texture obtained with the continuum model, which yields a skyrmion winding number of $N = 1$. Though not a one-to-one conversion, the skyrmion winding number of the layer pseudospin texture is intricately connected to the Chern number of the low energy moiré bands in twisted TMDs. The key difference is that this DFT method takes into account the full effects of lattice relaxations within the entire moiré superlattice, whereas the continuum model relies on a local stacking approximation that can differ significantly from the true atomic positions. We thus compare our STM data to DFT calculations throughout this chapter, and address the effects of lattice relaxations directly throughout. We also use the continuum model of $tMoTe_2$ as a tool to explain the fundamental origins and symmetry properties of the layer pseudospin texture.

Details of DFT calculations

We use neural network (NN) potentials to perform lattice relaxations of moiré superlattices. The NN potentials are parameterized using the deep potential molecular dynamics (DPMD) method.[150,151] To

generate training datasets, we perform 5000-step *ab initio* molecular dynamics (AIMD) simulations for $\theta = 6^\circ$ $tMoTe_2$ at $T = 500$ K using the VASP package,[152] with van der Waals corrections considered within the D2 formalism.[153] More details on parameterizing NN potentials can be found in Ref.[140] Subsequently, the trained NN potentials are employed to relax the moiré superlattice using the LAMMPS package[154] until the maximum atomic force is less than 10^{-4} eV/Å.

The moiré band structures and LDOS are calculated using the SIESTA package,[155] with the inclusion of spin-orbit coupling. We employ the optimized norm-conserving Vanderbilt (ONCV) pseudopotential,[156] the Perdew-Burke-Ernzerhof (PBE) functional,[157] and a double-zeta plus polarization basis. To sample the moiré Brillouin zone for LDOS calculations, a k-grid of $3 \times 3 \times 1$ is utilized, where k is the wavevector. The real-space distribution of the wavefunction is approximated by the weight of projected wavefunction onto the Mo and Te atomic orbitals. Gaussian smearing with a width of 33 meV is applied to smooth the LDOS curves for comparison to experimental data. For the calculated LDOS curves corresponding to specific stacking sites, we average LDOS values within a circle of radius 10 Å for MX, XM, and MM.

5.2 Summary of devices

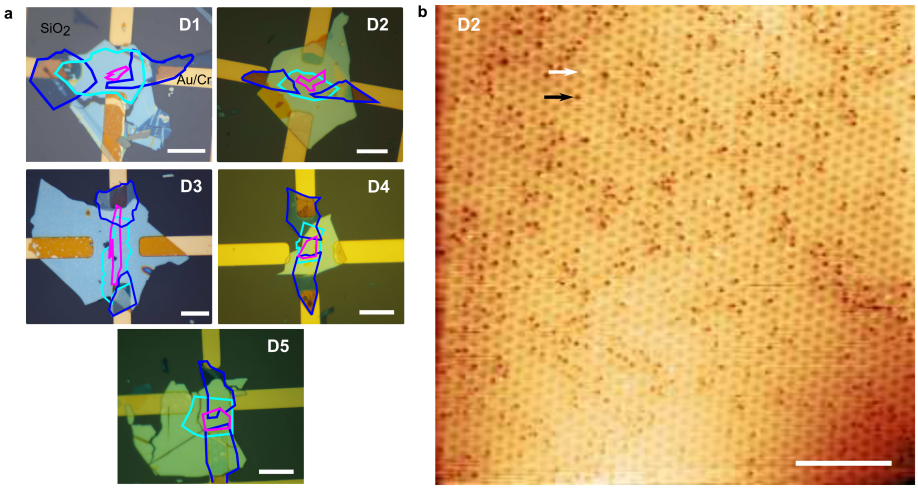

Figure 5.2: **Summary of open-faced $tMoTe_2$ devices. a**, Optical micrographs of the devices used in this study. Flake boundaries are outlined using the following convention: blue - graphite, cyan - monolayer graphene, pink - $tMoTe_2$. Scale bars are 20 μm. **b**, STM topograph of a large area of clean monolayer $MoTe_2$ showing two types of atomic defects,[158] bright and dark, emphasized by the white and black arrows. A graphene-hBN moiré pattern is also visible in this region. $(I_t, V_{bias}) = (100 \text{ pA}, -1.6 \text{ V})$, scale bar is 40 nm.

For this study, we fabricated and measured a total of five $tMoTe_2$ surface-exposed devices, summarized in figure 5.2. The $MoTe_2$ flakes for device D1 and D5 are from homegrown crystals grown using Te flux; those for device D2, D3, and D4 are from commercial crystals from HQ Graphene.

Because $MoTe_2$ degrades when exposed to air, all vdW device assembly steps involving $MoTe_2$ are performed in an argon environment in a glovebox (<0.1 ppm O_2 and H_2O). The completed device is transferred directly from the glovebox into the STM load lock chamber using a vacuum transfer suitcase. This process results in clean $MoTe_2$ surface that is almost entirely free of residue. Figure 5.2c shows a representative STM topograph of a 100 nm by 100 nm region of a $tMoTe_2$ sample, showing that atomic defects in the $MoTe_2$ are the primary form of disorder in our samples (rather than sample degradation).

We use a graphene substrate in our devices owing to challenges in otherwise forming Ohmic contact to $tMoTe_2$ at cryogenic temperatures. We find that monolayer graphene efficiently collects electrons tunneled into the $tMoTe_2$. Because of the large mismatch in the atomic lattice constants of graphene and $MoTe_2$, states at the K points of each material are separated by a large crystal momentum and do not strongly hybridize. We estimate the size of the Fermi pocket around the K point in $tMoTe_2$ from the calculated dispersion of untwisted bilayer $MoTe_2$. Similarly, we estimate the size of the Fermi pocket in graphene by assuming a linear dispersion, $E = \hbar v_F k$, with $v_F = 1.1 \times 10^6$ m/s.[25] We find that at energies up to 1 eV below the valence band edge of $tMoTe_2$, and with no interlayer twist, the Fermi pockets of $MoTe_2$ and graphene are separated by at least 2 nm^{-1} and thus do not hybridize. Twisting the two materials further separates the low-energy states. Therefore, we expect that the primary effects of the graphene substrate compared to a standard dielectric (such as hBN) are: (i) creating an isopotential surface for the bottom $MoTe_2$ layer, and (ii) weakly modifying the precise form of the $tMoTe_2$ lattice relaxations (see Supplementary Information section Effects of Twist Angle and Strain on the Localization of Γ-point States for additional discussion). Lastly, at a practical level, the graphene substrate also precludes gating experiments since it partially screens the electric field effect from the silicon back gate.

5.3 Twist angle dependent lattice relaxations

We first examine the moiré lattice structure of $tMoTe_2$ at various twist angles. When two $MoTe_2$ monolayers are twisted atop one another, three high-symmetry stacking sites can be identified based on the relative arrangement of the metal (molybdenum) and chalcogen (tellurium) atoms: MM, in which metal atoms sit atop each other; MX, in which a metal atom sits atop a chalcogen atom; and XM, in which a chalcogen atom sits atop a metal atom (figure 5.3b). Atomic relaxation effects, including in-plane strain and out-of-plane buckling, result in different heights of the top $MoTe_2$ layer at each of these three stacking sites. These effects are captured by our DFT simulations, as shown in figure 5.3c for $\theta = 2.88°$. The black curves in figure 5.3d show the calculated heights of both $MoTe_2$ layers, plotted along a cut across the moiré unit cell. The MX and XM stacking registries are related by C_{2x} symmetry (rotation by 180° around the axis connecting nearest-neighbor MM sites).

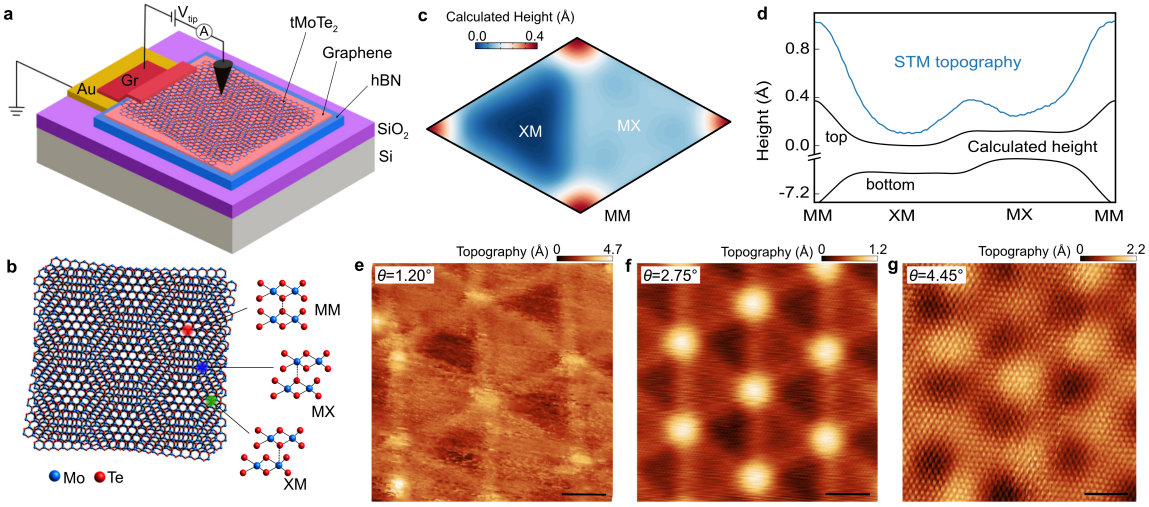

Figure 5.3: **Topographic characterization of tMoTe$_2$. a**, Schematic of the device. tMoTe$_2$ sits atop monolayer graphene and hBN. The entire stack sits on a Si/SiO$_2$ substrate. The monolayer graphene is connected to a Au electrode by a graphite flake, and is held at ground. **b**, Schematic illustration of a tMoTe$_2$ moiré superlattice. The interlayer stacking configuration is shown at the three high symmetry points: MM, MX, and XM. **c**, Height of the top layer of tMoTe$_2$ with $\theta = 2.88°$ predicted by an atomic relaxation DFT calculation (see Methods for details). **d**, Comparison between the calculated layer heights and height measured with STM topography. The black curves are line cuts of top and bottom layer heights from the calculation in **c**. The blue curve is a line cut from the topograph shown in **f**. **e-g**, STM topographs of tMoTe$_2$ regions with varying twist angle and heterostrain. The tunneling current, I_t, and sample bias, V_{bias}, setpoints along with the structural characterization parameters are: **e**, $(I_t, V_{bias}) = (100 \text{ pA}, -1.8 \text{ V})$, $\theta = 1.20$, $\varepsilon = 0.24\%$ oriented at 32 with respect to the moiré; **f**, $(I_t, V_{bias}) = (50 \text{ pA}, -1.5 \text{ V})$, $\theta = 2.75$, $\varepsilon_{uni} = 0.00\%$, $\varepsilon_{bi} = 0.11\%$; **g**, $(I_t, V_{bias}) = (140 \text{ pA}, -1.3 \text{ V})$, $\theta = 4.45$, $\varepsilon_{uni} = 0.71\%$ oriented at 17 with respect to the moiré, $\varepsilon_{bi} = 0.56\%$ (see Methods for extraction of strain values, ε, ε_{uni}, and ε_{bi}). Scale bars are **e**, 10 nm, **f**, 5 nm, and **g**, 2 nm.

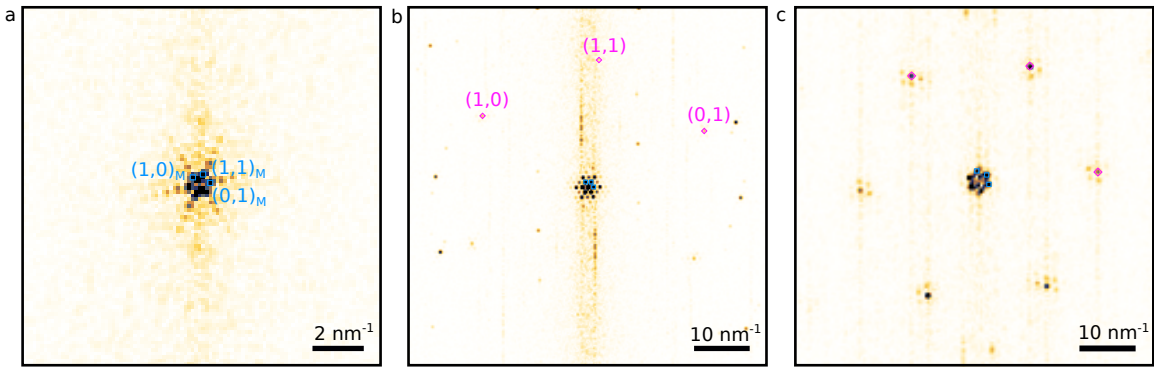

Figure 5.4: **Fast Fourier transform of STM topographs a-c**, FFT signal associated with STM topographs of regions with varying twist angle and heterostrain, coresponding respectively to topographs from figures 5.3e-f. The colorscale is set so that light is low FFT amplitude and dark is large FFT amplitude. The blue squares emphasize the moiré (M) Bragg peaks and the pink diamonds denote the MoTe$_2$ atomic Bragg peaks.

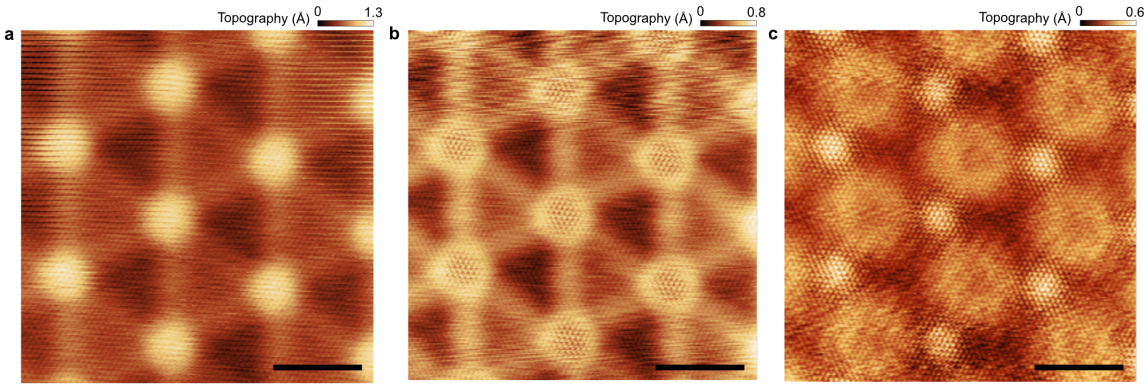

Figure 5.5: **Dependendence of STM topography on tunneling parameters.** STM topographs of the same $\theta = 2.75°$ region as shown in figure 5.3f, but with different tunneling setpoint parameters (I_t, V_{bias}): **a**, $(50$ pA$, -1.0$ V$)$, **b**, $(110$ pA$, -0.9$ V$)$, and **c**, $(300$ pA$, -0.8$ V$)$. Scale bars are 5 nm.

These predictions allow us to determine the corresponding high-symmetry stacking sites in our STM topographs. Figures 5.3e-g show topography images of $tMoTe_2$ with twist angles of $\theta = 1.20°$, $2.75°$, and $4.45°$, respectively. The blue curve in figure 5.3d shows the measured height of the $\theta = 2.75°$ sample along the same cut through the moiré lattice as for the black curves. The topographic measurement is performed using a large tip bias, typically over 0.4 V away from the bias of the valence band edge, such that the effects of the spatially varying LDOS are minimized (see figure 5.5 for topographs acquired with different tunneling parameters). We find that our measurement is qualitatively consistent with the calculation, allowing us to assign the highest topography point to the MM stacking site, the second highest to MX, and the lowest to XM.

These topographs further reveal the substantial effects of lattice relaxations in $tMoTe_2$. These effects play only a subtle role at $\theta = 4.45°$, for which the MM, MX, and XM regions account for roughly comparable areas within the moiré unit cell. However, relaxation effects are easily visible at $\theta = 2.75°$, with the area of the MM regions shrinking relative to the triangular MX and XM domains, along with the formation of solitonic domain walls connecting the MM sites. Relaxation effects are especially prominent at $\theta = 1.20°$, in which there are very large triangular MX and XM domains and comparatively small regions of MM stacking. The obvious effects of relaxations even at twist angles approaching $3°$ are a consequence of the relative softness of the $MoTe_2$ membrane (as compared to much stiffer materials such as graphene).[44] Notably, large lattice relaxations play a key role in determining the topology of the flat bands in theoretical modeling.[140] Understanding their microscopic properties is thus crucial for learning more about the nature of the observed FQAH states.

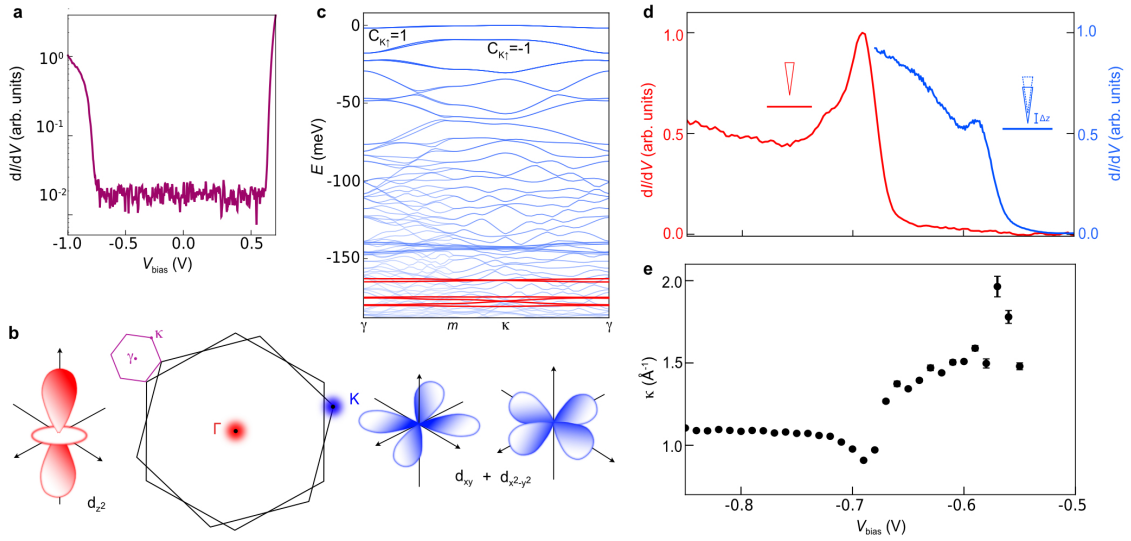

Figure 5.6: **Identification of spectroscopic features of tMoTe$_2$.** **a**, Representative constant-height dI/dV spectrum acquired over a wide range of bias on an MX site in a region with a $1.29°$ twist angle. The initial tunneling parameters are $(I_t, V_{bias}) = (50\text{ pA}, -1.0\text{ V})$. **b**, Schematic of the two rotated Brillouin zones of each monolayer MoTe$_2$ (black hexagons) and their resultant moiré Brillouin zone (magenta). Cartoons schematically illustrate the orbital composition of states arising from the Γ- and K-points of the monolayer Brillouin zones. **c**, Calculated band structure of tMoTe$_2$ with $\theta = 2.88°$ in the moiré Brillouin zone. Bands colored in blue (red) originate from the K (Γ) point of monolayer MoTe$_2$. **d**, Representative constant-height dI/dV spectrum in a region with a $2.75°$ twist angle with initial tunneling setpoint $(I_t, V_{bias}) = (110\text{ pA}, -0.9\text{ V})$ (red), and reduced-height dI/dV spectrum with initial tunneling setpoint $(I_t, V_{bias}) = (50\text{ pA}, -1.0\text{ V})$ (blue). In the latter, the tip was moved towards the sample by $\Delta z = 0.2$ nm before the bias sweep, as indicated by the cartoon schematics of the tip. Both curves were acquired at the MX stacking site. **e**, Measured decay constant, κ, as a function of bias voltage (see Methods for a description of the measurement). Error bars are defined as the standard deviation of the fit for κ (see Methods for details of fitting). The measurement is taken in the same location as the spectra in **d**.

5.4 Spectroscopic fingerprints of topological and topologically trivial moiré bands

We now turn our attention to the key spectroscopic features of tMoTe$_2$. Figure 5.6a shows a representative differential conductance (dI/dV) spectrum obtained over a large range of sample bias, V_{bias}. The broad region of very small differential conductance surrounding $V_{bias} = 0$ corresponds to the semiconducting band gap of tMoTe$_2$. Although careful measurements reveal the valence band edge to be at $V_{bias} \approx -0.55$ V, the onset of large differential conductance in figure 5.6a instead appears at $V_{bias} \approx -0.68$ V. This discrepancy stems from the high variation of the tunneling decay constant, κ, within the tMoTe$_2$ valence band, which effectively conceals the valence band edge in conventional constant-height dI/dV spectroscopy.

States at the valence band edge originate from the K point of the monolayer $MoTe_2$ Brillouin zone,[127,147,159] and therefore have a large decay constant in tunneling experiments owing to a large crystal momentum mismatch between the K point and the s-wave of an ideal STM tip. An additional contribution to their large decay constant comes from the phase mismatch between the s-wave of the tip and the d_{xy}+$d_{x^2-y^2}$ orbital character of the K-point states in $MoTe_2$,[160] as sketched in figure 5.6b. In a twisted $MoTe_2$ bilayer, the electronic bands of each monolayer hybridize and are folded into a smaller moiré Brillouin zone (as depicted by the purple hexagon in figure 5.6b). As a consequence, the highest energy moiré valence bands share a similarly large decay constant. Figure 5.6c shows a DFT calculation of the resulting band structure for t$MoTe_2$ with $\theta = 2.88°$, with bands colored in blue (red) arising from the K (Γ) point of the monolayer $MoTe_2$ Brillouin zone. The first few valence bands originating from the K point are relatively flat and isolated, and carry non-zero valley Chern numbers, $C_{K\uparrow} = -C_{K'\downarrow}$, where K↑ and K'↓ represent the locked valley and spin degrees of freedom. States originating from the Γ point are well separated from these K-point bands, first emerging at an energy of approximately 150 meV below the edge of the valence band.

In order to acquire dI/dV spectra of the moiré flat band states with adequate resolution, we perform a modified version of the conventional constant-height spectroscopy. We first stabilize the tip at a fixed height above the sample, then turn off the feedback loop and move the tip towards the sample by a fixed distance (typically between $0.2 - 1$ nm), and finally sweep V_{bias} while measuring dI/dV. We refer to this technique as "reduced-height spectroscopy" (see Methods for additional details). The blue curve in figure 5.6d shows a representative spectrum acquired in this way. The bump at $V_{bias} \approx -0.59$ V corresponds to the first few flat bands of t$MoTe_2$, all smeared into a single feature. The red curve in figure 5.6d shows a conventional constant-height dI/dV spectrum acquired from the same area of the sample. In this measurement, dI/dV is almost immeasurably small over the range of V_{bias} in which we see the K-band states with reduced-height spectroscopy. Instead, we see a large dI/dV peak at $V_{bias} \approx -0.69$ V that arises from bands which originate from the Γ point of the monolayer $MoTe_2$ Brillouin zone. These states have small crystal momentum and primarily out-of-plane d_{z^2} character,[159] and thus result in a large dI/dV signal compared with K-point states.

We verify the origin of these features by measuring κ as a function of bias (see figure 5.6e). We observe a dip in κ coincident with the large dI/dV peak seen in the red curve in figure 5.6d. This dip is consistent with the prediction that these states primarily arise from bands originating from the Γ point. Additionally, the increased decay constant for $V_{bias} \gtrsim -0.68$ V confirms the K-point origin of the valence band edge. The offset between K- and Γ-point states is consistent with the calculation, in which bands from Γ are first found at an energy of approximately 150 meV below the top of the moiré valence band.

5.4.1 Details of constant-height and reduced-height spectroscopy

The dI/dV spectra are acquired using a phase-sensitive detection with a $V_{mod} = 5$ mV peak-to-peak AC voltage modulation at a frequency of either 317 Hz or 419 Hz. The first harmonic of the demodulated signal is proportional to dI/dV and thus to the local density of states. The energy resolution for spectroscopy is $\Delta E = \sqrt{(3.5k_BT)^2 + (eV_{mod})^2} \approx 5$ meV where the first term corresponds to the thermal broadening and the second accounts for the instrumental broadening from the lock-in modulation. We note that the total experimental broadening is very likely underestimated by this simple analysis. Further energy smearing is expected due to the reduced lifetime of tunneling quasiparticles away from the Fermi level as a result of an increase in the number of decay channels. Detailed theoretical work is needed to estimate the quasiparticle lifetime and thus the resultant smearing.[161]

To perform constant-height spectroscopy, the tip is first stabilized at a given current and bias setpoint, (I_t, V_{bias}). Then the feedback loop is turned off and V_{bias} is swept across the range of interest while measuring dI/dV. Such measurements can also be acquired over a spatially resolved grid of points, generating a series of LDOS maps with high energy resolution, high tip stability, and minimal tip-induced doping (since the tip is kept relatively far the sample at all times). We use this technique mainly to study bands originating from the Γ point.

When performing reduced-height spectroscopy, the spectra are acquired in the same way, however the tip is moved closer to the sample by a fixed distance, Δz, before V_{bias} is swept. This allows for stabilization far away from the sample, avoiding artifacts stemming from position-dependent height variations and tip-sample interactions that arise when the tip is stabilized closer to the sample (appendix **?**). The pre-measurement height reduction serves to enhance the dI/dV signal from states with larger κ originating from the K points. Because small fluctuations in the stabilization condition can be exponentially amplified at a decreased tip-sample separation, we normalize individual spectra by the initial current, I_0, to make comparisons across spectra more consistent (appendix **?**).

5.4.2 Details of decay constant measurements

Decay constant measurements are performed by fitting measurements of $I(z)$ at different V_{bias}. For each bias voltage, the tip is first stabilized at a current setpoint of 10 pA and then gradually retracted by a distance of 1 nm while the tunneling current is measured. $I(z)$ curves are fit to the function, $I(z) = Ae^{-2\kappa z}$, using a non-linear least squares analysis where z is the tip-sample separation, κ is the decay constant, and A is left as a free parameter. See figure 5.7 for representative examples.

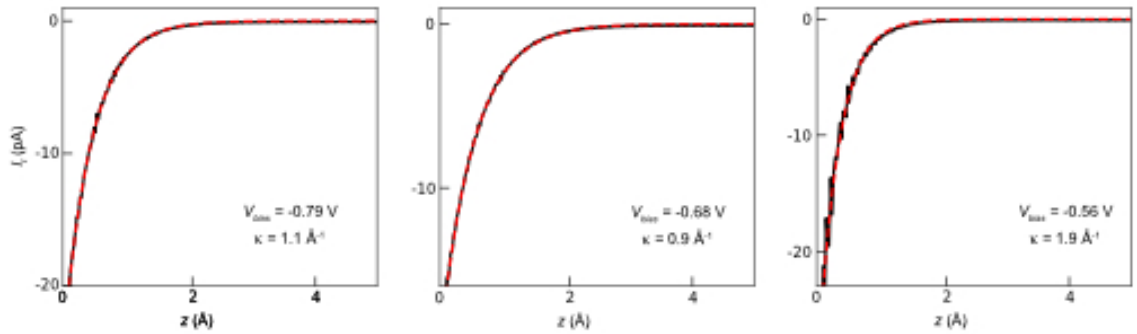

Figure 5.7: **Representative *I*(z) curves used to determine decay constant, κ** Solid black curves correspond to *I*(z) data taken at the specified bias. Dashed red curves show the best exponential fit for κusing the equation specified in the Methods section.

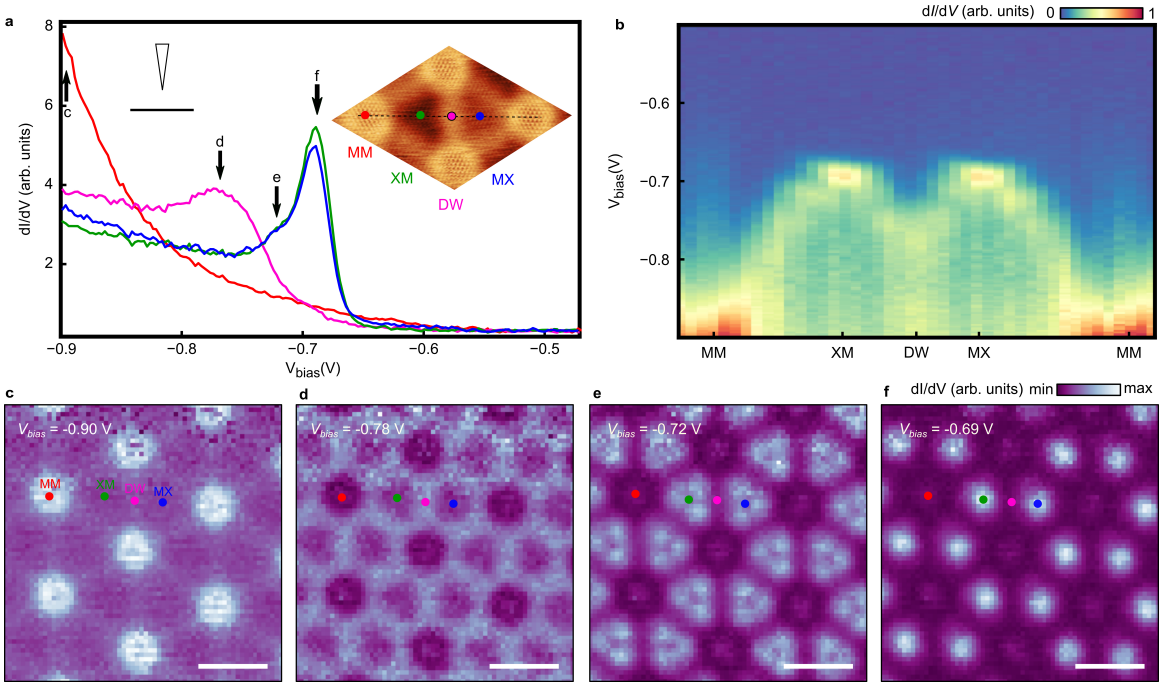

Figure 5.8: **Localization of Γ-point states.** **a**, Constant-height dI/dV spectra acquired at different high symmetry points (each averaged across 2x2 pixels, 0.62 nm^2) for a tMoTe$_2$ region with $\theta = 2.75°$ (the same as in figure 5.3f). The insets show a sketch of the tip and sample in the constant-height measurement scheme, and the associated STM topograph for this region with indicators for the positions of the high symmetry points. The markers are color-coded to match the corresponding dI/dV spectra. The dashed line is 10 nm long. **b**, Line cut of constant-height dI/dV spectra acquired along the dashed path shown in the inset of **a**. **c**-**f**, dI/dV maps acquired at different V_{bias}, as indicated by the arrows in **a**. All maps are assembled from a grid spectroscopy measurement with initial tunneling setpoint $(I_t, V_{bias}) = (110$ pA, -0.9 V$)$. The scale bar is 5 nm.

5.5 Spatial localization of valence band wavefunctions

Figure 5.8a shows four representative dI/dV spectra taken at different positions within the moiré unit cell. These spectra are acquired with standard constant-height spectroscopy, such that observed features originate primarily from Γ-point moiré bands. The green and blue curves are taken at the XM and MX stacking sites, the red at MM, and the pink at the center of a solitonic domain wall (DW) connecting MM sites. We see that these dI/dV spectra exhibit considerable spatial variation within the moiré unit cell. Figure 5.8b shows a line-cut of dI/dV spectra obtained along the dashed black line in the inset of figure 5.8a. From this map, we see a large dI/dV peak that is at its lowest energy at the MX and XM sites, and smoothly drifts to its largest energy at the MM sites.

The spatial variation of the Γ-point states can be best seen in maps of dI/dV acquired at fixed V_{bias} (figures 5.8c-f), which provide a direct visualization of the wavefunction distribution within the moiré unit cell and its energy dependence. Consistent with the spectra in figures 5.8a-b, we see that dI/dV at $V_{bias} = -0.90$V is largest at the MM sites, then shifts to the domain walls as the bias is lowered to -0.78 V, further develops into a more complex geometry at $V_{bias} = -0.72$ V that is not localized on any high-symmetry stacking site, and finally localizes onto the MX and XM sites at $V_{bias} = -0.69$ V. Collectively, these measurements show that the Γ-point wavefunctions can reside at any position within the moiré unit cell, with the details depending sensitively on energy. The precise localization of these states is highly dependent on the exact combination of twist angle, heterostrain, and interlayer separation (see appendix E). Similar behavior was observed over a wide range of twist angles, shown in figure E3 for $\theta = 3.48°$ and figure E2 for $\theta = 1.20°$.

In sharp contrast, we find that the flat-band states originating from the K points only reside at certain positions within the moiré unit cell. Figure 5.9a shows a representative reduced-height dI/dV spectroscopy map acquired with $V_{bias} = -0.59$ V (additional maps are shown in figure 5.10). The map is normalized by the initial current of the spectrum, I_0, in order to mitigate artifacts inherent to the reduced-height spectroscopy technique (see Supplementary Information section Reduced Height Spectroscopy for a discussion of this normalization, and Supplementary Information Fig. S2 for the raw dI/dV spectra). The normalized dI/dV is largest at the MX stacking site, and becomes progressively weaker at MM and XM. Fig. 5.9b shows the reduced-height spectroscopy spanning a small range of V_{bias} at these three stacking sites. We see that the dI/dV peak previously identified in Fig. 5.6d exists only on the MX stacking site, and that dI/dV is largest at MX over nearly the entire range of V_{bias} shown (see appendix F). A replication of this behavior at $\theta = 3.48°$ is shown in figure E.3, and its evolution in the small-θ limit is shown in figure E.4.

The reduced-height spectra in figure 5.9a show a residual signal on MM for a small range of V_{bias}

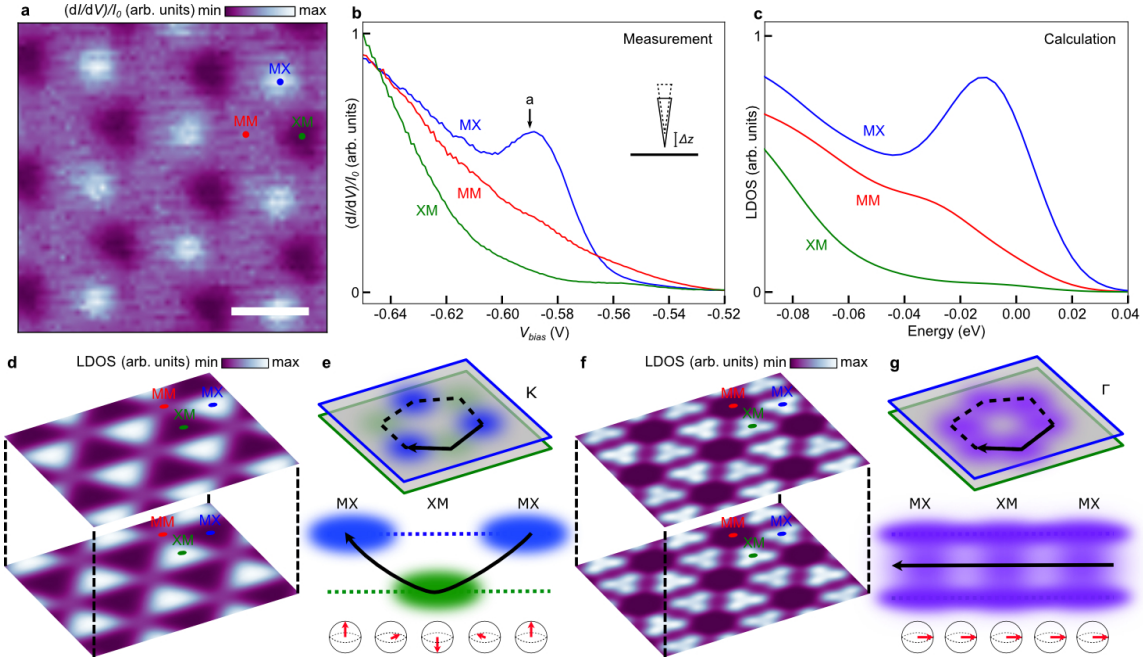

Figure 5.9: **Localization of K-point states and connection to band topology.** **a**, $\mathrm{d}I/\mathrm{d}V$ map, normalized by the initial current, I_0, acquired using reduced-height spectroscopy with $V_{bias} = -0.59$ V over the same region as in figure 5.8c. **b**, Reduced-height $\mathrm{d}I/\mathrm{d}V$ spectra normalized by I_0 at different high symmetry points (each averaged across 3x3 pixels, 0.88 nm^2). The inset shows a sketch of the tip and sample in the reduced-height measurement scheme. Data in **a-b** was assembled from grid spectroscopy with initial tunneling setpoint $(I_t, V_{bias}) = (50\ \text{pA}, -1.0\ \text{V})$. The tip was moved towards the sample by $\Delta z = 0.2$ nm before the bias sweep. **c**, Calculation of the LDOS at MM, MX, and XM for the top layer of $tMoTe_2$ with $\theta = 2.88°$ over a comparable energy range as the measurement shown in **b**. The value of energy $E = 0$ corresponds to the top of the first moiré valence band. A Gaussian smearing is applied to better reflect the experimental measurements. **d**, Calculated spatially resolved LDOS at $E = -10$ meV for both the top and bottom $MoTe_2$ layers. These states originate from the K points of the monolayer $MoTe_2$ Brillouin zone. The calculation is performed without any external electric field induced by the STM tip (see figure 5.11 for a similar calculation with this effect included). **e**, Schematic representation of the layer-pseudospin winding in the K bands of $tMoTe_2$ along a closed path encircling the moiré unit cell. Blue and green shaded regions correspond to wavefunctions polarized to the top and bottom layers, respectively. The red arrow in the Bloch sphere indicates the orientation of the layer pseudospin. **f**, Calculated spatially resolved LDOS at $E = -170$ meV, corresponding to states arising from the Γ point. **g**, Schematic representation of interlayer hybridization of wavefunctions in the Γ bands of $tMoTe_2$, and the corresponding Bloch sphere.

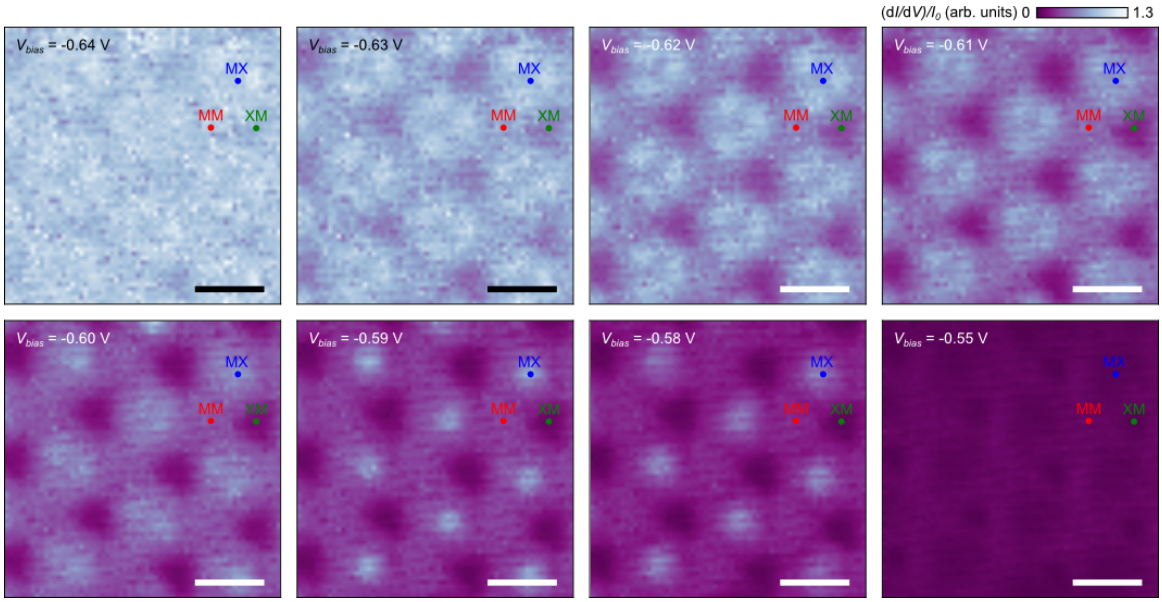

Figure 5.10: **Additional dI/dV maps of K-point states in the $\theta = 2.75°$ sample.** Reduced-height dI/dV maps in the same region as figure 5.9a, shown for additional values of V_{bias} with the same color scale across all maps. Scale bars are 5 nm.

below the MX peak. Figure E.3h further shows this residual signal appears at both MM and the DWs. We attribute this mainly to position-dependent tip-induced doping caused by the out-of-plane buckling of the t$MoTe_2$ layers. There may be more tip-induced electron doping when the top $MoTe_2$ layer is furthest from the grounded graphene, causing the the band edge to shift towards $V = 0$ at regions with larger interlayer spacing (i.e., MM and the DWs). Additionally, tip-induced deformations of the layers can cause an increase in the tunneling current or create additional inelastic tunneling channels which might offset the measured dI/dV signal. Closer to $V_{bias} = 0$, a faint residual signal is visible on XM, which is shown in Supplementary Video 2. This can be explained by enhanced tunneling into the underlying graphene at XM, where the tip is physically closest to the graphene.

5.6 Layer-pseudospin textures and band topology

The particular spatial localization of the flat bands we observe is well captured by our machine-learning assisted large-scale DFT calculations. Figure 5.9c shows the calculated LDOS at MX, XM, and MM in the top $MoTe_2$ layer over the same range of energy as in figure 5.9b. The calculation is in excellent qualitative agreement with our experimental observations, in particular showing the largest LDOS at MX over the entire range of energy shown. Figure 5.9d further shows a spatial map of the calculated LDOS for both the top and bottom layers of the twisted $MoTe_2$ (corresponding to an energy of -10 meV in

figure 5.9c). Since tunneling from the STM tip is primarily sensitive to the top layer of $tMoTe_2$, we directly compare our $(dI/dV)/I_0$ map in figure 5.9a with the calculation for the top $MoTe_2$ layer shown in figure 5.9d. The calculated LDOS is largest around the MX sites in the top $MoTe_2$ layer, consistent with our experimental observation of largest dI/dV at MX.

The layer-dependent localization of the flat-band wavefunctions to different high-symmetry stacking sites in the moiré unit cell is the key feature responsible for generating nontrivial band topology. The local layer polarization can be mapped onto a pseudospin Bloch sphere, in which the top (bottom) of the sphere corresponds to a wavefunction polarized to the top (bottom) $MoTe_2$ layer. Under this mapping, the MX site is the north pole and the XM site the south pole. As the electron hops inside the moiré unit cell, the trajectory of the layer pseudospin will cover the entire Bloch sphere, giving rise to winding number of 1 (illustrated schematically in figure 5.9e).[162] This skyrmion lattice generates a pseudo-magnetic field responsible for the anomalous Hall effect seen in transport experiments,[142] analogous to the topological Hall effect driven by skyrmions of electron spin found in certain magnetic materials.[163] We note, however, that despite the close correspondence between the skyrmion winding number and the Chern number, they need not be identical; the Chern number is further determined by the exact quantum geometry of each band.[140]

Because our measurements are performed on charge-neutral $tMoTe_2$, states in the time-reversed K and K' valleys remain degenerate. The layer-pseudospin texture in the two valleys is therefore related by time-reversal symmetry, which reverses only the y-component of the in-plane layer pseudospin. Thus, the assignment of the north (south) pole to the MX (XM) site is the same for both the K and K' valleys, irrespective of the differences in their in-plane pseudospin textures. Since our STM measurements probe only the out-of-plane component of the layer pseudospin, the layer polarization of the wavefunction directly reflects the positions of the north and south poles of the pseudospin skyrmions identically for the two valleys.

The layer-polarizion of the flat-band wavefunctions contrasts that of the Γ-point states, which can appear at any position within the moiré unit cell (figure 5.8c). This is anticipated theoretically, since these Γ-point states are strongly interlayer-hybridized and are thus unable to polarize to a single $MoTe_2$ sheet. Figure 5.9f shows a calculation of the LDOS at an energy of 170 meV below the valence band edge, comparable to the dI/dV map acquired at $V_{bias} = -0.69$ V in figure 5.8c. The experiment and theory agree very well, in that both show wavefunction localization nearly equivalently onto the MX and XM sites in both layers (see Supplementary Information section Effects of Twist Angle and Strain on the Localization of Γ-point States for a discussion of weak C_{2x} symmetry-breaking terms). For these interlayer-hybridized bonding states, the layer pseudospin is pinned to a narrow region on the equator of

the Bloch sphere and the resulting texture is topologically trivial (illustrated schematically in figure 5.9g, with the direction along the equator chosen arbitrarily).

5.6.1 Effects of a tip-induced electric field on the K- and Γ-point wavefunctions.

A potential complication in interpreting our measurements lies in understanding the effect of a local electric field under the STM tip, arising from the large V_{bias} and an intrinsic work function mismatch between the tip and the sample.[164,165] Previous studies of tMoTe$_2$ have shown that an electric field can modify the nature of the correlated states.[104–107,133,134] To estimate the electric displacement field, D, across the tMoTe$_2$, we assume a uniform potential from the tip to the grounded graphene. We calculate $D = (\Phi_{tip} - \Phi_{gr} - V_{bias})/(d + 2t)$, where $\Phi_{tip} - \Phi_{gr}$ is the work function mismatch between the gold tip and graphene, d is the tip-sample separation, and t is the thickness of monolayer MoTe$_2$. Using $\Phi_{tip} - \Phi_{gr} \approx 1$ eV,[166] $V_{bias} \approx -1$ V, and $(d + 2t) \approx 3$ nm, we estimate a value of $D \approx 200$ mV/nm in our experiment.

We have performed additional DFT calculations similar to those described above, but also including a realistic tip-induced external electric field. Figures 5.11a-b show zoom-ins of the moiré band structure near the band edge for both $D = 0$ and $300\ \mathrm{mV/nm}$. Although the $D = 0$ band structure features several Chern bands, the presence of a finite electric displacement field, D, causes band inversions and splittings that result in topologically trivial bands. We find that the states originating from the Γ point have an almost negligible dependence on the external field owing to their interlayer hybridization. In contrast, the relative weight of the K-point states shifts towards one of the two MoTe$_2$ layers, depending on the sign of the external field. Nevertheless, the geometry of the LDOS localization within the moiré unit cell remains unchanged. Thus, a tip-induced field does not meaningfully impact the primary conclusions of our analysis. More specifically, we see that the system retains the overall geometry of LDOS localization at MX in the top layer even with an applied field, so our measurements are still an effective probe of the pole positions within the layer pseudospin texture.

5.7 Implications of experimentally observed layer-pseudospin texture

Our STM/S study of tMoTe$_2$ provides a microscopic visualization of this unique topological material. Accurately predicting the Chern numbers and quantum geometry of the flat valence bands has been challenging owing to their notable sensitivity to the modeling parameters.[140,141,146,167–171] Detailed energy-dependent LDOS maps and atomically-resolved topographs now provide strong experimental constraints for theory. In particular, our observation of MX-localized wavefunctions in the top MoTe$_2$ layer is in excellent agreement with our modeling for twist angles $\theta \gtrsim 2^\circ$, where FQAH states have previously

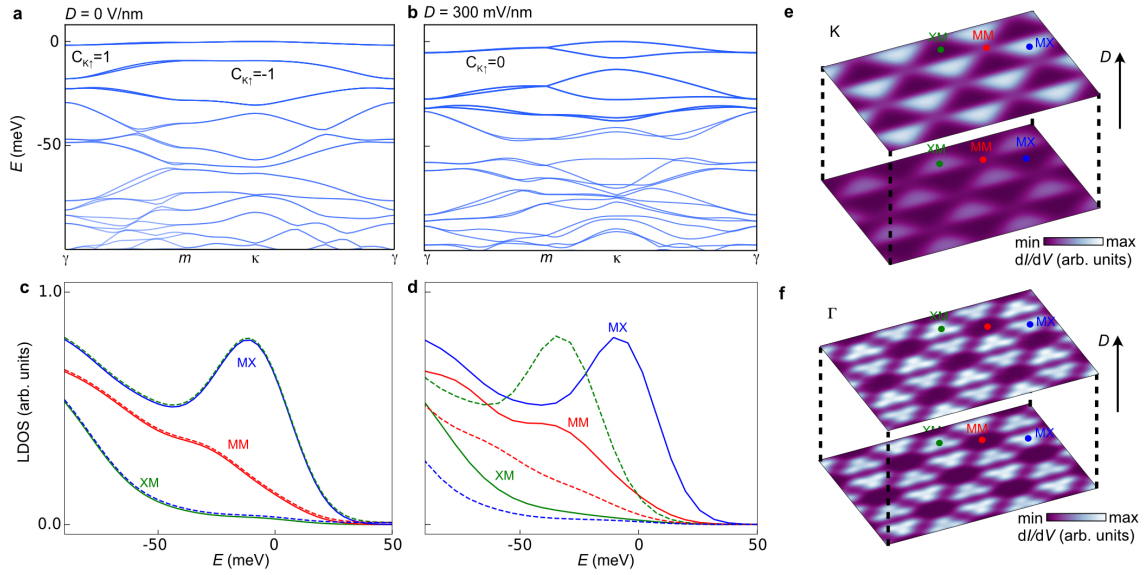

Figure 5.11: **Predicted effects of displacement field on the K-point states. a-b**, Calculated bandstructure for tMoTe$_2$ with $\theta = 2.88°$ with **a**, $D = 0$ mV/nm, and **b**, $D = 300$ mV/nm. **c-d**, Calculated LDOS at different high symmetry points within the moiré unit cell. The top (bottom) layer is shown as the solid (dashed) curve. For $D = 0$, the curves from the top and bottom layer are perfectly C_{2x} symmetric (note that the curves from the bottom layer are offset by 0.0002 for visual clarity). For $D \neq 0$, C_{2x} symmetry is broken and there is an energy splitting between the LDOS of different stacking sites in the two layers. **e**, Calculated spatially resolved LDOS at $E = -10$ meV for both the top and bottom MoTe$_2$ layers with $D = 300$ mV/nm. The top layer shows localization on MX, while the bottom shows localization on XM, similar to in figure 5.9d. However, in this calculation the overall value of the LDOS across the moiré is notably larger on the top layer as a consequence of the displacement field. **f**, Calculated spatially resolved LDOS at $E = -170$ meV and $D = 300$ mV/nm, corresponding to states arising from the Γ point. Because of their interlayer hybridization, these states depend only very weakly on D, and this calculation is nearly indistinguishable from the $D = 0$ case shown in figure 5.9f.

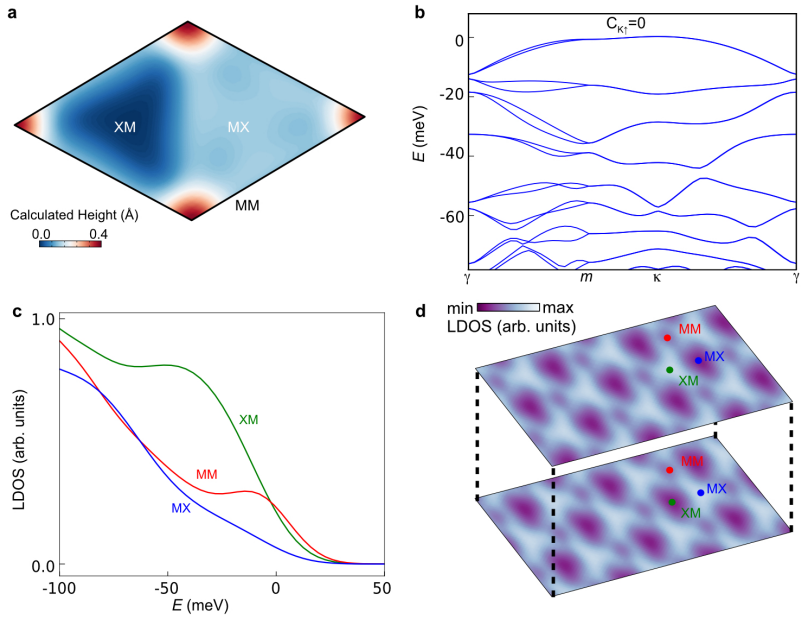

Figure 5.12: **Calculated LDOS excluding the in-plane lattice relaxations. a**, Height of top layer in 2.88° $tMoTe_2$ predicted by an atomic relaxation DFT calculation excluding in-plane lattice relaxations (but retaining the out-of-plane relaxations). The height profile is identical to that shown in figure 5.3c. **b**, Calculated band structure with in-plane lattice relaxations excluded. The first moiré valence band has a valley Chern number of 0, in contrast to its value of 1 when in-plane relaxations are included. **c**, Corresponding calculations of LDOS at MM, MX, and XM in the top $MoTe_2$ layer as a function of energy near the valence band edge. **d**, Layer-resolved LDOS at -10 meV, showing localization on the XM sites in the top layer and the MX sites in the bottom layer. This result is in contrast to the calculated LDOS including in-plane lattice relaxations shown in figure 5.9, in which the LDOS is localized on MX in the top layer near the band edge.

been reported. However, ambiguity remains for smaller twist angles where calculations remain challenging due to the very large moiré unit cell (figure E.4), pointing to the need for further investigation in this regime. Our analysis further reveals that the in-plane atomic lattice relaxations within the moiré lattice are instrumental in controlling the topological properties of the material. In calculations with in-plane lattice relaxations artificially excluded, the north and south poles of the pseudospin lattice flip positions between MX and XM and also change the Chern numbers of the flat bands (figure 5.12). This additional understanding unveils the intimate connection between the precise atomic lattice structure of $tMoTe_2$ and its quantum geometric properties.

Looking forward, the structure of the LDOS within the moiré unit cell and its evolution with energy can now be used to further refine theories beyond simply predicting the correct Chern number. This will help to provide sharper constraints on the FQAH effect in $tMoTe_2$, likely resulting in a better understanding of experimentally observed states and aiding predictions for entirely new phases. Our results also provide

insights into the atomic-scale electric polarization structure of $tMoTe_2$ arising from the microscopic effects of ferroelectricity and lattice relaxations, informing ongoing studies of the moiré ferroelectricity found in twisted TMD bilayers[111,140,143–145] and opening new pathways towards engineering the FQAH states with strain.[172] Lastly, our foundational atomic-scale understanding of the system enables future STM/S experiments probing the intertwined correlated and topological states that emerge upon hole doping. Progress in this direction will require the development of new device geometries with Ohmic contacts to the $tMoTe_2$, obviating the need for a graphene substrate and enabling gating to the integer and fractional Chern insulator states.

5.8 Towards STM measurements of correlated phases in $tMoTe_2$

It was recently shown that ohmic contact to 2H tungsten diselenide (WSe_2) can be achieved by introducing ruthenium trichloride ($RuCl_3$) to the vdW device structure.[173] Due to it's comparatively large work function, $RuCl_3$ induces a large hole doping in WSe_2 when the two materials are layered together. Inserting thin $RuCl_3$ flakes below the contacts to a WSe_2 flake lowers the Shottky barrier at the contacts, enabling contact resistance on the order of 20-30 kΩ at very low hole densities (around $3 \times 10^{11}\,\mathrm{cm}^{-2}$). We have implemented a similar strategy to fabricate gated $tMoTe_2$ devices for STM with well-functioning Ohmic contacts. The effectiveness of this method in $MoTe_2$ is not surprising as it has a similar work function and band gap to WSe_2. Figure 5.13 illustrates the contact geometry that we found to be effective: $tMoTe_2$ is sandwiched between few layer graphite and thin $RuCl_3$. Since this method uses all vdW flakes, it is easily integrate with our methods of fabricating surface exposed devices (section 2.1.3).

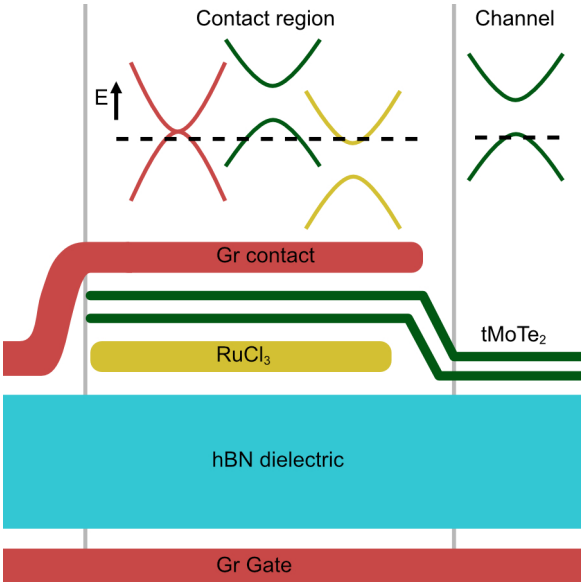

Figure 5.13: **Graphite-$RuCl_3$ contacts to $tMoTe_2$,** Schematic diagram of stack structure used for graphite-$RuCl_3$ contacts and corresponding band alignment of graphite, $RuCl_3$, and $MoTe_2$ bands in and out of the contact region.

Even with this new Ohmic contact scheme, one more fundamental difficulty remains in measuring the correlated phase diagram of $tMoTe_2$ with STM. Devices with an exposed $tMoTe_2$ surface are limited to one electrostatic gate, so the carrier density and displacement field cannot be tuned independently like in

a dual-gated device. Instead, tuning the gate voltage makes a single diagonal path through n-D space, with each gate voltage corresponding to a single n and D value determined by the capacitance of the hBN dielectric.[174] In addition, any work function mismatch between the tip and the $MoTe_2$ layers creates an electric field between them that adds an overall offset to n and D. Thus, we cannot study the entire n and D phase space of $tMoTe_2$ using a surface-exposed device. This is especially problematic since the integer and fractional quantum anomalous (IQAH,FQAH) are destroyed with large enough D. Furthermore, D induces topological phase transitions from IQAH/FQAH states to trivial correlated insulating states which may exhibit discrete translational symmetry breaking.[105, 107, 133, 134] STM measurement of $tMoTe_2$ as a function of D could thus reveal the spectroscopic and spatial evolution of these phase transitions.

In an attempt to study the local properties of $tMoTe_2$ within the full n-D phase diagram, we fabricated and measured graphene sensor style STM devices.[136, 137, 175] The device structure, shown in figure 5.14a, consists of the following vdW layers listed from top to bottom: (1) a graphite back gate, (2) a standard hBN dielectric (20-40 nm thick), (3) tMoTe2, contacted using the scheme illustrated in figure 5.13, (4) a thin hBN dielectric (5-10 nm), (5) monolayer graphene. In the STM measurement, the graphene is held at ground while a bias voltage is applied to the tip. By applying gate voltages to the $MoTe_2$ layers and the graphite gate, V_M and V_{Gr} respectively, we can tune n and D independently using a modified version of equation 2.1,

$$\begin{aligned} n_{\mathrm{tMoTe_2}} &= \frac{1}{e}(-C_t V_M + C_b(V_{Gr} - V_M)) \\ D_{\mathrm{tMoTe_2}} &= \frac{1}{2\epsilon_0}(-C_t V_M - C_b(V_{Gr} - V_M)) \end{aligned} \tag{5.5}$$

where C_b and C_t are the capacitances of the thick bottom hBN and the thin top hBN respectively. At the same time, we can measure the spatially resolved tunneling current and $\mathrm{d}I/\mathrm{d}V$ signal between the tip and the graphene, which may be coupled to the $tMoTe_2$ via Coulomb interactions through the thin hBN dielectric barrier. This graphene-sensing technique has been used to image generalized-wigner crystal states in other TMD moiré systems with spatial resolution on the order of the thickness of the top hBN barrier.[136, 137] The main downside of this technique is that it does not directly probe the spectrum of $tMoTe_2$ and thus provides more limited information than a direct tunneling geometry.

Figures 5.14b-d show representative STM data acquired from one nanoscale area of a graphene-sensor $tMoTe_2$ device. The topography image of the graphene sensor surface, shown in 5.14b, shows a clear moiré pattern which we associate with the $tMoTe_2$ below. Since the variations in z that correspond to this moiré pattern are relatively small, we believe they arise from large corrugations of the $MoTe_2$ layers that are transmitted to the graphene sensor. This scale of out-of-plane deformation of the $MoTe_2$ layers is supported by our previous topography measurements of $tMoTe_2$ on a graphene substrate, figure 5.3. Figures 5.14c and d show maps of $\mathrm{d}I/\mathrm{d}V$ between the tip and grounded graphene layer as a function

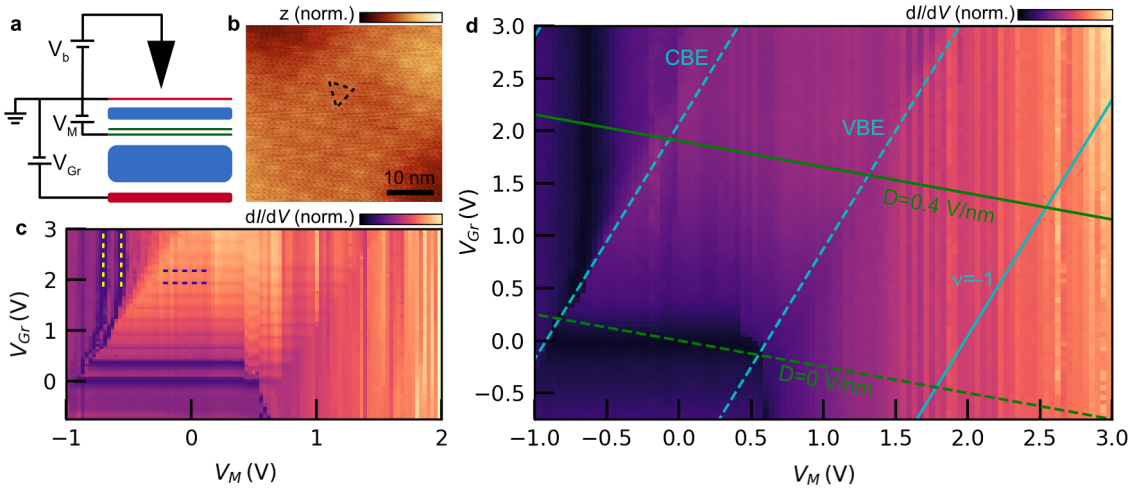

Figure 5.14: **STM measurements of graphene sensor tMoTe$_2$ devices**, **a**, Schematic of graphene-sensor geometry and relevant circuit for electrostatic gating. **b**, Topography of graphene surface in sensor device showing corrugations due to buried tMoTe$_2$ moiré. Black dashed triangle denotes tMoTe$_2$ moiré unit cell. Smaller periodicity in the image is due to the moiré between graphene and hBN substrate. **c**-**d**, Maps of the zero-bias conductance of the graphene sensor as a function of V_{Gr} and V_M acquired at a magnetic field of **c** 5 T and **d** 0 T. Dashed lines in **c** highlight the spacing between Landau levels formed in the graphene sensor at high field. Lines in **d** denote countour of constant doping and displacement field in the tMoTe$_2$.

of V_M and V_{Gr} with an applied perpendicular magnetic field of $B = 3$ T and $B = 0$ T respectively. Both maps show three distinct regions: (1) At low V_M and V_{Gr},(middle region of 2D maps) features are purely horizontal indicating that only V_{Gr} can tune $\mathrm{d}I/\mathrm{d}V$. This suggests that the chemical potential of the tMoTe$_2$ lies within its semiconducting band gap, making it electrostatically transparent. (2) At large positive V_M and large negative V_{Gr} (right region of maps), features are purely vertical, indicating that only V_M can tune $\mathrm{d}I/\mathrm{d}V$. Based on the expected direction of the electric field within the hBN layers, this indicates that the chemical potential of tMoTe$_2$ lies in its conduction band, such that the tMoTe$_2$ acts like a metal and screens any effect of V_{Gr}. (3) At large negative V_M and large positive V_{Gr}, features are similarly vertical, indicating that the chemical potential of tMoTe$_2$ lies in its valence band. There is additionally an abrupt diagonal feature that marks the boundaries between these regions, which we associate with the onset of a transition from insulating to conducting behavior in the tMoTe$_2$. These observations indicate a fully functioning dual-gated tMoTe$_2$ device.

We can convert V_M and V_{Gr} to $n_{\mathrm{tMoTe_2}}$ and $D_{\mathrm{tMoTe_2}}$ in the tMoTe$_2$ using equation 3.5. We obtain the values of C_t and C_b by measuring the spacing between graphene landau levels in the left and middle regions of the 2D map in figure 5.14c. Since these regions are independently controlled by one gate voltage, we can use them to calculate C_t and C_b exactly. Cyan lines in figure 5.14 denote contours of

constant $D_{\mathrm{tMoTe_2}}$ while green lines denote contours of constant $n_{\mathrm{tMoTe_2}}$. We judge the onset of hole and electron doping by aligning the conduction and valence band edge with the sharp diagonal features that mark the boundaries between the three main regions. It is worth noting that the slope of these features matches the slope of constant $n_{\mathrm{tMoTe_2}}$, which validates our assignment of C_t and C_b. The calculated lines of constant $n_{\mathrm{tMoTe_2}}$ and $D_{\mathrm{tMoTe_2}}$ indicate that we can tune the electrostatic conditions of the tMoTe$_2$ layer to the ranges relevant for both IQAH, FQAH, and translational symmetry broken insulating states.[105,107,133,134]

However, we do not observe any evidence of any interaction-driven phases at integer or fractional fillings. Since transport devices with a wide range of twist angles have exhibited signatures of correlated physics, it is more likely that this sensor geometry is not sufficiently sensitive enough to the exact phases that occur in this device. This could be due to a number of factors. First, the temperature of our STM (5K) is higher than optimal for FQAH and trivial insulators at fractional filling observed in transport measurements. However, the IQAH effect as well as a trivial correlated insulator at $\nu = 1$ and high D are present in nearly all transport studies of tMoTe$_2$ at temperatures well above our base temperature.[105,107,133,134] Another possibility is that the exact strain present in this region is not optimal, but given the robustness of transport results across multiple devices, this is unlikely. A more believable scenario is that the correlated phases present do not have any strong spatial order that couples to the graphene sensor. On this note, the thickness of the top hBN in this geometry may require more tuning to facilitate effective coupling between tMoTe$_2$ and the graphene sensor; if the hBN is too thick, Coulomb interactions may be too small to cause a measurable change in the graphene tunneling signal, but if it is too thin, the proximity of graphene to tMoTe$_2$ may screen electron-electron interactions and kill any correlated phases. Lastly, one may expect that an appreciable correlated gap in the tMoTe$_2$ would weaken it's ability to screen the electric field created by nonzero V_{Gr},and lead to some short lived horizontal features within the valence band regions of the 2D maps presented in figure 5.14c-d. One explanation of why this does not appear in our data is that the device resistance within these gaps at 5K is not large enough to prevent screening of the graphite gate.

Though we cannot observe any local properties of correlated phases in tMoTe$_2$, our study nevertheless informs future local probe measurements of gated tMoTe$_2$. Future efforts could include a more systematic study of graphene sensor devices with varying top hBN thickness, which may yield more fruitful results. Another option would be to adapt the graphite-$RuCl_3$ contact geometry into surface-exposed devices, which provide direct spectroscopic information but preclude controlled tuning of D. These may nevertheless yield useful insights into the local behavior of selected correlated phases within the values of n and D available in single gated devices.

Chapter 6
CONCLUSIONS AND FUTURE WORK

The experimental work presented in this thesis highlights one central conclusion: moiré engineering has strong implications in a multitude of vdW systems beyond TBG. I want to stress that this is not a new idea; the universality of moiré flat bands has been a core driving principle of vdW material research in the last ten years. In fact, the ability to create controllable periodic potentials in systems with any arbitary number of electronic properties presents an exciting opportunity to create designer many-body electron phases, which may have real technological applications. Our experiments probe several important pieces of this rapidly evolving puzzle.

Chapters 3 and 4 address the role of layer number in moiré vdW heterostructures, one of the simplest and tractable tuning knobs available. In chapter 3, we extend the correlated and topological physics of TBG to a family of tM+N multilayer graphene structures. Though they exhibit similar isospin-symmetry broken correlated insulating states, they differ fundamentally from TBG, and related alternating twisted graphene structures like twisted trilayer graphene, due to their broken inversion symmetry. This enables a continuously deformable conduction band which can be flattened and isolated form the valence band and remote conduction band at finite displacement field. This is in stark contrast to TBG's two flat bands pinned to zero energy by the symmetry protected Dirac points of its monolayer graphene constituents. Through systematic electronic transport measurements, we show that this family of structures exhibit similar single particle and correlated features and are capable of hosting various topological phases. In addition, we identify twisted bilayer-trilayer graphene as a particularly rich correlated electronic system which exhibits certain previously unobserved phases including a correlated insulating state at charge neutrality and zero displacement field and intriguing spin and valley symmetry breaking at low ν. The latter has been explored further in a more recent study which finds a possible anomalous Hall crystal phase at $\nu = \frac{1}{4}$.[176] In chapter 4, we extend the tM+N family even further into the limit of bulk Bernal stacked graphite. Our measurements show that adding a single moiré interface on one end of a graphite thin film (t1+Z) fundamentally modifies its transport properties. This can be explained by the formation of narrow moiré bands spatially localized near the moiré interface which coexist with conventional bulk graphite bands. The moiré interface drives more exotic behavior at large perpendicular magnetic fields. The evolution of Landau fan features with gate voltage suggests that Hofstadter states localized to the

moiré interface are coupled to bulk graphite quantum Hall states via a quasi-1D standing wave in the z direction.

Still, there are many aspects of these tM+N and t1+Z that we do not fully understand. One such mystery is the absence of superconductivity in thin tM+N structures compared to the robust superconducting states in TBG and alternating twisted multilayer graphene structures near $\nu = 2, -2.$,[15,16,50,81–83,85] This may be related to fundamental symmetry differences between the two classes of structures, but future studies of these systems could clarify this difference. This question is complicated by the recent observation of superconductivity in t2+2 graphene proximitized by WSe_2 which has been shown to induce enhanced spin-orbit coupling.[177] Another elusive aspect of these multilayer systems is how the geometry and strength of the moiré potential evolve with increasing layer number. Theoretical modeling suggests that the exact structure of the layer resolved local density of states in moiré systems depends on the number of layers added on either side of the interface.[122] While our theoretical modeling predicts localization of the layer resolved density of states to the moiré interface, we cannot model the precise spatially resolved LDOS. This is because the continuum model only considers interlayer tunneling between the two layers closest to the moiré interface and does not take into account the thickness dependence of atomic lattice relaxations. Finally, the isospin ordering of correlated phases at integer ν are determined by the interplay of several sub-meV energy scales, which are difficult to control in a system with so many free experimental parameters: twist angle, strain, layer number, dielectric environment, etc. Thus, it is often difficult to engineer the emergence of specific correlated phases within individual devices.

Many of these open questions could be addressed at least partially with STM studies of twisted multilayer graphene. As established in chapters 2 and 5, STM provides nanometer scale structural and electronic information, which which would allow more detailed analysis of changes to the LDOS with layer number. STM also tells you the strain in a moiré superlattice in addition to the twist angle, which determines an additional degree of freedom in these structures that is inaccessible through transport measurements.[80] Another potentially interesting experiment would be to study the local spectroscopic properties of novel correlated phases in twisted-bilayer trilayer graphene, such as the insulating state at charge neutrality or the apparent anomalous Hall crystal at $\nu = \frac{1}{4}$. Lastly, a natural extension of our work is to apply the tM+N or t1+Z framework to rhombohedral graphite, which has been shown to exhibit superconductivity and various topological phases with and without a moiré with an hBN substrate.[101,102,178–181]

In chapter 5, we use STM to investigate the evolution of the sub-moiré scale layer resolved wavefunction with energy in $tMoTe_2$. We present clear experimental evidence for a topological skyrmion texture of the layer pseudospin degree of freedom which manifests as a C_{2Z} symmetry broken LDOS distribution.

Furthermore, combining our STM measurements with advanced theoretical modeling suggests that interlayer piezoelectric polarizations induced by atomic lattice relaxations are integral in determining the shape of the layer pseudospin texture and thus the topological properties of the system. This manifestation of topology in real space is unique to twisted 2H TMDs and introduces a new paradigm for understanding topology in vdW materials.

In the future, similar local probe studies of twisted 2H TMDs may enhance our understanding of layer pseudospin textures. A recent STM study has already shown that twisted tungsten diselenide ($tWSe_2$) hosts a similar layer peudospin texture.[182] One intriguing detail is that the observed layer pseudospin texture in $tWSe_2$ has winding number that is opposite to what we observe in $tMoTe_2$, i.e. the positions of the north and south poles are flipped with respect to our data. This is surprising since DFT calculations using the same method as the theory presented in chapter 6 predict that $tWSe_2$ should have the same sign of skyrmion winding number in the relevant twist angle range of the two experiments.[140] One possibility is that the $tWSe_2$ sample studied in this instance did not exhibit the same type of lattice relaxations since it is fabricated through direct chemical vapor deposition onto a graphene substrate and thus may be anchored differently to the substrate. Nevertheless, this discrepancy warrants more detailed studies of the evolution of the layer pseudospin texture in both materials with twist angle and strain.

Developing a deeper understanding of the correlated phase diagram of $tMoTe_2$ will necessarily involve microscopic studies of its competing correlated and topological phases. However, as explained in detail in chapter 6, this is challenging with STM and will most likely require novel device geometries or careful work function engineering of STM tips. This requirement warrants novel methods to fabricate STM devices which accomodate a wider variety of contact and gate materials or geometries. We recently adapted one such method based on controlled disassembly of vdW heterostructres, which was initially developed by Pack *et al.*[183] The basic procedure is as follows: (1) assemble the desired final heterostructure top down underneath a protective sacrificial hBN flake, (2) Desposit the entire stack onto pre-patterned contacts (it is also possible to deposit it onto a blank substrate and fabricate contacts afterwards, since the system of interest in protected by the sacrificial hBN), (3) Use a non-invasive stamp to slide the sacrificial hBN off of the exposed surface to be probed with STM. So far, we have used this technique to fabricate tungsten ditelluride (WTe_2) devices for STM, and verified that it yields a pristine exposed surface.* This new fabrication knowledge will enable us to assemble previously unachievable sensor or contact geometries to facilitate gated experiments. It may also lead to a more pristine $tMoTe_2$ surface, making it easier to perform repeated reduced-height spectroscopy measurements that are extremely sensitive to tip condition.

---

*We chose WTe_2 as a test subject because it is extremely air-sensitive. After exfoliation, WTe_2 monolayers oxidize instantaneously in air and within a few hours in an inert glovebox environment. This means that they cannot survive the length of the fabrication procedure described in section 2.1.

Looking forward, there are many more opportunities to discover new physics in moiré systems beyond those studied in this thesis. All the systems studied here have hexagonal crystal symmetry, but a moiré pattern can be created between misaligned atomic crystals of any symmetry. One previously studied example is twisted WTe_2, which inherits a highly nonisotropic rectangular symmetry from the monolayer crystals.[184] Previous transport studies of tWTe_2 posit that it hosts a coupled network 1 dimensional Luttinger liquid channels within moiré domain walls.[185,186] However, this has not yet been verified directly by scanning probe measurements. With STM, we could verify this experimentally and use it as a tunable platform to study 1D correlated physics. Another direction is to explore hexagonal crystalline materials whose low energy bands lie at different crystal momenta. This thesis stresses the unique topological properties of materials with band touching at the K and K' points of a hexagonal Brilluoin zone, but certain crystal structures may produce bands with low energy extrema at other high symmetry points that will impart different topological properties onto resulting moiré bands.[187] In many ways, the world of moiré materials is still in its infancy and has the potential to grow into a more rich, broadly-focused, and applied field.

BIBLIOGRAPHY

[1] von Klitzig, K. The quantized Hall effect. *Reviews of Modern Physics* **58**, 519–531 (1986).

[2] Manfra, M. J. Molecular Beam Epitaxy of Ultra-High-Quality AlGaAs/GaAs Heterostructures: Enabling Physics in Low-Dimensional Electronic Systems. *Annual Review of Condensed Matter Physics* **5**, 347–373 (2014).

[3] Novoselov, K. S. *et al.* Electric Field Effect in Atomically Thin Carbon Films. *Science* **306**, 666–669 (2004).

[4] Novoselov, K. S., Mishchenko, A., Carvalho, A. & Castro Neto, A. H. 2D materials and van der Waals heterostructures. *Science* **353**, aac9439 (2016).

[5] Gibertini, M., Koperski, M., Morpurgo, A. F. & Novoselov, K. S. Magnetic 2D materials and heterostructures. *Nature Nanotechnology* **14**, 408–419 (2019).

[6] Dean, C. R. *et al.* Boron nitride substrates for high-quality graphene electronics. *Nature Nanotechnology* **5**, 722–726 (2010).

[7] Wang, L. *et al.* One-dimensional electrical contact to a two-dimensional material. *Science* **342**, 614–617 (2013).

[8] Kim, K. *et al.* van der waals heterostructures with high accuracy rotational alignment. *Nano Letters* **16**, 1989–1995 (2016).

[9] Li, H. *et al.* Electrode-free anodic oxidation nanolithography of low-dimensional materials. *Nano Letters* **18**, 8011–8015 (2018).

[10] Andrei, E. Y. *et al.* The marvels of moiré materials. *Nature Reviews Materials* **6**, 201–206 (2021).

[11] Yankowitz, M. *et al.* Emergence of superlattice dirac points in graphene on hexagonal boron nitride. *Nat. Phys.* **8**, 382–386 (2012).

[12] Dean, C. R. *et al.* Hofstadter's butterfly and the fractal quantum hall effect in moire superlattices. *Nature* **497**, 598–602 (2013).

[13] Wang, L. *et al.* Evidence for a fractional fractal quantum Hall effect in graphene superlattices. *Science* **350**, 1231–1234 (2015).

[14] Cao, Y. *et al.* Correlated insulator behaviour at half-filling in magic-angle graphene superlattices. *Nature* **556**, 80–84 (2018). 1802.00553.

[15] Cao, Y. *et al.* Unconventional superconductivity in magic-angle graphene superlattices. *Nature* **556**, 43–50 (2018).

[16] Yankowitz, M. *et al.* Tuning superconductivity in twisted bilayer graphene. *Science* **363**, 1059–1064 (2019).

[17] Jeckelmann, B. & Jeanneret, B. The quantum Hall effect as an electrical resistance standard. *Reports on Progress in Physics* **64**, 1603–1655 (2001).

[18] Tong, D. The Quantum Hall Effect. Tech. Rep., University of Cambridge (2016). URL `https://www.damtp.cam.ac.uk/user/tong/qhe.html`.

[19] Tsui, D. C., Stormer, H. L. & Gossard, A. C. Two-Dimensional Magnetotransport in the Extreme Quantum Limit. *Physical Review Letters* **48**, 1559–1562 (1982).

[20] Zhang, Y., Tan, Y.-W., Stormer, H. L. & Kim, P. Experimental observation of the quantum Hall effect and Berry's phase in graphene. *Nature* **438**, 201–204 (2005).

[21] Novoselov, K. S. *et al.* Unconventional quantum Hall effect and Berry's phase of 2 in bilayer graphene. *Nature Physics* **2**, 177–180 (2006).

[22] Xiao, D., Chang, M.-C. & Niu, Q. Berry phase effects on electronic properties. *Reviews of Modern Physics* **82**, 1959–2007 (2010).

[23] Thouless, D. J., Kohmoto, M., Nightingale, M. P. & den Nijs, M. Quantized hall conductance in a two-dimensional periodic potential. *Physical Review Letters* **49**, 405 (1982).

[24] Castro Neto, A. H., Guinea, F., Peres, N. M. R., Novoselov, K. S. & Geim, A. K. The electronic properties of graphene. *Reviews of Modern Physics* **81**, 109–162 (2009).

[25] Wallace, P. R. The band theory of graphite. *Physical Review* **71**, 622–634 (1947). URL `https://link.aps.org/doi/10.1103/PhysRev.71.622`.

[26] McCann, E. & Fal'ko, V. I. Landau-Level Degeneracy and Quantum Hall Effect in a Graphite Bilayer. *Physical Review Letters* **96**, 086805 (2006).

[27] Koshino, M. Interlayer screening effect in graphene multilayers with aba and abc stacking. *Phys. Rev. B* **81**, 125304 (2010).

[28] Zhang, Y., Tan, Y.-W., Stormer, H. L. & Kim, P. Experimental observation of the quantum Hall effect and Berry's phase in graphene. *Nature* **438**, 201–204 (2005).

[29] Novoselov, K. S. *et al.* Unconventional quantum Hall effect and Berry's phase of 2 in bilayer graphene. *Nature Physics* **2**, 177–180 (2006).

[30] Novoselov, K. S. *et al.* Two-dimensional gas of massless Dirac fermions in graphene. *Nature* **438**, 197–200 (2005).

[31] Manzeli, S., Ovchinnikov, D., Pasquier, D., Yazyev, O. V. & Kis, A. 2D transition metal dichalcogenides. *Nature Reviews Materials* **2**, 17033 (2017).

[32] Xiao, D., Yao, W. & Niu, Q. Valley-Contrasting Physics in Graphene: Magnetic Moment and Topological Transport. *Physical Review Letters* **99**, 236809 (2007).

[33] Xiao, D., Liu, G.-B., Feng, W., Xu, X. & Yao, W. Coupled Spin and Valley Physics in Monolayers of MoS 2 and Other Group-VI Dichalcogenides. *Physical Review Letters* **108**, 196802 (2012).

[34] Mueller, T. & Malic, E. Exciton physics and device application of two-dimensional transition metal dichalcogenide semiconductors. *npj 2D Materials and Applications* **2**, 29 (2018).

[35] Kane, C. L. & Mele, E. J. Quantum Spin Hall Effect in Graphene. *Physical Review Letters* **95**, 226801 (2005).

[36] Liu, G.-B., Shan, W.-Y., Yao, Y., Yao, W. & Xiao, D. Three-band tight-binding model for monolayers of group-VIB transition metal dichalcogenides. *Physical Review B* **88**, 085433 (2013).

[37] Balents, L., Dean, C. R., Efetov, D. K. & Young, A. F. Superconductivity and strong correlations in moiré flat bands. *Nature Physics* **16**, 725–733 (2020).

[38] Andrei, E. Y. & MacDonald, A. H. Graphene bilayers with a twist. *Nature Materials* **19**, 1265–1275 (2020).

[39] Bistritzer, R. & MacDonald, A. H. Moiré bands in twisted double-layer graphene. *Proceedings of the National Academy of Sciences of the United States of America* 12233–12237. 1009.4203.

[40] Suárez Morell, E., Correa, J. D., Vargas, P., Pacheco, M. & Barticevic, Z. Flat bands in slightly twisted bilayer graphene: Tight-binding calculations. *Phys. Rev. B* **82**, 121407 (2010).

[41] Zhang, Y.-A., Mao, D., Cao, Y., Jarillo-Herrero, P. & Senthil, T. Nearly flat Chern bands in moiré superlattices. *Physical Review B* **99**, 075127 (2019).

[42] Nam, N. N. T. & Koshino, M. Lattice relaxation and energy band modulation in twisted bilayer graphene. *Physical Review B* **96**, 075311 (2017).

[43] Yankowitz, M., Watanabe, K., Taniguchi, T., San-Jose, P. & LeRoy, B. J. Pressure-induced commensurate stacking of graphene on boron nitride. *Nature Communications* **7**, 13168 (2016).

[44] Mohammed, M. A. E., Gayani, N. P. & Shaffique, A. Analytical model for atomic relaxation in twisted moiré materials (2023). ArXiv:2401.00498.

[45] Koshino, M. & Nam, N. N. T. Effective continuum model for relaxed twisted bilayer graphene and moiré electron-phonon interaction. *Physical Review B* **101**, 195425 (2020).

[46] Zak, J. Magnetic Translation Group. *Physical Review* **134**, A1602–A1606 (1964).

[47] Hofstadter, D. R. Energy levels and wave functions of bloch electrons in rational and irrational magnetic fields. *Physical Review B* **14**, 2239 (1976).

[48] Barrier, J. *et al.* Long-range ballistic transport of Brown-Zak fermions in graphene superlattices. *Nature Communications* **11**, 5756 (2020).

[49] Stoner, E. C. Collective electron ferromagnetism. *Proceedings of the Royal Society* **165**, 372–414 (1938).

[50] Lu, X. *et al.* Superconductors, orbital magnets and correlated states in magic-angle bilayer graphene. *Nature* **574**, 653–657 (2019).

[51] Sharpe, A. L. *et al.* Emergent ferromagnetism near three-quarters filling in twisted bilayer graphene. *Science* **365**, 605–608 (2019).

[52] Serlin, M. *et al.* Intrinsic quantized anomalous Hall effect in a moiré heterostructure. *Science* **367**, 900–903 (2020).

[53] Nuckolls, K. P. *et al.* Quantum textures of the many-body wavefunctions in magic-angle graphene. *Nature* **620**, 525–532 (2023).

[54] Li, H. *et al.* Electrode-Free Anodic Oxidation Nanolithography of Low-Dimensional Materials. *Nano Letters* **18**, 8011–8015 (2018).

[55] Dean, C. R. *et al.* Boron nitride substrates for high-quality graphene electronics. *Nature Nanotechnology* **5**, 722–726 (2010).

[56] Choi, Y. *et al.* Electronic correlations in twisted bilayer graphene near the magic angle. *Nature Physics* **15**, 1174–1180 (2019).

[57] Girvin, S. & Yang, K. *Modern Condensed Matter Physics*, chap. 8, 164–197 (Cambridge University Press, Cambridge, UK, 2019).

[58] Chen, S. *et al.* Electrically tunable correlated and topological states in twisted monolayer–bilayer graphene. *Nature Physics* **17**, 374–380 (2021).

[59] Polshyn, H. *et al.* Electrical switching of magnetic order in an orbital Chern insulator. *Nature* **588**, 66–70 (2020).

[60] Xu, S. *et al.* Tunable van Hove singularities and correlated states in twisted monolayer–bilayer graphene. *Nature Physics* 1–8 (2021).

[61] He, M. *et al.* Competing correlated states and abundant orbital magnetism in twisted monolayer-bilayer graphene. *Nature Communications* **12**, 4727 (2021).

[62] Burg, G. W. *et al.* Correlated insulating states in twisted double bilayer graphene. *Physical Review Letters* **123**, 197702 (2019).

[63] Shen, C. *et al.* Correlated states in twisted double bilayer graphene. *Nature Physics* **16**, 520–525 (2020).

[64] Liu, X. *et al.* Tunable spin-polarized correlated states in twisted double bilayer graphene. *Nature* **583**, 221–225 (2020).

[65] Cao, Y. *et al.* Tunable correlated states and spin-polarized phases in twisted bilayer–bilayer graphene. *Nature* **583**, 215–220 (2020).

[66] He, M. *et al.* Symmetry breaking in twisted double bilayer graphene. *Nature Physics* **17**, 26–30 (2021).

[67] Kuiri, M. *et al.* Spontaneous time-reversal symmetry breaking in twisted double bilayer graphene. *Nature Communications* **13**, 6468 (2022).

[68] Liu, L. *et al.* Isospin competitions and valley polarized correlated insulators in twisted double bilayer graphene. *Nature Communications* **13**, 3292 (2022).

[69] Liu, L. *et al.* Observation of first-order quantum phase transitions and ferromagnetism in twisted double bilayer graphene. *Phys. Rev. X* **13**, 031015 (2023).

[70] Streda, P. Quantised Hall effect in a two-dimensional periodic potential. *Journal of Physics C: Solid State Physics* **15**, L1299 (1982).

[71] Saito, Y. *et al.* Hofstadter subband ferromagnetism and symmetry-broken Chern insulators in twisted bilayer graphene. *Nature Physics* **17**, 478–481 (2021).

[72] Yu, J. *et al.* Correlated Hofstadter spectrum and flavour phase diagram in magic-angle twisted bilayer graphene. *Nature Physics* **18**, 825–831 (2022).

[73] Shen, C. *et al.* Strongly correlated Hofstadter subbands in minimally twisted bilayer graphene. *Physical Review B* **110**, L161402 (2024).

[74] Tersoff, J. & Hamann, D. R. Theory of the scanning tunneling microscope. *Phys. Rev. B* **31**, 805–813 (1985).

[75] Li, G., Luican, A. & Andrei, E. Y. Self-navigation of a scanning tunneling microscope tip toward a micron-sized graphene sample. *Review of Scientific Instruments* **82**, 073701 (2011).

[76] Artaud, A. *et al.* Universal classification of twisted, strained and sheared graphene moiré superlattices. *Scientific Reports* **6**, 25670 (2016).

[77] Huder, L. *et al.* Electronic Spectrum of Twisted Graphene Layers under Heterostrain. *Physical Review Letters* **120**, 156405 (2018). URL `https://link.aps.org/doi/10.1103/PhysRevLett.120.156405`.

[78] Kerelsky, A. *et al.* Maximized electron interactions at the magic angle in twisted bilayer graphene. *Nature* **572**, 95–100 (2019).

[79] Duerloo, K.-A. N., Ong, M. T. & Reed, E. J. Intrinsic piezoelectricity in two-dimensional materials. *The Journal of Physical Chemistry Letters* **3**, 2871–2876 (2012).

[80] Mesple, F. *et al.* Heterostrain determines flat bands in magic-angle twisted graphene layers. *Phys. Rev. Lett.* **127**, 126405 (2021).

[81] Park, J. M., Cao, Y., Watanabe, K., Taniguchi, T. & Jarillo-Herrero, P. Tunable strongly coupled superconductivity in magic-angle twisted trilayer graphene. *Nature* **590**, 249–255 (2021).

[82] Hao, Z. *et al.* Electric field tunable superconductivity in alternating-twist magic-angle trilayer graphene. *Science* **371**, 1133–1138 (2021).

[83] Park, J. M. *et al.* Robust superconductivity in magic-angle multilayer graphene family. *Nature Materials* **21**, 877–883 (2022).

[84] Burg, G. W. *et al.* Emergence of correlations in alternating twist quadrilayer graphene. *Nature Materials* **21**, 884–889 (2022).

[85] Zhang, Y. *et al.* Promotion of superconductivity in magic-angle graphene multilayers. *Science* **377**, 1538–1543 (2022).

[86] Goodwin, Z. A. H. *et al.* Flat bands, electron interactions, and magnetic order in magic-angle mono-trilayer graphene. *Phys. Rev. Mater.* **5**, 084008 (2021).

[87] Fukui, T., Hatsugai, Y. & Suzuki, H. Chern numbers in discretized Brillouin zone: efficient method of computing (spin) Hall conductances. *J. Phys. Soc. Jpn.* **74**, 1674–1677 (2005).

[88] Zhou, H., Xie, T., Taniguchi, T., Watanabe, K. & Young, A. F. Superconductivity in rhombohedral trilayer graphene. *Nature* **598**, 434–438 (2021).

[89] He, M. *et al.* Symmetry-broken Chern insulators in twisted double bilayer graphene. *Nano Letters* **23**, 11066–11072 (2023).

[90] Ju, L. *et al.* Topological valley transport at bilayer graphene domain walls. *Nature* **520**, 650–655 (2015).

[91] Partoens, B. & Peeters, F. M. From graphene to graphite: Electronic structure around the k point. *Phys. Rev. B* **74**, 075404 (2006).

[92] Waters, D. *et al.* Mixed-dimensional moiré systems of twisted graphitic thin films. *Nature* **620**, 750–755 (2023).

[93] Ledwith, P. J., Khalaf, E. & Vishwanath, A. Strong coupling theory of magic-angle graphene: A pedagogical introduction. *Annals of Physics* **435**, 168646 (2021).

[94] Shi, Y. *et al.* Tunable Lifshitz transitions and multiband transport in tetralayer graphene. *Phys. Rev. Lett.* **120**, 096802 (2018).

[95] Martin, J., Feldman, B. E., Weitz, R. T., Allen, M. T. & Yacoby, A. Local compressibility measurements of correlated states in suspended bilayer graphene. *Phys. Rev. Lett.* **105**, 256806 (2010).

[96] Weitz, R. T., Allen, M. T., Feldman, B. E., Martin, J. & Yacoby, A. Broken-symmetry states in doubly gated suspended bilayer graphene. *Science* **330**, 812–816 (2010).

[97] Mayorov, A. S. *et al.* Interaction-driven spectrum reconstruction in bilayer graphene. *Science* **333**, 860–863 (2011).

[98] Velasco, J. *et al.* Transport spectroscopy of symmetry-broken insulating states in bilayer graphene. *Nature Nanotechnology* **7**, 156–160 (2012).

[99] Bao, W. *et al.* Stacking-dependent band gap and quantum transport in trilayer graphene. *Nature Physics* **7**, 948–952 (2011).

[100] Shi, Y. *et al.* Electronic phase separation in multilayer rhombohedral graphite. *Nature* **584**, 210–214 (2020).

[101] Liu, K. *et al.* Spontaneous broken-symmetry insulator and metals in tetralayer rhombohedral graphene. *Nature Nanotechnology* **19**, 188–195 (2024).

[102] Han, T. *et al.* Correlated insulator and Chern insulators in pentalayer rhombohedral-stacked graphene. *Nature Nanotechnology* **19**, 181–187 (2024).

[103] Grover, S. *et al.* Chern mosaic and Berry-curvature magnetism in magic-angle graphene. *Nature Physics* **18**, 885–892 (2022).

[104] Cai, J. *et al.* Signatures of fractional quantum anomalous Hall states in twisted $MoTe_2$. *Nature* **622**, 63–68 (2023).

[105] Park, H. *et al.* Observation of fractionally quantized anomalous Hall effect. *Nature* **622**, 74–79 (2023).

[106] Zeng, Y. *et al.* Thermodynamic evidence of fractional Chern insulator in moiré $MoTe_2$. *Nature* **622**, 69–73 (2023).

[107] Xu, F. *et al.* Observation of integer and fractional quantum anomalous hall effects in twisted bilayer mote_2. *Phys. Rev. X* **13**, 031037 (2023).

[108] Rickhaus, P. *et al.* Gap opening in twisted double bilayer graphene by crystal fields. *Nano Letters* **19**, 8821–8828 (2019).

[109] Cea, T., Walet, N. R. & Guinea, F. Twists and the electronic structure of graphitic materials. *Nano Letters* **19**, 8683–8689 (2019).

[110] Li, G. *et al.* Observation of van hove singularities in twisted graphene layers. *Nature Physics* **6**, 109–113 (2010).

[111] McGilly, L. J. *et al.* Visualization of moiré superlattices. *Nature Nanotechnology* **15**, 580–584 (2020).

[112] Soule, D. E. Magnetic field dependence of the hall effect and magnetoresistance in graphite single crystals. *Phys. Rev.* **112**, 698–707 (1958).

[113] Charlier, J.-C., Gonze, X. & Michenaud, J.-P. First-principles study of the electronic properties of graphite. *Physical Review B* **43**, 4579 (1991).

[114] Mañes, J. L., Guinea, F. & Vozmediano, M. A. H. Existence and topological stability of fermi points in multilayered graphene. *Phys. Rev. B* **75**, 155424 (2007).

[115] McClure, J. W. Analysis of multicarrier galvanomagnetic data for graphite. *Phys. Rev.* **112**, 715–721 (1958).

[116] Yin, J. *et al.* Dimensional reduction, quantum hall effect and layer parity in graphite films. *Nature Physics* **15**, 437–442 (2019).

[117] McClure, J. W. & Spry, W. J. Linear magnetoresistance in the quantum limit in graphite. *Phys. Rev.* **165**, 809–815 (1968).

[118] Brown, E. Bloch electrons in a uniform magnetic field. *Phys. Rev.* **133**, A1038–A1044 (1964).

[119] Hunt, B. *et al.* Massive dirac fermions and hofstadter butterfly in a van der waals heterostructure. *Science* **340**, 1427–1430 (2013).

[120] Ponomarenko, L. A. *et al.* Cloning of dirac fermions in graphene superlattices. *Nature* **497**, 594–597 (2013).

[121] Kumar, R. K. *et al.* High-temperature quantum oscillations caused by recurring bloch states in graphene superlattices. *Science* **357**, 181–184 (2017).

[122] Halbertal, D. *et al.* Multi-layered atomic relaxation in van der waals heterostructures. *arXiv:2206.06395* (2022).

[123] Zhou, H. *et al.* Isospin magnetism and spin-polarized superconductivity in bernal bilayer graphene. *Science* **375**, 774–778 (2022).

[124] Wang, L. *et al.* Correlated electronic phases in twisted bilayer transition metal dichalcogenides. *Nature Materials* **19**, 861–866 (2020).

[125] Waters, D. *et al.* Flat Bands and Mechanical Deformation Effects in the Moiré Superlattice of MoS_2-WSe_2 Heterobilayers. *ACS Nano* **14**, 7564–7573 (2020).

[126] Regan, E. C. *et al.* Mott and generalized Wigner crystal states in WSe_2/WS_2 moiré superlattices. *Nature* **579**, 359–363 (2020).

[127] Zhang, Z. *et al.* Flat bands in twisted bilayer transition metal dichalcogenides. *Nature Physics* **16**, 1093–1096 (2020).

[128] Li, H. *et al.* Imaging moiré flat bands in three-dimensional reconstructed WSe_2/WS_2 superlattices. *Nature Materials* **20**, 945–950 (2021).

[129] Ghiotto, A. *et al.* Quantum criticality in twisted transition metal dichalcogenides. *Nature* **597**, 345–349 (2021).

[130] Huang, X. *et al.* Correlated insulating states at fractional fillings of the WS_2/WSe_2 moiré lattice. *Nature Physics* **17**, 715–719 (2021).

[131] Anderson, E. *et al.* Programming correlated magnetic states via gate controlled moiré geometry. *Science* **381**, 325–330 (2023).

[132] Kang, K. *et al.* Evidence of the fractional quantum spin Hall effect in moiré $MoTe_2$. *Nature* **628**, 522–526 (2024).

[133] Park, H. *et al.* Ferromagnetism and topology of the higher flat band in a fractional chern insulator (2024). ArXiv:2406.09591.

[134] Xu, F. *et al.* Interplay between topology and correlations in the second moiré band of twisted bilayer mote2 (2024). ArXiv:2406.09687.

[135] Foutty, B. A. *et al.* Mapping twist-tuned multi-band topology in bilayer WSe_2. *Science* **384**, 343–347 (2024).

[136] Li, H. *et al.* Imaging two-dimensional generalized Wigner crystals. *Nature* **597**, 650–654 (2021).

[137] Li, H. *et al.* Mapping charge excitations in generalized Wigner crystals. *Nature Nanotechnology* (2024).

[138] Redekop, E. *et al.* Direct magnetic imaging of fractional chern insulators in twisted $MoTe_2$ with a superconducting sensor (2024). ArXiv:2405.10269.

[139] Ji, Z. *et al.* Local probe of bulk and edge states in a fractional chern insulator (2024). ArXiv:2404.07157.

[140] Zhang, X.-W. *et al.* Polarization-driven band topology evolution in twisted $MoTe_2$ and WSe_2. *Nature Communications* **15**, 4223 (2024).

[141] Wu, F., Lovorn, T., Tutuc, E., Martin, I. & MacDonald, A. H. Topological insulators in twisted transition metal dichalcogenide homobilayers. *Phys. Rev. Lett.* **122**, 086402 (2019).

[142] Yu, H., Chen, M. & Yao, W. Giant magnetic field from moiré induced Berry phase in homobilayer semiconductors. *National Science Review* **7**, 12–20 (2020).

[143] Wang, X. *et al.* Interfacial ferroelectricity in rhombohedral-stacked bilayer transition metal dichalcogenides. *Nature Nanotechnology* **17**, 367–371 (2022).

[144] Molino, L. *et al.* Ferroelectric Switching at Symmetry-Broken Interfaces by Local Control of Dislocations Networks. *Advanced Materials* **35** (2023).

[145] Zhang, S. *et al.* Visualizing moiré ferroelectricity via plasmons and nano-photocurrent in graphene/twisted-WSe_2 structures. *Nature Communications* **14**, 6200 (2023).

[146] Mao, N. *et al.* Transfer learning relaxation, electronic structure and continuum model for twisted bilayer MoTe2. *Communications Physics* **7**, 1–7 (2024). URL `https://www.nature.com/articles/s42005-024-01754-y`. Publisher: Nature Publishing Group.

[147] Zhang, C. *et al.* Probing critical point energies of transition metal dichalcogenides: surprising indirect gap of single layer WSe_2. *Nano Letters* **15**, 6494–6500 (2015).

[148] Pan, Y. *et al.* Quantum-confined electronic states arising from moiré pattern of MoS_2-WSe_2 heterobilayers. *Nano Letters* **18**, 1849–1855 (2018).

[149] Tilak, N., Li, G., Taniguchi, T., Watanabe, K. & Andrei, E. Y. Moiré potential, lattice relaxation, and layer polarization in marginally twisted MoS_2 bilayers. *Nano Letters* **23**, 73–81 (2023).

[150] Zhang, L., Han, J., Wang, H., Car, R. & Weinan, E. Deep potential molecular dynamics: a scalable model with the accuracy of quantum mechanics. *Physical review letters* **120**, 143001 (2018).

[151] Wang, H., Zhang, L., Han, J. & Weinan, E. Deepmd-kit: A deep learning package for many-body potential energy representation and molecular dynamics. *Computer Physics Communications* **228**, 178–184 (2018).

[152] Kresse, G. & Furthmüller, J. Efficiency of ab-initio total energy calculations for metals and semiconductors using a plane-wave basis set. *Computational materials science* **6**, 15–50 (1996).

[153] Grimme, S. Semiempirical gga-type density functional constructed with a long-range dispersion correction. *Journal of computational chemistry* **27**, 1787–1799 (2006).

[154] Thompson, A. P. *et al.* Lammps-a flexible simulation tool for particle-based materials modeling at the atomic, meso, and continuum scales. *Computer Physics Communications* **271**, 108171 (2022).

[155] Soler, J. M. *et al.* The siesta method for ab initio order-n materials simulation. *Journal of Physics: Condensed Matter* **14**, 2745 (2002).

[156] Hamann, D. Optimized norm-conserving vanderbilt pseudopotentials. *Physical Review B* **88**, 085117 (2013).

[157] Perdew, J. P., Burke, K. & Ernzerhof, M. Generalized gradient approximation made simple. *Physical review letters* **77**, 3865 (1996).

[158] Edelberg, D. *et al.* Approaching the intrinsic limit in transition metal diselenides via point defect control. *Nano Letters* **19**, 4371–4379 (2019).

[159] Zhao, W. *et al.* Direct measurement of the electronic structure and band gap nature of atomic-layer-thick 2H-$MoTe_2$ (2020). ArXiv:2001.05894.

[160] Liu, G.-B., Shan, W.-Y., Yao, Y., Yao, W. & Xiao, D. Three-band tight-binding model for monolayers of group-vib transition metal dichalcogenides. *Phys. Rev. B* **88**, 085433 (2013).

[161] Li, G., Luican, A. & Andrei, E. Y. Scanning tunneling spectroscopy of graphene on graphite. *Phys. Rev. Lett.* **102**, 176804 (2009).

[162] Hasan, M. Z. & Kane, C. L. *Colloquium* : Topological insulators. *Reviews of Modern Physics* **82**, 3045–3067 (2010).

[163] Nagaosa, N. & Tokura, Y. Topological properties and dynamics of magnetic skyrmions. *Nature Nanotechnology* **8**, 899–911 (2013).

[164] Aftab, S. *et al.* Carrier polarity modulation of molybdenum ditelluride (mote2) for phototransistor and switching photodiode applications. *Nanoscale* **12**, 15687–15696 (2020).

[165] Mleczko, M. J. *et al.* Contact engineering high-performance n-type mote2 transistors. *Nano Letters* **19**, 6352–6362 (2019). PMID: 31314531.

[166] Yu, Y.-J. *et al.* Tuning the graphene work function by electric field effect. *Nano Letters* **9**, 3430–3434 (2009).

[167] Wang, T. *et al.* Topology, magnetism and charge order in twisted mote2 at higher integer hole fillings (2023). URL `http://arxiv.org/abs/2312.12531`. ArXiv:2312.12531.

[168] Wang, C. *et al.* Fractional Chern Insulator in Twisted Bilayer $\mathrm{MoTe_2}$. *Phys. Rev. Lett.* **132**, 036501 (2024).

[169] Jia, Y. *et al.* Moiré fractional chern insulators I: first-principles calculations and continuum models of twisted bilayer $MoTe_2$. *Phys. Rev. B* **109**, 205121 (2024).

[170] Ahn, C.-E., Lee, W., Yananose, K., Kim, Y. & Cho, G. Y. First Landau level physics in second moiré band of 2.1° twisted bilayer $MoTe_2$ (2024). ArXiv:2403.19155 [cond-mat].

[171] Xu, C., Mao, N., Zeng, T. & Zhang, Y. Multiple chern bands in twisted MoTe$_2$ and possible non-abelian states (2024). URL `http://arxiv.org/abs/2403.17003`. ArXiv:2403.17003.

[172] Liu, Z. *et al.* Continuously tunable uniaxial strain control of van der Waals heterostructure devices (2024). ArXiv:2404.00905 [cond-mat].

[173] Pack, J. *et al.* Charge-transfer contacts for the measurement of correlated states in high-mobility WSe2. *Nature Nanotechnology* **19**, 948–954 (2024).

[174] Zhang, C. *et al.* Local spectroscopy of a gate-switchable moiré quantum anomalous Hall insulator. *Nature Communications* **14**, 3595 (2023).

[175] Chiu, C.-L. *et al.* High spatial resolution charge sensing of quantum Hall states. *Proceedings of the National Academy of Sciences* **122**, e2424781122 (2025).

[176] Su, R. *et al.* Moiré-driven topological electronic crystals in twisted graphene. *Nature* **637**, 1084–1089 (2025).

[177] Su, R., Kuiri, M., Watanabe, K., Taniguchi, T. & Folk, J. Superconductivity in twisted double bilayer graphene stabilized by WSe2. *Nature Materials* **22**, 1332–1337 (2023).

[178] Lu, Z. *et al.* Fractional quantum anomalous Hall effect in multilayer graphene. *Nature* **626**, 759–764 (2024).

[179] Choi, Y. *et al.* Superconductivity and quantized anomalous Hall effect in rhombohedral graphene. *Nature* **639**, 342–347 (2025).

[180] Waters, D. *et al.* Chern Insulators at Integer and Fractional Filling in Moir\'e Pentalayer Graphene. *Physical Review X* **15**, 011045 (2025).

[181] Han, T. *et al.* Signatures of chiral superconductivity in rhombohedral graphene. *Nature* **643**, 654–661 (2025).

[182] Zhang, F. *et al.* Experimental signature of layer skyrmions and implications for band topology in twisted WSe2 bilayers. *Nature Physics* **21**, 1217–1223 (2025).

[183] Pack, J. *et al.* Sliding Disassembly of van der Waals Heterostructures (2025). ArXiv:2510.19064 [cond-mat].

[184] Lüpke, F. *et al.* Quantum Spin Hall Edge States and Interlayer Coupling in Twisted Bilayer WTe2. *Nano Letters* **22**, 5674–5680 (2022).

[185] Wang, P. *et al.* One-dimensional Luttinger liquids in a two-dimensional moiré lattice. *Nature* **605**, 57–62 (2022).

[186] Yu, G. *et al.* Evidence for two dimensional anisotropic Luttinger liquids at millikelvin temperatures. *Nature Communications* **14**, 7025 (2023).

[187] Călugăru, D. *et al.* Moiré materials based on M-point twisting. *Nature* **643**, 376–381 (2025).

[188] Olin, S., Jmukhadze, E., MacDonald, A. H. & Lee, W.-C. Ab-initio study of the energy competition between Γ and K valleys in bilayer transition metal dichalcogenides (2023). ArXiv:2310.17824 [cond-mat].

[189] Brzezińska, M., Grytsiuk, S., Rösner, M., Gibertini, M. & Rademaker, L. Pressure-tuned many-body phases through Γ-K valleytronics in moiré bilayer WSe_2 (2024). ArXiv:2404.07165 [cond-mat].

Appendix A

SUPPLEMENTARY DATA FOR CHAPTER 3

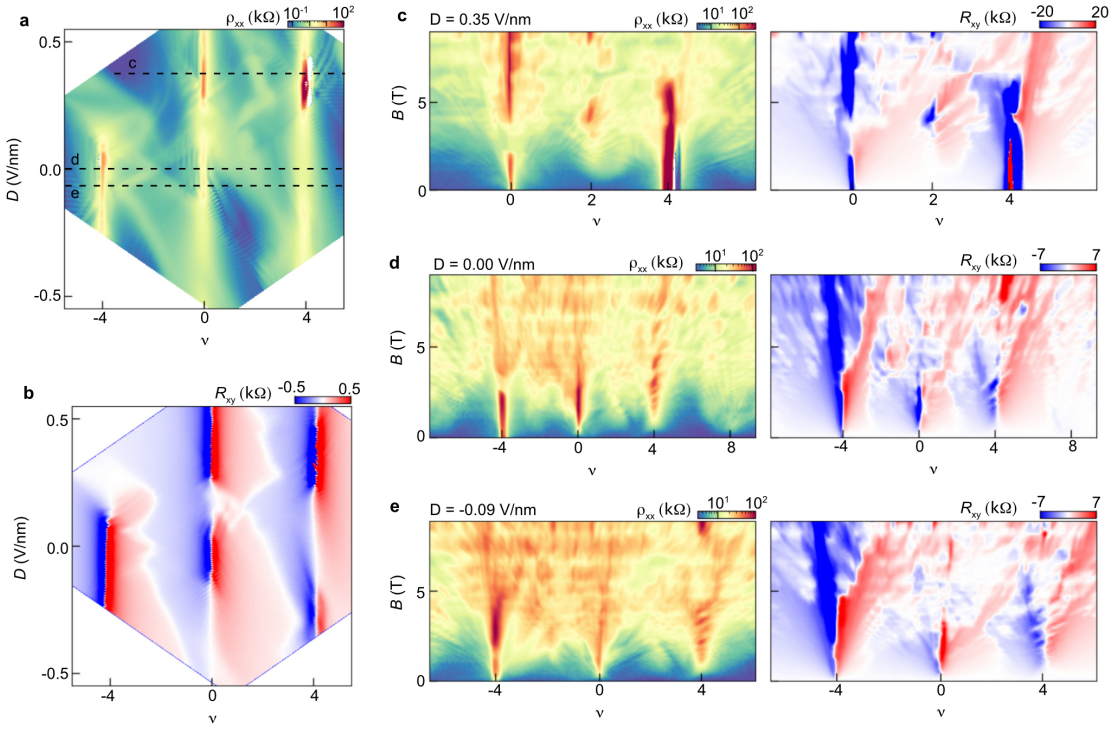

Figure A.1: **Additional Data for t2 + 4 a**, Longitudinal and **b,** Hall resistance maps in the t2+4 device $\theta = 1.42°$. The longitudinal (Hall) maps are symmetrized (anti-symmetrized) at $B = 0.5$ T. **c-e**, Landau fan diagrams acquired at fixed displacement fields of **(c)** $D = 0.35$ V/nm, **(d)** $D = 0$, and **(e)** $D = -0.09$ V/nm. All measurements in figure were acquired at $T = 100$ mK.

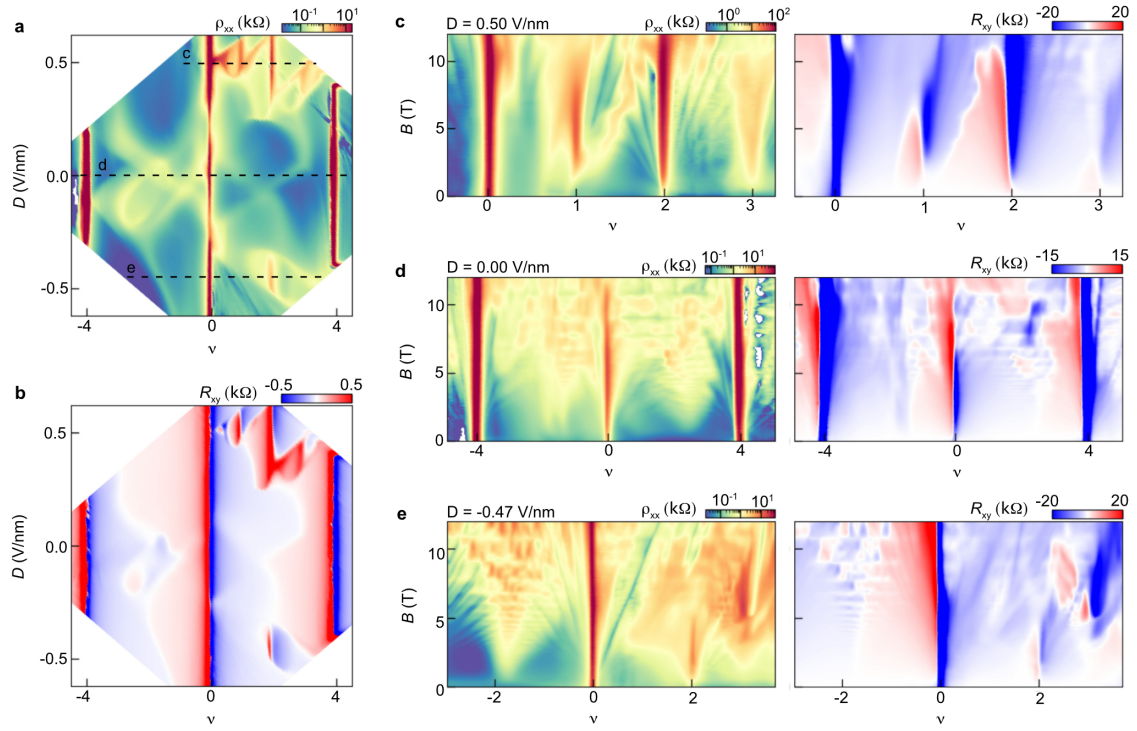

Figure A.2: **Additional Data for t2 + 3**, **a**, Longitudinal and **b,** Hall resistance maps in the t2+3 device with $\theta = 1.50°$. The longitudinal (Hall) maps are symmetrized (anti-symmetrized) at $B = 0.1$ T. **c-e**, Landau fan diagrams acquired at fixed displacement fields of **(c)** $D = 0.50$ V/nm, **d** $D = 0$, and **e** $D = -0.47$ V/nm. All measurements in figure were acquired at $T = 1.5$ K.

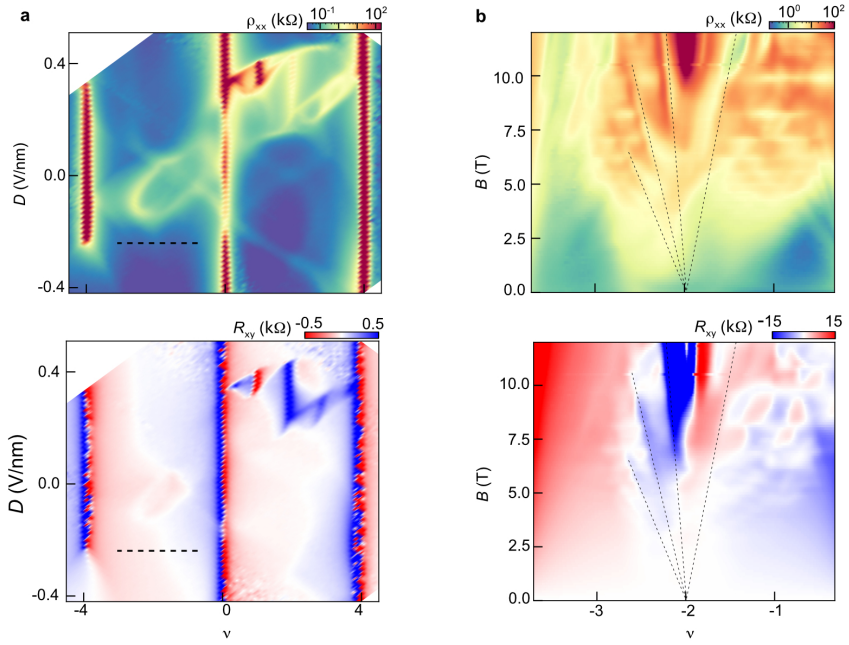

Figure A.3: **Correlated states at high field in a t2+3 device with $\theta = 1.41°$, a**, ρ_{xx} (top) and R_{xy} (bottom) maps. The longitudinal (Hall) maps are symmetrized (anti-symmetrized) at $B = 0.1$ T **b**, Landau fans acquired at $D = -0.25$ V/nm over the doping range indicated by dashed line in **a**. The data shows clear quantum oscillations projecting to $\nu = -2$ at $B = 0$, associated with a high-resistance state accompanied by an abrupt sign reversal in R_{xy} above $B \approx 10$ T. Together, these observations indicate the emergence of a symmetry-broken state at $\nu = 2$ in a magnetic field. All measurements were acquired at $T = 1.5$ K.

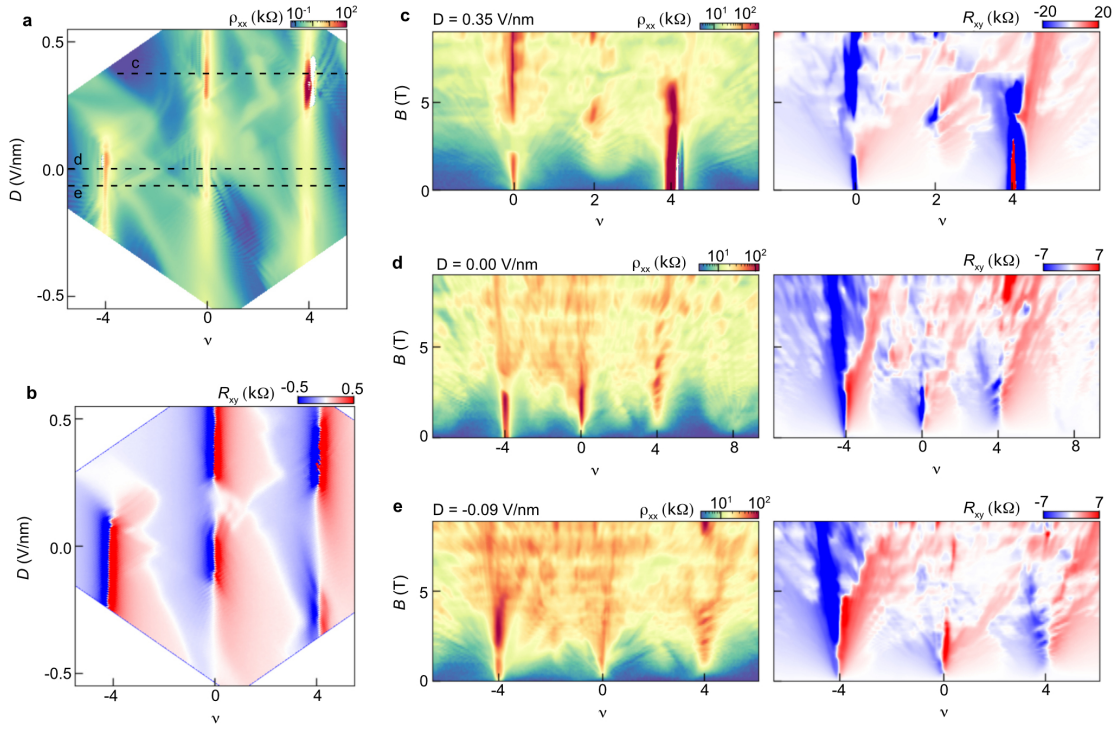

Figure A.4: **Additional Data for t1 + 3**, **a,** Longitudinal and **b,** Hall resistance maps in the t1+3 device. The longitudinal (Hall) maps are symmetrized (anti-symmetrized) at $B = 0.5$ T. **c-e,** Longitudinal and Hall resistances as a function of B at fixed displacement field of **c** $D = 0.67$ V/nm, **d** $D = 0.56$ V/nm, **e** $D = -0.00$ V/nm. All measurements in figure were acquired at $T = 1.5$ K.

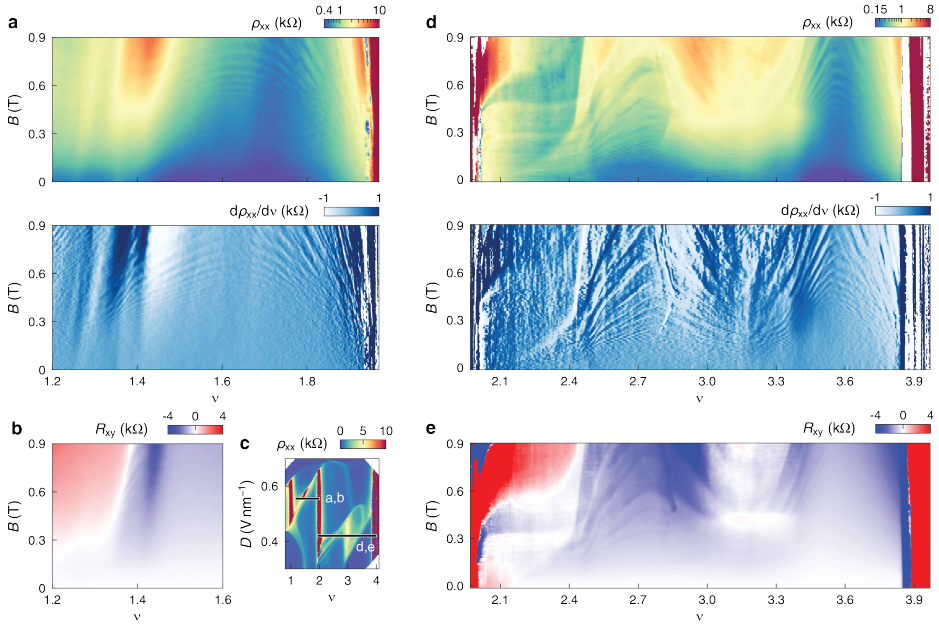

Figure A.5: **Signatures of multiband transport in the t2+3 device with $\theta = 1.50°$. a**, Longitudinal resistance and its numerical derivative obtained between $\nu = 1$ and 2, highlighting the evolution of curved quantum Hall states developing at low-B. **b**, Hall resistance as a function of B. **c**, Zoomed-in view of the phase diagram shown in the main text for reference. Horizontal lines indicate the displacement fields $D = 0.555$ V/nm and $D = 0.450$ V/nm where panels (**a**,**b**) and (**d**,**e**) were respectively obtained. **d**, **e**, Longitudinal and Hall resistance obtained near $\nu = 3$. Measurements were obtained at the base mixing chamber temperature of $T = 10$ mK.

Appendix B

REPRESENTATIVE LANDAU FAN FITTING RESULTS FOR T1+Z DEVICES

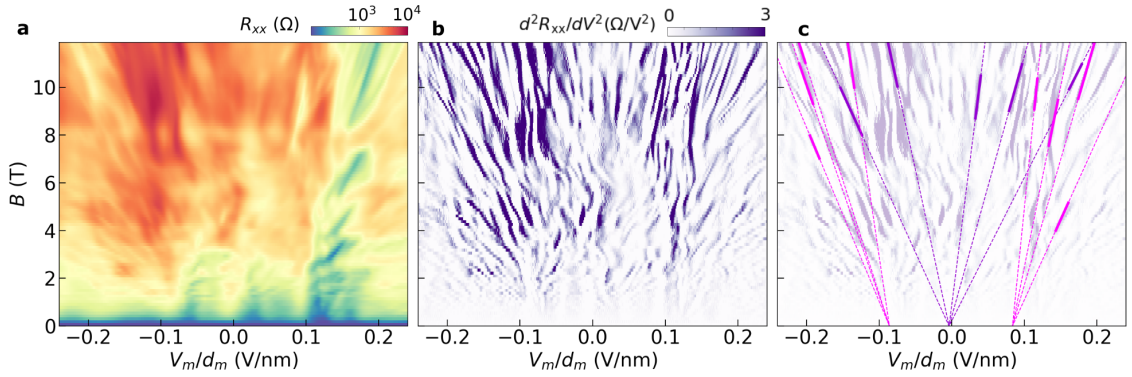

Figure B.1: **Representative constrained fit results for Landau fans acquired by sweeping V_m in the t1+10 device.** **a**, Landau fan diagram of R_{xx} in the t1+10 device, acquired by sweeping V_m with $V_{gr}/d_{gr} = 0.01$ V/nm. **b**, Numerical second derivative of the data in **a**. The color scale is saturated to only show positive values, as in figure 4.14. **c**, Results of the constrained fit overlaid on the second derivative data from **b**, with reduced opacity for clarity. Solid segments denote the range of magnetic field over which the QOs were fit, and the dashed segments denote the projection over the entire range of magnetic field.

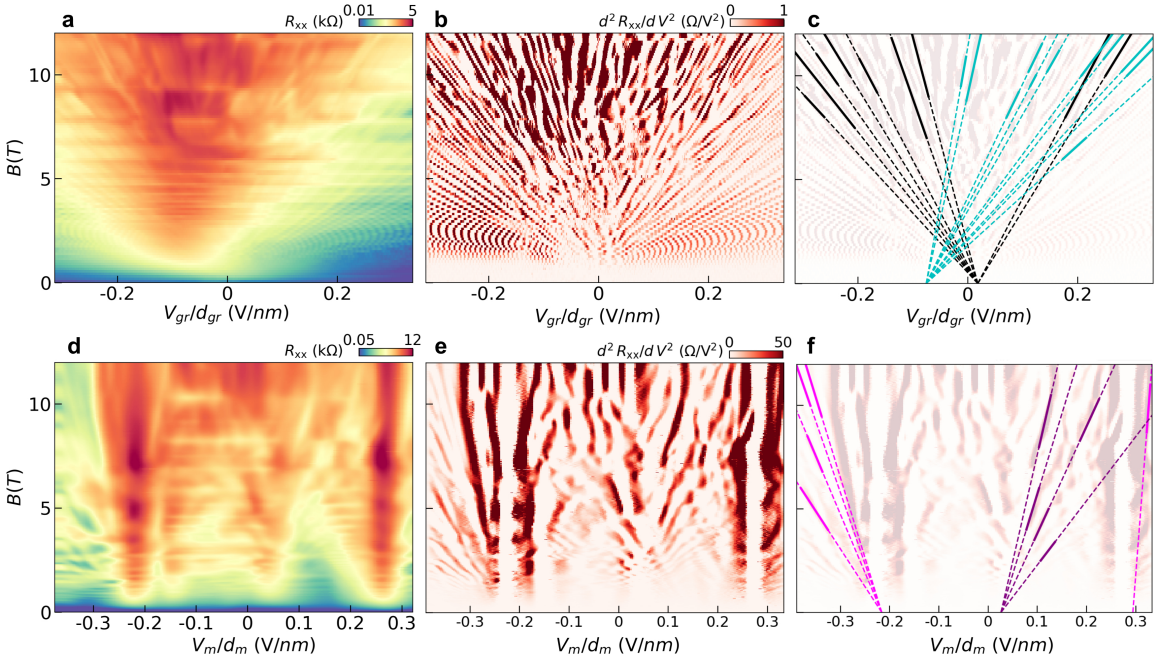

Figure B.2: **Representative constrained fit results for the t1+17 device.** Same plots as in figure B.1, but for the t1+17 device. **a-c**, Landau fan acquired by sweeping V_{gr} with $V_m/d_m = 0.14$ V/nm, and associated QO fits. **d-e**, Landau fan acquired by sweeping V_m with $V_{gr}/d_{gr} = 0$, and associated QO fits.

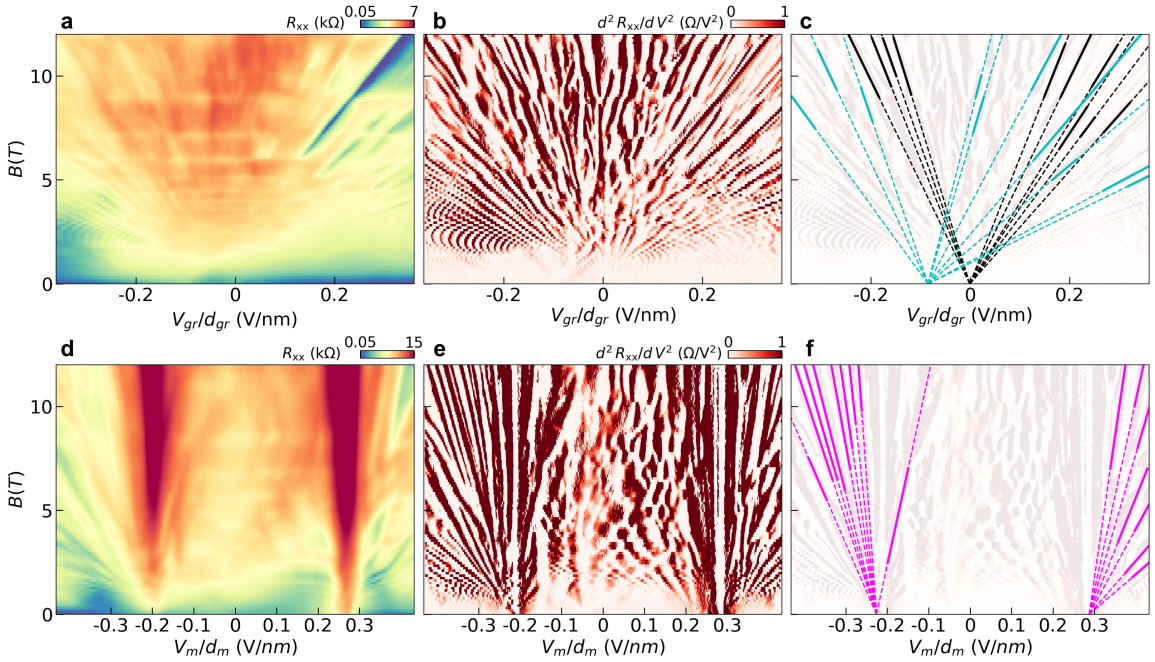

Figure B.3: **Representative constrained fit results for t1+6 device.** Same plots as in figure B.1, but for the t1+6 device. **a-c**, Landau fan acquired by sweeping V_{gr} with $V_m/d_m = 0.09$ V/nm, and associated QO fits. **d-e**, Landau fan acquired by sweeping V_m with $V_{gr}/d_{gr} = -0.02$ V/nm, and associated QO fits.

Appendix C

SUPPLEMENTARY DATA CHAPTER 4

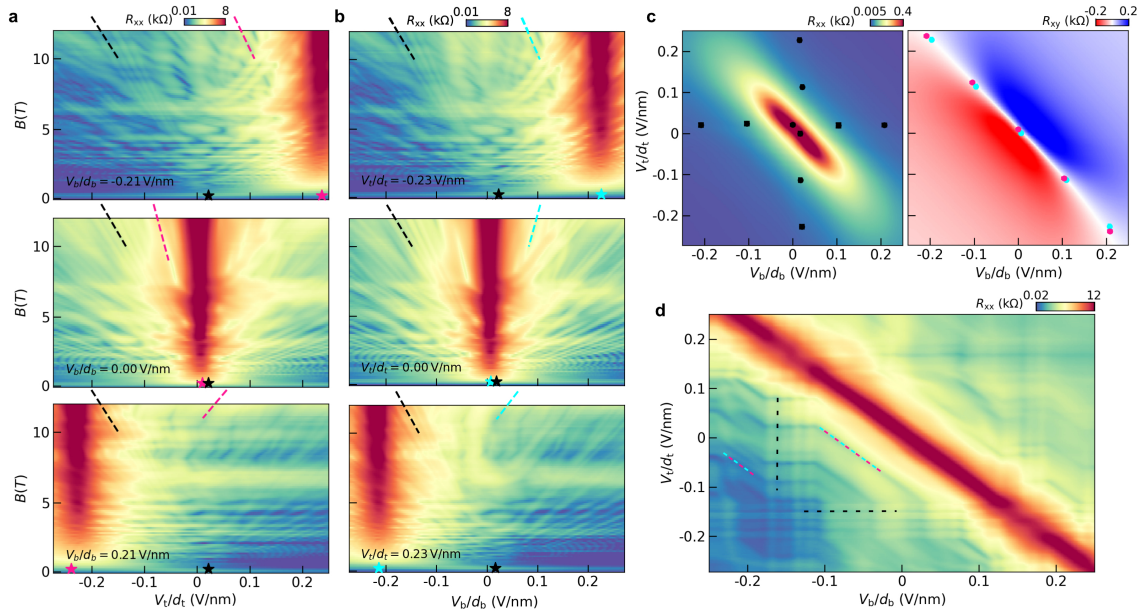

Figure C.1: **High-field transport in Bernal graphite.** **a**, Landau fan diagrams from a 24-layer graphite device (different from the one shown in the main text) acquired by sweeping the top gate voltage, V_t, at various fixed values of the bottom gate voltage, V_b, as indicated in each panel. The black dashed lines denote selected QOs that project to $V_t \approx 0$ at $B = 0$, and the pink lines denote QOs that project to a $V_t \neq 0$ that depends on the value of V_b. **b**, Similar Landau fans, but with fixed V_t and sweeping V_b. The QOs projecting to $V_b \neq 0$ are denoted in blue. **c**, Longitudinal (left) and Hall (right) resistance maps acquired at $B = 0.5$ T. The QOs projecting to approximately zero gate voltage in each Landau fan, corresponding to surface-localized states, are overlaid on the R_{xx} map and form a cross. The QOs projecting to non-zero gate voltages, corresponding to extended bulk states, are overlaid on the R_{xy} map and closely track the condition of overall charge neutrality. **d**, R_{xx} map acquired at $B = 12$ T. Dashed black lines denote selected QOs that depend only on a single gate, which arise from localized states on either the top or bottom graphite surfaces. The blue/pink dashed lines denote QOs that depend on both gates, which evolve parallel to the line of overall charge neutrality, arising from the extended bulk states.

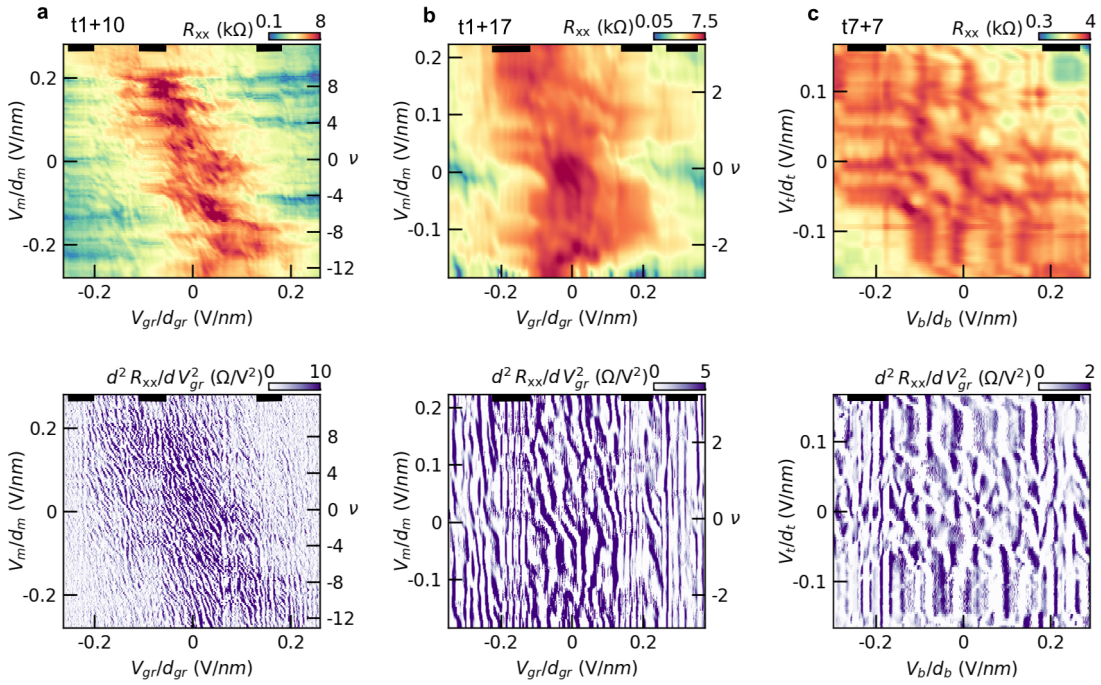

Figure C.2: **High field dual-gate maps for the t1+10, t1+17, and t7+7 devices. a-c**, Dual-gate R_{xx} maps (top) and corresponding numerical second derivative (bottom) acquired for the (**a**) t1+10 device at $B = 9$ T, (**b**) t1+17 device at $B = 12$ T, and (**c**) t7+7 device at $B = 12$ T. Solid black bars at the top of each map denote regions of gate voltage dominated by vertical QOs, which correspond to surface-localized states. Other regions, though more complicated, contain diagonal QOs which depend on the value of both gate voltages. These features correspond to extended bulk standing wave states. Data in panel **a** was acquired in a dilution refrigerator with a nominal base temperature of $T \approx 20$ mK, all other data was acquired at 1.7 K.

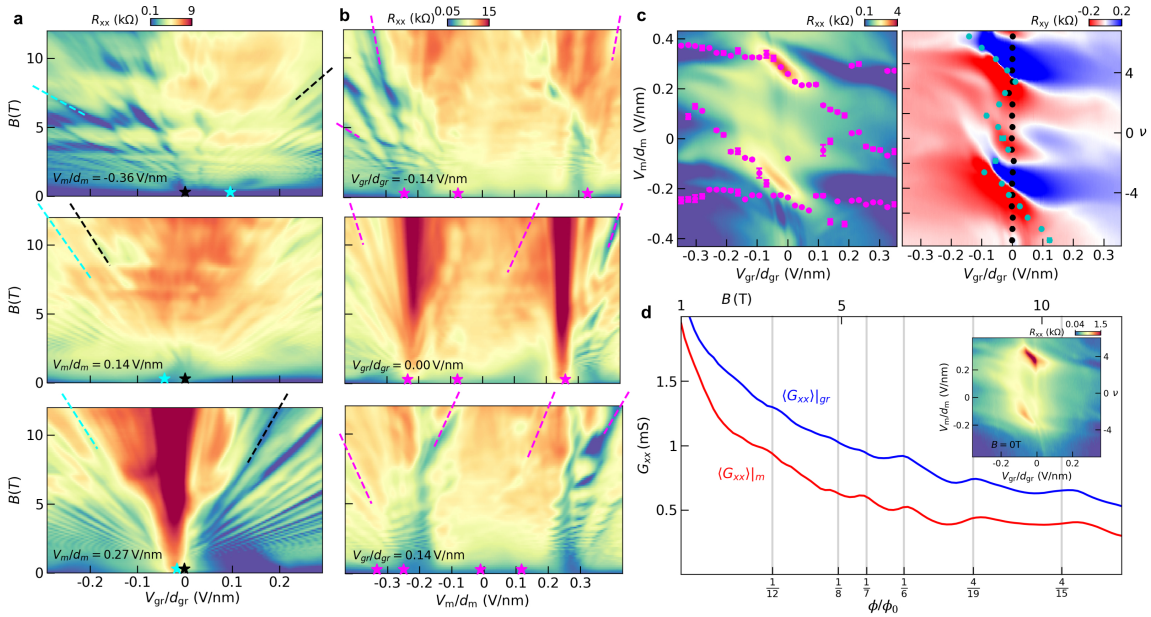

Figure C.3: **High-field transport in a t1+6 device with $\theta = 1.27°$. a**, Landau fan diagrams acquired by sweeping V_{gr} at various fixed values of V_m. The black dashed lines denote selected QOs that project to $V_{gr} \approx 0$ at $B = 0$. The blue lines denote selected QOs that project to a $V_{gr} \neq 0$ that depends on V_m. **b**, Landau fan diagrams acquired by sweeping V_m at fixed values of V_{gr}. The pink dashed lines denote selected QOs from each of the distinct sequences we observe. **c**, Longitudinal (left) and Hall (right) resistance maps acquired at $B = 0.5$ T. Zero-field projections of all observed sequences of QOs from the V_m Landau fans are overlaid on the R_{xx} map. Zero-field projections of QOs from the V_{gr} Landau fans are overlaid on the R_{xy} map. We note that, in this device, the observed sequence of QOs in the V_m Landau fans is very complex, and there is not always a clear delineation between QO sequences arising from neutrality ($\nu = 0$) and full filling ($\nu = \pm 4$) of the moiré bands. This may be a consequence of the relatively thin nature of the sample, which exhibits features of both atomically-thin graphene and bulk graphite. **d**, Conductance, G_{xx}, as a function of magnetic field. The blue curve is averaged over all values of V_{gr} for the Landau fan acquired at $V_m/d_m = -0.05\,\mathrm{V/nm}$. The red curve is averaged over a range of V_m values corresponding to $|\nu| < 4$ for the Landau fan in **b** acquired at $V_{gr} = 0$. Brown-Zak oscillations case be seen upon sweeping either gate. (Inset) Longitudinal resistance map acquired at $B = 0$ T.

Appendix D

ADDITIONAL SEQUENCES OF QUANTUM OSCILLATIONS IN T1+Z DEVICES

In the main text, we have identified two primary sequences of QOs from the Landau fans acquired by sweeping V_{gr} at various fixed values of V_m. Each of these two sequences comprises many individual QOs that all project to the same V_{gr} at $B = 0$. However, in the t1+10 and t1+17 devices, we have additionally found that there are one or more extra sequences comprising just a small number of individual QOs. Figure D.1a-c (e-g) shows an example of these states from the t1+10 (t1+17) device. Figures D.1d and h summarize all of the additional QO sequences we see in these devices. For each data point, we require that there are at least three clear and distinct QOs that project to the same value of V_{gr}.

We do not understand the origin of these features. They may arise owing to Hofstadter states that penetrate deep into the graphite bulk from the opposite moiré surface. Although some of these projection points are close to $|\nu| = 4$, most are not. In principle, any integer value of $|\nu|$ is viable within the Hofstadter butterfly, though $\nu = 1$, 2, or 3 additionally require a broken symmetry. For now, we leave a full understanding of these additional states to future work. We stress, however, that these states are vastly outnumbered by those from the primary two sequences of QOs analyzed in the main text.

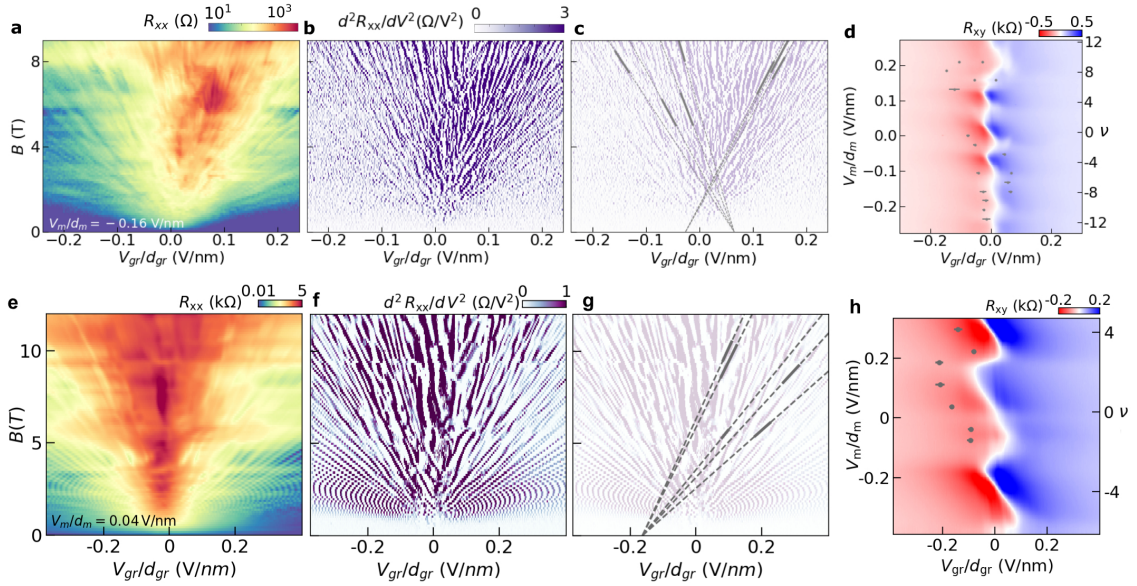

Figure D.1: **Additional sequences of quantum oscillations in the t1+10 and t1+17 devices.** **a**, Representative Landau fan diagram of R_{xx} in the t1+10 device, acquired by sweeping V_{gr} with $V_m/d_m = -0.16$ V/nm. **b**, Numerical second derivative of the data in **a**. The color range is saturated to only show positive values. **c**, Results of the constrained fit overlaid on the second derivative data from **b**, with reduced opacity for clarity. The solid segments denote the range of magnetic field over which the selected QOs were fit, and the dashed segments denote the projection over the entire range of magnetic field. **d**, Zero-field projections of the additional QO sequences plotted on the Hall resistance map. Only sequences that were not fit in the main text are shown here. **e-h**, Similar plots for the $t1 + 17$ device.

Appendix E

TWIST ANGLE DEPENDENCE OF WAVEFUNCTION LOCALIZATION IN TMOTE$_2$

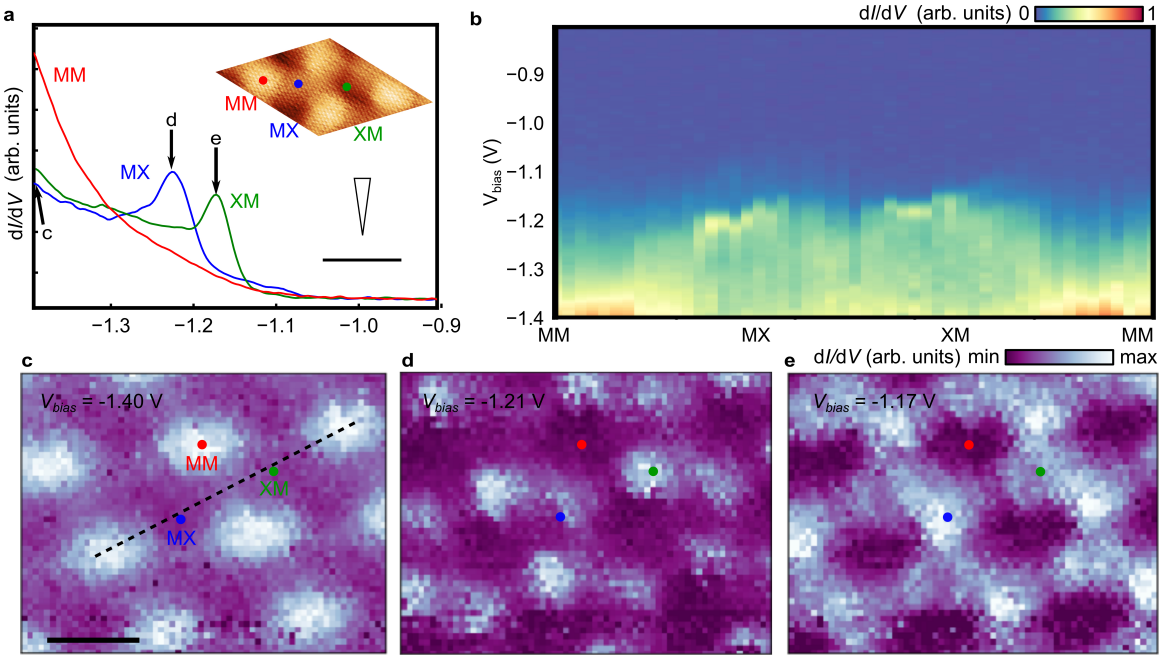

Figure E.1: **Localization of Γ-point states for tMoTe$_2$ with $\theta = 3.52°$.** **a**, Averaged constant-height dI/dV spectra at MM, MX, and XM (4x4 pixels, 1.24 nm^2). The insets show a sketch of the measurement technique and the STM topograph of the region, with $\varepsilon_{uni} = 1.90\%$, and $\varepsilon_{bi} = 0.24\%$, oriented at $-21°$ with respect to the . The tunneling parameters are $(I_t, V_{bias}) = (140\ \text{pA}, -2.5\ \text{V})$. **b**, Line cut of constant-height dI/dV spectra acquired along the dashed path shown in **c**. **c-e**, dI/dV maps acquired at different V_{bias}, as indicated by the arrows in **a**. All maps are assembled from a grid spectroscopy measurement with initial tunneling setpoint $(I_t, V_{bias}) = (200\ \text{pA}, -1.4\ \text{V})$. The scale bar is 5 nm.

We have measured the localization of Γ-point states using constant-height spectroscopy at several regions of tMoTe$_2$ with varying twist angle and uniaxial strain, ε_{uni}, which both modify the local atomic stacking arrangements within the moiré lattice. We find that that the dI/dV peak from the edge of the Γ-point bands is always localized on the XM and MX regions. We additionally find that this localization pattern often breaks C_{2x} symmetry, such that the amplitude and bias of the dI/dV peak differ between the XM and MX regions. The magnitude of this symmetry breaking varies widely for different stacking configurations. This is weakly visible in the region with $\theta = 2.75°$ in figure 5.8 of the main text, where the

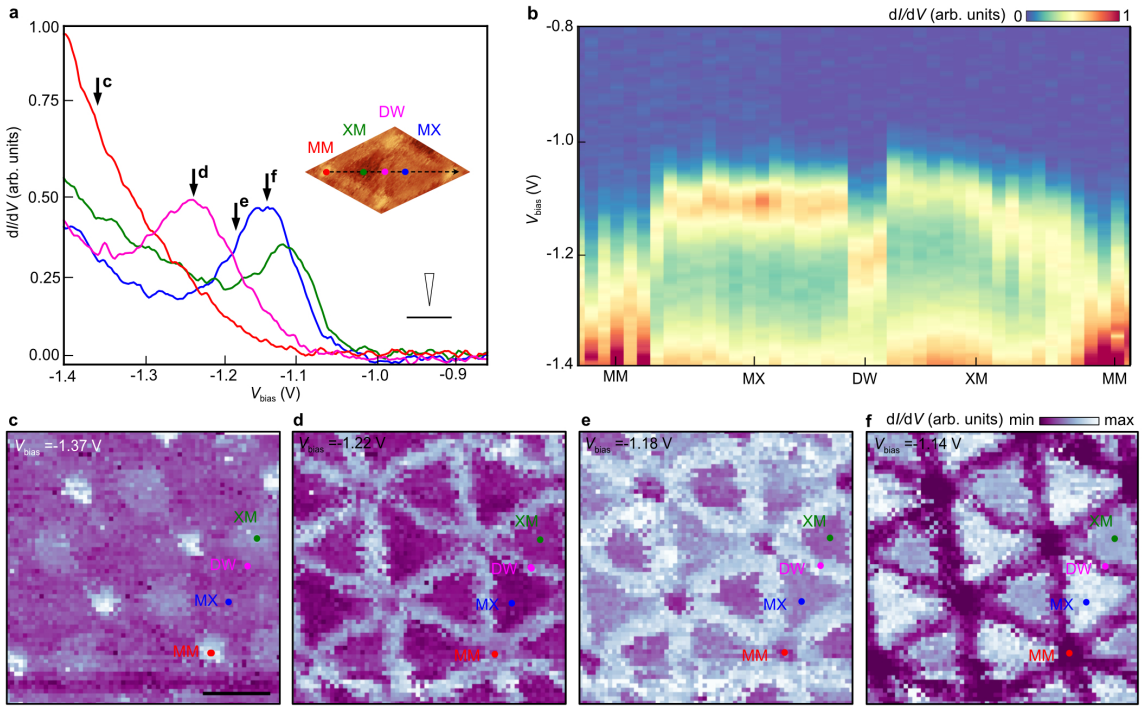

Figure E.2: **Localization of Γ-point states for tMoTe$_2$ with $\theta = 1.20°$.** **a**, Constant-height dI/dV spectra at various points within the moiré unit cell, acquired at the same region as figure 5.3e. Insets show a sketch of the measurement technique and a representative STM topograph of the region. **b**, Line cut of constant-height dI/dV spectra acquired along the dashed path shown in the inset of **a**. **c-f**, dI/dV maps acquired at different V_{bias}, as indicated by the arrows in **a**. All maps are assembled from a grid spectroscopy measurement with initial tunneling setpoint $(I_t, V_b) = (200$ pA, -1.4 V$)$. The scale bar is 16 nm.

Γ-peak at XM has a slightly larger amplitude than at MX. In contrast, the region with $\theta = 3.48°$ shown in figure E.1 features a larger Γ peak on MX. In addition, the two peaks are split in bias by ≈ 50 mV in this region.

We also observe complex spatial localization structures of the Γ-point feature within the MX and XM regions, visible in the localization patterns at intermediate energies shown in figure 5.8c of the main text. This is further exemplified by measurements of a region with very large strain, figure E.5a, with stacking arrangement $\theta = 3.47°$, $\varepsilon_{uni} = 3.24\%$ and $\varepsilon_{bi} = -0.73\%$. In this case, the Γ-point states in the MX and XM region appear as shoulder-like rather than as peaks in dI/dV, and differ both in energy and amplitude between the sites (similar to the data shown in figure E.1). figure E.5b shows a line cut of constant height spectra along a path that crosses the MM, MX, and XM regions, indicated by the black dashed line in the inset of panel a. This map shows that the Γ-point states shift rapidly in

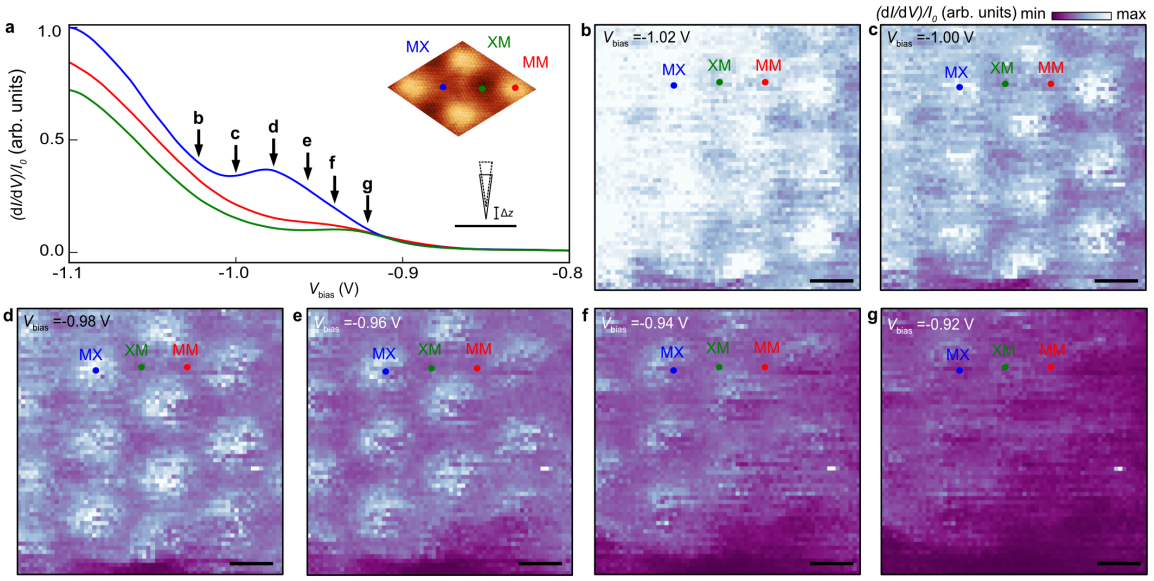

Figure E.3: **Localization of K-point states for tMoTe$_2$ with $\theta = 3.48°$. a**, Averaged reduced-height dI/dV spectra at MM, MX, and XM (3x3 pixels, 0.71 nm^2). Insets show a sketch of the measurement technique and a representative STM topograph of the region, with $\varepsilon_{uni} = 0.74\%$, and $\varepsilon_{bi} = 0.00\%$, oriented at 2° with respect to the . The tunneling parameters are $(I_t, V_{bias}) = (50$ pA, -2.0 V). **b-g**, dI/dV maps acquired at different values of V_{bias}, as specified in each panel, with the same color scale across all maps. All maps are assembled from a grid spectroscopy measurement with initial tunneling setpoint $(I_t, V_{bias}) = (10$ pA, -1.2 V). The tip was moved towards the sample by $\Delta z = 0.36$ nm before the bias sweep. The scale bars are all 3 nm. See Supplementary Video 3 for animation of the full evolution with V_{bias}.

V_{bias} across the MX and XM regions. Spatial maps of dI/dV acquired at various fixed V_{bias} (figure 5.8) further show the LDOS localization along strained elongated bright regions surrounding MX and XM. These sharply contrast the maps shown in figure 5.8c of the main text which form an almost perfectly symmetric hexagonal structure owing to the reduced uniaxial strain.

Collectively, these observations suggest that localization of the Γ-point states depends sensitively on twist angle and strain. In figure E.5d, we plot the energy difference, ΔE_Γ, and normalized amplitude ratio, $\frac{\Delta dI/dV_\Gamma}{dI/dV_{MX}+dI/dV_{XM}}$, between the Γ-point features at MX and XM for a variety of regions of tMoTe$_2$. The amplitude ratio appears to correlate better with θ, whereas the energy splitting correlates better with ε_{uni}. However, neither show a definitive trend, possibly due to the large number of intertwined factors that can affect the localization of the Γ-point bands. One especially important parameter is the local interlayer separation, which can selectively shift the edge of Γ bands in TMD heterobilayers.[125, 188, 189] This may explain why the Γ-point features shift significantly from the MX/XM regions to the domain walls to the MM regions, which all have notably different interlayer separation based on the DFT calculations

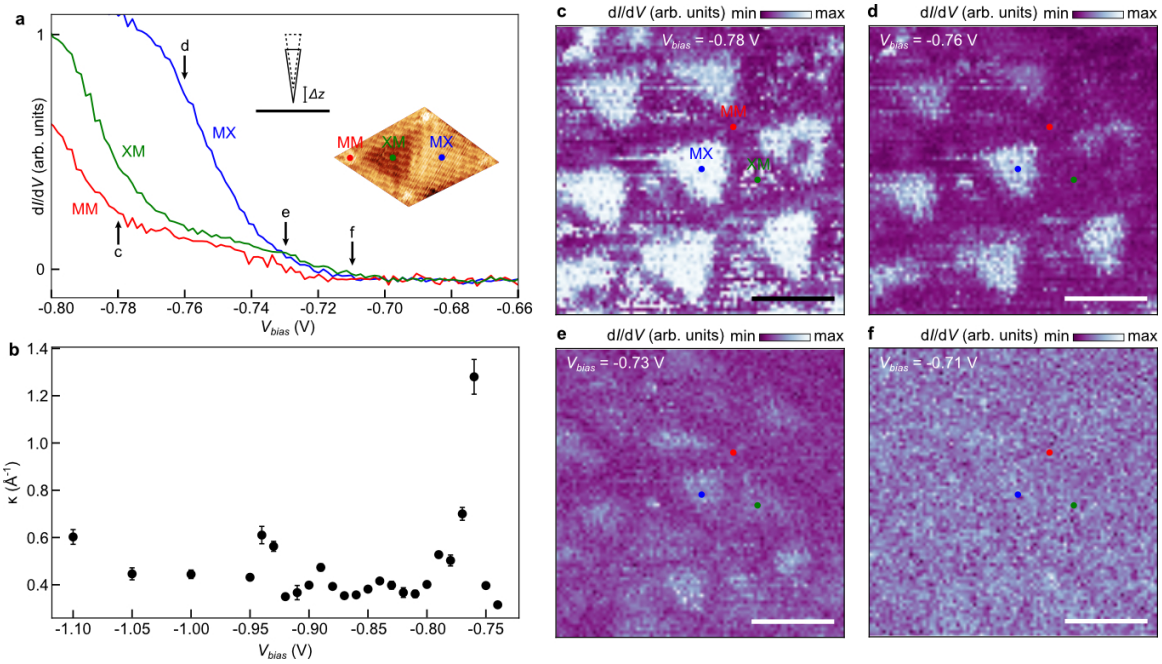

Figure E.4: **Localization of K-point states for tMoTe$_2$ with $\theta = 0.84°$. a**, Averaged reduced-height dI/dV spectra at MM (2x2 pixels, 2.71 nm^2), MX, and XM (4x4 pixels, 10.85 nm^2). Insets show a sketch of the measurement technique and a representative STM topograph of the region, where $\varepsilon = 0.38\%$. **b**, Decay constant as a function of V_{bias} in this region, measured at MX. **c-f**, dI/dV maps acquired at different values of V_{bias}, as specified in each panel and by the arrows in **a**. All maps are assembled from a grid spectroscopy measurement with initial tunneling setpoint $(I_t, V_{bias}) = (90$ pA, -1.1 V$)$. The tip was moved towards the sample by $\Delta z = 0.3$ nm before the bias sweep. The scale bars are all 20 nm. The precise localization of the flat bands at small twist angle appears ambiguous, based on the almost simultaneous rise of dI/dV at around $V_{bias} = -0.72$ V at MX, XM and MM, as well as the lack of a distinct spectral peak (in contrast with the MX case in figure 5.9). Although we are unable to unambiguously determine the layer pseudospin skyrmion texture at this twist angle, our measurements are most consistent with the north pole being at MX given the that we see the largest values of dI/dV there.

shown in figure 5.3c of the main text. Although these calculations predict a similar interlayer separation for MX and XM, they do not account for the presence of the graphene substrate or weak tip-sample interactions that can change the relative interlayer spacing. For instance, the XM region is closer to the graphene than the MX, which may have the effect of slightly changing the XM spacing compared to MX. Figure E.6 shows our calculations of the LDOS at different high symmetry points for different values of the interlayer separation at the MX and XM regions. We see that a splitting in the energy of the Γ-point band edge appears when the interlayer spacing differs between MX and XM, pointing to this effect as a plausible explanation for our observations in strained tMoTe$_2$. Additionally, other electrostatic factors, such at a large electric field from the tip and the effect of the graphene isopotential, may lead to slight

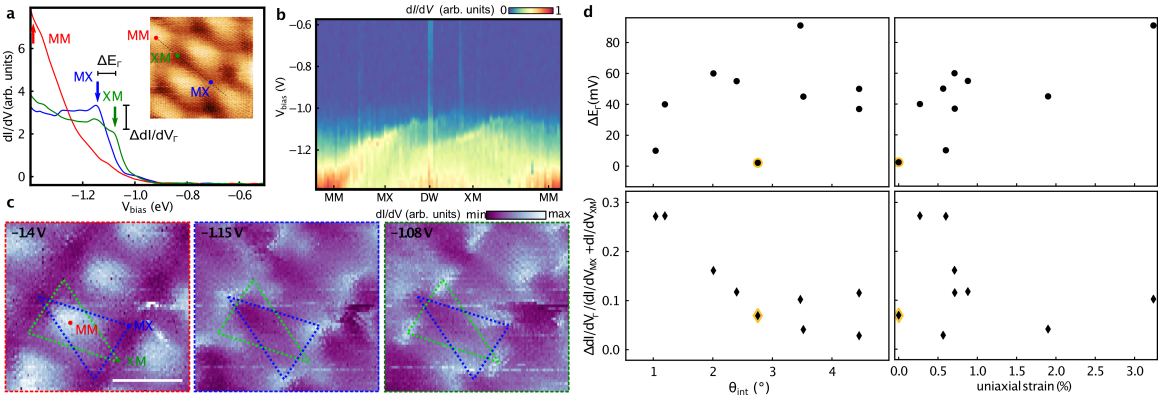

Figure E.5: **Dependence of the localization of Γ states on the local stacking configuration.** **a**, Constant-height tunneling spectra acquired at different high symmetry points for a highly strained region with stacking configuration $\theta = 3.47°$, $\varepsilon_{uni} = 3.24\%$ oriented at 34° with respect to the moiré, $\varepsilon_{bi} = -0.73\%$. **b**, Line cut of the constant-height spectra acquired along the 10 nm long dashed path in **a**, showing shifting of the Γ band edge within the MX/XM regions. **c**, dI/dV maps acquired at different V_{bias} values as indicated by the arrows in **a**, showing an evolution of LDOS localization from MM regions to MX/XM regions. Localization in MX/XM regions is deformed uniaxially along the direction of the heterostrain. All data in this figure is assembled from a grid spectroscopy measurement with initial tunneling setpoint $(I, V_{bias}) = (300$ pA, -1.4 V). Scale bar is 5 nm. **d**, Systematic study of the energy splitting, ΔE_Γ, and the amplitude ratio between the dI/dV peaks at MX and XM, plotted as a function of twist angle and uniaxial heterostrain, ε_{uni}. We find that the amplitude ratio is best correlated with θ, whereas the energy splitting with ε_{uni}. The points highlighted in yellow correspond to the region shown in Figures 5.6, 5.8, and 5.9 of the main text.

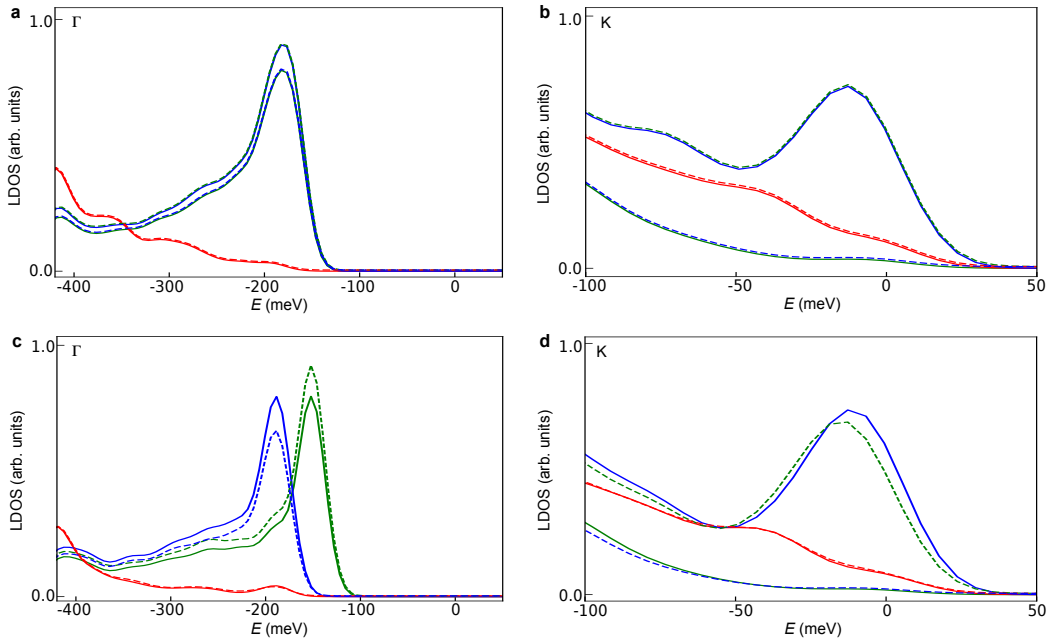

Figure E.6: **Effect of the interlayer distance on the calculated LDOS. a-b**, Calculated LDOS at different stacking sites within the unit cell for $\theta = 3.48°$ in the top layer (solid lines) and bottom layer (dashed lines). The calculation in **a** is for Γ-point states, and for **b** it is for K-point states. **c-d**, Similar calculations but with the interlayer separation artificially increased by .05 at the MX region and decreased by .05 at the XM region. This difference in interlayer separation clearly induces a splitting between Γ-point peaks at the MX and XM regions, but has negligible effect on the K-point states.

differences between the magnitude of the LDOS between the MX and XM regions (see figure 5.11).

Appendix F

COMPARISON OF SPECTROSCOPY METHODS IN $TMOTE_2$

F.0.1 Comparison of spectroscopy methods

In addition to the constant-height spectroscopy techniques employed in the main text, we have also studied $tMoTe_2$ using constant-current spectroscopy. This is a dynamic spectroscopy measurement in which the current feedback loop is maintained during the entire V_{bias} sweep, allowing the tip height to fluctuate with the current maintained at a constant value while a $\mathrm{d}I/\mathrm{d}V$ spectrum is acquired. Representative constant-current spectroscopy data is shown in Figure F.1.

Assuming the tip DOS is featureless in energy and operating at zero temperature, the tunneling current is a function of the sample LDOS, $\nu(E)$, and tunneling probability, $T(E,V,z)$:

$$I(V) \propto \int_{E_F}^{E_F+eV} \nu(E)T(E,V,z)dE, \quad T(E,V,z) = e^{-2\kappa(E,V)z} \tag{F.1}$$

where κ is the decay constant, z is the tip-sample distance, and V is the tip-sample bias. It follows that several terms contribute to the measured differential tunneling conductance, $\mathrm{d}I/\mathrm{d}V$:

$$\frac{\mathrm{d}I}{\mathrm{d}V} \propto \nu(E_F+eV)T(E_F+eV,V,z) + \int_{E_F}^{E_F+eV} \nu(E)\frac{\mathrm{d}T(E,V,z)}{\mathrm{d}V}dE. \tag{F.2}$$

With standard constant-height spectroscopy, the second term above is often neglected as z remains constant and κ is assumed to vary slowly over the bias sweep. With constant-current spectroscopy, however, z is not fixed and is instead a function of V set by the constraint $I = \text{const}$; still the $\mathrm{d}I/\mathrm{d}V$ signal can be attributed mostly to DOS[127,147] (i.e., the first term in Supplementary Information Eq. (F.2)) as long as the tip height and decay constant variations are sufficiently small. In a case where any of these conditions break down, this second term in Supplementary Information Eq. (F.2) represents a non-negligible contribution the the measured $\mathrm{d}I/\mathrm{d}V$. This contribution can be separated into two terms dominated by the variation of κ and z:

$$\frac{\mathrm{d}T(E,V,z)}{\mathrm{d}V} = -2\left[\kappa(E,V)\frac{\mathrm{d}z(V)}{\mathrm{d}V} + z(V)\frac{\partial\kappa(E,V)}{\partial V}\right]e^{-2\kappa(E,V)z(V)}. \tag{F.3}$$

To examine the effect of these two terms, $\kappa(E,V)$ can first be estimated via the expression,

$$\kappa = \sqrt{\frac{2m(\phi_0 - E - e|V|/2)}{\hbar^2} + k_{||}^2(E)}, \tag{F.4}$$

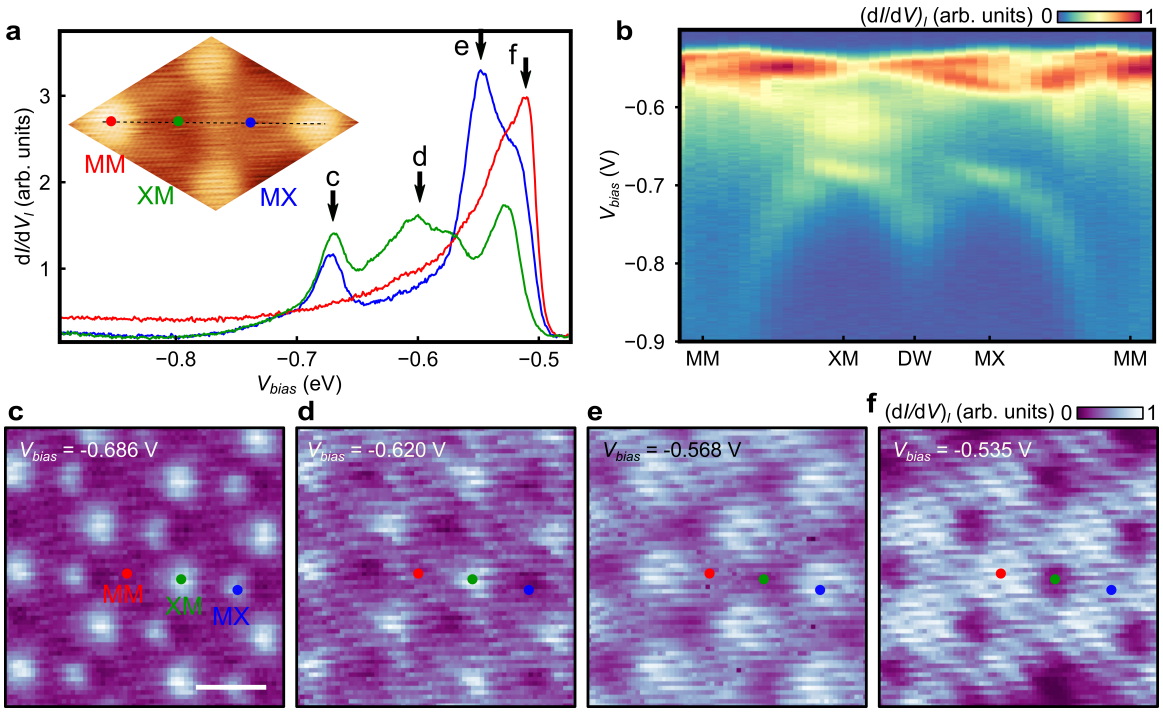

Figure F.1: **Constant-current spectroscopy of the valence band edge. a**, Constant-current $\mathrm{d}I/\mathrm{d}V_I$ spectra acquired at different high symmetry points (2x2 pixels, 0.62 nm^2) for the same $\theta = 2.75°$ region shown in figures 5.3e, 5.8 and 5.9a-b of the main text. The highest intensity peaks correspond to the valence band edge, where the signal can have non-negligible contribution from the $\mathrm{d}z/\mathrm{d}V$ component that diverges when the tip-sample separation reduces in order to tunnel directly into the underlying graphene p_z orbitals. This signal is thus likely to be very dependent on the relative height of the different $tMote_2$ regions, and could produce artifacts at the MM region owing to its large height. The inset shows the topography for this region, and a 10 nm long dashed line. **b**, Line cut of the constant-current spectra along the dashed path from **a**, showing the smooth spatial variation of the band-edge localization. The arch-like features for $V_{bias} \lessapprox -0.67$ V correspond to Γ-point states, consistent with the behavior seen in figure 5.8b of the main text. **c-f**, Corresponding $\mathrm{d}I/\mathrm{d}V_I$ maps at various V_{bias} showing spatial localization of LDOS at the MX/XM, XM, MX, and then MM regions, successively, from left to right. The origin of the localization on XM at $V_{bias} = -0.62$ V is currently unclear. Initial tunneling setpoint is $(I_t, V_{bias}) = (10\ \text{pA}, -0.9\ \text{V})$, scale bar is 5 nm.

where ϕ_0 is the average work function of the tip and the sample and $k_{||}$ is the parallel momentum. Here, because the relevant work functions are a few times larger than the applied bias,[164,165] the variation of κ with V will be small and the second term in Supplementary Information Eq. (F.3) still gives negligible contribution.

However, as the bias is tuned out of the valence band and into the semiconducting gap of $MoTe_2$ and the dominant tunneling channel switches, the tip experiences a sudden drop in height towards the sample. As a consequence, the assumption of a slowly varying z as a function of bias breaks down, and the first term in Supplementary Information Eq. (F.3) can become relevant as $\mathrm{d}z(V)/\mathrm{d}V$ is now a large negative quantity. This is particularly true at the MM regions of the $tMoTe_2$, where the distance between the top layer of $MoTe_2$ and the graphene is largest and a more pronounced drop in tip height is expected. This may explain the large peak in the constant-current spectra on MM denoted by the red arrow in figure F.1a, which is not seen in the reduced-height spectroscopy shown in figure 5.9b of the main text.

In summary, the constant-current spectroscopy technique can enable a good identification of the energy of the band edge even when κ is large, as in $tMoTe_2$. However, we also find that it can be prone to artifacts owing to the complexity of both physical and electronic structure of $tMoTe_2$. In particular, the moiré-scale corrugations of the $tMoTe_2$ can result in additional complications not present in flat monolayer TMDs.[147] Therefore, a direct interpretation of the constant-current spectroscopy in the context of the LDOS requires careful consideration and modeling of κ and z as a function of energy and bias, which is beyond the scope of our study.

F.0.2 Normalization

When performing reduced-height spectroscopy (which is fundamentally the same as constant-height spectroscopy), z is kept constant with the feedback loop open. Because the relevant work functions are a few times larger than the applied bias,[164,165] the tunneling barrier and thus κ is effectively V-independent according to Supplementary Information Eq. (F.4). The second term in Supplementary Information Eq. (F.2) can therefore be neglected. In the case of tunneling primarily into the K-point states of $MoTe_2$, which is true near the band edge, κ can be further approximated to be E-independent. This gives

$$I \propto e^{-2\kappa z} \int_{E_F}^{E_F+eV} \nu(E) dE \implies \frac{\mathrm{d}I}{\mathrm{d}V} \propto e^{-2\kappa z} \nu(E_F + eV). \tag{F.5}$$

Although the $\mathrm{d}I/\mathrm{d}V$ signal is purely proportional to the LDOS here (as opposed to the case of constant-current spectroscopy described above), the proportionality factor can still vary from spectrum to spectrum due to slight differences in the stabilization condition leading to slightly different z. At small z, in particular, this effect is exponentially amplified. This artifact can be mitigated by normalizing the

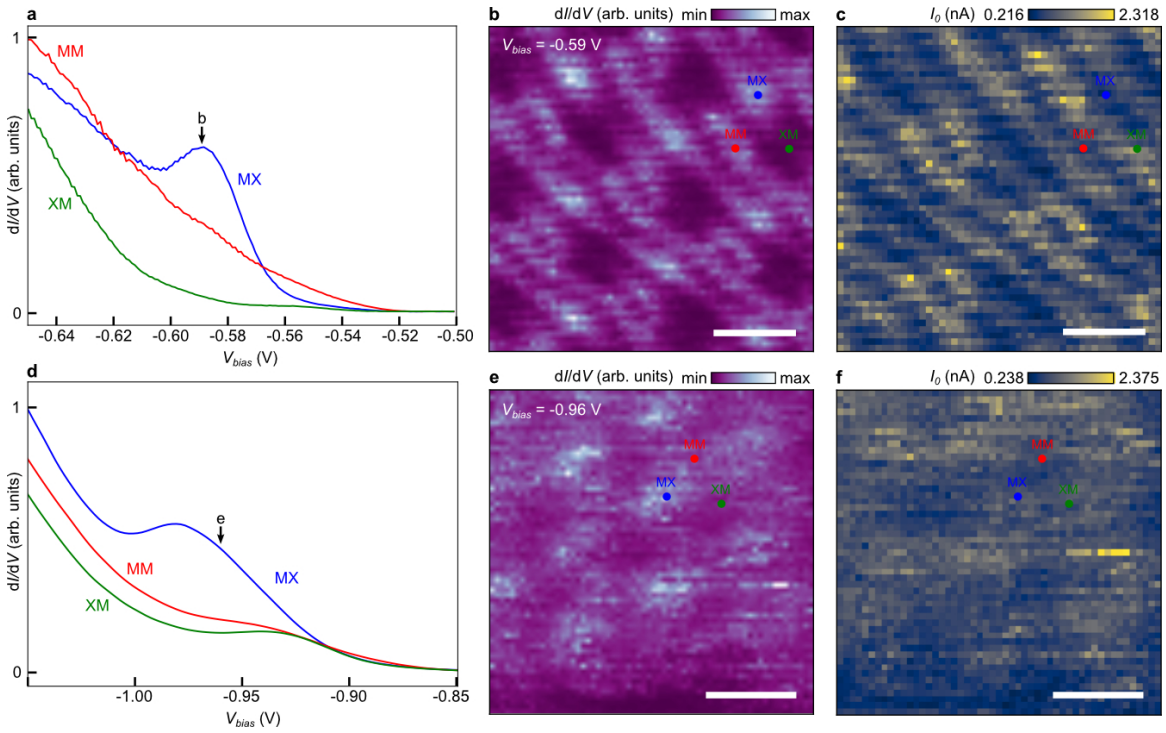

Figure F.2: **Unnormalized reduced-height spectroscopy a**, Representative unnormalized reduced-height spectra averaged at three different high-symmetry sites on the $\theta = 2.75°$ region. **b**, $\mathrm{d}I/\mathrm{d}V$ map at the MX peak energy indicated by the arrow in **a**, obtained from the same set of reduced-height spectra. **c**, Initial current, I_0, of the reduced height spectra taken at each point in space. **a-c** are from the same dataset as figure 5.9a-b of the main text. **d-f**, Same as **a-c**, but for a $\theta = 3.48°$ region, from the same dataset as figure E.3. All scale bars are 5 nm.

measured $\mathrm{d}I/\mathrm{d}V$ by the current at a specific bias, $I_0 = I(V_0)$, which gives

$$\frac{1}{I_0}\frac{\mathrm{d}I}{\mathrm{d}V} \propto \frac{\nu(E_F + eV)}{\int_{E_F}^{E_F+eV_0} \nu(E)\mathrm{d}E}. \tag{F.6}$$

This quantity is proportional to the DOS and does not depend on z, which makes the comparison between spectra taken at positions with similar $\nu(E)$ structure, i.e. in the vicinity of equivalent high-symmetry sites, more consistent. In our case, I_0 was chosen to be the initial current of each spectrum. However, since $\nu(E)$ varies across the unit cell, the denominator in Supplementary Information Eq. (F.6) can be highly position-dependent. Therefore, special care has to be taken when comparing normalized spectra across different points in the unit cell.

Figure F.2a(d) shows the unnormalized reduced-height $\mathrm{d}I/\mathrm{d}V$ spectra averaged at three different high-symmetry sites for $tMoTe_2$ with $\theta = 2.75°$ ($3.48°$). The shapes of the spectra are largely the same as the normalized cases shown in figure 5.9b (E.3a), exhibiting a spectral peak only at the MX site. Figure F.2b(e) shows a $\mathrm{d}I/\mathrm{d}V$ map acquired at a value of V_{bias} within the peak, assembled from the same unnormalized reduced-height spectra. Similarly, the map reflects the same hierarchy of localization at different stacking sites as shown in the normalized map in figure 5.9a (figure E.3e), albeit with noticeable noise. This noise is primarily a consequence of fluctuations in the stabilization condition of each spectrum, appearing also in the I_0 map shown in figure F.2c(f). Normalizing by I_0 thus eliminates this noise, yielding the spectra and maps shown in figures 5.9a-b (figure E.33). Furthermore, I_0 shows minimal correlation to the real-space position at which the corresponding spectrum is taken. This demonstrates that the normalization procedure introduces minimal artifacts and instead simply removes a significant portion of the noise.